Contents

Section A

General Chaos Control Methods

Chapter 1

ROBUST SYNCHRONIZATION OF CHAOTIC SYSTEMS BASED ON TIME-DELAYED FEEDBACK CONTROL

H. Huang and G. Feng

Department of Manufacturing Engineering and Engineering Management, City University of Hong Kong, Kowloon, Hong Kong, hhuang@student.cityu.edu.hk; megfeng@cityu.edu.hk

The master-slave synchronization problem for chaotic Lur'e systems is studied in this chapter based on time-delayed feedback control. It is assumed that the master system of the synchronization scheme is subject to noise disturbances. Delay-independent and delay-dependent synchronization criteria are presented such that the controlled slave system can robustly track the noise-disturbed master system with guaranteed H_∞ performance. It is shown that the design of the time-delayed feedback controller can be accomplished by means of the feasibility of linear matrix inequalities. A simulation example is finally given to demonstrate the effectiveness and performance of the developed approaches.

1.1. Introduction

Since the pioneering work of Pecora and Carroll [1], chaotic synchronization has been an active research topic and achieved many successful applications, such as secure communication, chemical reactions and information processing (see, e.g., [2–8]). On the other hand, the so-called Lur'e systems are regarded as a class of feedback systems whose forward path is a linear time-invariant system and whose feedback path is a memoryless (possibly time-varying) nonlinearity satisfying a sector condition [9]. As is well known now, many nonlinear systems can be represented in this form, such as Chua's Circuit [10], n-scroll attractors [11] and hyperchaotic attractors [12], and so on. The master-slave synchronization problem for chaotic Lur'e systems has recently attracted considerable interest. It basically relates to give sufficient conditions for master-slave synchronization for

identical or nonidentical Lur'e systems. A unified framework for synchronization of dynamical systems was presented in [13], as well as the relation between synchronization and global asymptotical stability. The absolute stability theory was utilized in the development of synchronization conditions for master-slave Lur'e systems via static and linear feedback in [4, 5]. By applying the vector modulation and either full static state feedback or linear dynamic output error feedback, the authors in [14–18] investigated the master-slave synchronization schemes for identical or nonidentical Lur'e systems. A unifying definition for synchronization between stationary finite dimensional deterministic dynamical systems was presented in [2]. An excellent overview of various methods for synchronization of chaotic systems was available in [3].

It is also known that time delay is often encountered in various control systems, which is one of the main sources for instability and poor performance [19–21]. From the point of view of control, time-delayed systems have received special attention over the past few years [22]. The propagation delay was firstly introduced into the chaotic synchronization problem in [23]. The authors called this problem a phase sensitivity because of the distance between two remote chaotic systems and showed that the existence of time delay may destroy synchronization. During the past few years, the master-slave synchronization problem via time-delayed feedback control has received much attention, and many results have been reported in the open literature. In [24–27], several delay-independent and delay-dependent synchronization conditions have been proposed to ensure the error system to be globally asymptotically stable. However, it is worth noting that in those works, the feedback gain matrices can be designed only when a nonlinear programming problem corresponding to the derived matrix inequalities conditions is solved. Recently, the linear matrix inequality (LMI) approach has been widely used in circuits, systems, and control community, because it can be solved efficiently by the standard numerical packages [28, 29]. The authors in [30, 31] have presented some LMI based synchronization criteria such that the controlled slave system can track the master system. The existing results related to this issue can be generally classified into two categories: delay-independent synchronization criteria [24, 26, 27] and delay-dependent synchronization criteria [25, 30, 31]. The delay-independent conditions are irrespective of the size of time delay. While the delay-dependent conditions are related to the size of time delay. Generally, the delay-dependent conditions are considered to be less conservative than the delay-independent conditions, especially when the size of

time delay is small.

In recent years, a wide variety of synchronization approaches have been proposed to handle the master-slave synchronization problem, which includes adaptive control [32, 33], fuzzy control [34, 35], coupling control [36], manifold-based method [37], active control [38], impulsive-control method [39], and time-delayed feedback approach [25, 27], etc. In this chapter, our attention is focused on the master-slave synchronization problem for chaotic Lur'e systems by using the *time-delayed feedback control method*. In the synchronization scheme, the master system is assumed to be disturbed by the exogenous noise input. The main objective of this chapter is to study the master-slave synchronization for chaotic Lur'e systems with guaranteed performance in H_∞ sense. A delay-independent synchronization criterion is first given such that the controlled slave system can robustly track the master system. As mentioned above, the delay-independent conditions are often more conservative than the delay-dependent conditions. Then, delay-dependent conditions are presented to ensure the existence of the desired time-delayed feedback controller such that the master system and the slave system are synchronized. Moreover, several slack variables are introduced to further reduce the conservatism of the synchronization conditions. It is also shown that the design of the time-delayed feedback controller can be achieved by solving some LMIs. Finally, the Chua's Circuit system [10, 40] is used as an example to demonstrate the application of the proposed time-delayed feedback controller design approaches and their performance.

The rest of this chapter is organized as follows. The master-slave synchronization scheme is formulated in Section 1.2 for chaotic Lur'e systems with time-delayed feedback control, and some preliminaries are also given. Section 1.3 is dedicated to presenting a delay-independent synchronization criterion such that the existence of the feedback controller can be guaranteed by means of the feasibility of an LMI. In Section 1.4, delay-dependent synchronization conditions without/with slack variables are obtained by using the well-known Jensen's inequality and a newly established bounding technique, respectively, such that the controlled slave system can synchronize the master system with guaranteed H_∞ performance. An example with simulation results is used to demonstrate the effectiveness of the developed approach in Section 1.5, which is followed by conclusions in Section 1.6.

1.2. Problem Formulation

Notations: The following notations adopted in this chapter are standard. Let $\mathbb{R}$ denote the set of real numbers, $\mathbb{R}^n$ the n-dimensional Euclidean space and $\mathbb{R}^{n\times m}$ the set of all $n\times m$ real matrices. The superscript "T" stands for matrix transposition. I is the identity matrix with appropriate dimension. For a real square matrix X, the notation $X > 0$ ($X \geq 0, X < 0, X \leq 0$) means that X is real symmetric and positive definite (positive semi-definite, negative definite, negative semi-definite, respectively). For $\tau > 0$, $\mathcal{C}([-\tau, 0]; \mathbb{R}^n)$ denotes the family of continuous functions φ from $[-\tau, 0]$ to $\mathbb{R}^n$ with the norm $\|\varphi\| = \sup_{-\tau\leq\vartheta\leq 0} |\varphi(\vartheta)|$, where $|\cdot|$ is the Euclidean norm in $\mathbb{R}^n$. Let $L_2[0,\infty)$ be the space of square-integrable vector functions over $[0,\infty)$. The shorthand notation $\mathrm{diag}\{M_1, M_2, \ldots, M_N\}$ denotes a block diagonal matrix with diagonal blocks being the matrices $M_1, M_2, \ldots, M_N$. The notation $*$ always denotes the symmetric block in a symmetric matrix, e.g.,

$$\begin{bmatrix} X & Y \\ * & Z \end{bmatrix} = \begin{bmatrix} X & Y \\ Y^T & Z \end{bmatrix}.$$

Matrices, if not explicitly stated, are assumed to have compatible dimensions. Sometimes, the arguments of a function will be omitted in the analysis when no confusion can arise.

Consider a master-slave synchronization scheme for chaotic Lur'e systems with time-delayed feedback control, in which the master system is subject to noise input:

$$\begin{aligned} \mathcal{M}: &\begin{cases} \dot{x}(t) = Ax(t) + B\sigma(Cx(t)) + Dw(t) \\ p(t) = Hx(t) \end{cases} \\ \mathcal{S}: &\begin{cases} \dot{y}(t) = Ay(t) + B\sigma(Cy(t)) + u(t) \\ q(t) = Hy(t) \end{cases} \\ \mathcal{C}: &\ u(t) = M(p(t-\tau) - q(t-\tau)) \end{aligned} \tag{1.1}$$

with master system $\mathcal{M}$, slave system $\mathcal{S}$ and time-delayed feedback controller $\mathcal{C}$. Fig. 1.1 is a block diagram of the master-slave synchronization scheme (1.1). The master and slave systems are the so-called Lur'e systems with state vectors $x(t), y(t) \in \mathbb{R}^n$ and output vectors $p(t), q(t) \in \mathbb{R}^l$, respectively. $w(t) \in \mathbb{R}^m$ is the disturbance term belonging to $L_2[0,\infty)$. The real matrices $A \in \mathbb{R}^{n\times n}, B \in \mathbb{R}^{n\times n_h}, C \in \mathbb{R}^{n_h\times n}, D \in \mathbb{R}^{n\times m}$ and $H \in \mathbb{R}^{l\times n}$ are known

constant matrices. $\tau \geq 0$ is a constant time delay. As in [9, 15, 27], the diagonal nonlinearity $\sigma(\cdot) : \mathbb{R}^{n_h} \mapsto \mathbb{R}^{n_h}$ satisfies a sector condition with $\sigma_i(\cdot)$ $(i = 1, 2, \ldots, n_h)$ belonging to sector $[0, k]$. That is,

$$\sigma_i(\xi)(\sigma_i(\xi) - k\xi) \leq 0, \forall\ \xi,\ \text{for } i = 1, 2, \ldots, n_h. \tag{1.2}$$

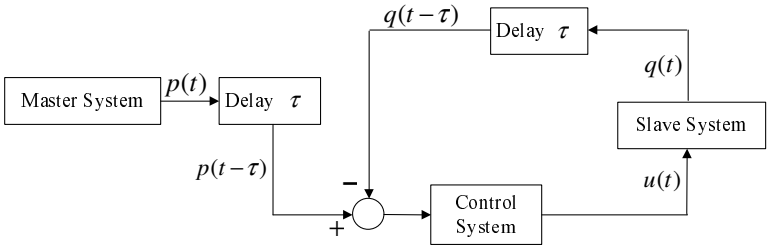

Fig. 1.1. Time-delayed feedback control based master-slave synchronization scheme.

The scheme aims at robustly synchronizing the slave system $\mathcal{S}$ to the noise-perturbed master system $\mathcal{M}$ with a guaranteed performance by utilizing the time-delayed feedback to the slave system $\mathcal{S}$ with control signal $u(t) \in \mathbb{R}^n$ with feedback gain matrix $M \in \mathbb{R}^{n\times l}$ and time delay τ.

Remark 1.1. The time-delayed feedback control based master-slave synchronization scheme for Lur'e systems is assumed to be subject to noise perturbation, which may be more practical than those studied in [5, 18, 24, 26, 27]. When $w(t) = 0$ and $\tau = 0$, the master-slave synchronization scheme (1.1) reduces to the one studied in [5, 18]. When $w(t) = 0$, the master-slave synchronization scheme (1.1) degenerates into the one discussed in [27]. The purpose of this chapter is to develop several approaches to dealing with the guaranteed performance synchronization problem for chaotic Lur'e systems. It should be pointed out that based on the developed approaches, some delay-independent and delay-dependent synchronization criteria can be easily obtained for Lur'e systems studied in [5, 18, 24, 26, 27].

Define the errors $e(t) = x(t) - y(t)$ and $z(t) = p(t) - q(t)$, then the error system can be obtained as follows:

$$\mathcal{E} : \dot{e}(t) = Ae(t) - MHe(t-\tau) + B\eta(Ce(t), y(t)) + Dw(t), \tag{1.3}$$

$$z(t) = He(t), \tag{1.4}$$

with $\eta(Ce(t), y(t)) = \sigma(Ce(t) + Cy(t)) - \sigma(Cy(t))$.

Let $C = \left[\begin{array}{cccc} c_1 & c_2 & \dots & c_{n_h} \end{array} \right]^T$ with $c_i \in \mathbb{R}^n$ (i.e., c_i^T denotes the ith row vector of C). As in [4, 18, 27], to obtain synchronization criteria for the master-slave synchronization scheme (1.1), the following assumption is made:

$\mathcal{A}$: The nonlinearity $\eta(Ce, y)$ belongs to sector $[0, k]$, namely,

$$0 \leq \frac{\eta_i(c_i^T e, y)}{c_i^T e} = \frac{\sigma_i(c_i^T e + c_i^T y) - \sigma_i(c_i^T y)}{c_i^T e} \leq k, \\ \forall e, y; i = 1, 2, \dots, n_h (c_i^T e \neq 0). \quad (1.5)$$

Then, it follows from (1.5) that

$$\eta_i(c_i^T e, y)(\eta_i(c_i^T e, y) - k c_i^T e) \leq 0, \quad \forall\ e,\ y; \quad i = 1, 2, \dots, n_h. \quad (1.6)$$

The objective of this chapter is to develop several delay-independent and delay-dependent approaches to the design of the time-delayed feedback controller, such that controlled slave system $\mathcal{S}$ can robustly synchronize the master system $\mathcal{M}$ with a guaranteed performance in the H_∞ sense. That is, given a prescribed level of noise attenuation $\gamma > 0$, find a suitable time-delayed feedback controller $\mathcal{C}$ such that the error system (1.3) with $w(t) = 0$ is globally asymptotically stable, and

$$\|z(t)\|_2 < \gamma \|w(t)\|_2 \quad (1.7)$$

under zero-initial conditions for all nonzero $w(t) \in L_2[0, \infty)$, where the norm $\|\cdot\|_2$ is defined as

$$\|\psi\|_2 := \sqrt{\int_0^\infty \psi^T(t)\psi(t)dt}.$$

In this case, the master system $\mathcal{M}$ and the slave system $\mathcal{S}$ are said to be synchronized with guaranteed H_∞ performance γ.

We end this section by recalling two lemmas.

Lemma 1.1 (Schur complement [28]). *The LMI*

$$\left[\begin{array}{cc} S_{11} & S_{12} \\ S_{12}^T & -S_{22} \end{array} \right] < 0,$$

where $S_{11} = S_{11}^T, S_{22} = S_{22}^T$, is equivalent to

$$S_{22} > 0, \quad S_{11} + S_{12} S_{22}^{-1} S_{12}^T < 0.$$

Lemma 1.2 (Jensen inequality [19]). *For any constant matrix* $\mathcal{X} \in \mathbb{R}^{m\times m}, \mathcal{X} = \mathcal{X}^T$*, scalar* $\delta > 0$*, vector function* $\omega : [0, \gamma] \to \mathbb{R}^m$ *such that the integrations concerned are well defined, then*

$$\delta \int_0^\delta \omega^T(s)\mathcal{X}\omega(s)ds \geq \Big(\int_0^\delta \omega(s)ds\Big)^T \mathcal{X}\Big(\int_0^\delta \omega(s)ds\Big).$$

1.3. Delay-Independent Synchronization Criterion

First of all, a delay-independent approach is proposed to deal with the master-slave synchronization problem of chaotic systems, which is applicable to time delay of arbitrary size. An LMI synchronization condition is derived for the design of time-delayed feedback controller, such that the controlled slave system can robustly synchronize the noise-disturbed master system with guaranteed H_∞ performance.

Theorem 1.1. *Assume that the feedback gain matrix* M *is given. The master system* $\mathcal{M}$ *and the slave system* $\mathcal{S}$ *are synchronized with guaranteed* H_∞ *performance* γ*, if there exist real matrices* $P > 0, Q > 0$ *and a diagonal matrix* $\Lambda = diag(\lambda_1, \lambda_2, \ldots, \lambda_{n_h}) > 0$ *such that the following LMI holds:*

$$\begin{bmatrix} \Omega_1 & -PMH & PB + kC^T\Lambda & PD & H^T \\ * & -Q & 0 & 0 & 0 \\ * & * & -2\Lambda & 0 & 0 \\ * & * & * & -\gamma^2 I & 0 \\ * & * & * & * & -I \end{bmatrix} < 0, \tag{1.8}$$

where

$$\Omega_1 = PA + A^T P + Q.$$

Proof. We first show that the error system (1.3) with $w(t) = 0$ is globally asymptotically stable under the condition of Theorem 1.1. When $w(t) = 0$, the error system (1.3) can be rewritten as:

$$\dot{e}(t) = Ae(t) - MHe(t-\tau) + B\eta(Ce(t), y(t)). \tag{1.9}$$

It is clear that the LMI (1.8) results in

$$\Omega_2 = \begin{bmatrix} \Omega_1 & -PMH & PB + kC^T\Lambda \\ * & -Q & 0 \\ * & * & -2\Lambda \end{bmatrix} < 0. \tag{1.10}$$

It follows from (1.6) that for any diagonal matrix $\Lambda = \mathrm{diag}(\lambda_1, \lambda_2, \ldots, \lambda_{n_h}) > 0$,

$$\begin{aligned} 0 \leq & -2\sum_{i=1}^{n_h} \lambda_i \eta_i(c_i^T e, y)(\eta_i(c_i^T e, y) - k c_i^T e) \\ & = -2\eta^T(Ce(t), y(t))\Lambda\eta(Ce(t), y(t)) \\ & \quad +2ke^T(t)C^T\Lambda\eta(Ce(t), y(t)). \end{aligned} \tag{1.11}$$

Choose a Lyapunov functional candidate as

$$V_1(t) = e^T(t)Pe(t) + \int_{t-\tau}^{t} e^T(s)Qe(s)ds, \tag{1.12}$$

where $P > 0, Q > 0$ are to be determined. Then, by directly calculating the time-derivative of $V_1(t)$ along the trajectory of system (1.9) and taking (1.11) into account, one has

$$\begin{aligned} \dot{V}_1(t) &= 2e^T(t)P\dot{e}(t) + e^T(t)Qe(t) - e^T(t-\tau)Qe(t-\tau) \\ &= e^T(t)(PA + A^TP)e(t) - 2e^T(t)PMHe(t-\tau) \\ &\quad +2e^T(t)PB\eta(Ce(t), y(t)) + e^T(t)Qe(t) \\ &\quad -e^T(t-\tau)Qe(t-\tau) \\ &\leq e^T(t)(PA + A^TP + Q)e(t) - 2e^T(t)PMHe(t-\tau) \\ &\quad +2e^T(t)PB\eta(Ce(t), y(t)) - e^T(t-\tau)Qe(t-\tau) \\ &\quad -2\eta^T(Ce(t), y(t))\Lambda\eta(Ce(t), y(t)) \\ &\quad +2ke^T(t)C^T\Lambda\eta(Ce(t), y(t)) \\ &= \sigma_1^T(t)\Omega_2\sigma_1(t), \end{aligned} \tag{1.13}$$

with

$$\sigma_1(t) = \left[\begin{array}{ccc} e^T(t) & e^T(t-\tau) & \eta^T(Ce(t), y(t)) \end{array}\right]^T.$$

Since $\Omega_2 < 0$, there must exist a sufficiently small $\epsilon > 0$ such that

$$\Omega_2 + \mathrm{diag}\{\epsilon I, 0, 0\} \leq 0,$$

which implies

$$\dot{V}_1(t) \leq -\epsilon e^T(t)e(t).$$

According to the stability theory of [20], the error system (1.9) is globally asymptotically stable.

Next, to establish the H_∞ performance to the master-slave synchronization scheme (1.1) under zero initial condition, we introduce

$$J(t) = \int_0^\infty \Big[z^T(t)z(t) - \gamma^2 w^T(t)w(t)\Big]dt. \tag{1.14}$$

Under the zero initial condition, from (1.12) one has $V_1(0) = 0$ and $V_1(t) \geq 0$ for $t > 0$. Then

$$\begin{aligned} J(t) &\leq \int_0^\infty \Big[z^T(t)z(t) - \gamma^2 w^T(t)w(t)\Big]dt + V_1(t)|_{t=\infty} - V_1(0) \\ &= \int_0^\infty \Big[z^T(t)z(t) - \gamma^2 w^T(t)w(t) + \dot{V}_1(t)\Big]dt. \end{aligned} \tag{1.15}$$

Following the similar line of the proof of (1.13), it is not difficult to derive that

$$z^T(t)z(t) - \gamma^2 w^T(t)w(t) + \dot{V}_1(t) \leq \sigma_2^T(t)\Omega_3\sigma_2(t) \tag{1.16}$$

with

$$\sigma_2(t) = \left[\begin{array}{cccc} e^T(t) & e^T(t-\tau) & \eta^T(Ce(t), y(t)) & w^T(t) \end{array}\right]^T,$$

$$\Omega_3 = \left[\begin{array}{cccc} \Omega_1 + H^T H & -PMH & PB + kC^T\Lambda & PD \\ * & -Q & 0 & 0 \\ * & * & -2\Lambda & 0 \\ * & * & * & -\gamma^2 I \end{array}\right].$$

By employing Lemma 1.1, the LMI (1.8) is equivalent to $\Omega_3 < 0$. From (1.16), one thus has that for $w(t) \neq 0$

$$z^T(t)z(t) - \gamma^2 w^T(t)w(t) + \dot{V}_1(t) < 0. \tag{1.17}$$

which implies $J(t) < 0$ for $w(t) \neq 0$. That is to say, $\|z(t)\|_2 < \gamma\|w(t)\|_2$. Therefore, the master system $\mathcal{M}$ and the slave system $\mathcal{S}$ are synchronized with guaranteed H_∞ performance γ. This completes the proof. □

The following theorem presents a delay-independent synchronization controller design method to ensure that the slave system $\mathcal{S}$ can synchronize the master system $\mathcal{M}$ with guaranteed H_∞ performance γ, which is formulated by means of the feasibility of an LMI.

Theorem 1.2. *Let $\gamma > 0$ be a prescribed constant scalar. The master system $\mathcal{M}$ and the slave system $\mathcal{S}$ are synchronized with guaranteed H_∞*

performance γ, if there exist real matrices $P > 0, Q > 0, G$ and a diagonal matrix $\Lambda = diag(\lambda_1, \lambda_2, \ldots, \lambda_{n_h}) > 0$ such that the following LMI holds:

$$\begin{bmatrix} \Omega_4 & -GH & PB + kC^T\Lambda & PD & H^T \\ * & -Q & 0 & 0 & 0 \\ * & * & -2\Lambda & 0 & 0 \\ * & * & * & -\gamma^2 I & 0 \\ * & * & * & * & -I \end{bmatrix} < 0, \tag{1.18}$$

where

$$\Omega_4 = PA + A^T P + Q.$$

And the feedback gain matrix can be designed as

$$M = P^{-1}G.$$

Proof. It can be directly deduced from Theorem 1.1 by applying the change of the variable $M = P^{-1}G$. □

Remark 1.2. It should be noted that the performance index γ described in Theorem 1.2 can be optimized by the convex optimization algorithm [28, 29].

Algorithm 1.1. $\min_{P,Q,G,\Lambda} \gamma^2$, subject to the LMI (1.18).

Remark 1.3. The master-slave synchronization scheme (1.1) with $w(t) = 0$ was studied in [26, 27], where the obtained delay-independent synchronization criteria were expressed in terms of matrix inequalities. From Theorems 1.1 and 1.2, an LMI based synchronization condition can be immediately derived shown in the following corollary.

Corollary 1.1. *The master-slave synchronization described in* (1.1) *with $w(t) = 0$ can be achieved with $M = P^{-1}G$, if there exist real matrices $P > 0, Q > 0, G$ and a diagonal matrix $\Lambda > 0$ such that*

$$\begin{bmatrix} \Omega_4 & -GH & PB + kC^T\Lambda \\ * & -Q & 0 \\ * & * & -2\Lambda \end{bmatrix} < 0, \tag{1.19}$$

where Ω_4 is the same as the one in Theorem 1.2.

In general, the delay-independent synchronization condition is viewed to be more conservative than the delay-dependent counterpart, especially when the size of time delay is small. It is thus worth developing delay-dependent synchronization criteria. The following section is to this purpose.

1.4. Delay-Dependent Synchronization Criteria

By utilizing the well-known Jensen inequality [22], a delay-dependent synchronization condition is first proposed in this section.

Theorem 1.3. *Assume that the feedback gain matrix M is given. The master system $\mathcal{M}$ and the slave system $\mathcal{S}$ are synchronized with guaranteed H_∞ performance γ, if there exist real matrices $P > 0, Q > 0, R > 0$ and a diagonal matrix $\Lambda = diag(\lambda_1, \lambda_2, \ldots, \lambda_{n_h}) > 0$ such that the following LMI holds:*

$$\begin{bmatrix} \Sigma_1 & -PMH + R & \Sigma_2 & PD & \tau A^T R & H^T \\ * & -Q - R & 0 & 0 & -\tau H^T M^T R & 0 \\ * & * & -2\Lambda & 0 & \tau B^T R & 0 \\ * & * & * & -\gamma^2 I & \tau D^T R & 0 \\ * & * & * & * & -R & 0 \\ * & * & * & * & * & -I \end{bmatrix} < 0, \quad (1.20)$$

where

$$\Sigma_1 = PA + A^T P + Q - R,$$
$$\Sigma_2 = PB + kC^T \Lambda.$$

Proof. As in the proof of Theorem 1.1, we first prove that the error system (1.3) with $w(t) = 0$ is globally asymptotically stable under the condition of Theorem 1.3. It follows from the LMI (1.20) that

$$\Sigma_3 = \begin{bmatrix} \Sigma_1 & -PMH + R & \Sigma_2 & \tau A^T R \\ * & -Q - R & 0 & -\tau H^T M^T R \\ * & * & -2\Lambda & \tau B^T R \\ * & * & * & -R \end{bmatrix} < 0. \quad (1.21)$$

By using Lemma 1.1, the LMI (1.21) is equivalent to $\Sigma_4 + \tau^2 \Sigma_5^T R \Sigma_5 < 0$, with

$$\Sigma_4 = \begin{bmatrix} \Sigma_1 & -PMH + R & PB + kC^T \Lambda \\ * & -Q - R & 0 \\ * & * & -2\Lambda \end{bmatrix},$$
$$\Sigma_5 = \begin{bmatrix} A & -MH & B \end{bmatrix}.$$

Then, there must exist a sufficiently small scalar $\epsilon > 0$ such that

$$\Sigma_4 + \tau^2 \Sigma_5^T R \Sigma_5 + \mathrm{diag}\{\epsilon I, 0, 0\} \leq 0. \quad (1.22)$$

In addition, for any diagonal matrix $\Lambda = \mathrm{diag}(\lambda_1, \lambda_2, \ldots, \lambda_{n_h}) > 0$,

$$\begin{aligned} 0 \leq & -2\sum_{i=1}^{n_h} \lambda_i \eta_i(c_i^T e, y)(\eta_i(c_i^T e, y) - k c_i^T e) \\ = & -2\eta^T(Ce(t), y(t))\Lambda\eta(Ce(t), y(t)) \\ & +2ke^T(t)C^T\Lambda\eta(Ce(t), y(t)). \end{aligned} \tag{1.23}$$

Choose a Lyapunov functional candidate as:

$$\begin{aligned} V_2(t) = & e^T(t)Pe(t) + \int_{t-\tau}^{t} e^T(s)Qe(s)ds \\ & +\tau\int_{-\tau}^{0}\int_{t+\theta}^{t} \dot{e}^T(s)R\dot{e}(s)dsd\theta, \end{aligned} \tag{1.24}$$

where $P > 0, Q > 0$ and $R > 0$ are to be determined. By calculating the time-derivative of $V_2(t)$ along the solution of system (1.9), one can derive

$$\begin{aligned} \dot{V}_2(t) = & 2e^T(t)P\dot{e}(t) + e^T(t)Qe(t) - e^T(t-\tau)Qe(t-\tau) \\ & +\tau^2\dot{e}^T(t)R\dot{e}(t) - \tau\int_{t-\tau}^{t}\dot{e}^T(s)R\dot{e}(s)ds \\ = & e^T(t)\Big[PA + A^TP + Q\Big]e(t) \\ & -2e^T(t)PMHe(t-\tau) + 2e^T(t)PB\eta(Ce(t), y(t)) \\ & -e^T(t-\tau)Qe(t-\tau) + \tau^2\dot{e}^T(t)R\dot{e}(t) \\ & -\tau\int_{t-\tau}^{t}\dot{e}^T(s)R\dot{e}(s)ds. \end{aligned} \tag{1.25}$$

By Lemma 1.2, one has

$$\begin{aligned} -\tau\int_{t-\tau}^{t}\dot{e}^T(s)R\dot{e}(s)ds \leq & -\Big(\int_{t-\tau}^{t}\dot{e}(s)ds\Big)^T R\int_{t-\tau}^{t}\dot{e}(s)ds \\ = & -[e(t) - e(t-\tau)]^T R[e(t) - e(t-\tau)] \\ = & -e^T(t)Re(t) + 2e^T(t)Re(t-\tau) \\ & -e^T(t-\tau)Re(t-\tau). \end{aligned} \tag{1.26}$$

Therefore, from (1.22), (1.23), (1.25) and (1.26), it is not difficult to derive

$$\begin{aligned}\dot{V}_2(t) &\le e^T(t)\Big[PA + A^TP + Q - R\Big]e(t)\\ &\quad +2e^T(t)(-PMH + R)e(t-\tau) + 2e^T(t)(PB + kC^T\Lambda)\eta(Ce(t), y(t))\\ &\quad -e^T(t-\tau)(Q+R)e(t-\tau) - 2\eta^T(Ce(t), y(t))\Lambda\eta(Ce(t), y(t))\\ &\quad +\tau^2\dot{e}^T(t)R\dot{e}(t)\\ &= \xi_1^T(t)\Big[\Sigma_4 + \tau^2\Sigma_5^T R\Sigma_5\Big]\xi_1(t),\\ &\le -\epsilon e^T(t)e(t), \end{aligned} \tag{1.27}$$

with

$$\xi_1(t) = \left[\begin{array}{cccc} e^T(t) & e^T(t-\tau) & \eta^T(Ce(t), y(t)) \end{array}\right]^T.$$

It follows from [20] that the error system (1.9) is globally asymptotically stable.

Next, to establish the H_∞ performance to the master-slave synchronization scheme (1.1) under zero initial condition, we introduce

$$J(t) = \int_0^\infty \Big[z^T(t)z(t) - \gamma^2 w^T(t)w(t)\Big]dt. \tag{1.28}$$

Under the zero initial condition, it follows from (1.24) that $V_2(0) = 0$ and $V_2(t) \ge 0$ for $t > 0$. Then

$$\begin{aligned} J(t) &\le \int_0^\infty \Big[z^T(t)z(t) - \gamma^2 w^T(t)w(t)\Big]dt + V_2(t)|_{t=\infty} - V_2(0)\\ &= \int_0^\infty \Big[z^T(t)z(t) - \gamma^2 w^T(t)w(t) + \dot{V}_2(t)\Big]dt. \end{aligned} \tag{1.29}$$

Following the similar line of the proof of (1.27), it is easy to obtain that

$$z^T(t)z(t) - \gamma^2 w^T(t)w(t) + \dot{V}_2(t) \le \xi_2^T(t)\Big[\Sigma_6 + \tau^2\Sigma_7^T R\Sigma_7\Big]\xi(t) \tag{1.30}$$

with

$$\begin{aligned} \xi_2(t) &= \left[\begin{array}{cccc} e^T(t) & e^T(t-\tau) & \eta^T(Ce(t), y(t)) & w^T(t) \end{array}\right]^T,\\ \Sigma_6 &= \left[\begin{array}{cccc} \Sigma_1 + H^TH & -PMH + R & PB + kC^T\Lambda & PD\\ * & -Q - R & 0 & 0\\ * & * & -2\Lambda & 0\\ * & * & * & -\gamma^2 I \end{array}\right],\\ \Sigma_7 &= \left[\begin{array}{cccc} A & -MH & B & D \end{array}\right]. \end{aligned}$$

By utilizing Lemma 1.1, the LMI (1.20) results in

$$\Sigma_6 + \tau^2 \Sigma_7^T R \Sigma_7 < 0.$$

It follows from (1.30) that for $w(t) \neq 0$

$$z^T(t)z(t) - \gamma^2 w^T(t)w(t) + \dot{V}_2(t) < 0. \tag{1.31}$$

and thus $J(t) < 0$ for any $w(t) \neq 0$. It leads to $\|z(t)\|_2 < \gamma \|w(t)\|_2$. Therefore, the slave system $\mathcal{S}$ is synchronized to the master system $\mathcal{M}$ with guaranteed H_∞ performance γ. This completes the proof. □

Then we have the following result.

Theorem 1.4. *Let $\gamma > 0$ be a prescribed constant scalar. The master system $\mathcal{M}$ and the slave system $\mathcal{S}$ are synchronized with guaranteed H_∞ performance γ, if there exist real matrices $P > 0, Q > 0, R > 0, G$ and a diagonal matrix $\Lambda > 0$ such that the following LMI holds*

$$\begin{bmatrix} \Sigma_8 & -GH+R & \Sigma_9 & PD & \tau A^T P & H^T \\ * & -Q-R & 0 & 0 & -\tau H^T G^T & 0 \\ * & * & -2\Lambda & 0 & \tau B^T P & 0 \\ * & * & * & -\gamma^2 I & \tau D^T P & 0 \\ * & * & * & * & -2P+R & 0 \\ * & * & * & * & * & -I \end{bmatrix} < 0, \tag{1.32}$$

where

$$\Sigma_8 = PA + A^T P + Q - R,$$
$$\Sigma_9 = PB + kC^T \Lambda.$$

And the feedback gain matrix can be designed as

$$M = P^{-1} G.$$

Proof. By Theorem 1.3, it is only to show that the LMI (1.20) holds. In fact, for $P > 0, R > 0$,

$$P^T R^{-1} P - 2P + R = (P-R)^T R^{-1} (P-R) \geq 0,$$

which gives $-P^T R^{-1} P \leq -2P + R$. It then follows from (1.32) that

$$\begin{bmatrix} \Sigma_8 & -GH+R & \Sigma_9 & PD & \tau A^T P & H^T \\ * & -Q-R & 0 & 0 & -\tau H^T G^T & 0 \\ * & * & -2\Lambda & 0 & \tau B^T P & 0 \\ * & * & * & -\gamma^2 I & \tau D^T P & 0 \\ * & * & * & * & -P^T R^{-1} P & 0 \\ * & * & * & * & * & -I \end{bmatrix} < 0. \tag{1.33}$$

Now, pre- and post multiplying the above matrix inequality (1.33) by $\text{diag}\{I, I, I, I, RP^{-1}, I\}$ and $\text{diag}\{I, I, I, I, P^{-1}R, I\}$, respectively, and noting the change of variable $M = P^{-1}G$, it can be seen that the resulting LMI is the same as (1.20). Therefore, by Theorem 1.3, the master-slave synchronization scheme (1.1) is synchronized with guaranteed H_∞ performance γ. This completes the proof. □

Remark 1.4. It is noted that the performance index γ described in Theorem 1.4 can also be optimized by the convex optimization algorithm [28, 29].

Algorithm 1.2. $\min_{P,Q,R,G,\Lambda} \gamma^2$, subject to the LMI (1.32).

Remark 1.5. The authors in [24, 27] have investigated the master-slave synchronization scheme with $w(t) = 0$. The proposed delay-dependent synchronization criteria in [24, 27] were formulated by means of matrix inequalities. It implies that to obtain the time-delayed feedback controller, one needs to solve a corresponding nonlinear programming problem. By Theorem 1.4, an LMI-based delay-dependent synchronization condition can be obtained shown in the following corollary, which can be facilitated readily by the Matlab LMI Control Toolbox [29].

Corollary 1.2. *The master-slave synchronization described in* (1.1) *with* $w(t) = 0$ *can be achieved with* $M = P^{-1}G$*, if there exist real matrices* $P > 0, Q > 0, R > 0, G$ *and a diagonal matrix* $\Lambda > 0$ *such that*

$$\begin{bmatrix} \Sigma_8 & -GH + R & PB + kC^T\Lambda & \tau A^T P \\ * & -Q - R & 0 & -\tau H^T G^T \\ * & * & -2\Lambda & \tau B^T P \\ * & * & * & -2P + R \end{bmatrix} < 0, \tag{1.34}$$

where Σ_8 *is the same as the one in Theorem 1.4.*

In order to further reduce the conservatism of the synchronization condition, we will introduce some slack variables in our design.

Before proceeding further, we present a useful lemma to estimate the term $-\int_{t-\tau}^{t} \dot{e}^T(s)R\dot{e}(s)ds$, which plays a key role in the derivation of the main results in this section.

Lemma 1.3. *For the error system* (1.3) *and any real matrices* $R > 0, N_1, N_2, N_3, N_4$ *with appropriate dimensions, the following inequality*

holds:

$$-\int_{t-\tau}^{t}\dot{e}^T(s)R\dot{e}(s)ds \le \tau\pi_1^T(t)N^TR^{-1}N\pi_1(t) + 2\pi_1^T(t)N^T[e(t)-e(t-\tau)], \tag{1.35}$$

with

$$\pi_1(t) = \left[\begin{array}{cccc} e^T(t) & e^T(t-\tau) & \eta^T(Ce(t),y(t)) & w^T(t) \end{array}\right]^T,$$
$$N = \left[\begin{array}{cccc} N_1 & N_2 & N_3 & N_4 \end{array}\right].$$

Proof. Let

$$\Pi_1 = \left[\begin{array}{cc} N^TR^{-1}N & N^T \\ N & R \end{array}\right],$$
$$\Pi_2 = \left[\begin{array}{cc} I & -N^TR^{-1} \\ 0 & I \end{array}\right].$$

Then, one has

$$\Pi_2\Pi_1\Pi_2^T = \left[\begin{array}{cc} 0 & 0 \\ 0 & R \end{array}\right] \ge 0,$$

which implies $\Pi_1 \ge 0$. Noting the fact that

$$\int_{t-\tau}^{t}\dot{e}(s)ds = e(t)-e(t-\tau), \tag{1.36}$$

it yields that

$$\begin{aligned}
&-\int_{t-\tau}^{t}\dot{e}^T(s)R\dot{e}(s)ds \\
&\le -\int_{t-\tau}^{t}\dot{e}^T(s)R\dot{e}(s)ds + \int_{t-\tau}^{t}\left[\begin{array}{c}\pi_1(t)\\ \dot{e}(s)\end{array}\right]^T\Pi_1\left[\begin{array}{c}\pi_1(t)\\ \dot{e}(s)\end{array}\right]ds \\
&= -\int_{t-\tau}^{t}\dot{e}^T(s)R\dot{e}(s)ds + \int_{t-\tau}^{t}\Big\{\pi_1^T(t)N^TR^{-1}N\pi_1(t) \\
&\quad +2\pi_1^T(t)N^T\dot{e}(s) + \dot{e}^T(s)R\dot{e}(s)\Big\}ds \\
&= \tau\pi_1^T(t)N^TR^{-1}N\pi_1(t) + 2\int_{t-\tau}^{t}\pi_1^T(t)N^T\dot{e}(s)ds \\
&= \tau\pi_1^T(t)N^TR^{-1}N\pi_1(t) + 2\pi_1^T(t)N^T[e(t)-e(t-\tau)].
\end{aligned} \tag{1.37}$$

That is, the inequality (1.35) is true. This completes the proof. □

Now, we are in a position to present our main results.

Theorem 1.5. *Assume that the feedback gain matrix M is given. The master system $\mathcal{M}$ and the slave system $\mathcal{S}$ are synchronized with guaranteed H_∞ performance γ, if there exist real matrices $P > 0, Q > 0, R > 0, N_1, N_2, N_3, N_4$ and a diagonal matrix $\Lambda = diag(\lambda_1, \lambda_2, \ldots, \lambda_{n_h}) > 0$ such that the following LMI holds:*

$$\begin{bmatrix} \Theta_{11} & \Theta_{12} & \Theta_{13} & \Theta_{14} & \tau A^T R & \tau N_1^T & H^T \\ * & \Theta_{22} & -N_3 & -N_4 & -\tau H^T M^T R & \tau N_2^T & 0 \\ * & * & -2\Lambda & 0 & \tau B^T R & \tau N_3^T & 0 \\ * & * & * & -\gamma^2 I & \tau D^T R & \tau N_4^T & 0 \\ * & * & * & * & -\tau R & 0 & 0 \\ * & * & * & * & * & -\tau R & 0 \\ * & * & * & * & * & * & -I \end{bmatrix} < 0, \quad (1.38)$$

where

$$\begin{aligned} \Theta_{11} &= PA + A^T P + Q + N_1 + N_1^T, \\ \Theta_{12} &= -PMH - N_1^T + N_2, \\ \Theta_{13} &= PB + kC^T \Lambda + N_3, \\ \Theta_{14} &= PD + N_4, \\ \Theta_{22} &= -Q - N_2 - N_2^T. \end{aligned}$$

Proof. Firstly, we show that the error system (1.3) with $w(t) = 0$ is globally asymptotically stable under the condition of Theorem 1.5. When $w(t) = 0$, the error system (1.3) can be given as follows:

$$\dot{e}(t) = Ae(t) - MHe(t - \tau) + B\eta(Ce(t), y(t)). \quad (1.39)$$

From the LMI (1.38), it is obvious that

$$\begin{bmatrix} \Theta_{11} & \Theta_{12} & \Theta_{13} & \tau A^T R & \tau N_1^T \\ * & \Theta_{22} & -N_3 & -\tau H^T M^T R & \tau N_2^T \\ * & * & -2\Lambda & \tau B^T R & \tau N_3^T \\ * & * & * & -\tau R & 0 \\ * & * & * & * & -\tau R \end{bmatrix} < 0. \quad (1.40)$$

Let

$$\Pi_3 = \begin{bmatrix} \Theta_{11} & \Theta_{12} & \Theta_{13} \\ * & \Theta_{22} & -N_3 \\ * & * & -2\Lambda \end{bmatrix},$$
$$\Pi_4 = \begin{bmatrix} A & -MH & B \end{bmatrix},$$
$$\Pi_5 = \begin{bmatrix} N_1 & N_2 & N_3 \end{bmatrix}.$$

By employing Lemma 1.1, the LMI (1.40) is equivalent to

$$\Pi_3 + \tau\Pi_4^T R\Pi_4 + \tau\Pi_5^T R^{-1}\Pi_5 < 0. \tag{1.41}$$

Then, there must exist a sufficiently small scalar $\epsilon > 0$ such that

$$\Pi_3 + \tau\Pi_4^T R\Pi_4 + \tau\Pi_5^T R^{-1}\Pi_5 + \text{diag}\{\epsilon I, 0, 0\} \leq 0. \tag{1.42}$$

It follows from (1.6) that for any diagonal matrix $\Lambda = \text{diag}(\lambda_1, \lambda_2, \ldots, \lambda_{n_h}) > 0$,

$$\begin{aligned} 0 \leq & -2\sum_{i=1}^{n_h} \lambda_i \eta_i(c_i^T e, y)(\eta_i(c_i^T e, y) - kc_i^T e) \\ = & -2\eta^T(Ce(t), y(t))\Lambda\eta(Ce(t), y(t)) \\ & +2ke^T(t)C^T\Lambda\eta(Ce(t), y(t)). \end{aligned} \tag{1.43}$$

Choose a Lyapunov functional candidate as

$$\begin{aligned} V_3(t) = & e^T(t)Pe(t) + \int_{t-\tau}^{t} e^T(s)Qe(s)ds \\ & + \int_{-\tau}^{0}\int_{t+\theta}^{t} \dot{e}^T(s)R\dot{e}(s)dsd\theta, \end{aligned} \tag{1.44}$$

where $P > 0, Q > 0, R > 0$ are to be determined. Then, by directly computing the time-derivative of $V_3(t)$ along the trajectory of system (1.39), one can derive

$$\begin{aligned} \dot{V}_3(t) = & 2e^T(t)P\dot{e}(t) + e^T(t)Qe(t) - e^T(t-\tau)Qe(t-\tau) \\ & +\tau\dot{e}^T(t)R\dot{e}(t) - \int_{t-\tau}^{t} \dot{e}^T(s)R\dot{e}(s)ds \\ = & e^T(t)(PA + A^TP + Q)e(t) - 2e^T(t)PMHe(t-\tau) \\ & +2e^T(t)PB\eta(Ce(t), y(t)) - e^T(t-\tau)Qe(t-\tau) \\ & +\tau\dot{e}^T(t)R\dot{e}(t) - \int_{t-\tau}^{t} \dot{e}^T(s)R\dot{e}(s)ds. \end{aligned} \tag{1.45}$$

By following the similar line of the proof of Lemma 1.3, it can be easily derived that

$$-\int_{t-\tau}^{t} \dot{e}^T(s)R\dot{e}(s)ds \le \tau\pi_2^T(t)\Pi_5^T R^{-1}\Pi_5\pi_2(t) + 2\pi_2^T(t)\Pi_5^T[e(t)-e(t-\tau)], \tag{1.46}$$

with

$$\pi_2(t) = \left[\begin{array}{ccc} e^T(t) & e^T(t-\tau) & \eta^T(Ce(t),y(t)) \end{array}\right]^T.$$

This together with (1.42), (1.43) and (1.45) gives

$$\begin{aligned}
\dot{V}_3(t) &\le e^T(t)(PA + A^TP + Q)e(t) - 2e^T(t)PMHe(t-\tau) \\
&\quad +2e^T(t)PB\eta(Ce(t),y(t)) - e^T(t-\tau)Qe(t-\tau) \\
&\quad +\tau\dot{e}^T(t)R\dot{e}(t) + \tau\pi_2^T(t)\Pi_5^T R^{-1}\Pi_5\pi_2(t) \\
&\quad +2\pi_2^T(t)\Pi_5^T[e(t)-e(t-\tau)] \\
&\quad -2\eta^T(Ce(t),y(t))\Lambda\eta(Ce(t),y(t)) \\
&\quad +2ke^T(t)C^T\Lambda\eta(Ce(t),y(t)) \\
&= \pi_2^T(t)\Big[\Pi_3 + \tau\Pi_4^T R\Pi_4 + \tau\Pi_5^T R^{-1}\Pi_5\Big]\pi_2(t) \\
&\le -\epsilon e^T(t)e(t).
\end{aligned} \tag{1.47}$$

According to the stability theory in [20], the error system (1.39) is globally asymptotically stable.

Next, to establish the guaranteed H_∞ performance to the master-slave synchronization scheme (1.1) under zero initial condition, we introduce

$$J(t) = \int_0^\infty \Big[z^T(t)z(t) - \gamma^2 w^T(t)w(t)\Big]dt. \tag{1.48}$$

Under the zero initial condition, from the definition of $V_3(t)$, one has $V_3(0) = 0$ and $V_3(t) \ge 0$ for $t > 0$. Then

$$\begin{aligned}
J(t) &\le \int_0^\infty \Big[z^T(t)z(t) - \gamma^2 w^T(t)w(t)\Big]dt + V_3(t)|_{t=\infty} - V_3(0) \\
&= \int_0^\infty \Big[z^T(t)z(t) - \gamma^2 w^T(t)w(t) + \dot{V}_3(t)\Big]dt.
\end{aligned} \tag{1.49}$$

By using Lemma 1.3 and following the similar line of the proof of (1.47), one can deduce that

$$\begin{aligned}
&z^T(t)z(t) - \gamma^2 w^T(t)w(t) + \dot{V}_3(t) \\
&\le \pi_1^T(t)\Big[\Pi_6 + \tau\Pi_7^T R\Pi_7 + \tau N^T R^{-1}N\Big]\pi_1(t),
\end{aligned} \tag{1.50}$$

with $\pi_1(t)$ and N being the same as those in Lemma 1.3,

$$\Pi_6 = \begin{bmatrix} \Theta_{11} + H^T H & \Theta_{12} & \Theta_{13} & \Theta_{14} \\ * & -Q - N_2 - N_2^T & -N_3 & -N_4 \\ * & * & -2\Lambda & 0 \\ * & * & * & -\gamma^2 I \end{bmatrix},$$

$$\Pi_7 = \begin{bmatrix} A & -MH & B & D \end{bmatrix}.$$

Applying Lemma 1.1 again, the LMI (1.38) can guarantee

$$\Pi_6 + \tau \Pi_7^T R \Pi_7 + \tau N^T R^{-1} N < 0.$$

It implies that for $w(t) \neq 0$,

$$z^T(t)z(t) - \gamma^2 w^T(t)w(t) + \dot{V}_3(t) < 0, \tag{1.51}$$

and thus $J(t) < 0$ for any $w(t) \neq 0$. That is, $\|z(t)\|_2 < \gamma \|w(t)\|_2$. Therefore, the master-slave synchronization scheme (1.1) can be achieved with guaranteed H_∞ performance γ. This completes the proof. □

Next is our result on the feedback controller design.

Theorem 1.6. *Let $\gamma > 0$ be a prescribed constant scalar. The master system $\mathcal{M}$ and the slave system $\mathcal{S}$ are synchronized with guaranteed H_∞ performance γ, if there exist real matrices $P > 0, Q > 0, R > 0, N_1, N_2, N_3, N_4, G$ and a diagonal matrix $\Lambda > 0$ such that the following LMI holds:*

$$\begin{bmatrix} \Xi_{11} & \Xi_{12} & \Xi_{13} & \Xi_{14} & \tau A^T P & \tau N_1^T & H^T \\ * & \Xi_{22} & -N_3 & -N_4 & -\tau H^T G^T & \tau N_2^T & 0 \\ * & * & -2\Lambda & 0 & \tau B^T P & \tau N_3^T & 0 \\ * & * & * & -\gamma^2 I & \tau D^T P & \tau N_4^T & 0 \\ * & * & * & * & \Xi_{55} & 0 & 0 \\ * & * & * & * & * & -\tau R & 0 \\ * & * & * & * & * & * & -I \end{bmatrix} < 0, \tag{1.52}$$

where

$$\begin{aligned} \Xi_{11} &= PA + A^T P + Q + N_1 + N_1^T, \\ \Xi_{12} &= -GH - N_1^T + N_2, \\ \Xi_{13} &= PB + kC^T \Lambda + N_3, \\ \Xi_{14} &= PD + N_4, \\ \Xi_{22} &= -Q - N_2 - N_2^T, \\ \Xi_{55} &= -2\tau P + \tau R. \end{aligned}$$

And the feedback gain matrix can be designed as:

$$M = P^{-1}G.$$

Proof. By Theorem 1.5, to prove Theorem 1.6, it is sufficient to show that the LMI (1.38) holds. In view of the inequality

$$P^T R^{-1} P \geq 2P - R$$

resulting from

$$(P-R)^T R^{-1}(P-R) = P^T R^{-1} P - 2P + R \geq 0,$$

the LMI (1.52) implies that

$$\begin{bmatrix} \Xi_{11} & \Xi_{12} & \Xi_{13} & \Xi_{14} & \tau A^T P & \tau N_1^T & H^T \\ * & \Xi_{22} & -N_3 & -N_4 & -\tau H^T G^T & \tau N_2^T & 0 \\ * & * & -2\Lambda & 0 & \tau B^T P & \tau N_3^T & 0 \\ * & * & * & -\gamma^2 I & \tau D^T P & \tau N_4^T & 0 \\ * & * & * & * & -\tau P^T R^{-1} P & 0 & 0 \\ * & * & * & * & * & -\tau R & 0 \\ * & * & * & * & * & * & -I \end{bmatrix} < 0. \quad (1.53)$$

Pre- and post multiplying the above matrix inequality (1.53) by $\mathrm{diag}\{I, I, I, I, RP^{-1}, I, I\}$ and $\mathrm{diag}\{I, I, I, I, P^{-1}R, I, I\}$, respectively, and applying the change of variable $M = P^{-1}G$, one can see that the resulting LMI is the same as (1.38) in Theorem 1.5. Therefore, the master system $\mathcal{M}$ and the slave system $\mathcal{S}$ are synchronized with guaranteed H_∞ performance γ. This completes the proof. □

Remark 1.6. The performance index γ described in Theorem 1.6 can be optimized by the convex optimization algorithm [28, 29].

Algorithm 1.3. $\min_{P,Q,R,N_1,N_2,N_3,N_4,G,\Lambda} \gamma^2$, subject to the LMI (1.52).

Remark 1.7. Theorem 1.6 presents a delay-dependent synchronization condition to the design of the time-delayed feedback controller, such that the slave system is synchronized to the master system with guaranteed H_∞ performance γ. It should be pointed out that several slack variables N_1, N_2, N_3 and N_4 have been introduced into the LMI condition (1.52) by employing the developed bounding technique (Lemma 1.3). The matrices N_1, N_2, N_3 and N_4 are even not required to be symmetric. The purpose of the introduction of the slack variables is to further reduce the conservatism of the derived synchronization criterion. It is thus expected that Theorem

1.6 will be less conservative than Theorems 1.2 and 1.4 due to the increasing freedom of these slack variables.

When $w(t) = 0$, the following corollary can be directly deduced from Theorem 1.6.

Corollary 1.3. *The master-slave synchronization described in* (1.1) *with* $w(t) = 0$ *can be achieved with* $M = P^{-1}G$, *if there exist real matrices* $P > 0, Q > 0, R > 0, N_1, N_2, N_3, G$ *and a diagonal matrix* $\Lambda > 0$ *such that*

$$\begin{bmatrix} \Xi_{11} & \Xi_{12} & \Xi_{13} & \tau A^T P & \tau N_1^T \\ * & \Xi_{22} & -N_3 & -\tau H^T G^T & \tau N_2^T \\ * & * & -2\Lambda & \tau B^T P & \tau N_3^T \\ * & * & * & \Xi_{55} & 0 \\ * & * & * & * & -\tau R \end{bmatrix} < 0, \tag{1.54}$$

where $\Xi_{11}, \Xi_{12}, \Xi_{13}, \Xi_{22}$ *and* Ξ_{55} *are the same as those in Theorem 1.6.*

Remark 1.8. As can be seen in Corollary 1.3, several slack variables have been used to reduce the conservatism of the synchronization condition. Therefore, Corollary 1.3 may be less conservative than the results reported in [26, 27, 31].

1.5. A Simulation Example

The Chua's Circuit [10, 40] is used as an example to illustrate the application of the proposed time-delayed feedback controller design approaches and their performance. The advantage of the delay-dependent approach with slack variables over the delay-independent approach and the delay-dependent approach without slack variables are also demonstrated.

Consider the Chua's Circuit subject to noise disturbances:

$$\begin{cases} \dot{x} = a(y - h(x)) + w(t) \\ \dot{y} = x - y + z - w(t) \\ \dot{z} = -by + w(t) \end{cases} \tag{1.55}$$

with nonlinear characteristic

$$h(x) = m_1 x + \frac{1}{2}(m_0 - m_1)(|x + c| - |x - c|)$$

and parameters $a = 9$, $b = 14.28$, $c = 1$, $m_0 = -(1/7)$, $m_1 = (2/7)$. The noise disturbance is taken as

$$w(t) = 0.01e^{-0.0001t} \sin(2\pi \times 0.005t).$$

The system can be represented in Lur'e form with noise input by

$$
\begin{aligned}
A &= \begin{bmatrix} -am_1 & a & 0 \\ 1 & -1 & 1 \\ 0 & -b & 0 \end{bmatrix}, \\
B &= \begin{bmatrix} -a(m_0 - m_1) \\ 0 \\ 0 \end{bmatrix}, \\
C = H &= \begin{bmatrix} 1 & 0 & 0 \end{bmatrix}, \\
D &= \begin{bmatrix} 1 & -1 & 1 \end{bmatrix}^T,
\end{aligned}
$$

and $\sigma(\xi) = \frac{1}{2}(|\xi + c| - |\xi - c|)$ belonging to sector $[0, k]$ with $k = 1$. This representation results in $n_h = 1$. Let $\tau = 0.1$, then the following results have been obtained by applying Algorithm 1.3:

$$
\begin{aligned}
P &= \begin{bmatrix} 0.7823 & -1.1055 & 0.2156 \\ -1.1055 & 3.6897 & -0.2491 \\ 0.2156 & -0.2491 & 0.2547 \end{bmatrix}, \\
Q &= \begin{bmatrix} 1.3625 & -2.7241 & 0.1868 \\ -2.7241 & 5.4542 & -0.3705 \\ 0.1868 & -0.3705 & 0.0277 \end{bmatrix}, \\
R &= \begin{bmatrix} 0.5645 & -0.2728 & 0.0233 \\ -0.2728 & 1.2742 & -0.0865 \\ 0.0233 & -0.0865 & 0.0119 \end{bmatrix}, \\
N_1 &= \begin{bmatrix} -5.6351 & 2.7237 & -0.2313 \\ 2.7182 & -12.7378 & 0.8635 \\ -0.2321 & 0.8646 & -0.1186 \end{bmatrix}, \\
N_2 &= \begin{bmatrix} 5.6375 & -2.7169 & 0.2316 \\ -2.7205 & 12.7298 & -0.8638 \\ 0.2322 & -0.8642 & 0.1186 \end{bmatrix}, \\
N_3 &= \begin{bmatrix} -0.0097 \\ 0.0103 \\ -0.0005 \end{bmatrix}, \quad N_4 = \begin{bmatrix} 0.0055 \\ -0.0062 \\ 0.0003 \end{bmatrix}, \\
\Lambda &= 2.2872, \quad G = \begin{bmatrix} 2.8512 \\ -0.8993 \\ -0.6346 \end{bmatrix},
\end{aligned}
$$

$$M = P^{-1}G = \begin{bmatrix} 8.1453 \\ 1.6736 \\ -7.7490 \end{bmatrix}$$

with the optimal H_∞ performance index $\gamma_{\min} = 1.5359$. The simulation results for the master-slave synchronization scheme of the Chua's Circuits (1.55) are shown in Fig. 1.2. The initial conditions are taken as $x(0) = \begin{bmatrix} 0.15 & -0.21 & -0.32 \end{bmatrix}^T$ and $y(0) = \begin{bmatrix} -0.3 & 0.15 & 0.11 \end{bmatrix}^T$. In Fig. 1.2, (a) and (b) represent the state $x(t)$ of the master system and the state $y(t)$ of the slave system, respectively; (c) is the responses of the error state $e(t)$ of the error system. The simulation results confirm the effectiveness of Theorem 1.6 for the design of the time-delayed feedback controller for the master-slave synchronization scheme of Chua's Circuits (1.55).

In order to further demonstrate the advantage of Theorem 1.6 over Theorems 1.2 and 1.4, a more detailed comparison between the minimum H_∞ performance indexes for different time delays are summarized in Table 1.1. The results clearly demonstrate the much better performance of the delay-dependent approach with slack variables over the other two approaches.

Table 1.1. Comparison of the minimum H_∞ performances for different time delays.

Methods	$\tau = 0.001$	$\tau = 0.01$	$\tau = 0.1$	$\tau = 0.14534$
Algorithm 1.1	infeasible	infeasible	infeasible	infeasible
Algorithm 1.2	infeasible	infeasible	infeasible	infeasible
Algorithm 1.3	0.0021	0.0254	1.5359	$3.8349e+003$

Furthermore, by solving the LMI (1.52) via the Matlab LMI Control Toolbox, the maximum allowed time delay in Theorem 1.6 is $\tau_{\max} = 0.14534$. In this case, the time-delayed feedback gain matrix can be designed as

$$M = \begin{bmatrix} 5.5363 \\ 0.9019 \\ -6.0015 \end{bmatrix}, \tag{1.56}$$

and the simulation results for $\tau = 0.14534$ are shown in Fig. 1.3. However, it has been observed throughout simulations that with the same time-delayed feedback controller (1.56), the Chua's Circuits can be synchronized for any $\tau \in [0, 0.3)$. Figs. 1.4 and 1.5 are the simulation results when $\tau = 0.2999$ and $\tau = 0.3$, respectively. This clearly demonstrates that there still exists some extent of conservatism in the proposed design approaches and thus suggests an interesting future research topic.

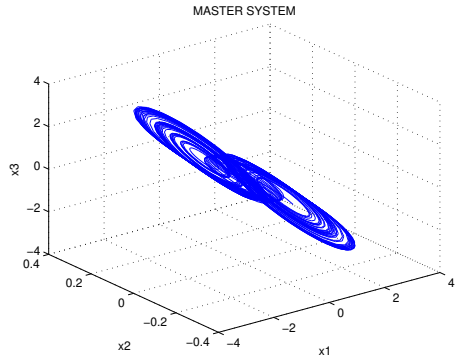

(a)

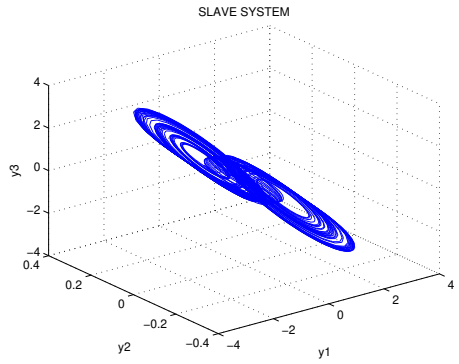

(b)

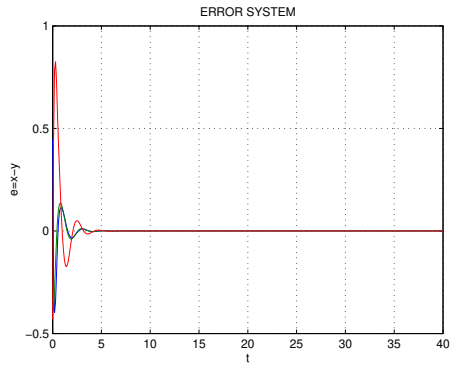

(c)

Fig. 1.2. Simulation results for master-slave synchronization of Chua's Circuits (1.55) when $\tau = 0.1$.

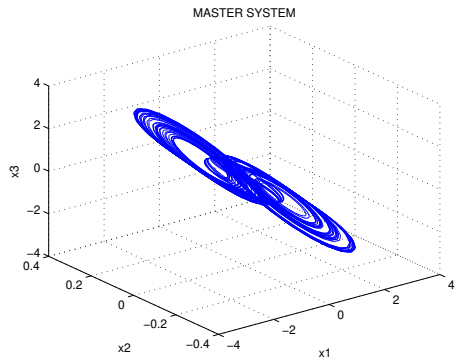

(a)

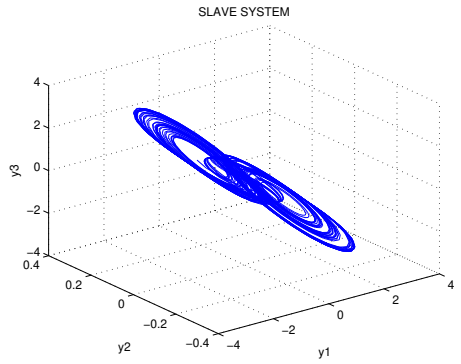

(b)

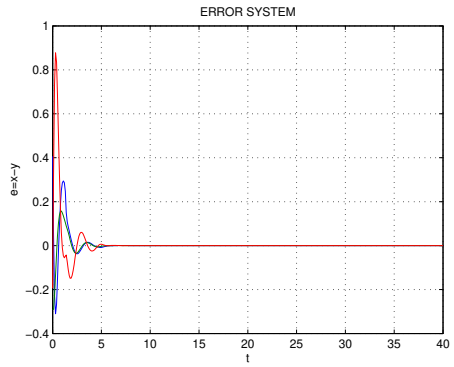

(c)

Fig. 1.3. Simulation results for master-slave synchronization of Chua's Circuits (1.55) when $\tau = 0.14534$.

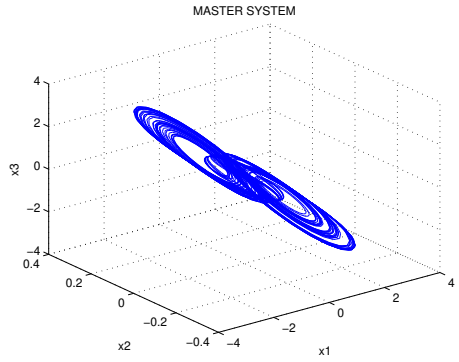

(a)

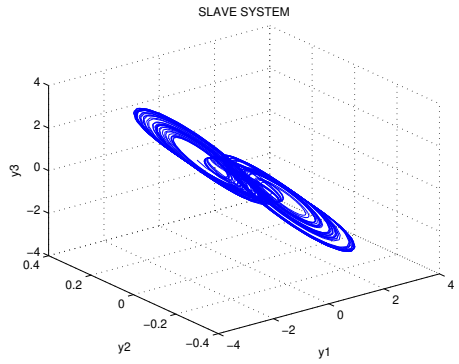

(b)

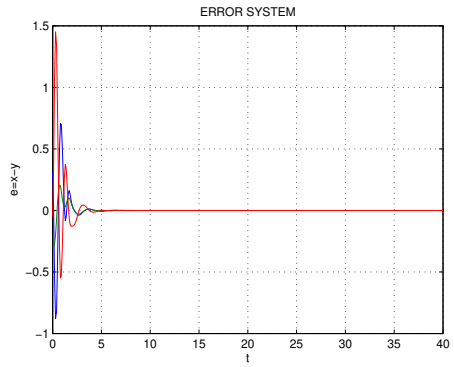

(c)

Fig. 1.4. Simulation results for master-slave synchronization of Chua's Circuits (1.55) when $\tau = 0.2999$.

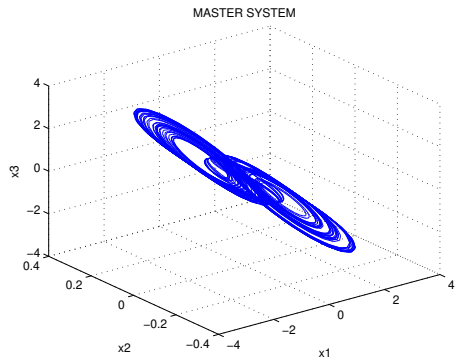

(a)

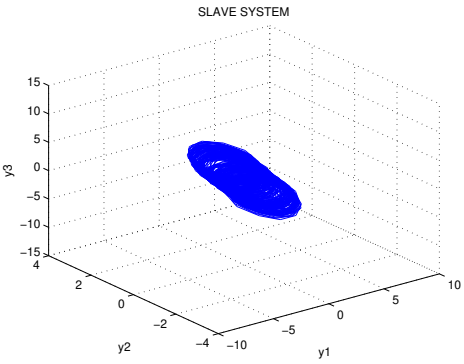

(b)

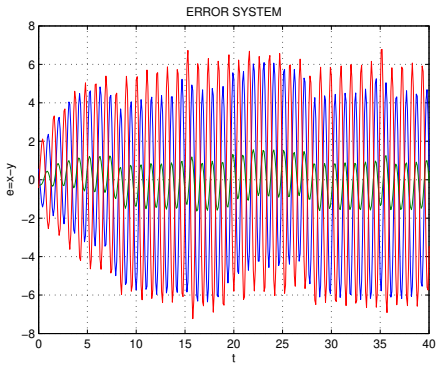

(c)

Fig. 1.5. Simulation results for master-slave synchronization of Chua's Circuits (1.55) when $\tau = 0.3$.

Table 1.2. Comparison of the maximum value $\tau_{\max}$ of the allowed time delay .

Methods	Maximum allowed time delay $\tau_{\max}$
Corollary 1.1 (Delay-independent)	infeasible
Yalcin *et al.* [27]	0.039
Han [31]	0.1411
Corollary 1.3 (Delay-dependent)	0.14537

On the other hand, to show that Corollary 1.3 is less conservative than the results in [27, 31], we consider the above Chua's Circuit (1.55) with $w(t) = 0$. By solving the LMI (1.54) in Corollary 1.3 via Matlab LMI Control Toolbox, the maximum allowed time delay is $\tau_{\max} = 0.14537$ with the following feasible solution:

$$P = 1.0e+003 \times \begin{bmatrix} 0.2618 & -0.5135 & 0.1355 \\ -0.5135 & 1.7996 & -0.2138 \\ 0.1355 & -0.2138 & 0.1333 \end{bmatrix},$$

$$Q = 1.0e+003 \times \begin{bmatrix} 0.4782 & -1.1636 & 0.1551 \\ -1.1636 & 2.8315 & -0.3774 \\ 0.1551 & -0.3774 & 0.0504 \end{bmatrix},$$

$$R = \begin{bmatrix} 132.6923 & -170.9180 & 22.9523 \\ -170.9180 & 667.6112 & -89.1729 \\ 22.9523 & -89.1729 & 12.0424 \end{bmatrix},$$

$$N_1 = \begin{bmatrix} 204.0386 & -681.3601 & 258.2893 \\ -750.4066 & 62.6136 & -200.4339 \\ 100.4606 & -9.5308 & 26.2343 \end{bmatrix},$$

$$N_2 = \begin{bmatrix} 359.8469 & -190.2322 & 25.6369 \\ 743.8114 & -622.2504 & 82.7985 \\ -98.6266 & 82.5678 & -10.0928 \end{bmatrix},$$

$$N_3 = \begin{bmatrix} -485.4716 \\ 556.2536 \\ -74.8843 \end{bmatrix}, \quad G = \begin{bmatrix} 173.2172 \\ 63.2663 \\ -243.1735 \end{bmatrix},$$

$$\Lambda = 487.4069, \quad M = P^{-1}G = \begin{bmatrix} 5.5358 \\ 0.9015 \\ -6.0021 \end{bmatrix}.$$

Table 1.2 gives the comparisons of the maximum allowed time delay $\tau_{\max}$, from which one can clearly see that Corollary 1.3 is less conservative than the results in [27, 31].

1.6. Conclusion

The master-slave synchronization problem has been studied for a class of chaotic systems based on the time-delayed feedback control. Delay-independent and delay-dependent synchronization criteria have been derived such that the controlled slave system can robustly synchronize the noise-perturbed master system with guaranteed H_∞ performance. It is shown that the time-delayed feedback controller can be determined by solving some LMIs. An example with simulation results is provided to demonstrate the performance of the proposed approaches and the advantages of the delay-dependent synchronization condition with slack variables over the delay-independent condition and the delay-dependent condition without slack variables.

Acknowledgement

This work is partially supported by a grant from the Research Grants Council of the Hong Kong Special Administrative Region of China under Project CityU-113205.

References

[1] L. M. Pecora and T. L. Carroll, Synchronization in chaotic systems, *Phys. Rev. Lett.* **64**, 821-824, (1990).
[2] R. Brown and L. Kocarev, A unifying definition of synchronization for dynamical systems, *Chaos* **10**, 344-349, (2000).
[3] G. Chen and X. Dong, *From Chaos to Order-Perspectives, Methodologies, and Applications*. (World scientific, Singapore, 1998).
[4] P. F. Curran and L. O. Chua, Absolute stability theory and the synchronization problem, *Int. J. Bifurcation and Chaos* **7**, 1375-1382, (1997).
[5] P. F. Curran, J. A. K. Suykens, and L. O. Chua, Absolute stability theory and master-slave synchronization, *Int. J. Bifurcation and Chaos* **7**, 2891-2896, (1997).
[6] G. Feng and T. Zhang, Output regulation of discrete-time piecewise-linear systems with applications to controlling chaos, *IEEE Trans. Circuits Syst.-II* **53**, 249-253, (2006).
[7] M. Hasler, Synchronization principles and applications, in *Circuits and Systems: Tutorials IEEE-ISCAS'94*, pp. 314-326, (1994).
[8] M. Hasler, Y. Maistrenko, and O. Popovich, Simple examples of partial synchronization of chaotic systems, *Phys. Rev. E* **58**, 6843-6843, (1998).
[9] M. Vidyasagar, *Nonlinear Systems Analysis*. (Prentice-Hall, Englewood Cliffs, NJ, 1993).

[10] R. N. Madan, Eds., *Chua's Circuit: A Paradigm for Chaos*, (World Scientific, Signapore, 1993).
[11] M. E. Yalçin, J. A. K. Suykens, and J. Vandewalle, Experimental confirmation of 3- and 5-scroll attractors from a generalized Chua's Circuit, *IEEE Trans. Circuits Syst. -I* **47**, 425-429, (2000).
[12] T. Kapitaniak and L. O. Chua, Hyperchaotic attractors of unidirectionally-coupled Chua's circuit, *Int. J. Bifurcation and Chaos* **4**, 477-482, (1994).
[13] C. W. Wu and L. O. Chua, A unified framework for synchronization and control of dynamical systems, *Int. J. Bifurcation and Chaos* **4**, 979-998, (1994).
[14] J. A. K. Suykens, P. F. Curran, and L. O. Chua, Robust synthesis for master-slave synchronization of Lur'e systems, *IEEE Trans. Circuits Syst. -I* **46**, 841-850, (1999).
[15] J. A. K. Suykens, P. F. Curran, J. Vandewalle, and L. O. Chua, Robust nonlinear H_∞ synchronization of chaotic Lur'e systems, *IEEE Trans. Circuits Syst. -I* **44**, 891-904, (1997a).
[16] J. A. K. Suykens, J. Vandewalle, and L. O. Chua, Nonlinear H_∞ synchronization of chaotic Lur'e systems, *Int. J. Bifurcation and Chaos* **7**, 1323-1335, (1997b).
[17] J. A. K. Suykens, P. F. Curran, T. Yang, J. Vandewalle, and L. O. Chua, Nonlinear H_∞ synchronization of Lur'e systems: dynamic output feedback case, *IEEE Trans. Circuits Syst. -I* **44**, 1089-1092, (1997c).
[18] J. A. K. Suykens and J. Vandewalle, Master-slave synchronization of Lur'e systems, *Int. J. Bifurcation and Chaos* **7**, 665-669, (1997).
[19] K. Gu, V. Kharitonov, and J. Chen, *Stability of Time-Delay Systems*. (Birkhauser, Boston, 2003).
[20] J. K. Hale and S. M. V. Lunel, *Introduction to Functional Differential Equations*. (Springer-Verlag, New York, 1993).
[21] V. B. Kolmanovskii and V. R. Nosov, *Stability of Functional Differential Equations*. (Mathematics in Science and Engineering 180, Academic Press, New York, 1986).
[22] K. Gu and S. I. Niculescu, Survey on recent results in the stability and control of time-delay systems, *ASME J. Dyn. Syst. Meas. Cont.* **125**, 158-165, (2003).
[23] H. F. Chen and J. M. Liu, Open-loop chaotic synchronization of injection-locked semiconductor lasers with Gigahertz range modulation, *IEEE J. Quant. Electron.* **36**, 27-34, (2000).
[24] J. Cao, H.-X. Li, and D. W. C. Ho, Synchronization criteria of Lur'e systems with time-delay feedback control, *Chaos Solit. Fract* **23**, 1285-1298, (2005).
[25] H. Huang, H.-X., Li, and J. Zhong, Master-slave synchronization of general Lur'e systems with time-varying delay and parameter uncertainty, *Int. J. Bifurcation and Chaos* **16**, 281-294, (2006).
[26] X. Liao and G. Chen, Chaos synchronization of general Lur'e systems via time-delay feedback control, *Int. J. Bifurcation and Chaos* **13**, 207-213, (2003).
[27] M. E. Yalçin, J. A. K. Suykens, and J. Vandewalle, Master-slave synchro-

nization of Lur'e systems with time-delay, *Int. J. Bifurcation and Chaos* **11**, 1707-1722, (2001).

[28] S. Boyd, L. EI Ghaoui, E. Feron, and V. Balakrishnan, *Linear Matrix Inequalities in System and Control Theory*. (SIAM, Philadelphia, PA, 1994).

[29] P. Gahinet, A. Nemirovsky, A. J. Laub, and M. Chilali, *LMI Control Toolbox: for Use With Matlab*. (The Math Works, Inc, 1995).

[30] Q.-L. Han, On designing time-varying delay feedback controllers for master-slave synchronization of Lur'e systems, *IEEE Trans. Circuits Syst. -I* **54**, 1573-1583, (2007a).

[31] Q.-L. Han, New delay-dependent synchronization criteria for Lur'e systems using time delay feedback control, *Phys. Lett. A* **360**, 563-569, (2007b).

[32] A. S. Hegazi, H. N. Gaiza, and M. N. EL-Dessoky, Adaptive synchronization for Rössler and Chua's circuit systems, *Int. J. Bifurcation and Chaos* **12**, 1565-1577, (2002).

[33] J. Lu and J. Cao, Adaptive complete synchronization of two identical or different chaotic (hyperchaotic) systems with fully unknown parameters, *Chaos* **15**, art. no. 043901, (2005).

[34] C.-L. Chen, G. Feng, D. Sun, and X.-P. Guan, H_∞ output feedback control of discrete-time fuzzy systems with application to chaos control, *IEEE Trans. Fuzzy Syst.* **13**, 531-543, (2005).

[35] K.-Y. Lian, T.-S. Chiang, C.-S. Chiu, and P. Liu, Synthesis of fuzzy model-based designs to synchronization and secure communications for chaotic systems, *IEEE Trans. Syst. Man Cybern. B* **31**, 66-83, (2001).

[36] J. F. Heagy, T. L. Carroll, and L. M. Pecora, Experimental and numerical evidence for riddled basins in coupled chaotic systems, *Phys. Rev. Lett.* **73**, 3528-3531, (1994).

[37] J.-Q. Fang, Y. Hong, and G. Chen, Switching manifold approach to chaos synchronization, *Phys. Rev. E* **59**, 2523-2526, (1999).

[38] H. N. Agiza and M. T. Yassen, Synchronization of Rossler and Chen chaotic dynamical systems using active control, *Phys. Lett. A* **278**, 191-197, (2001).

[39] T. Yang, L.-B. Yang, and C.-M. Yang, Impulsive control of Lorenz system, *Physica D* **110**, 18-24, (1997).

[40] L. O. Chua, M. Komuro, and T. Matsumoto, The double scroll family, *IEEE Trans. Circuits Syst. -I* **33**, 1072-1118, (1986).

CHAPTER 2

SYNCHRONIZATION OF UNCERTAIN CHAOTIC SYSTEMS BASED ON FUZZY-MODEL-BASED APPROACH

H.K. Lam[*] and F.H.F. Leung[**]

[*]*Department of Electronic Engineering, Division of Engineering,*
The King's College London, WC2R 2LS, United Kingdom
E-mail: hak-keung.lam@kcl.ac.uk
[**]*Centre for Multimedia Signal Processing,*
Department of Electronic and Information Engineering,
The Hong Kong Polytechnic University,
Hung Hom, Kowloon, Hong Kong
E-mail: enfrank@polyu.edu.hk

This chapter investigates the synchronization of chaotic systems subject to parameter uncertainties. Based on the fuzzy-model-based approach, a fuzzy model is first employed to represent the chaotic systems. A switching controller is then proposed to deal with the synchronization problem of which the system states of the response chaotic system is driven to approach those of the drive chaotic system. Stability conditions in terms of linear matrix inequalities are derived based on the Lyapunov stability theory. The tracking performance and parameter design of the proposed switching controller are formulated as a generalized eignevalue minimization problem which can be solved numerically using some convex programming techniques. Simulation examples are given to show the effectiveness of the proposed approach.

2.1. Introduction

Chaotic control is a challenging task due to the complex characteristic of the chaotic systems. Chaos stabilization and synchronization are important topics which has drawn a great deal of attention from researchers. Comparing to the chaos stabilization problem, chaos

synchronization is much harder to be achieved. To stabilize the chaos behaviour, the control objective is only to suppress the chaotic dynamics and drive the system states to the equilibrium. However, chaos synchronization requires driving the system states of the response chaotic system to follow those of the drive chaotic system. In such a case, the tracking control problem is considered. Furthermore, the synchronization problem will become more complex if the chaotic systems are subject to parameter uncertainties.

Various control approaches such as nonlinear controllers [1, 2], active controllers [3, 4], fuzzy controllers [5-7] and adaptive controllers [8, 9], were reported to realize the synchronization of identical or different chaos systems. In general, synchronization is achieved by modifying the chaotic behaviour of the response chaotic system with the controller [1-4], which is typically designed with the pole-placement or nonlinearity compensation techniques. If the fuzzy-model-based control approach [5-7] is adopted, a fuzzy model is derived to represent the dynamics of the chaotic system as a weighted sum of some linear sub-systems. The fuzzy model gives a fixed framework to model some general chaotic systems. This particular structure is in favour of the system analysis and controller synthesis. Adaptability was granted to controllers [8, 9] of which the controller parameters were updated in an online manner according to some adaptive laws to cope with the changes of the operating conditions. Consequently, the adaptive controller offered an outstanding robustness property. However, the complex adaptive laws will always increase the computational demand and structural complexity of the fuzzy controllers.

In this chapter, the synchronization of chaotic systems subject to parameter uncertainties is handled based on the fuzzy-model-based approach. A fuzzy model will first be employed to represent the chaotic system. To deal with the parameter uncertainties and achieve synchronization, a switching controller is proposed. A switching law is then derived to guarantee the convergence of the error states between the response and the drive chaotic systems based on the Lyapunov stability theory. The conditions for system stability and tracking performance are formulated as a generalized eigenvalue minimization problem (GEVP), which can be solved readily using some convex programming technique.

This chapter is organized as follows. In section 2.2, the fuzzy model representing the dynamics of the chaotic system subject to parameter uncertainties is presented. A switching controller is proposed based on the fuzzy model of the chaotic system. In section 2.3, the stability conditions and the switching laws are derived based on the Lyapunov approach. In section 2.4, numerical examples on synchronizing two different chaotic systems are given to demonstrate the effectiveness of the proposed approach. A conclusion is drawn in section 2.5.

2.2. Fuzzy Model and Switching Controller

In this section, a fuzzy model [5] is employed to represent the chaotic system subject to parameter uncertainties. Based on the fuzzy model, a switching controller is then proposed to realize the synchronization of two chaotic systems. The switching activity of the controller is able compensate the uncertain nonlinearity of chaotic systems. Stability conditions in terms of linear matrix inequalities (LMIs) are derived to guarantee the system stability based on the Lyapunov stability theory.

2.2.1. Fuzzy Model

Let p be the number of fuzzy rules describing the uncertain response chaotic system with control input term. The i-th rule is of the following format,

$$\text{Rule } i\text{: IF } f_1(\mathbf{x}(t)) \text{ is } \mathrm{M}_1^i \text{ AND } \ldots \text{ AND } f_\Psi(\mathbf{x}(t)) \text{ is } \mathrm{M}_\Psi^i$$

$$\text{THEN } \dot{\mathbf{x}}(t) = \mathbf{A}_i\mathbf{x}(t) + \mathbf{B}\mathbf{u}(t) \tag{2.1}$$

where M_α^i is a fuzzy term of rule i corresponding to the function $f_\alpha(\mathbf{x}(t))$ with known form, $\alpha = 1, 2, ..., \Psi$; $i = 1, 2, ..., p$; Ψ is a positive integer. $\mathbf{A}_i \in \Re^{n\times n}$ and $\mathbf{B} \in \Re^{n\times n}$ are known constant system and input matrices respectively. It is required that $\mathbf{B}$ is invertible. $\mathbf{x}(t) \in \Re^{n\times 1}$ is the system state vector and $\mathbf{u}(t) \in \Re^{n\times 1}$ is the input vector. The system dynamics are described by,

$$\dot{\mathbf{x}}(t) = \sum_{i=1}^{p} w_i(\mathbf{x}(t))\left(\mathbf{A}_i\mathbf{x}(t) + \mathbf{B}\mathbf{u}(t)\right) \tag{2.2}$$

where

$$\sum_{i=1}^{p} w_i(\mathbf{x}(t)) = 1,\ w_i(\mathbf{x}(t)) \in \begin{bmatrix} 0 & 1 \end{bmatrix} \text{ for all } i \tag{2.3}$$

$$w_i(\mathbf{x}(t)) = \frac{\mu_{\mathrm{M}_1^i}(f_1(\mathbf{x}(t))) \times \mu_{\mathrm{M}_2^i}(f_2(\mathbf{x}(t))) \times \cdots \times \mu_{\mathrm{M}_\psi^i}(f_\psi(\mathbf{x}(t)))}{\sum_{k=1}^{p}\left(\mu_{\mathrm{M}_1^k}(f_1(\mathbf{x}(t))) \times \mu_{\mathrm{M}_2^k}(f_2(\mathbf{x}(t))) \times \cdots \times \mu_{\mathrm{M}_\psi^k}(f_\psi(\mathbf{x}(t)))\right)} \tag{2.4}$$

is a nonlinear function of $\mathbf{x}(t)$ and $\mu_{\mathrm{M}_\alpha^i}(x_\alpha(t))$ is the grade of membership corresponding to the fuzzy terms M_α^i. It should be noted that the grades of membership, $\mu_{\mathrm{M}_\alpha^i}(x_\alpha(t))$, are uncertain in value as the chaotic system is subject to parameter uncertainties.

Similarly, the dynamics of the drive chaotic system can be represented by a fuzzy model with q fuzzy rules in the format of (2.1) but without the control input. Consequently, the dynamics of the drive chaotic system can be represented as,

$$\dot{\hat{\mathbf{x}}}(t) = \sum_{j=1}^{q} \hat{w}_j(\hat{\mathbf{x}}(t))\hat{\mathbf{A}}_j\hat{\mathbf{x}}(t) \tag{2.5}$$

where $\hat{\mathbf{x}}(t) \in \Re^{n\times 1}$ is the system state vector. $\hat{\mathbf{A}}_j \in \Re^{n\times n}$ is a known constant system matrix; $\hat{w}_j(\hat{\mathbf{x}}(t)) \in \begin{bmatrix} 0 & 1 \end{bmatrix}$ is the grade of the membership and $\sum_{j=1}^{q} \hat{w}_j(\hat{\mathbf{x}}(t)) = 1$.

2.2.2. Switching Controller

A switching controller is proposed to drive the system states of the response chaotic system of (2.2) to follow those of the drive chaotic system of (2.5). The proposed switching controller is defined as follows,

$$\mathbf{u}(t) = \sum_{i=1}^{p} m_i(\mathbf{e}(t))\mathbf{B}^{-1}\mathbf{G}_i\mathbf{e}(t) \tag{2.6}$$

where $\mathbf{e}(t) = \mathbf{x}(t) - \hat{\mathbf{x}}(t)$ is the error system state vector, $\mathbf{G}_i \in \Re^{n\times n}$ is the feedback gain to be designed and $m_i(\mathbf{e}(t))$ is a scalar function to be determined later. The scalar function of $m_i(\mathbf{e}(t))$ is a switching function which takes either 0 or 1 to compensate the uncertainties in the membership functions of the fuzzy models.

2.2.3. Error System

The error system is formed by the response and drive chaotic systems of (2.2) and (2.5). From (2.2) and (2.5), with the property that $\sum_{i=1}^{p} w_i(\mathbf{x}(t)) = 1$, we have,

$$\begin{aligned}
\dot{\mathbf{e}}(t) &= \dot{\mathbf{x}}(t) - \dot{\hat{\mathbf{x}}}(t) \\
&= \sum_{i=1}^{p} w_i(\mathbf{x}(t))\mathbf{A}_i\mathbf{x}(t) + \mathbf{B}\mathbf{u}(t) - \sum_{j=1}^{q} \hat{w}_j(\hat{\mathbf{x}}(t))\hat{\mathbf{A}}_j\hat{\mathbf{x}}(t) \\
&= \sum_{i=1}^{p} w_i(\mathbf{x}(t))\mathbf{A}_i\mathbf{x}(t) - \sum_{i=1}^{p} w_i(\mathbf{x}(t))\mathbf{A}_i\hat{\mathbf{x}}(t) + \sum_{i=1}^{p} w_i(\mathbf{x}(t))\mathbf{A}_i\hat{\mathbf{x}}(t) \\
&\quad + \mathbf{B}\mathbf{u}(t) - \sum_{j=1}^{q} \hat{w}_j(\hat{\mathbf{x}}(t))\hat{\mathbf{A}}_j\hat{\mathbf{x}}(t) \\
&= \sum_{i=1}^{p} w_i(\mathbf{x}(t))\mathbf{A}_i\mathbf{e}(t) + \mathbf{B}\mathbf{u}(t) + \sum_{i=1}^{p} w_i(\mathbf{x}(t))\mathbf{A}_i\hat{\mathbf{x}}(t) - \sum_{j=1}^{q} \hat{w}_j(\hat{\mathbf{x}}(t))\hat{\mathbf{A}}_j\hat{\mathbf{x}}(t) \\
&= \sum_{i=1}^{p} w_i(\mathbf{x}(t))\mathbf{A}_i\mathbf{e}(t) + \mathbf{B}\mathbf{u}(t) + \mathbf{m}_{\mathbf{e}}(\mathbf{x}(t), \hat{\mathbf{x}}(t))
\end{aligned} \tag{2.7}$$

where $\mathbf{m}_{\mathbf{e}}\left(\mathbf{x}(t), \hat{\mathbf{x}}(t)\right) = \sum_{i=1}^{p} w_i(\mathbf{x}(t))\mathbf{A}_i\hat{\mathbf{x}}(t) - \sum_{j=1}^{q} \hat{w}_j(\hat{\mathbf{x}}(t))\hat{\mathbf{A}}_j\hat{\mathbf{x}}(t)$. It should be noted that $w_i(\mathbf{x}(t))$, $\hat{w}_j(\hat{\mathbf{x}}(t))$ and $\hat{\mathbf{x}}(t)$ are bounded due to the nature of the membership functions and chaotic drive system. From (2.6) and (2.7), we have,

$$\dot{\mathbf{e}}(t) = \sum_{i=1}^{p} w_i(\mathbf{x}(t))\mathbf{A}_i\mathbf{e}(t) + \mathbf{B}\sum_{i=1}^{p} m_i(\mathbf{e}(t))\mathbf{B}^{-1}\mathbf{G}_i\mathbf{e}(t) + \mathbf{m}_{\mathbf{e}}\left(\mathbf{x}(t), \hat{\mathbf{x}}(t)\right)$$

$$
\begin{aligned}
&= \sum_{i=1}^{p} w_i(\mathbf{x}(t))\mathbf{A}_i\mathbf{e}(t) + \sum_{i=1}^{p} m_i(\mathbf{e}(t))\mathbf{G}_i\mathbf{e}(t) + \sum_{i=1}^{p} w_i(\mathbf{x}(t))\mathbf{G}_i\mathbf{e}(t) \\
&- \sum_{i=1}^{p} w_i(\mathbf{x}(t))\mathbf{G}_i\mathbf{e}(t) + \mathbf{m}_\mathbf{e}\left(\mathbf{x}(t), \hat{\mathbf{x}}(t)\right) \\
&= \sum_{i=1}^{p} w_i(\mathbf{x}(t))\left(\mathbf{A}_i + \mathbf{G}_i\right)\mathbf{e}(t) \\
&+ \sum_{i=1}^{p} \left(m_i(\mathbf{e}(t)) - w_i(\mathbf{x}(t))\right)\mathbf{G}_i\mathbf{e}(t) + \mathbf{m}_\mathbf{e}\left(\mathbf{x}(t), \hat{\mathbf{x}}(t)\right)
\end{aligned} \tag{2.8}
$$

2.3. Stability Analysis

In this section, the stability of the error system of (2.8) is investigated based on the Lyapunov stability theory. In the following, $w_i(\mathbf{x}(t))$, $\hat{w}_j(\hat{\mathbf{x}}(t))$, $m_i(\mathbf{e}(t))$ and $\mathbf{m}_\mathbf{e}(\mathbf{x}(t), \hat{\mathbf{x}}(t))$ are denoted as w_i, $\hat{w}_j$, m_i and $\mathbf{m}_\mathbf{e}$ respectively for brevity. To investigate the stability of the error system of (2.8), the following quadratic Lyapunov function candidate is considered.

$$
V(t) = \mathbf{e}(t)^{\mathrm{T}}\mathbf{P}\mathbf{e}(t) \tag{2.9}
$$

where $\mathbf{P} \in \Re^{n\times n}$ is a symmetric positive definite matrix. It is going to show that $\dot{V}(t) \le 0$ (equality holds when $\mathbf{e}(t) = \mathbf{0}$) which implies the synchronization of both drive and response chaotic systems are achieved. From (2.8) and (2.9), we have,

$$
\begin{aligned}
\dot{V}(t) &= \dot{\mathbf{e}}(t)^{\mathrm{T}}\mathbf{P}\mathbf{e}(t) + \mathbf{e}(t)^{\mathrm{T}}\mathbf{P}\dot{\mathbf{e}}(t) \\
&= \left(\sum_{i=1}^{p} w_i\left(\mathbf{A}_i + \mathbf{G}_i\right)\mathbf{e}(t) + \sum_{i=1}^{p}\left(m_i - w_i\right)\mathbf{G}_i\mathbf{e}(t) + \mathbf{m}_\mathbf{e}\right)^{\mathrm{T}}\mathbf{P}\mathbf{e}(t) \\
&+ \mathbf{e}(t)^{\mathrm{T}}\mathbf{P}\left(\sum_{i=1}^{p} w_i\left(\mathbf{A}_i + \mathbf{G}_i\right)\mathbf{e}(t) + \sum_{i=1}^{p}\left(m_i - w_i\right)\mathbf{G}_i\mathbf{e}(t) + \mathbf{m}_\mathbf{e}\right) \\
&= \sum_{i=1}^{p} w_i\mathbf{e}(t)^{\mathrm{T}}\left(\left(\mathbf{A}_i + \mathbf{G}_i\right)^{\mathrm{T}}\mathbf{P} + \mathbf{P}\left(\mathbf{A}_i + \mathbf{G}_i\right)\right)\mathbf{e}(t) \\
&+ 2\sum_{i=1}^{p}\left(m_i - w_i\right)\mathbf{e}(t)^{\mathrm{T}}\mathbf{P}\mathbf{G}_i\mathbf{e}(t) + \mathbf{m}_\mathbf{e}{}^{\mathrm{T}}\mathbf{P}\mathbf{e}(t) + \mathbf{e}(t)^{\mathrm{T}}\mathbf{P}\mathbf{m}_\mathbf{e}
\end{aligned} \tag{2.10}
$$

Let the switching law be

$$m_i = \frac{1}{2}\left(1 - \mathrm{sgn}\left(\mathbf{e}(t)^{\mathrm{T}}\mathbf{P}\mathbf{G}_i\mathbf{e}(t)\right)\right) \tag{2.11}$$

where the sign function is defined as follows.

$$\mathrm{sgn}(z) = \begin{cases} 1 & z > 0 \\ -1 & \text{otherwize} \end{cases} \tag{2.12}$$

From (2.10) and (2.11), we have,

$$\begin{aligned}
\dot{V}(t) &= \sum_{i=1}^{p} w_i \mathbf{e}(t)^{\mathrm{T}}\left(\left(\mathbf{A}_i + \mathbf{G}_i\right)^{\mathrm{T}}\mathbf{P} + \mathbf{P}\left(\mathbf{A}_i + \mathbf{G}_i\right)\right)\mathbf{e}(t) \\
&\quad + 2\sum_{i=1}^{p}\left(\frac{1}{2}\left(1 - \mathrm{sgn}\left(\mathbf{e}(t)^{\mathrm{T}}\mathbf{P}\mathbf{G}_i\mathbf{e}(t)\right)\right) - w_i\right)\mathbf{e}(t)^{\mathrm{T}}\mathbf{P}\mathbf{G}_i\mathbf{e}(t) \\
&\quad + \mathbf{m}_{\mathbf{e}}{}^{\mathrm{T}}\mathbf{P}\mathbf{e}(t) + \mathbf{e}(t)^{\mathrm{T}}\mathbf{P}\mathbf{m}_{\mathbf{e}} \\
&= \sum_{i=1}^{p} w_i \mathbf{e}(t)^{\mathrm{T}}\left(\left(\mathbf{A}_i + \mathbf{G}_i\right)^{\mathrm{T}}\mathbf{P} + \mathbf{P}\left(\mathbf{A}_i + \mathbf{G}_i\right)\right)\mathbf{e}(t) \\
&\quad + 2\sum_{i=1}^{p}\left(-\frac{1}{2}\mathrm{sgn}\left(\mathbf{e}(t)^{\mathrm{T}}\mathbf{P}\mathbf{G}_i\mathbf{e}(t)\right) - \left(w_i - \frac{1}{2}\right)\right)\mathbf{e}(t)^{\mathrm{T}}\mathbf{P}\mathbf{G}_i\mathbf{e}(t) \\
&\quad + \mathbf{m}_{\mathbf{e}}{}^{\mathrm{T}}\mathbf{P}\mathbf{e}(t) + \mathbf{e}(t)^{\mathrm{T}}\mathbf{P}\mathbf{m}_{\mathbf{e}} \\
&\le \sum_{i=1}^{p} w_i \mathbf{e}(t)^{\mathrm{T}}\left(\left(\mathbf{A}_i + \mathbf{G}_i\right)^{\mathrm{T}}\mathbf{P} + \mathbf{P}\left(\mathbf{A}_i + \mathbf{G}_i\right)\right)\mathbf{e}(t) \\
&\quad + 2\sum_{i=1}^{p}\left(-\frac{1}{2} + \left|w_i - \frac{1}{2}\right|\right)\left|\mathbf{e}(t)^{\mathrm{T}}\mathbf{P}\mathbf{G}_i\mathbf{e}(t)\right| + \mathbf{m}_{\mathbf{e}}{}^{\mathrm{T}}\mathbf{P}\mathbf{e}(t) + \mathbf{e}(t)^{\mathrm{T}}\mathbf{P}\mathbf{m}_{\mathbf{e}}
\end{aligned} \tag{2.13}$$

From the property of (2.3), we have $\left|w_i - \frac{1}{2}\right| \le \frac{1}{2}$ which implies $-\frac{1}{2} + \left|w_i - \frac{1}{2}\right| \le 0$. Consequently, we have,

$$\begin{aligned}
\dot{V}(t) &\le \sum_{i=1}^{p} w_i \mathbf{e}(t)^{\mathrm{T}}\left(\left(\mathbf{A}_i + \mathbf{G}_i\right)^{\mathrm{T}}\mathbf{P} + \mathbf{P}\left(\mathbf{A}_i + \mathbf{G}_i\right)\right)\mathbf{e}(t) \\
&\quad + \mathbf{m}_{\mathbf{e}}{}^{\mathrm{T}}\mathbf{P}\mathbf{e}(t) + \mathbf{e}(t)^{\mathrm{T}}\mathbf{P}\mathbf{m}_{\mathbf{e}} + \mathbf{e}(t)^{\mathrm{T}}\mathbf{P}\mathbf{e}(t) - \mathbf{e}(t)^{\mathrm{T}}\mathbf{P}\mathbf{e}(t) \\
&\quad + \eta\mathbf{m}_{\mathbf{e}}{}^{\mathrm{T}}\mathbf{P}\mathbf{m}_{\mathbf{e}} - \eta\mathbf{m}_{\mathbf{e}}{}^{\mathrm{T}}\mathbf{P}\mathbf{m}_{\mathbf{e}}
\end{aligned}$$

$$= \sum_{i=1}^{p} w_i \begin{bmatrix} \mathbf{e}(t) \\ \mathbf{m_e} \end{bmatrix}^{\mathrm{T}} \begin{bmatrix} (\mathbf{A}_i + \mathbf{G}_i)^{\mathrm{T}}\mathbf{P} + \mathbf{P}(\mathbf{A}_i + \mathbf{G}_i) + \mathbf{P} & \mathbf{P} \\ \mathbf{P} & -\eta\mathbf{P} \end{bmatrix} \begin{bmatrix} \mathbf{e}(t) \\ \mathbf{m_e} \end{bmatrix} \quad (2.14)$$
$$- \mathbf{e}(t)^{\mathrm{T}}\mathbf{P}\mathbf{e}(t) + \eta \mathbf{m_e}^{\mathrm{T}}\mathbf{P}\mathbf{m_e}$$

Let

$$\begin{bmatrix} (\mathbf{A}_i + \mathbf{G}_i)^{\mathrm{T}}\mathbf{P} + \mathbf{P}(\mathbf{A}_i + \mathbf{G}_i) + \mathbf{P} & \mathbf{P} \\ \mathbf{P} & -\eta\mathbf{P} \end{bmatrix} < 0 \text{ , } i = 1, 2, ..., p \quad (2.15)$$

From (2.14) and (2.15), we have,

$$\dot{V}(t) \le -\mathbf{e}(t)^{\mathrm{T}}\mathbf{P}\mathbf{e}(t) + \eta \mathbf{m_e}^{\mathrm{T}}\mathbf{P}\mathbf{m_e} \quad (2.16)$$

It can be seen from (2.16) that the tracking performance is partially governed by the value of η. A small value of η is required to attenuate the effect of $\mathbf{m_e}$ to the tracking performance. It can be seen from (2.16) that $\dot{V}(t) > 0$ happens when the value of $\eta \mathbf{m_e}^{\mathrm{T}}\mathbf{P}\mathbf{m_e}$ is sufficiently large. Under this case, it can be seen from (2.9) that $\mathbf{e}(t)$ will be increasing. When $\mathbf{e}(t)$ increases to a sufficient large value which makes $\dot{V}(t) < 0$ happen again, $\mathbf{e}(t)$ will be decreasing. Hence, it can be seen that a smaller value of η, which gives smaller value of $\eta \mathbf{m_e}^{\mathrm{T}}\mathbf{P}\mathbf{m_e}$, can provide a better tracking performance with a smaller tracking error of $\mathbf{e}(t)$.

In the following, the problem of minimizing the value of η is formulated as a generalized eignevalue problem (GEVP), which can be solved numerically using some convex programming techniques, e.g. MATLAB LMI toolbox. Denote $\mathbf{X} = \mathbf{P}^{-1}$ and $\mathbf{G}_i = \mathbf{N}_i\mathbf{X}^{-1}$ where $\mathbf{N}_i \in \Re^{n \times n}$ is an arbitrary matrix, pre-multiply and post-multiply diag{$\mathbf{X}$, $\mathbf{X}$} to the stability condition of (2.15), we have,

$$\begin{bmatrix} \mathbf{X} & \mathbf{0} \\ \mathbf{0} & \mathbf{X} \end{bmatrix} \begin{bmatrix} (\mathbf{A}_i + \mathbf{N}_i\mathbf{X}^{-1})^{\mathrm{T}}\mathbf{X}^{-1} + \mathbf{X}^{-1}(\mathbf{A}_i + \mathbf{N}_i\mathbf{X}^{-1}) + \mathbf{X}^{-1} & \mathbf{X}^{-1} \\ \mathbf{X}^{-1} & -\eta\mathbf{X}^{-1} \end{bmatrix}$$
$$\times \begin{bmatrix} \mathbf{X} & \mathbf{0} \\ \mathbf{0} & \mathbf{X} \end{bmatrix} < 0$$

$$\Rightarrow \begin{bmatrix} \mathbf{X}\mathbf{A}_i^{\mathrm{T}} + \mathbf{A}_i\mathbf{X} + \mathbf{N}_i^{\mathrm{T}} + \mathbf{N}_i + \mathbf{X} & \mathbf{X} \\ \mathbf{X} & -\eta\mathbf{X} \end{bmatrix} < 0 \tag{2.17}$$

The analysis results are summarized in the following Theorem.

Theorem 2.1. The error system of (2.8) is guaranteed to be input-to-state stable if $m_i(\mathbf{e}(t)) = \frac{1}{2}\left(1 - \mathrm{sgn}\left(\mathbf{e}(t)^{\mathrm{T}}\mathbf{P}\mathbf{G}_i\mathbf{e}(t)\right)\right)$ and there exists a scalar η, a symmetric matrix $\mathbf{X}$ and an arbitrary matrix $\mathbf{N}_i$ such that the following GEVP is satisfied,

$$\underset{\mathbf{X},\mathbf{N}_i}{\text{minimize}}\ \eta \ \text{ subject to}$$

$$\eta > 0;\ \mathbf{X} > 0;$$

$$\begin{bmatrix} \mathbf{X}\mathbf{A}_i^{\mathrm{T}} + \mathbf{A}_i\mathbf{X} + \mathbf{N}_i^{\mathrm{T}} + \mathbf{N}_i - \mathbf{X} & \mathbf{X} \\ \mathbf{X} & -\eta\mathbf{X} \end{bmatrix} < 0\ ,\ i = 1, 2, ..., p.$$

As the sign function in (2.11) is a switching function, it will introduce an undesired chattering effect to the system states and control signals. To attenuate the chattering effect, a saturation function [10] is employed to replace the sign function in the switching controller to produce smooth control signal near the origin. Hence, we have,

$$m_i = \frac{1}{2}\left(1 - \mathrm{sat}\left(\mathbf{e}(t)^{\mathrm{T}}\mathbf{P}\mathbf{G}_i\mathbf{e}(t), T\right)\right) \tag{2.18}$$

where the saturation function is defined as follows.

$$\mathrm{sat}(z,T) = \begin{cases} 1 & \text{for } \dfrac{z}{T} \geq 1 \\ -1 & \text{for } \dfrac{z}{T} \leq -1 \\ \dfrac{z}{T} & \text{otherwise} \end{cases}$$

and T is a non-zero positive scalar to be determined. It should be noted that the complexity of the proposed switching controller will increase

when the number of fuzzy rules of the response and drive chaotic systems is large.

2.4. Simulation Examples

Two simulation examples on dealing with the synchronization of chaotic systems are given in this section.

2.4.1. Rössler and Lorenz Systems

In this simulation example, the Rössler system is taken as the response system while the Lorenz system is taken as the drive system. Both chaotic systems are subject to uncertain parameters in this example. The proposed switching controller is employed to synchronize both Rössler and Lorenz systems.

2.4.1.1. The Dynamics of the Response Rössler's System

The dynamics of the response Rössler's system with input term are described as follows,

$$\dot{\mathbf{x}}(t) = \mathbf{A}(\mathbf{x}(t))\mathbf{x}(t) + \mathbf{B}u(t) \tag{2.19}$$

where $\mathbf{x}(t) = \begin{bmatrix} x_1(t) \\ x_2(t) \\ x_3(t) \end{bmatrix}$, $\mathbf{A}(\mathbf{x}(t)) = \begin{bmatrix} 0 & -1 & -1 \\ 1 & a & 0 \\ b & 0 & -(c(t) - x_1(t)) \end{bmatrix}$ and $\mathbf{B} = \begin{bmatrix} 1 & 0 & 0 \\ 0 & 1 & 0 \\ 0 & 0 & 1 \end{bmatrix}$; $a = 0.34$, $b = 0.4$, $c(t) = \frac{c_2 + c_1}{2} + \frac{c_2 - c_1}{2}\sin(t) \in [c_{\min}$ $c_{\max}] = [c_1 \quad c_2] > 0$ is an uncertain value, $c_1 = 4.5$, and $c_2 = 7.7$. It is assumed that $x_1(t) \in [c_{\min} - d \quad c_{\max} + d]$ and $d \in \Re^+ = 25$. The exact fuzzy model of the response Rössler system [5] is represented by the following fuzzy rules.

Rule i: IF $x_1(t)$ is M^i THEN $\dot{\mathbf{x}}(t) = \mathbf{A}_i\mathbf{x}(t) + \mathbf{B}\mathbf{u}(t)$, $i = 1, 2$. (2.20)

The inferred response Rössler system is defined as

$$\dot{\mathbf{x}}(t) = \sum_{i=1}^{2} w_i(\mathbf{x}(t))\left(\mathbf{A}_i\mathbf{x}(t) + \mathbf{B}u(t)\right) \tag{2.21}$$

where $\mathbf{A}_1 = \begin{bmatrix} 0 & -1 & -1 \\ 1 & a & 0 \\ b & 0 & -d \end{bmatrix}$ and $\mathbf{A}_2 = \begin{bmatrix} 0 & -1 & -1 \\ 1 & a & 0 \\ b & 0 & d \end{bmatrix}$;

$w_1(\mathbf{x}(t)) = \mu_{\mathrm{M}^1}(x_1(t)) = \frac{1}{2}\left(1 + \frac{c(t) - x_1(t)}{d}\right)$ and $w_2(\mathbf{x}(t)) = \mu_{\mathrm{M}^2}(x_1(t)) = 1 - \mu_{\mathrm{M}^1}(x_1(t))$. It can be seen that the grades of membership are unknown as the values of $c(t)$ is uncertain.

2.4.1.2. The Dynamics of the Lorenz System

The dynamics of the Lorenz system are given as follows,

$$\dot{\hat{\mathbf{x}}}(t) = \hat{\mathbf{A}}\left(\hat{\mathbf{x}}(t)\right)\hat{\mathbf{x}}(t) \tag{2.22}$$

where $\hat{\mathbf{x}}(t) = \begin{bmatrix} \hat{x}_1(t) \\ \hat{x}_2(t) \\ \hat{x}_3(t) \end{bmatrix}$ and $\hat{\mathbf{A}}\left(\hat{\mathbf{x}}(t)\right) = \begin{bmatrix} -\hat{a} & \hat{a} & 0 \\ \hat{c} & -1 & -\hat{x}_1(t) \\ 0 & \hat{x}_1(t) & -\hat{b} \end{bmatrix}$. It was reported in [5] that the Lorenz system of (2.22) with $\hat{x}_1(t) \in \left[-\hat{d} \quad \hat{d}\right]$ can be represented by the fuzzy model with the following rules [5].

Rule i: IF $\hat{x}_1(t)$ is N^i THEN $\dot{\hat{\mathbf{x}}}(t) = \hat{\mathbf{A}}_i\hat{\mathbf{x}}(t)$, i = 1, 2. (2.23)

The inferred drive Lorenz system is defined as

$$\dot{\hat{\mathbf{x}}}(t) = \sum_{i=1}^{2} \hat{w}_i(\hat{\mathbf{x}}(t))\hat{\mathbf{A}}_i\hat{\mathbf{x}}(t) \tag{2.24}$$

where $\hat{\mathbf{A}}_1 = \begin{bmatrix} -\hat{a} & \hat{a} & 0 \\ \hat{c} & -1 & -\hat{d} \\ 0 & \hat{d} & -\hat{b} \end{bmatrix}$ and $\hat{\mathbf{A}}_2 = \begin{bmatrix} -\hat{a} & \hat{a} & 0 \\ \hat{c} & -1 & \hat{d} \\ 0 & -\hat{d} & -\hat{b} \end{bmatrix}$;

$\hat{w}_1(\mathbf{x}(t)) = \frac{1}{2}\left(1 + \frac{\hat{x}_1(t)}{\hat{d}}\right)$ and $\hat{w}_2(\mathbf{x}(t)) = 1 - \hat{w}_1(\mathbf{x}(t))$; $\hat{a} = 10$, $\hat{b} = \frac{8}{3}$,

$\hat{c} = 28$ and $\hat{d} = 25$. The values of the parameters of the drive system are assumed to be unknown in this example.

2.4.1.3. The Dynamics of the Proposed Switching Controller

The proposed switching controller of (2.6) is employed to handle the synchronization problem. The switching controller is defined as,

$$\mathbf{u}(t) = \sum_{i=1}^{2} m_i(\mathbf{e}(t))\mathbf{B}^{-1}\mathbf{G}_i\mathbf{e}(t) \tag{2.25}$$

With the help of MATLAB LMI toolbox, we have

$$\mathbf{X} = \begin{bmatrix} 20023.3489 & -0.1122 & 1.1919 \\ -0.1122 & 20019.6460 & -0.0917 \\ 1.1919 & -0.0917 & 20000.3992 \end{bmatrix},$$

$$\mathbf{G}_1 = \begin{bmatrix} -2037.4428 & 0.1460 & 1.1303 \\ 0.1460 & -2033.3414 & -0.0904 \\ 1.1274 & -0.0902 & -2010.4778 \end{bmatrix},$$

$$\mathbf{G}_2 = \begin{bmatrix} -2037.4754 & 0.1497 & 0.9385 \\ 0.1497 & -2033.3418 & -0.0506 \\ 0.9381 & -0.0506 & -2049.0775 \end{bmatrix}$$

and $\eta = 2.5215 \times 10^{-4}$ such that the stability conditions in Theorem 2.1 are satisfied. It can be seen that the value of η is a small value to ensure a good tracking performance.

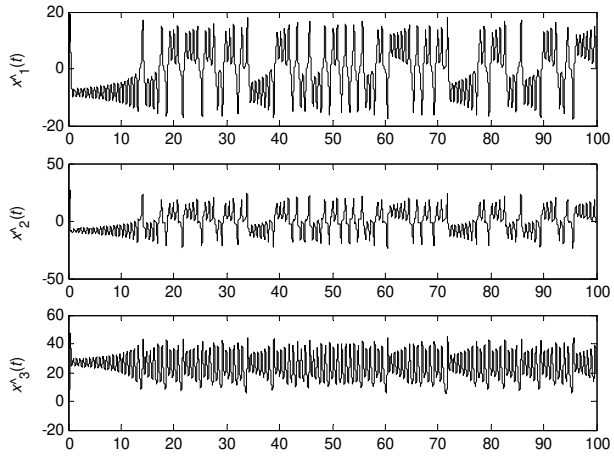

Fig. 2.1. System state responses of the drive Lorenz system.

Fig. 2.1 shows the system state responses of the drive chaotic systems under the initial condition of $\hat{\mathbf{x}}(0) = \begin{bmatrix} -1 & -1 & -1 \end{bmatrix}^{\mathrm{T}}$. Fig. 2.2 shows the system state responses of the response system with the proposed switching controller subject to the initial state conditions of $\mathbf{x}(0) = \begin{bmatrix} -1 & -1 & -1 \end{bmatrix}^{\mathrm{T}}$. In this simulation, $\mathbf{u}(t) = \mathbf{0}$ is employed for $0 \le t < 50$s and the switching controller is applied for $t \ge 50$s. In order to alleviate the chattering effect, the saturation function with $T = 10^{-5}$ is employed to replace the sign function in the switching controller. The tracking error is shown in Fig. 2.3. Referring to these figures, it can be seen that the proposed switching controller, which is applied for $t \ge 50$s, is able to drive the system states of the uncertain Rössler system to follow those of the uncertain Lorenz system with a sufficiently small tracking error.

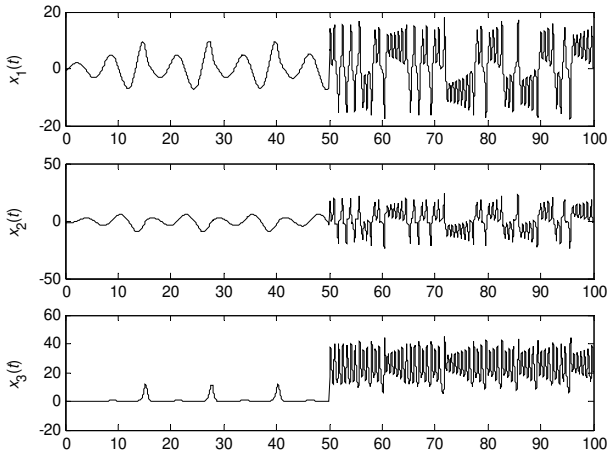

Fig. 2.2. System state responses of the response Rössler system with $\mathbf{u}(t) = \mathbf{0}$ for $0 \leq t < 50$s and the switching controller applied for $t \geq 50$s.

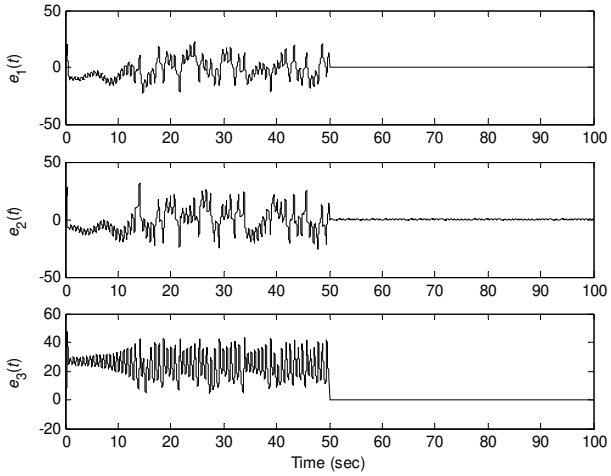

Fig. 2.3. The tracking error of the response Rössler to the drive Lorenz chaotic systems.

2.4.2. Chua's and Lorenz Systems

In this example, the Chua's system is taken as the response system while the Lorenz system in the previous example is taken as the drive system.

2.4.2.1. The Dynamics of the Response Chua's System

The dynamics of the response Chua's system with input term are described as follows,

$$\dot{\mathbf{x}}(t) = \mathbf{A}\big(\mathbf{x}(t)\big)\mathbf{x}(t) + \mathbf{B}u(t) + \mathbf{E} \tag{2.26}$$

where $\mathbf{x}(t) = \begin{bmatrix} x_1(t) \\ x_2(t) \\ x_3(t) \end{bmatrix}$, $\mathbf{A}\big(\mathbf{x}(t)\big) = \begin{bmatrix} -a & a & 0 \\ 1 & -1 & 1 \\ 0 & -b & 0 \end{bmatrix}$, $\mathbf{B} = \begin{bmatrix} 1 & 0 & 0 \\ 0 & 1 & 0 \\ 0 & 0 & 1 \end{bmatrix}$

$\mathbf{E} = \begin{bmatrix} c\big(x_1(t)\big) \\ 0 \\ 0 \end{bmatrix}$; $a = 9$, $b = 14.2850$,

$c\big(x_1(t)\big) = g_b x_1(t) + \frac{1}{2}\big(g_a(t) - g_b\big)\big(|x_1(t)+1| - |x_1(t)-1|\big)$,

$g_a(t) = \frac{g_{a_1} + g_{a2}}{2} + \frac{g_{a_1} - g_{a2}}{2}\sin(t)$ is an uncertain value, $g_{a_1} = -1.3428$, $g_{a2} = -1.5285$ and $g_b = 0.7143$. It is assumed that $x_1(t) \in [-25 \quad 25]$. The exact fuzzy model of the response Chua's system[7] is represented by the following fuzzy rules.

Rule i: IF $x_1(t)$ is M^i THEN $\dot{\mathbf{x}}(t) = \mathbf{A}_i\mathbf{x}(t) + \mathbf{B}\mathbf{u}(t)$, $i = 1, 2$. (2.27)

The inferred response Chua's system is defined as

$$\dot{\mathbf{x}}(t) = \sum_{i=1}^{2} w_i(\mathbf{x}(t))\big(\mathbf{A}_i\mathbf{x}(t) + \mathbf{B}u(t)\big) \tag{2.28}$$

where $\mathbf{A}_1 = \begin{bmatrix} (d-1)a & a & 0 \\ 1 & -1 & 1 \\ 0 & -b & 0 \end{bmatrix}$ and $\mathbf{A}_2 = \begin{bmatrix} -(d-1)a & a & 0 \\ 1 & -1 & 1 \\ 0 & -b & 0 \end{bmatrix}$;

$w_1(\mathbf{x}(t)) = \mu_{M^1}(x_1(t)) = \frac{1}{2}\left(1 - \frac{\phi(x_1(t))}{d}\right)$ and

$w_2(\mathbf{x}(t)) = \mu_{M^2}(x_1(t)) = 1 - \mu_{M^1}(x_1(t))$ where

$\phi(x_1(t)) = \begin{cases} \dfrac{c(x_1(t))}{x_1(t)} & \text{for } x_1(t) > 0 \\ g_a & \text{otherwise} \end{cases}$ and $d = 19 \geq \max_{x_1(t)} |\phi(x_1(t))|$. It can be seen that the grades of membership are unknown as the value of $c(x_1(t))$ is uncertain.

2.4.2.2. The Dynamics of the Lorenz System

The same Lorenz system of the previous example is employed as the drive system. The dynamics and the fuzzy model of the Lorenz system are given in the previous example.

2.4.2.3. The Dynamics of the Switching Controller

The switching controller in the same form of (2.25) with the corresponding $m_i(\mathbf{e}(t))$, i = 1, 2, will be employed to handle the synchronization problem. With the MATLAB LMI toolbox, we have

$$\mathbf{X} = \begin{bmatrix} 19708.8320 & -0.9457 & -0.6280 \\ -0.9457 & 19761.2134 & 3.4415 \\ -0.6280 & 3.4415 & 19760.5041 \end{bmatrix},$$

$$\mathbf{G}_1 = \begin{bmatrix} -2127.7885 & -4.9454 & -0.0630 \\ -4.9546 & -2050.6775 & 7.3297 \\ -0.0610 & 7.3298 & -2051.8293 \end{bmatrix},$$

$$\mathbf{G}_2 = \begin{bmatrix} -1984.2310 & -4.6171 & -0.0880 \\ -4.6323 & -2050.7217 & 7.3324 \\ -0.0908 & 7.3324 & -2051.8293 \end{bmatrix}$$

and $\eta = 2.5870 \times 10^{-4}$ such that the stability conditions in Theorem 2.1 are satisfied. The value of η is small enough to ensure a good tracking performance.

The system state responses of the drive Lorenz system is shown in Fig. 2.1. Fig. 2.4 shows the system state responses with the proposed switching controller using a saturation function with $T = 10^{-5}$ subject to the initial state condition of $\mathbf{x}(0) = \begin{bmatrix} -1 & -1 & -1 \end{bmatrix}^{\mathrm{T}}$. In this simulation, $\mathbf{u}(t) = \mathbf{0}$ is employed for $0 \le t < 50$s and the switching controller is applied for $t \ge 50$s. The tracking error is shown in Fig. 2.5. It can be seen from these figures that the proposed switching controller applied for $t \ge 50$s is able to drive the system states of the uncertain Chua's system to follow those of the uncertain Lorenz system with a sufficiently small tracking error.

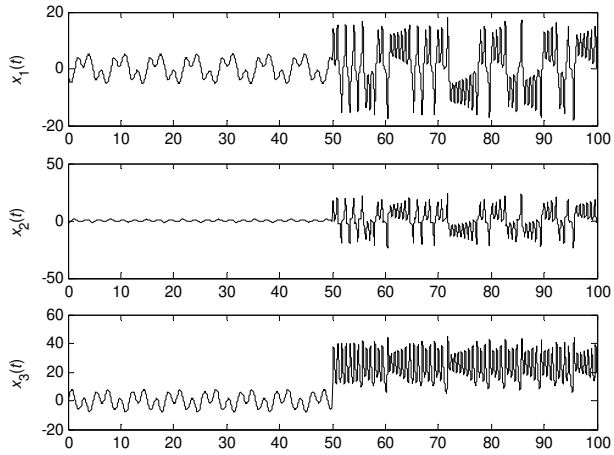

Fig. 2.4. System state responses of the response Chua's system with $\mathbf{u}(t) = \mathbf{0}$ for $0 \leq t < 50$s and the switching controller applied for $t \geq 50$s.

2.5. Conclusion

The synchronization of chaotic systems subject to parameter uncertainties has been investigated in this chapter. Based on the fuzzy models of the response and drive chaotic systems, a switching controller has been proposed to handle the synchronization problem. Stability conditions have been derived based on the Lyapunov approach to guarantee the system stability. The guarantee of the tracking performance and the parameter design of the switching controller have been formulated as a generalized eigenvalue minimization problem, which can be solved numerically using some convex programming techniques. Simulation examples have been given to show the effectiveness of the proposed approach.

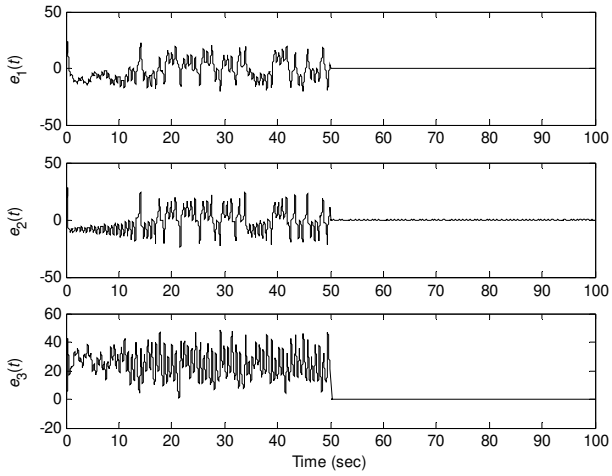

Fig. 2.5. The tracking error of the response Chua's to the drive Lorenz chaotic systems.

Acknowledgement

The work described in this chapter was supported by King's College London and the Centre for Signal Processing, the Hong Kong Polytechnic University (Project No. 1-BB9E).

References

[1] L. Huang, R. Feng and M. Wang, Synchronization of chaotic systems via nonlinear control, *Phys. Lett. A* **320**, 271-275, (2004).

[2] J. H. Park, Controlling chaotic systems via nonlinear feedback control, *Chaos, Solitons and Fractals* **23**(3), 1049-1054, (2005).

[3] E. W. Bai and K. E. Lonngren, Sequential synchronization of two Lorenz systems using active control, *Chaos, Solitons and Fractals* **11**(7), 1041-1044, (2000).

[4] H. N. Agiza and M. T. Yassen, A unified approach to controlling chaos via an LMI-based fuzzy control system design, *Phys. Lett. A* **278**(4), 191-197, (2001).

[5] K. Tanaka, T. Ikeda and H. O. Wang, A unified approach to controlling chaos via an LMI-based fuzzy control system design, *IEEE Trans. Circuits and Systems – I: Fundamental and Applications* **45**(10), 1021-1040, (1998).

[6] Y. W. Wang, Z. H. Guan and H. O. Wang, LMI-based fuzzy stability and synchronization of Chen's system, *Phys. Lett. A* **320**(2-3), 154-159, (2003).
[7] K. Y. Lian, P. Liu, T. C. Wu and W. C. Lin, Chaotic control using fuzzy model-based methods, *International Journal of Bifurcation and Chaos* **12**(8), 1827-1841, (2002).
[8] M. Feki, An adaptive feedback control of linearizable chaotic systems, *Chaos, Solitons and Fractals* **15**(5), 883-890, (2003).
[9] W. Jiang, Q. G. Dong and D. Bin, Observer-based robust adaptive variable universe fuzzy control for chaotic system, *Chaos, Solitons and Fractals* **23**(3), 1013-1032, (2005).
[10] J. J. E. Slotine and W. Li, *Applied Nonlinear Control* (Prentice Hall, 1991).

CHAPTER 3

SLIDING MODE CONTROL OF CHAOTIC SYSTEMS

Y. Feng and X. Yu

School of Electrical and Computer Engineering,
Royal Melbourne Institute of Technology,
Melbourne Vic 3001, Australia
E-mail: {yong.feng, x.yu}@rmit.edu.au

This chapter introduces the sliding model control of chaotic systems. The main two branches of chaos control, chaos control and chaos synchronization are discussed. Three kinds of sliding mode control methods, traditional sliding mode control, terminal sliding mode control and non-singular terminal sliding mode control are used to control a chaotic system to realize two different control objectives, to force it to converge to zeros or to track desired trajectories, such as an unstable limit cycle. In addition, observer based chaos synchronization is described. The synchronization for two kinds of chaotic systems with single nonlinearity and multi-nonlinearities are presented, respectively. In order to realize chaos synchronization via one single transmission channel, a time division multiplex based method is used.

3.1. Introduction

Chaotic systems are characterized by being extremely sensitive to initial conditions, deterministically random and hence ultimately unpredictable, and continually unstable, displaying no true cyclic behaviors. Chaotic systems do not follow any simple, regular, and predictable trajectories. The motion of chaotic systems is complex, irregular, and random-like. Chaos has been found in many different physical systems, such as chemical reactors, fluid flow systems, forced oscillators, feedback control devices, and laser systems [1].

Generally speaking, chaos control includes two branches of research: chaos control and chaos synchronization. The former is to control the variables of a chaotic system to an unstable periodic orbit or an equilibrium point of the system [2]. The objectives of chaos control are generally to enhance existing chaos or create chaos in a dynamical system when it is useful or beneficial, and/or to eliminate or weaken it when it is harmful. The latter is a special kind of chaos control, which is to force the trajectories of the slave chaotic system to track that of the master system starting from arbitrary initial conditions. Because chaos synchronization is essential in the application of secure communications, this issue has received a lot of attentions from mathematicians, physicists and control engineers in the last decade.

Many methods and techniques for chaos control and chaos synchronization have been proposed, such as open loop control, feedback control, parameter-dependent control, adaptive control, fuzzy logic control, and neural network based control and sliding mode control, etc. Among these approaches, sliding mode control is an important approach, which is well known for its robustness. The sliding mode control is designed to drive and constrain the system states to lie within a neighborhood of the prescribed switching manifolds that exhibit the desired dynamics, by using switching type of control strategies. When in the sliding mode, the closed-loop responses of the systems become totally insensitive to both the internal parameter uncertainties and the external disturbances. Therefore, the sliding mode control can be used in chaos control and chaos synchronization.

In this chapter, we will discuss the sliding mode control of chaotic systems, including chaos control and chaos synchronization.

3.2. Sliding Mode Control

The basic principle of sliding mode control can be briefly summarized as follows: consider a 2nd-order uncertain nonlinear dynamical system

$$\begin{cases} \dot{x}_1 = x_2 \\ \dot{x}_2 = f(\boldsymbol{x}) + g(\boldsymbol{x}) + b(\boldsymbol{x})u \end{cases}, \tag{3.1}$$

where $\boldsymbol{x}=[x_1, x_2]^{\mathrm{T}}$ is the system state vector, $f(\boldsymbol{x})$ and $b(\boldsymbol{x})\neq 0$ are smooth nonlinear functions of $\boldsymbol{x}$, and $g(\boldsymbol{x})$ represents the uncertainties and disturbances satisfying $\|g(\boldsymbol{x})\| \le l_g$ where $l_g>0$, and u is the scalar control

input. The sliding mode is described by the following first-order linear sliding variable

$$s = x_2 + \beta x_1 , \tag{3.2}$$

where β>0 is a design constant.

In order to design the control law, a η–reachability condition guaranteeing an ideal sliding mode motion should be satisfied, which is given by

$$\frac{1}{2}\frac{d}{dt}s^2 < -\eta|s| , \tag{3.3}$$

where $\eta > 0$ is a constant.

Assume that the initial condition of the sliding mode manifold (3.2) is $s(0)$, integrating (3.3) gives the time t_s as follows:

$$t_s \le \frac{|s(0)|}{\eta} , \tag{3.4}$$

which means from time t=0 to t= t_s, the sliding mode manifold s (3.2) reaches 0 from $s(0)\neq 0$.

For system (3.1), a commonly used control design is

$$u = -b^{-1}(\boldsymbol{x})(f(\boldsymbol{x}) + \beta x_2 + (l_g + \eta)\,\mathrm{sgn}(s)) , \tag{3.5}$$

which ensures that the sliding mode occurs. Therefore, for system (3.1), the sliding mode control (3.5) can guarantee that the system is robust to its uncertainties.

Recently, a terminal sliding mode (TSM) controller was developed [19-21]. The TSM is described by the following first-order terminal sliding variable

$$s = x_2 + \beta x_1^{q/p} , \tag{3.6}$$

where β>0 is a design constant, and p and q are positive odd integers, which satisfy the following condition:

$$p > q . \tag{3.7}$$

For system (3.1), a commonly used TSM control design is

$$u = -b^{-1}(\boldsymbol{x})(f(\boldsymbol{x}) + \beta \frac{q}{p} x_1^{q/p-1} x_2 + (l_g + \eta)\,\mathrm{sgn}(s)) , \tag{3.8}$$

which ensures that TSM occurs.

It is clear that if $s(0)\neq 0$, according to equation (3.4) the system states will reach the sliding mode $s=0$ within the finite time $t_r \le |s(0)|/\eta$. When the sliding mode $s=0$ is reached, the system dynamics is determined by the following nonlinear differential equation:

$$x_2 + \beta x_1^{q/p} = \dot{x}_1 + \beta x_1^{q/p} = 0, \tag{3.9}$$

where $x_1 = 0$ is the terminal attractor of the system (3.9). The finite time t_s that is taken to travel from $x_1(t_r) \neq 0$ to $x_1(t_s+t_r)=0$ is given by

$$t_s = -\beta^{-1} \int_{x_1(t_r)}^{0} \frac{dx_1}{x_1^{q/p}} = \frac{p}{\beta(p-q)} |x_1(t_r)|^{1-q/p}. \tag{3.10}$$

This means that, in the TSM manifold (3.9), both the system states x_1 and x_2 converge to zero in finite time.

Compared with the linear hyperplane based sliding modes, TSM offers some superior properties such as fast finite time convergence. This controller is particularly useful for high precision control as it speeds up the rate of convergence near the equilibrium point. However, the TSM controller design methods still have a singularity problem. It can be seen in the TSM control (3.8) that the second term containing $x_1^{q/p-1}x_2$ may cause a singularity if $x_2\neq 0$ when $x_1= 0$. This situation does not occur in the sliding mode because when $s = 0$, $x_2 = -\beta x_1^{q/p}$, hence as long as $q<p<2q$, i.e. $1<p/q<2$, the term $x_1^{q/p-1}x_2$ is equivalent to $x_1^{(2q-p)/p}$ which is nonsingular. The singularity problem may occur in the reaching phase when there is an insufficient control to ensure that $x_2\neq 0$ while $x_1= 0$. The TSM controller (3.8) cannot guarantee a bounded control signal for the case of $x_2\neq 0$ when $x_1= 0$ before the system states reach the TSM $s = 0$. Furthermore, the singularity may also occur even after the sliding mode $s = 0$ is reached since, due to computation errors and uncertain factors, the system states cannot be guaranteed to always remain in the sliding mode especially near the equilibrium point ($x_1= 0$, $x_2= 0$), and the case of $x_2\neq 0$ while $x_1=0$ may occur from time to time. This underlines the importance of addressing the singularity problem in conventional TSM systems.

In order to overcome the singularity problem in the conventional TSM systems, a nonsingular TSM (NTSM) was proposed by [12, 13], which is able to avoid this problem completely. The NTSM model is described as follows:

$$s = x_1 + \frac{1}{\beta} x_2^{p/q}, \tag{3.11}$$

where β, p and q have been defined in (3.6). One can easily see that when $s = 0$, the NTSM (3.11) is equivalent to (3.6) so that the time taken to reach the equilibrium point x_1=0 when in the sliding mode is the same as in (3.10). Note that in using (3.11) the derivative of s along the system dynamics does not result in terms with negative (fractional) powers. This can be seen in the following theorem about the NTSM control.

Theorem 3.1. For the system (3.1) with the NTSM (3.11), if the control is designed as

$$u = -b^{-1}(\boldsymbol{x})(f(\boldsymbol{x}) + \beta \frac{q}{p} x_2^{2-p/q} + (l_g + \eta)\,\mathrm{sgn}(s)), \tag{3.12}$$

where $1<p/q<2$, $\eta>0$, then the NTSM manifold (3.11) will be reached in finite time. Furthermore, the states x_1 and x_2 will converge to zero in finite time.

In this section, the sliding mode control has been introduced, which provides the basis of chaos control and chaos synchronization to be described in the following sections.

3.3. Chaos Control

In order to demonstrate the principle of the sliding mode based chaos control, a simple example is given first.

Consider the Lorenz system described by the following equation:

$$\begin{cases} \dot{x}_1 = \sigma(x_2 - x_1) \\ \dot{x}_2 = rx_1 - x_2 - x_1 x_3 \\ \dot{x}_3 = -bx_3 + x_1 x_2 \end{cases}. \tag{3.13}$$

Assume that the desired trajectories of the chaotic system (3.13) are $x_{1\mathrm{ref}}$, $x_{2\mathrm{ref}}$, $x_{3\mathrm{ref}}$, which are all smooth. The control signal u is applied in the third equation in (3.13), that is, equation (3.13) is rewritten as follows:

$$\begin{cases} \dot{x}_1 = \sigma(x_2 - x_1) \\ \dot{x}_2 = rx_1 - x_2 - x_1 x_3 \\ \dot{x}_3 = -bx_3 + x_1 x_2 + u \end{cases}. \tag{3.14}$$

The objective of chaos control is to force the variables of the chaotic system (3.14) to track the desired trajectories.
A sliding mode manifold can be designed as follows:

$$s = a_1(x_1 - x_{1ref}) + a_2(x_2 - x_{2ref}) + (x_3 - x_{3ref}), \tag{3.15}$$

where a_1 and a_2 are design parameters, which guarantee that the system on the sliding mode is stable. A sliding mode control law which makes the system (3.14) satisfy the η–reachability condition (3.3) can be designed as follows:

$$u = a_1\sigma(x_2 - x_1) - a_2(rx_1 - x_2 - x_1x_3) - bx_3 - x_1x_2 + a_1\dot{x}_{1ref} + a_2\dot{x}_{2ref} + \dot{x}_{3ref} - \eta\,\mathrm{sgn}(s). \tag{3.16}$$

Therefore, the sliding mode control law (3.16) can realize the control of the chaotic system (3.14). The sliding mode control in the above example is the conventional method which characteristic is that the convergence of the system states to the equilibrium points is usually asymptotical due to the asymptotical convergence of the linear switching manifolds that are commonly chosen. We now design a NTSM controller, which is particularly useful for high precision control as it speeds up the rate of convergence near the equilibrium point.
Theorem 1 can be used for chaos control. Consider a hysteresis-based PWL system constructed using a second-order linear system with a feedback of a hysteresis series as shown in Fig. 3.1a, which can be described as follows:

$$\begin{cases} \dot{x}_1 = x_2 \\ \dot{x}_2 = -a_1x_1 - a_2x_2 + a_1u \end{cases}, \tag{3.17}$$

where u is the nonlinear state feedback given by

$$u = H(x,n) = \sum_{i=1}^{n} hys_i(x), \tag{3.18}$$

where $H(x,n)$ is the hysteresis-series as shown in Fig. 3.1b, n is the number of hystereses. In order to guarantee the existence of the chaotic motion in system (3.17), the parameters should satisfy

$$\begin{cases} a_2 < 0 \\ a_2^2 - 4a_1 < 0 \end{cases}, \tag{3.19}$$

which gives rise to a pair of complex conjugate eigenvalues with positive real parts that result in useful oscillatory motions for generating chaos.

The trajectory of system (3.17) can be considered as being governed by piecing together trajectory parts in the subspaces, centered at the equilibrium points, respectively.

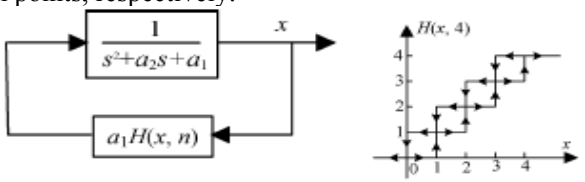

(a) (b)

Fig. 3.1. (a) Second-order linear system with a feedback of hysteresis-series. (b) A hysteresis-series ($n = 4$).

In order to control chaotic system (3.17), a control signal v is applied in the system, that is, equation (3.17) is rewritten as follows:

$$\begin{cases} \dot{x}_1 = x_2 \\ \dot{x}_2 = -a_1 x_1 - a_2 x_2 + a_1 u + v \end{cases}. \tag{3.20}$$

If the objective of chaos control is to control the variables of a chaotic system to an equilibrium point of the system, the following theorem can be used:

Theorem 3.2. For the chaotic system (3.20), if a linear sliding mode and a terminal sliding mode are chosen as equations (3.21) and (3.22), and a control law is designed as equation (3.23), the variable states of system (3.30) can converge to zeros asymptotically:

$$s_1(t) = x_1 + \lambda_1 x_2 , \tag{3.21}$$

$$l_1(t) = \gamma_1 \dot{s}_1^{\,p_1/q_1} + s_1 , \tag{3.22}$$

$$v = v_1 + v_2 , \tag{3.23a}$$

$$v_1 = a x_1 - b x_2 - a u - \frac{1}{\lambda_1} x_2 , \tag{3.23b}$$

and

$$v_2 = -\frac{1}{\lambda_1} \int_0^t \frac{q_1}{\gamma_1 p_1} \dot{s}_1^{\,2-p_1/q_1} + \eta_1 \operatorname{sgn}(l_1)] d\tau , \tag{3.23c}$$

where $\lambda_1>0$, $\gamma_1>0$, and $\eta_1>0$ are design parameters; p_1 and q_1 are positive odd integers, which satisfy the condition $p > q$.

Proof. The following Lyapunov function is considered:

$$V_1(t) = \frac{1}{2} l_1^2(t)$$

Differentiating $V_1(t)$ with respect to time, it gets:

$$\dot{V}_1(t) = l_1 \dot{l}_1$$

$$= l_1 \gamma_1 \frac{p_1}{q_1} \dot{s}_1^{\,p_1/q_1-1} (\ddot{s}_1 + \frac{1}{\gamma_1} \frac{q_1}{p_1} \dot{s}_1^{\,2-p_1/q_1})$$

$$= l_1 \gamma_1 \frac{p_1}{q_1} \dot{s}_1^{\,p_1/q_1-1} (\lambda_1 \dot{v}_2 + \frac{1}{\gamma_1} \frac{q_1}{p_1} \dot{s}_1^{\,2-p_1/q_1})$$

$$= -\eta_1 \gamma_1 \frac{p_1}{q_1} \dot{s}_1^{\,p_1/q_1-1} |l_1| \le 0,$$

when $l_1 \neq 0$, two different cases are discussed as follows:

1) $\dot{s}_1 \neq 0$. Since p_1 and q_1 are positive odd integers, satisfying $\dot{s}_1^{\,p_1/q_1-1}>0$, it can be obtained $\dot{V}_1 < 0$.

2) $\dot{s}_1 = 0$, $s_1 \neq 0$. According to [12], the state variables of the system will not always stay on the points ($\dot{s}_1 = 0, s_1 \neq 0$) and will continue to cross the axis $\dot{s}_1 = 0$ in the phase plane 0-$s_1\dot{s}_1$.

Therefore, l_1 and s_1 can converge to zero in finite time. Then, the states (x_1, x_2) will converge to zero asymptotically. This completes the proof.

If the objective of chaos control is to force the variables of the chaotic system (3.20) to track the desired trajectories, for example, assuming that the desired trajectories of the chaotic system (3.20) are $x_{1\text{ref}}$ and $x_{2\text{ref}}$, which are all smooth, the following theorem can be used:

Theorem 3.3. For the chaotic system (3.20), if a linear sliding mode and a terminal sliding mode are chosen as equations (3.24) and (3.25), and a control law is designed as equation (3.26), the errors between the variable states of system (3.20) and its desired trajectories, $\boldsymbol{e} = [e_1,e_2]^T = x_{\text{ref}} - \boldsymbol{x}$, can converge to zeros asymptotically:

$$s_2(t) = \lambda_2 e_1 + \dot{e}_1, \tag{3.24}$$

$$l_2(t) = \gamma_2 \dot{s}_2^{\,p_2/q_2} + s_2\,, \tag{3.25}$$

$$v = v_1' + v_2'\,, \tag{3.26a}$$

$$v_1' = -\lambda_2(x_2 - \dot{x}_{1ref}) + ax_1 - bx_2 - au + \dot{x}_{2ref}\,, \tag{3.26b}$$

and

$$v_2' = -\int_0^t \frac{q_2}{\gamma_2 p_2} \dot{s}_2^{\,2-p_2/q_2} + \eta_2 \operatorname{sgn}(l_2)]d\tau\,, \tag{3.26c}$$

where λ_2>0, γ_2>0, and η_2>0 are design parameters; p_2 and q_2 are positive odd integers, which satisfy the condition p_2>q_2.

Proof. The proof of Theorem 3 is similar to that for Theorem 2.

Some simulation results of chaotic system (3.20) using Theorem 2 and Theorem 3 are shown in Fig. 3.2 – Fig. 3.11. For the purpose of the simplicity, n is chosen as 1 in chaotic system (3.20). The chaotic behavior of system (3.20) can be seen in Fig. 3.2 under the case of uncontrolled. Fig. 3.3a – Fig. 3.3d are simulation results using Theorem 2. The control signal is activated after 240 seconds. It can be seen that chaotic system (3.20) converges to zeros after 240 second.. Fig. 3.4a – Fig. 3.4d are simulation results using Theorem 3. The desired trajectory is a limit cycle. The control signal is activated after 270 seconds. It can be seen that chaotic system (3.20) tracks the limit cycle.

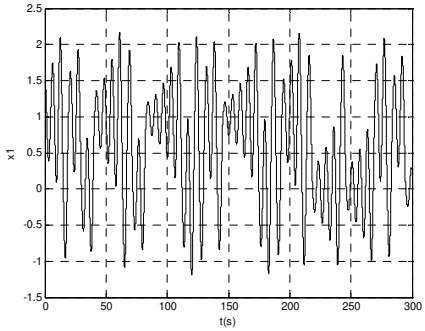

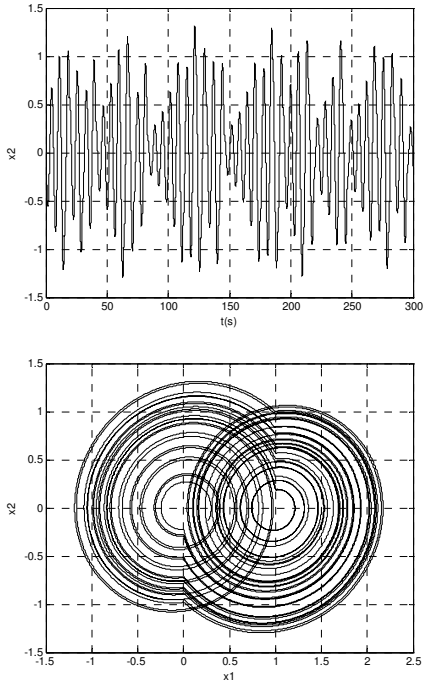

Fig. 3.2. chaotic behavior under the case of uncontrolled. a) state x_1. b) state x_2. c) phase plane.

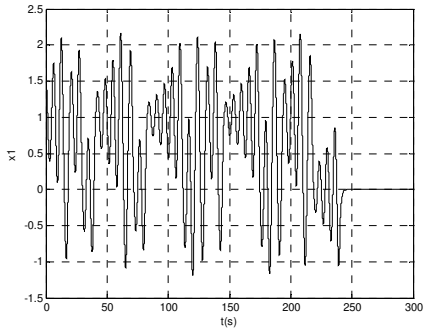

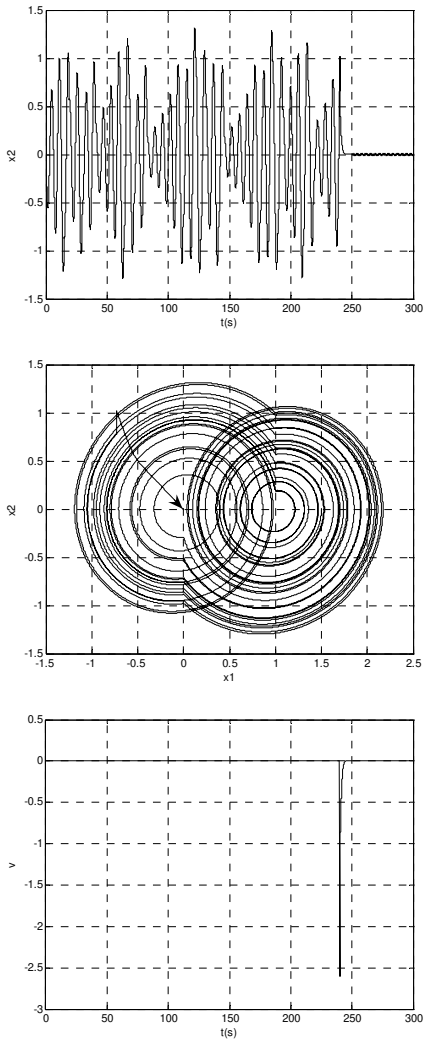

Fig. 3.3. chaotic behavior with the control in Theorem 2 after 240 seconds. a) state x_1. b) state x_2. c) phase plane. d) control signal.

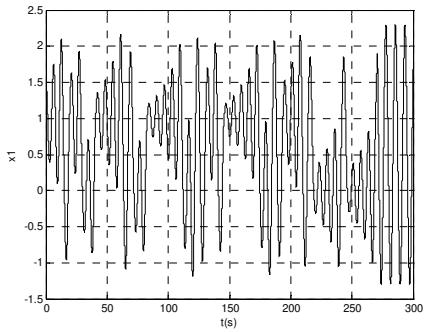
x1
t(s)

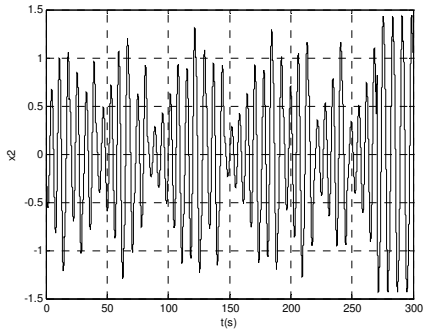
x2
t(s)

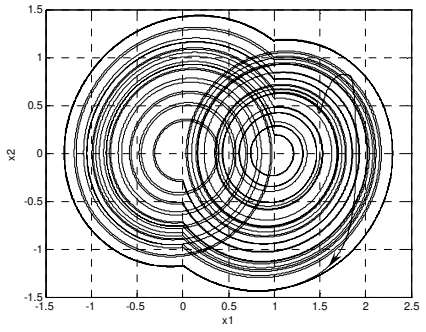
x2
x1

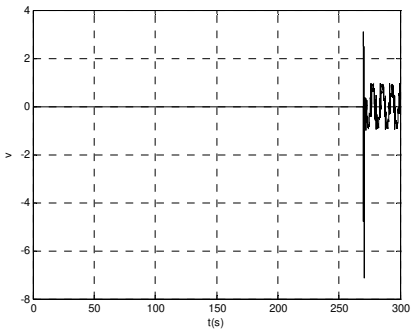

Fig. 3.4. chaotic behavior with the control in Theorem 2 after 240 seconds. a) state x_1. b) state x_2. c) phase plane. d) control signal.

3.4. Chaos Synchronization

Chaos synchronization is a special kind of chaos control. It usually appears in two chaotic systems consisting of a master system and a slave system, which are of identical structure and parameters except for different initial conditions. The chaos synchronization means that the trajectories of the slave system track that of the master system starting from arbitrary initial conditions [15, 17]. The pioneering work was done by [7]. Since then, many schemes for chaos synchronization have been proposed [5-8]. Generally speaking, two main classes of chaos synchronization schemes can be identified i.e. based on either the transverse stability or the observability. In the first case, sufficient conditions for the negativity of all transverse or conditional Lyapunov exponents are considered, ensuring synchronization of identical chaotic systems with unidirectional coupling. Considering the latter approach, the problem is formulated as an observation problem, i.e. the reconstruction of the system state from measurements of an output variable.

Although there are many methods of chaos synchronization, sliding mode based method is an important method of chaos synchronization because of its robustness and simplicity. In this section, we will use the sliding mode control concept to realize chaos synchronization.

3.4.1. Synchronization of Chaotic System Using Observer

Many chaotic systems, such as Chua′s circuit, Rössler system, Lorenz system, and so on, can be expressed one of the following form consisting of linearities and nonlinearities in [10]:

$$\dot{\boldsymbol{x}}(t) = \boldsymbol{A}\boldsymbol{x}(t) + \boldsymbol{b}f(\boldsymbol{x}) + \boldsymbol{D}, \tag{3.27a}$$

or

$$\dot{\boldsymbol{x}}(t) = \boldsymbol{A}\boldsymbol{x}(t) + \boldsymbol{B}\boldsymbol{f}(\boldsymbol{x}) + \boldsymbol{D}, \tag{3.27b}$$

where $\boldsymbol{x} \in R^n$ is the state vector; $\boldsymbol{A} \in R^{n\times n}$, $\boldsymbol{b} \in R^{n\times 1}$,$\boldsymbol{B} \in R^{n\times m}$, $\boldsymbol{D} \in R^{n\times 1}$ are constant real matrices, $n \geq m$; $f(\boldsymbol{x})$: $R^n \rightarrow R$ is a nonlinear scale function; $\boldsymbol{f}(\boldsymbol{x})$: $R^n \rightarrow R^m$ is a nonlinear vector function.

Another chaotic system reconstructed is similar to the master chaotic system, named slave chaotic system:

$$\dot{\tilde{\boldsymbol{x}}}(t) = \boldsymbol{A}\tilde{\boldsymbol{x}}(t) + \boldsymbol{b}f(\tilde{\boldsymbol{x}}) + \boldsymbol{D} + u, \tag{3.28a}$$

or

$$\dot{\tilde{\boldsymbol{x}}}(t) = \boldsymbol{A}\tilde{\boldsymbol{x}}(t) + \boldsymbol{B}\boldsymbol{f}(\tilde{\boldsymbol{x}}) + \boldsymbol{D} + \boldsymbol{u}, \tag{3.28b}$$

where $\tilde{\boldsymbol{x}} \in R^n$, $\boldsymbol{A}$, $\boldsymbol{b}$, $\boldsymbol{B}$, and $\boldsymbol{D}$ are the same as (3.27); control $\boldsymbol{u}$ is used to realize the synchronization of the system (3.27) and the system (3.28). $\boldsymbol{u}$ can be adopted two cases: $\boldsymbol{u} = \boldsymbol{u}(\tilde{\boldsymbol{x}}, \boldsymbol{x})$ or $\boldsymbol{u} = \boldsymbol{u}(\tilde{\boldsymbol{x}}, \boldsymbol{y})$, where $\boldsymbol{y} \in R^p$ and $p \geq m$, is the output of system (3.27). In the former, the chaos synchronization is merely a control of the nonlinear system. For the later case, the chaos synchronization is a more challenging task.

In order to realize chaos synchronization only using the output signal $y(t)$, one important method is to regard the slave system as an observer of the master system [10]. But the existing methods have some disadvantages. The first is that the chaotic systems used for synchronization are ideal. The second is that synchronization of chaotic systems with multi-nonlinearities was not well done. This section addresses these problems. A robust observer is proposed in [14] and used to realize the chaos synchronization. Since the method of the chaos synchronization makes the systems robust, it has significant meaning for practical applications.

3.4.2. Chaos Synchronization Using a Robust Sliding Mode Observer

Consider a class of uncertain chaotic systems:

$$\dot{\boldsymbol{x}}(t) = \boldsymbol{A}\boldsymbol{x}(t) + \boldsymbol{B}\boldsymbol{f}(\boldsymbol{x}) + \boldsymbol{D} + \boldsymbol{\xi}(t, \boldsymbol{x}), \tag{3.29}$$

where $\boldsymbol{A}$, $\boldsymbol{B}$, $\boldsymbol{D}$ and $\boldsymbol{f}(\boldsymbol{x})$ are the same as that in (3.27); $\boldsymbol{B}$ is of full rank matrix; $\boldsymbol{\xi}(t, \boldsymbol{x}) = \boldsymbol{B}\boldsymbol{\delta}(t, x)$ denotes the system uncertainties, $\|\boldsymbol{\delta}(t, \boldsymbol{x})\| \le r_2 + \alpha(t, y)$, where r_2 is a known positive constant and α is a known function.

Because the regions of the chaotic attractors are kept in a finite space, the states of the chaotic systems are bounded, that is $\|\boldsymbol{x}\| \le m$, where m is a positive real constant. For the nonlinear function $\boldsymbol{f}(\boldsymbol{x})$, which consists of the states of the chaotic system, therefore, it holds $\|\boldsymbol{f}(\boldsymbol{x})\| \le r_1$, where r_1 is a known positive constant.

3.4.3. Implementation of Chaos Synchronization

Based on the Walcott-Zak observer, a new robust sliding mode observer is designed, which avoids the strict conditions, so the design can be simplified. The synchronization signal is chosen as:

$$\boldsymbol{y}(t) = \boldsymbol{C}\boldsymbol{x}(t), \tag{3.30}$$

where $y(t) \in R^p$ is the output of the chaotic system (3.29) and $p \ge m$; $C \in R^n$ to be determined later.

For the master chaotic system (3.29), a robust sliding mode observer is proposed as follows:

$$\dot{\hat{\boldsymbol{x}}} = \boldsymbol{A}\hat{\boldsymbol{x}}(t) + \boldsymbol{B}\boldsymbol{f}(\hat{\boldsymbol{x}}) + \boldsymbol{D} - \boldsymbol{G}(\boldsymbol{C}\hat{\boldsymbol{x}} - \boldsymbol{y}) + \boldsymbol{B}\boldsymbol{v}(\hat{\boldsymbol{x}}, \boldsymbol{y}), \tag{3.31}$$

where $\hat{\boldsymbol{x}}(t) \in R^n$ represents the system states; A, B and D are the same as that of (3.27); $G \in R^{n\times 1}$ is a constant design matrix, and $\boldsymbol{v}(\hat{\boldsymbol{x}}, \boldsymbol{y}) \in R^m$ is the control input. The observer (3.31) is adopted as the slave system for chaos synchronization.

Define the error variable $e(t)$ as: $\boldsymbol{e}(t) = \hat{\boldsymbol{x}}(t) - \boldsymbol{x}(t)$. The error system is obtained from (3.31) and (3.29) as follows:

$$\dot{\boldsymbol{e}}(t) = \boldsymbol{A}_0\boldsymbol{e}(t) + \boldsymbol{B}(\boldsymbol{f}(\hat{\boldsymbol{x}}) - \boldsymbol{f}(\boldsymbol{x}) - \boldsymbol{\delta}(t, \boldsymbol{x})) + \boldsymbol{B}\boldsymbol{v}, \tag{3.32}$$

where $\boldsymbol{A}_0 = \boldsymbol{A} - \boldsymbol{G}\boldsymbol{C}$. For the sliding mode observer (3.31), a sliding mode manifold, which is the function of the output $y(t)$ of the master chaotic system (3.29) and the variable $\hat{\boldsymbol{x}}(t)$ of the slave system (3.31), is designed as the following form:

$$\boldsymbol{s} = \boldsymbol{Me} = \boldsymbol{FCe} = \boldsymbol{Fe}_y = \boldsymbol{F}(\boldsymbol{C}\hat{\boldsymbol{x}} - \boldsymbol{y}) \quad , \tag{3.33}$$

where $\boldsymbol{M} \in R^{m\times n}$, $\boldsymbol{F} \in R^{m\times 1}$, $\boldsymbol{M}=\boldsymbol{FC}$, the vector $\boldsymbol{C}$ is the output matrix of system (3.29). So the design of the sliding mode manifold (3.33) depends on the design of parameter matrix $\boldsymbol{M}$.

Define $\boldsymbol{e} = [\boldsymbol{e}_1^T \quad \boldsymbol{e}_2^T]$, $e_1 \in R^m$, $e_2 \in R^{n-m}$, and rewrite the error system (3.32) as the following decomposed form:

$$\dot{\boldsymbol{e}}_1(t) = \boldsymbol{A}_{011}\boldsymbol{e}_1(t) + \boldsymbol{A}_{012}\boldsymbol{e}_2(t) + \boldsymbol{B}_1(\boldsymbol{f}(\hat{\boldsymbol{x}}) - \boldsymbol{f}(\boldsymbol{x}) - \boldsymbol{\delta}(t,\boldsymbol{x})) + \boldsymbol{B}_1\boldsymbol{v} \quad , \tag{3.34a}$$

and

$$\dot{\boldsymbol{e}}_2(t) = \boldsymbol{A}_{021}\boldsymbol{e}_1(t) + \boldsymbol{A}_{022}\boldsymbol{e}_2(t) \quad . \tag{3.34b}$$

And rewrite $\boldsymbol{s}(t)$ (3.32) as the decomposed form: $\boldsymbol{s} = \boldsymbol{M}_1\boldsymbol{e}_1 + \boldsymbol{M}_2\boldsymbol{e}_2$, where $\boldsymbol{M}=[\boldsymbol{M}_1 \ \boldsymbol{M}_2]$, $\boldsymbol{M}_1 \in R^m$, $\boldsymbol{M}_2 \in R^{m\times(n-\mathrm{m})}$. We have the following result [16, 18].

Theorem 3.4. For the observer (3.31) of system (3.29), the following two conditions are satisfied, the chaos synchronization between systems (3.31) and (3.29) is guaranteed:

1) if the sliding mode manifold is chosen as (3.33) and the control strategy v is designed as follows:

$$\boldsymbol{v} = \boldsymbol{v}_l + \boldsymbol{v}_n \quad , \tag{3.35a}$$

$$\boldsymbol{v}_l = -\boldsymbol{f}(\hat{\boldsymbol{x}}) \quad , \tag{3.35b}$$

and

$$\boldsymbol{v}_n = -\frac{\left(\boldsymbol{s}^T\boldsymbol{MB}\right)^T}{\left\|\boldsymbol{s}^T\boldsymbol{MB}\right\|}\left(r_1 + r_2 + \alpha(t,y) + \beta\right) \quad , \tag{3.35c}$$

where r_1 and r_2 are known positive constants. β and η are positive scalars, $\beta>0$, $0<\eta<1$.

2) The matrix $\boldsymbol{G}$ makes $\boldsymbol{A}_0$ in (3.32) a Hurwitz matrix, the matrix $\boldsymbol{M}$ makes $\boldsymbol{A}_{022} - \boldsymbol{A}_{021}\boldsymbol{M}_1^{-1}\boldsymbol{M}_2$ a Hurwitz matrix, while the following condition is satisfied:

$$\lambda_{\max}(\boldsymbol{M}^T\boldsymbol{MA}_0 + \boldsymbol{A}_0^T\boldsymbol{M}^T\boldsymbol{M}) \le 0 \quad , \tag{3.36}$$

where $\lambda_{\max}(\boldsymbol{A}_s)$ presents the maximum eigenvalue of $\boldsymbol{A}_s$.

Proof. Consider the following Lyapunov function:

$$V(t) = \frac{1}{2}\boldsymbol{s}^T\boldsymbol{s} = \frac{1}{2}\|\boldsymbol{s}\|^2 = \frac{1}{2}(\boldsymbol{Me})^T\boldsymbol{Me} = \frac{1}{2}\boldsymbol{e}^T\boldsymbol{M}^T\boldsymbol{Me}.$$

The derivative of $V(t)$ along the error system (3.32) can be obtained:

$$\dot{V}(t) = \boldsymbol{s}^T\dot{\boldsymbol{s}} = \boldsymbol{e}^T\boldsymbol{M}^T\boldsymbol{M}\dot{\boldsymbol{e}} = \boldsymbol{e}^T\boldsymbol{M}^T\boldsymbol{M}\left(\boldsymbol{A}_0\boldsymbol{e} + \boldsymbol{B}\left(\boldsymbol{f}(\hat{\boldsymbol{x}}) - \boldsymbol{f}(\boldsymbol{x}) - \boldsymbol{\delta}(t,\boldsymbol{x})\right) + \boldsymbol{Bv}\right)$$

$$= \frac{1}{2}\boldsymbol{e}^T(\boldsymbol{M}^T\boldsymbol{MA}_0 + \boldsymbol{A}_0{}^T\boldsymbol{M}^T\boldsymbol{M})\boldsymbol{e} + \boldsymbol{s}^T\boldsymbol{MBf}(\hat{\boldsymbol{x}}) - \boldsymbol{s}^T\boldsymbol{MBf}(\boldsymbol{x}) + \boldsymbol{s}^T\boldsymbol{MB}\boldsymbol{\delta}(t,\boldsymbol{x}) + \boldsymbol{s}^T\boldsymbol{MBv}$$

From (3.36), the above equation becomes:

$$\dot{V}(t) \le \boldsymbol{s}^T\boldsymbol{MBf}(\hat{\boldsymbol{x}}) - \boldsymbol{s}^T\boldsymbol{MBf}(\boldsymbol{x}) + \boldsymbol{s}^T\boldsymbol{MB}\boldsymbol{\delta}(t,\boldsymbol{x}) + \boldsymbol{s}^T\boldsymbol{MBv}.$$

By substituting the sliding mode control strategy (3.35) into above equation, it can be obtained:

$$\dot{V}(t) \le \boldsymbol{s}^T\boldsymbol{MBf}(\boldsymbol{x}) + \boldsymbol{s}^T\boldsymbol{MB}\boldsymbol{\delta}(t,\boldsymbol{x}) + \boldsymbol{s}^T\boldsymbol{MBv}_n$$

$$\le \left\|\boldsymbol{s}^T\boldsymbol{MB}\right\|\left\|\boldsymbol{f}(\boldsymbol{x})\right\| + \left\|\boldsymbol{s}^T\boldsymbol{MB}\right\|\left\|\boldsymbol{\delta}(t,\boldsymbol{x})\right\| + \left\|\boldsymbol{s}^T\boldsymbol{MB}\right\|\left(r_1 + r_2 + \alpha(t,y) + \beta\right)$$

$$\le -\beta\left\|\boldsymbol{s}^T\boldsymbol{MB}\right\| \le -\beta\|\boldsymbol{MB}\|\|\boldsymbol{s}\|$$

that is $\dot{V}(t) \le -\gamma\|\boldsymbol{s}\| < 0$ for $\|\boldsymbol{s}\| \ne 0$, where $\gamma = -\beta\|\boldsymbol{MB}\| > 0$. Therefore, the error system (3.32) will reach sliding mode manifold surface $\boldsymbol{s}$=0 in a finite time $t_r \le |s(0)|/\gamma$. After the error system (3.32) reaches the sliding mode manifold surface s=0, the dynamic behaviour of the error system (3.32) will depend on the linear sliding mode manifold (3.33), that is:

$$\boldsymbol{e}_1 = -\boldsymbol{M}_1^{-1}\boldsymbol{M}_2\boldsymbol{e}_2. \tag{3.37}$$

Substituting (3.37) into the error system (3.35a), the reduced-order dynamic system of error system (3.32) can be obtained:

$$\dot{\boldsymbol{e}}_2(t) = \left(\boldsymbol{A}_{022} - \boldsymbol{A}_{021}\boldsymbol{M}_1^{-1}\boldsymbol{M}_2\right)\boldsymbol{e}_2(t) = \boldsymbol{A}_M\boldsymbol{e}_2(t). \tag{3.38}$$

Designing the sliding mode parameter matrix $\boldsymbol{M}$ to make $\boldsymbol{A_M}$ a Hurwitz matrix, then the system (3.38) will be asymptotically stable. That is, after reaching the sliding mode manifold surface s=0, the error system (3.32) will converge to the equilibrium point $\boldsymbol{e}$ = 0 asymptotically.

3.4.4. Multi-dimensional Signals Transmission via One Signal Transmission Channel

Chaos synchronization has numerous potential applications in mechanics, laser and chemical technologies, communications, biology and medicine, economics, ecology etc [3, 4, 9].

For practical applications such as signal, image, speech processing and secure communication, it is desirable to use a smaller number of channels of signals from the master chaotic system for chaos synchronization. The challenge is how to do it via a scalar transmission channel. One effective approach is by using observers [10, 11]. Synchronization of chaotic systems with a single nonlinearity such as Chua system and Rössler system can be well done by using an observer via a single transmission channel, whereas, for the chaotic systems with multi nonlinearities such as hyperchaotic Chua system and Lorenz system, synchronization can not be realized by using a single signal channel.

In order to realize chaos synchronization via one signal transmission channel, a method to transmit multi dimensional signals plus a synchronization signal of the master chaotic system using only one single transmission channel is proposed in [14] based on the idea of time division multiplex. The functional block diagram of the transmitter is shown in Fig. 3.5. There are three tasks in the transmitter. The first is to combine multi dimensional signals into one signal to be transmitted in one single transmission channel. The second is to add the bias level series, ε_i, i=1,…,p, to the transmission signal to distinguish each signal from the amplitudes. The third is to add another information to the transmission signal to represent the synchronization pulse signal.

The section proposes a hardware structure as shown in Fig. 3.6. The transmission signal $y_\varepsilon(t)$ is inputted to the two blocks: level adjustor and level comparator. The level adjustor is used to eliminate the bias level series, ε_i, i=1,…, p, from the transmission signal $y_\varepsilon(t)$. While the level comparator is used to extract the sampling pulse f_{syn} from the transmission signal $y_\varepsilon(t)$. The signal f_{syn} is the reconstructed sampling signal of f_{clk}.

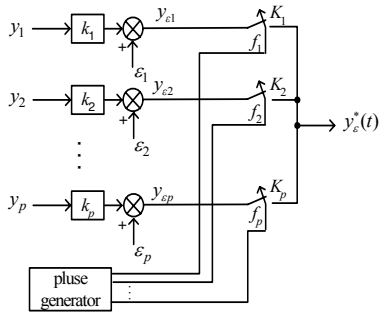

Fig. 3.5. The block diagram of the transmitter.

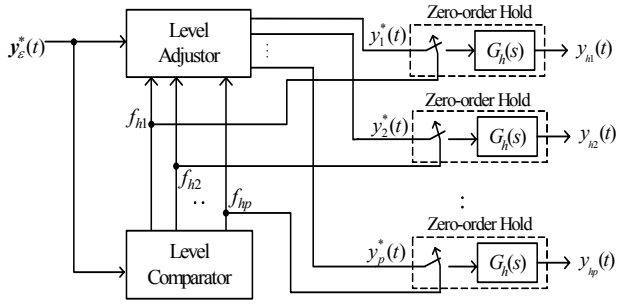

Fig. 3.6. The hardware structure of the receiver.

3.4.5. Synchronization of Chaotic Systems with Multi-nonlinearities

The principle of the synchronization of uncertain chaotic systems with multi-nonlinearties by using observers is shown in Fig. 3.7. In the transmitter terminal, $y_1(t)$, $y_2(t)$, … , $y_p(t)$ represent p output signals of the master chaotic system, which are to be transmitted. f_{clk} is the sampling pulse, which frequency must satisfy the Shannon's sampling theorem, while in the receiver terminal, y_{h1}, y_{h2}, … , $y_{hp}(t)$ represent p reconstructed output signals of the master chaotic system. It should be noticed that there is only one signal transmission channel between the transmitter and the receiver.

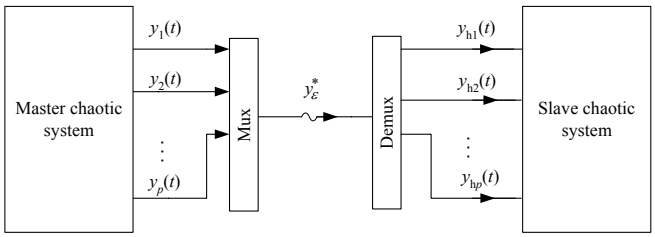

Fig. 3.7. Synchronization of uncertain chaotic systems.

The example is hyperchaotic system formed by a pair of coupled Chua′s circuits in [10]:

$$\dot{\boldsymbol{x}} = \boldsymbol{A}\boldsymbol{x} + \boldsymbol{B}\boldsymbol{f}(\boldsymbol{x}) + \boldsymbol{\xi}(t,\boldsymbol{x}) + \boldsymbol{D} = \boldsymbol{A}\boldsymbol{x} + \boldsymbol{B}\left(\boldsymbol{f}(\boldsymbol{x}) + \boldsymbol{\delta}(t,\boldsymbol{x})\right) + \boldsymbol{D}, \quad (3.39)$$

where

$\boldsymbol{D}$=0,

$$\boldsymbol{A}=\begin{bmatrix} -\alpha(b+1) & 0 & 0 & \alpha & 0 & 0 \\ 0 & -\alpha(b+1) & 0 & 0 & 10 & 0 \\ 0 & 0 & 0 & -\beta & 0 & 0 \\ 1 & 0 & 1 & -1-m & m & 0 \\ 0 & 1 & 0 & 0 & -1 & 1 \\ 0 & 0 & 0 & 0 & -\beta & 0 \end{bmatrix},$$

$$\boldsymbol{B}=\begin{bmatrix} -\alpha & 0 \\ 0 & -\alpha \\ 0 & 0 \\ 0 & 0 \\ 0 & 0 \\ 0 & 0 \end{bmatrix},$$

$$\boldsymbol{f}(\boldsymbol{x})=\begin{bmatrix} f_1(x_1) \\ f_2(x_4) \end{bmatrix},$$

and

$$\boldsymbol{\delta}(t,\boldsymbol{x})=\begin{bmatrix} 0.01\sin(3\pi t) \\ 0.01\sin(4\pi t) \end{bmatrix},$$

where $f_1(x_1)=(a-b)(|x_1+1|-|x_1-1|)/2$; $f_2(x_4)=(a-b)(|x_4+1|-|x_4-1|)/2$; α=10, β=14.87, m=1, a = –1.27, b=–0.68. The output matrix of the system (3.41) is designed as:

$$\boldsymbol{C}=\begin{bmatrix} 1 & 0 & 0 & 0 & 1 & 0 \\ 0 & 1 & 0 & 1 & 0 & 0 \end{bmatrix}.$$

According to Theorem 4, $\boldsymbol{A}_0$ is a Hurwitz matrix, choose the spectrum of the matrix A_0 as {–9, –8, –6, –20, –15, –7, }, the matrix G can be calculated:

$$\boldsymbol{G}=\begin{bmatrix} 25.1798 & -14.3051 & 30.9801 & 18.7690 & -0.2063 & 52.9225 \\ -27.2248 & 38.2535 & 29.3055 & -7.6269 & 29.6791 & 28.7371 \end{bmatrix}^T.$$

$\boldsymbol{F}$ is chosen as: $\boldsymbol{F}$=diag{0.005, 0.005}. According to Theorem 4, the parameters are designed as: r_2=0.9, r_3=0.2, $\alpha(t, y)$=0, β=0.2, ε_1=8, ε_2=0, k_1=k_2=1, T=1ms. The simulation results are shown in Fig. 3.8 - Fig. 3.10. Fig. 3.8 depicts the two output signals of the master chaotic system to be transmitted to the slave chaotic system, y_1 and y_2. Fig. 3.9 shows the one channel transmission signal y_ε contains two signals, y_1 and y_2, plus a synchronization signal. Fig. 3.10 shows phase trajectory of the hyperchaotic Chua′s circuit state variables x_1, x_2 and their estimates $\hat{x}_1$,

$\hat{x}_2$; Fig. 3.11 presents phase trajectory of the hyperchaotic Chua′s circuit state variables x_2, x_3 and its estimates.

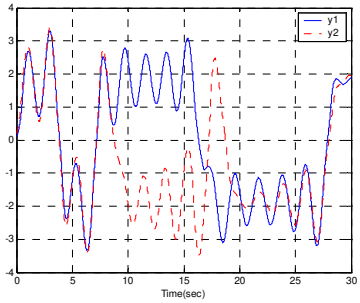

Fig. 3.8. Two outputs y_1 and y_2.

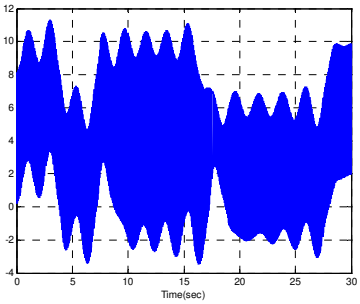

Fig. 3.9. One transmitted signal.

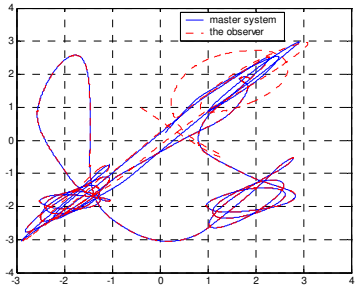

Fig. 3.10. Phase trajectory of (x_1,x_2) vs.($\hat{x}_1$, $\hat{x}_2$).

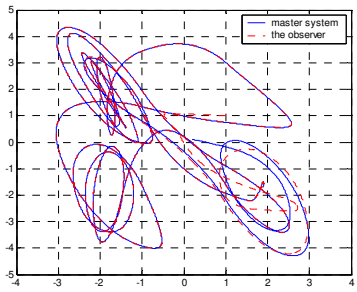

Fig. 3.11. Phase trajectory of (x_2,x_3) vs.$(\hat{x}_2,\hat{x}_3)$.

3.5. Conclusions

In this chapter, the sliding mode based chaos control has been discussed. Three methods of sliding mode methods, namely, traditional linear sliding mode, terminal sliding mode and nonsingular terminal sliding mode, have been used in chaos control. The advantages of the sliding mode based chaos control can be summarized as follows: it is robust to system uncertainties, suitable for realization, and simple to calculate.

Furthermore, a robust sliding mode observer based chaos synchronization method has also been described. Based on the time division multiplex technique, a transmission method of the synchronization signals from the master system to the slave system via one single transmission channel has been designed. The advantages of this method are as follows: (i) multi-dimensional signals can be transmitted using the single channel so that chaos synchronization can be realised more efficiently without incurring significant costs of additional equipment/devices for transmitting more than one-dimensional signals; (ii) it is robust to a class of chaotic systems including internal parameter uncertainties and/or the external disturbances (iii) it is a systematic design method of chaos synchronization; (iv) it can be used for highly chaotic systems.

References

[1] G. Chen and X. Dong, *From Chaos to Order: Perspectives and Applications*. (World Scientific, Singapore, 1998).

[2] W. D. Ditto, S. N. Rauseo and M. L. Spano, Experimental control of chaos, *Phys. Rev. Lett.* **65**, 3211-3214, (1990).

[3] M. Lakshmanan and K. Murali, *Chaos in Nonlinear Oscillators: Controlling and Synchronization*. (World, Singapore, 1996).

[4] K. S. Halle, W. C. Wu, M. Itoh and L. C. Chua, Spread spectrum communication through modulation of chaos, *Int. J. Bifurcation Chaos* **3**, 469-477, (1993).

[5] M. Itoh, W. C. Wu and L. C. Chua, Communication systems via chaotic signals from a reconstruction viewpoint, *Int. J. Bifurcation Chaos* **7**, 275-286, (1997).

[6] L. J. Kocarev and K. S. Halle, Experimental demonstration of secure communication via chaotic synchronization, *Int. J. Bifurcation Chaos* **2**, 709-713, (1992).

[7] L. M. Pecora and T. L. Carroll, Synchronization in chaotic systems, *Phys. Rev. Lett.* **64**, 821-824, (1990).

[8] T. L. Carroll and L. M. Pecora, Synchronizing chaotic circuits, *IEEE Trans. Circuits Syst.* **38**, 453-456, (1991).

[9] L. O. Chua, M. Itoh, L. Kocarev and K. Eckert, Chaos synchronization in Chua's circuit, *J. Circuits Syst. Computers* **3**, 93-108, (1993).

[10] D. Cafagna and G. Grassi, Synchronizing hyperchaos using a scalar signal: a unified framework for systems with one or several nonlinearities, *APCCAS* **1**, 575-580, (2002).

[11] G. Grassi and S. Mascolo, Nonlinear observer design to synchronize hyperchaotic systems with a scalar signal, *IEEE Trans. Circuits Syst.* **44**, 1011-1014, (1997).

[12] Y. Feng, X. Yu, and Z. Man, Nonsingular adaptive terminal sliding mode control of rigid manipulators, *Automatica* **38**, 2159-2167, (2002).

[13] Y. Feng, X. Han, Y. Wang and X. Yu, Second-order terminal sliding mode control of uncertain multivariable systems, *International Journal of Control* **80**(6), 856-862, (2007).

[14] Y. Feng, X. Yu and L. Sun, Synchronization of uncertain chaotic systems using a single transmission channel, *Chaos, Solitons and Fractals* **35**(4), 755-762, (2008).

[15] Y. Feng, L. Sun, and X. Yu, Finite time synchronization of chaotic systems with unmatched uncertainties, *The 30th Annual Conference of the IEEE Industrial Electronics Society* Busan, Korea, (November 2-6, 2004).

[16] Y. Feng, L. Sun and X. Yu, Synchronization of a class of uncertain chaotic systems via observer, *Dynamics of Continuous, Discrete and Impulsive Systems* **13**(c), 77-87, (2006).

[17] F. Han, L. Sun, Y. Feng, P. Wang and X. Yu, Synchronization of the Duffing oscillator by using terminal sliding mode control, *Proceedings of The IEEE Region 10 Technical Conference on Computer, Communication, Control and Power Engineering* (*IEEE TENCON*) **3**, 1362-1365, (2002).

[18] Y. Feng and L. Sun, Chaotic system synchronization using a robust sliding mode observer, *International Conference on Dynamics, Instrumentation and Control* (CDIC) Nanjing, China, (August 19-20, 2004).

[19] Y. Wu, L. X. Yu and Z. Man, Terminal sliding mode control design for uncertain dynamic systems, *Systems and Control Letters* **34**, 281-288, (1998).

[20] X. Yu and Z. Man, Model reference adaptive control systems with terminal sliding modes, *International Journal of Control* **64**, 1165-1176, (1996).
[21] Z. Man and X. Yu, Terminal sliding model control of MIMO linear systems, *IEEE Transactions on Circuits and Systems I: Fundamental Theory and Applications* **44**, 1065-1070, (1997).

CHAPTER 4

A NEW TWO-STAGE METHOD FOR NONPARAMETRIC REGRESSION WITH JUMP POINTS

C.Z. Wu[*], C.M. Liu**, K.L. Teo** and Q.X. Shao[***]

[*]*School of Mathematics and Computer Science,*
Chongqing Normal University, Chongqing, 40047, China.
E-mail:changzhiwu@yahoo.com
[**]*Department of Mathematics and Statistics,*
Curtin University of Technology, Perth, WA, 6102, Australia.
E-mail:jimmy_uwa@yahoo.com.tw and k.l.teo@curtin.edu.au
[***]*CSIRO Mathematical and Information Sciences,*
WA, 6104, Australia.
E-mail: Quanxi.Shao@csiro.au

In this chapter, a two-staged method is presented for nonparametric regression with jump points. After the rough location of all the possible jump points are identified using the existing efficient kernel method, a smoothing spline function is used to approximate each segment of the regression function. A time scaling transformation is derived so as to map the undecided jump points into fixed points. This approximation problem is formulated as an optimization problem which can be solved by many existing techniques. The method is applied to several examples. The results obtained show that the method is highly efficient.

4.1. Introduction

Statistical modelling generally assumes smoothness and continuity of the phenomena of interest. However, some phenomena may experience sudden or sharp change. For example, groundwater table may undergo drastic changes in very short periods of time [15] due to sudden changes in environment, such as land clearing. When we study the portfolio management, the amount of stocks of a particular investor can be viewed

as experiencing a jump when he/she purchases or sells his/her stocks. This sudden change is reflected as a jump in visual display. Without considering these jumps, we may make an serious error in drawing inference about the process under study. It is clearly important to estimate both the number of jumps and their locations and magnitudes.

Problems related to regression with jump points have been addressed and investigated for more than two decades. [11] proposed an algorithm to estimate regression functions when discontinuities are present. [20] used one-sided moving average to find the locations of jumps, [9] used Fourier analysis for jump detection. [8] made use of pairing pattern and linear filter to develop a discontinuity detector for the purpose of detecting the jumps and their magnitudes. [13] estimated the locations and magnitudes of the jumps by the boundary kernels. [19] used the kernel method to estimate both the locations and magnitudes of the jumps. [18] used wavelets to provide a useful procedure for the detection of the jump points and their magnitudes. [14] proposed a two-stage estimation scheme for the jump locations, where the asymptotic properties are also studied. Most of the estimators mentioned above are of the kernel type. The key idea is to investigate the difference between the estimators of the left- and right-hand side limits for the unknown regression functions. On this basis, the locations and magnitudes of the jumps can be estimated by using the maximization argument of the jump points estimation. However, the overall fittings obtained using these methods are not very satisfactory at around jump points and around end points.

At the same time, the spline method was also applied for detecting the jump points. [7] used linear splines to estimate discontinuities of the unknown regression functions. [12] applied the evolutionary algorithm to locate the optimal knots.

These methods are computationally expensive. In this chapter, a two-stage method is developed for detecting the number of jump points, their locations and magnitudes as well as finding the spline representations for the approximation of the unknown regression function with jump points. The following notations are used in this chapter. Let X be the response variable with respect to variable t. For a given set of observations $\{x_i, t_i\}$, $i = 1, 2, \cdots, n$, the regression function is written as:

$$x_i = m(t_i) + \varepsilon_i, \qquad i = 1, 2, \cdots, n \tag{4.1}$$

where m is an unknown function defined on $[0, T]$, $\{\varepsilon_i\}$, $i = 1, 2, \cdots, n$, are independent and identically distributed $N(0, \sigma^2)$ normal random variables. For each $i = 1, 2, \cdots, n$, $\{\varepsilon_i\}$ represents the variation of x_i around $m(t_i)$. Without loss of generality, we can let $T = 1$. Otherwise, a re-scaling of T can be used.

To form a segmented regression, we write $m(t)$ as:

$$m(t) = m_l(t), \quad \text{for } \tau_{l-1} < t \le \tau_l, \ l = 1, \cdots, N, \tag{4.2}$$

where $\tau_0 = 0$ and $\tau_N = T$, where τ_i, $i = 1, \cdots, N,$ are jump points. This setting covers the case of the change of mean values (step changes) as a special case by choosing $m_l(t)$ as constants. Note that the form of the regression $m_l(t)$ is usually unknown, and hence are nonparametric. It is well-known that spline functions are effective for approximating nonparametric regressions if they are smooth. However, the smoothing spline does not work well directly for regressions with jump points, since the smoothing spline is rather sensitive to the location of jump points. Some difficulties in jump point estimation have been demonstrated in [6] for linear regression with only one jump point. Intuitively, the jump points should be identified before applying the smoothing spline to each of the individual segments defined by the jump points. This is the motivation behind our proposed two-stage method.

The proposed method consists of two steps. First, we should locate all potential locations of jump points. Then, we use a time scaling transformation to transform the potential jump points and spline knots into pre-fixed points. By doing this, the parameter estimation using least squares becomes an optimization problem, which can be solved by efficiently techniques, such as the sequential quadratic approximation optimization method. Finally, the modified Akaike's information criterion is used to determine which potential jump points are real jump points. We then obtain the final model.

This chapter is organized as follows. In section 4.2, we employ the kernel method proposed by [19] to locate locations of all the potential possible jump points to within respective observation points. Then, the

problem formulation is given in section 4.3. section 4.4 introduces a time scaling transform, which is motivated by the one proposed in [16]. This time scaling transform is then used to derive a new time scaling transform, which maps the undecided jump points and spline knots into fixed points. The obtained optimization problem is solved by the sequential quadratic approximation optimization technique in the Optimization Toolbox within the Matlab environment. In section 4.5, we use the modified Akaike's information criterion to determine the number and locations of jump points and therefore obtain the last model. In section 4.6, several numerical examples are presented and solved by using the proposed method. Some concluding remarks are given in section 4.7.

4.2. Estimation for Potential Jump Points

In statistics, the kernel method is an efficient and powerful statistical tool to detect jump points. Therefore, it is used in our two-stage method to find potential jumps. We assume that the following conditions are satisfied.

1) The number of the observation points is sufficiently large to detect all the possible jump points. That is, the number of jump points is very small in comparison with the number of observation points and the number of observation points between consecutive jump points is sufficiently large for spline fitting.
2) The jump points should be located in the interval $[\delta, 1-\delta]$, where δ is some small positive constant. That is, there is no jump point in the neighborhoods of the boundary points on which they become undetectable.
3) There is at most one jump point between t_i and t_{i+1}, $i = 0,1,\cdots,n,$ where $t_0 = 0$ and $t_{n+1} = 1$.
4) The regression errors ε_i, $i = 0,1,\cdots,n,$ are independent and identically distributed (*i.i.d*) random variables with mean 0 and variance $\sigma^2 < \infty$.

Let K be the kernel function with the bandwidth h. There are two popular methods to construct kernel estimators, depending on the choice of weights by either direct kernel evaluation or the convolution of the

kernel with a histogram obtained from the data. Each estimator has several important advantages and disadvantages. A thorough review on this subject can be found in the paper by [2]. [4] make use of the first method to construct an estimator to detect the vicinity of the jump points. In our two-stage method, the second method is used to identify rough positions of the jump points.

For the kernel function K and the bandwidth h, the Gasser-Müller estimator is defined as:

$$\hat{m}(t)=\sum_{i=1}^{n} x_i \int_{s_{i-1}}^{s_i} K_h(t-\tau)d\tau, \quad \text{for } t\in(0,1), \tag{4.3}$$

where $K_h(\bullet)=h^{-1}K(\bullet/h)$, $s_n=0$, $s_i=(t_i+t_{i+1})/2$, $i=2,\cdots,n-1$, and $s_n=1$. Let $m_1(t)$ and $m_2(t)$ be two Gasser-Müller estimators obtained with the kernel functions K_1 and K_2, respectively, using the same bandwidth h. Let

$$J(t)=\hat{m}_1(t)-\hat{m}_2(t). \tag{4.4}$$

To continue, we need to analyze the value of $|J(t)|$.

If $m(t)$ has no jump point, then, under the usual regularity conditions, $m_1(t)$ and $m_2(t)$ are uniformly strongly consistent estimators of $m(t)$. Thus, the variation of $|J(t)|$ would not be obvious. If $m(t)$ has a jump point, then the value of $|J(t)|$ would have an obvious change around the jump point.

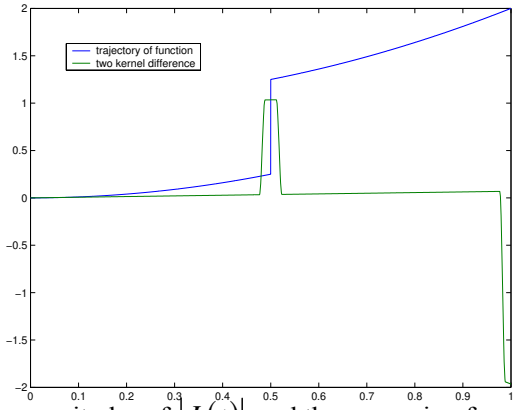

Fig. 4.1. The magnitudes of $|J(t)|$ and the regression function.

In Fig. 4.1., we give an example where $m(t)$ has a jump at $t=1/2$.

Write

$$m(t)=\varphi(t)+\psi(t), \tag{4.5}$$

where $\varphi(t)$ is the continuous part of $m(t)$, while $\psi(t)$ is a step function to characterize the jumps of $m(t)$. The magnitude of $|J(t)|$ corresponding to $\varphi(t)$ is of small order. However, the magnitude corresponding to $\psi(t)$ is symmetric and convex downward in the neighborhood of the jump point if the kernel functions K_1 and K_2 are chosen such that

$$K_1(t)=K_2(-t), \tag{4.6}$$

Furthermore, if K_1 and K_2 have compact support in $[-1,1]$, then the widths of the neighborhoods mentioned above are no more than $2h$. Based on the above discussions, we can give a numerical procedure to estimate rough locations (and hence, number) of the jump points.

Algorithm 4.1. (Kernel method to detect the potential jump points)

Step 1: Choose h such that $h=O\left(n^{-1/3}\right)$.

Step 2: Choose a nonnegative function $K(t)$ with a compact support in [-1,1] and is such that $\int_0^1 K \neq \int_{-1}^0 K$.

Step 3: Let $K_1(t)=K(t)$ and $K_2(t)=K(-t)$. Calculate $J(t)$ by using (4.3) and (4.4), where h is given in Step 1.

Step 4: Find all the points, which correspond to local maxima of $|J(t)|$.

The points obtained by Algorithm 4.1 are considered as potential jump points due to Step 4. In the next section, we will use a time scaling transformation to find the accurate positions of these jump points.

4.3. Segmented Regression with Constraints

Suppose that $\tau_1,\tau_2,\cdots,\tau_{N-1}$, is a set of potential jump points (obtained from the kernel method crudely). Then, the interval $[0,1]$ has been partitioned into N subintervals $[\tau_{l-1},\tau_l]$, $l=1,\cdots,N$. For each

$l = 1, \cdots, N$, let the observation points contained in the subinterval $[\tau_{l-1}, \tau_l]$ be denoted by $t_{1,1}, \cdots, t_{1,N_1}$, and let $x_{1,1}, \cdots x_{1,N_1}$ be the corresponding observations. The regression function is denoted by $m_l(t)$ in the subinterval $(\tau_{l-1}, \tau_l]$ where $l = 1, \cdots, N$, $\tau_0 = 0$, and $\tau_N = T$. Now, we use the segmented regression to fit the segment $m_l(t)$, $l = 1, \cdots, N$.

The most widely used approach to curve fitting is least squares. If we place no restrictions on the residual sum of squares, this method is in fact an intoporlant which may be caused a rapid fluctuation. To avoid this, we incorporate a smooth penalty in the cost function. In this chapter, we will introduce the cubic spline for fitting the segment $m_l(t)$.

A general cubic spline basis is defined as

$$\left\{1, t, t^2, t^3, (t-\theta_1)_+^3, \cdots, (t-\theta_K)_+^3\right\}. \tag{4.7}$$

where $(t-\theta_k)_+ = \max(0, t-\theta_k)$, θ_k, $k = 1, \cdots, K$, are the knot points. Since the smoothness is penalized in the cost, we need the estimator $\hat{m}_l(t)$ of $m_l(t)$ is continuously differentiable at the knot θ_k, $k = 1, \cdots, K$. Write

$$\hat{m}_l(t) = a_{l,1} + \sum_{k=1}^{3} a_{l,k+1} t^k + \sum_{k=1}^{i_l} a_{l,k+4} (t-\theta_{l,k})_+^3, \tag{4.8}$$

where $\theta_{l,1}, \cdots, \theta_{l,i_l}$, are the pre-fixed knots contained in the *l*-th segment, $a_{l,1}, \cdots, a_{l,l+4}$, are the coefficients. Since $(t-\theta_k)_+^3$ is twice continuously differentiable, there is no any need restrictions on $m_l(t)$. Define the cost functional as the following:

$$J(\boldsymbol{\tau}, \mathbf{a}) = \sum_{l=1}^{N} \sum_{i=1}^{N_l} \left(\hat{m}_l(t_{l,i}) - x_{l,i}\right)^2 + \lambda \sum_{i=1}^{N} \int_{\tau_{i-1}}^{\tau_i} \left(\hat{m}_i''(t)\right)^2 dt \tag{4.9}$$

where $\boldsymbol{\tau} = [\tau_1, \cdots, \tau_{N-1}]^T$, $\mathbf{a} = \left[a_{1,1}, \cdots, a_{1,i_1+4}, \cdots, a_{N,i_N+4}\right]^T$, λ is the smoothness parameter.

Under the least squares method with the smoothness penalty, our objective is to find $(\boldsymbol{\tau}, \mathbf{a})$ such that (4.9) is minimized subject to the following constraints

$$t_{l,N_l} \le \tau_l \le t_{l+1,1}. \tag{4.10}$$

For this optimization problem, the estimates of the jump locations and the optimal regression coefficients are obtained simultaneously. Let this problem be referred to as Problem (P).

For the penalized parameter λ, we can choose it by the generalized cross-validation method [3]. However, here we will choose it interactively for simplicity.

To solve Problem (P), we need to compute the cost. We note that the cost (4.9) is composed of two parts. Since the first part is only related to the coefficient vector $\mathbf{a}$, it is easily computed. The second part is the sum of some integrals with the integral limit related to the jump points. Thus, to compute it with its corresponding gradient is hard. To overcome this difficulty, we just introduce a time scaling transformation. By this transformation, the jump points and the spline knots are all mapped into some pre-fixed points.

4.4. A Time Scaling Transformation Method

We suppose that $\tau_1,\cdots,\tau_N$, are N variable times in the time interval $[0,T]$. A time scaling transformation is introduced such that the variable times $\tau_1,\cdots,\tau_N$, are transformed to pre-fixed times $\xi_1,\cdots,\xi_N$, in the new time scale. This transformation was known as the enhancing transform, which was introduced by [10] to overcome the numerical difficulties in the computation of some optimal control problems. It is defined by

$$\frac{dt}{ds} = v(s), \tag{4.11}$$

with initial condition

$$t(0) = 0,\ \frac{dt}{ds} = v(s), \tag{4.12}$$

where $v(s)$ satisfies the following conditions:

- $v(s) \ge 0$ for all s;
- $v(s)$ is a piecewise constant on the interval $(\xi_{i-1}, \xi_i]$;

$$\int_{\xi_{i-1}}^{\xi_i} v(s)\,ds = \tau_i - \tau_{i-1}\,, \tag{4.13}$$

where $\tau_0 = 0$, $\xi_0 = 0$.

Now we apply this transformation to our problem such that the jump points $\tau_1, \cdots, \tau_{N-1}$, are mapped into the fixed points $1, \cdots, N-1$, and the spline knots $\theta_{l,1}, \cdots, \theta_{l,i_l}$, are mapped into $l+1/(i_l+1), \cdots, l+i_l/(i_l+1)$, $l = 1, \cdots, N$. To achieve it, we just choose

$$v(s) = \sum_{k=1}^{N}\sum_{j=1}^{i_k+1} \xi_{k,j}\chi_{\left[k+(j-1)/(i_{k+1}),k+j/(i_{k+1})\right)}$$

where χ_I is the indicator function, *i.e.*,

$$\chi_I(s) = \begin{cases} 1, & if \quad s \in I, \\ 0, & otherwise. \end{cases}$$

$\xi_{k,j}$, $k = 1, \cdots, N$, $j = 1, \cdots, i_k$, satisfy the following conditions:

$$\xi_{k,j} \geq 0; k = 1, \cdots, N,\ j = 1, \cdots, i_k; \tag{4.14}$$

$$\sum_{k=1}^{N}\sum_{j=1}^{i_k+1} \xi_{k,j} = T; \tag{4.15}$$

$$\xi_{k,j} = (i_k+1)\left(\theta_{k,j} - \theta_{k,j-1}\right), k = 1, \cdots, N,\ j = 2, \cdots, i_k; \tag{4.16}$$

$$\frac{1}{i_k+1}\xi_{k,i_k+1} + \frac{1}{i_{k+1}+1}\xi_{k+1,1} = \theta_{k+1,1} - \theta_{k,i_k}, k = 1, \cdots, N. \tag{4.17}$$

By this transformation, we have

$$\sum_{i=1}^{N}\int_{\tau_{i-1}}^{\tau_i} \left(m_i''(t)\right)^2 dt = \sum_{i=1}^{N}\int_{i-1}^{i} \left(m_i''(t)\right)^2 v(s)\,ds. \tag{4.18}$$

Let

$$\overline{J}(\boldsymbol{\xi}, \mathbf{a}) = \sum_{l=1}^{N}\sum_{i=1}^{N_l}\left(\hat{m}_l(t_{l,i}) - x_{l,i}\right)^2 + \lambda\sum_{l=1}^{N}\int_{l-1}^{l}\left(m_l''(t(s))\right)^2 v(s)\,ds \tag{4.19}$$

where $\boldsymbol{\xi} = \left[\xi_{1,1}, \cdots, \xi_{1,i_1+1}, \cdots, \xi_{N,i_N+1}\right]^T$. Problem ($\hat{P}$) is stated as the following.

Problem ($\hat{P}$). $\min \overline{J}(\boldsymbol{\xi}, \mathbf{a})$ subject to (4.14), (4.15), (4.16) and (4.17).

Clearly, we have the following theorem.

Theorem 4.1. Problem (P) is equivalent to Problem ($\hat{P}$) in the sense that $(\boldsymbol{\tau}, \mathbf{a})$ is the optimal solution of Problem (P) if and only if $(\boldsymbol{\xi}, \mathbf{a})$ is an optimal solution of Problem (P). Furthermore, they have the same optimal cost.

4.5. Model Selection

Note that the kernel method in section 4.2 tries to detect all the potential jump points. The spline approximation method outlined in section 4.3 can be used in conjunction with the time transform introduced in section 4.4 to any possible combinations of potential jump points. Suppose that the number p is the candidate of jump points. Then, the number of jump points p is required to be chosen appropriately. Several methods for choosing it have been suggested in the literature. We propose to use the Akaike Information Criterion (AIC) [1] for the purpose of model selection. Tong [17] applied AIC for model selection in a threshold autoregression. Hurvich and Tsai [5] derived a modified Akaike information criterion AIC_c in small samples and claimed that the AIC_c dramatically reduces the bias and improves model selection. The AIC_c penalizes the RSS by a function of the number of free parameters and is given by

$$AIC_c = \ln \frac{RSS}{N} + \frac{N+p}{N+p-2}, \tag{4.20}$$

where N is the number of observations, p is the number of free parameters in the model and RSS is the first part of the cost (4.9). Note that AIC tends to overestimate the number of parameters, thus, we will use BIC as a criterion instead of AIC when the number of observation points is large enough, where

$$BIC = \ln \frac{RSS}{N} + \frac{p \ln N}{N}. \tag{4.21}$$

In our simulation, for those examples, where the data produced from a mathematical function, BIC will be used as the criterion as the data can be collected as much as we need. For the real data, we will use AIC_c as the criterion since the observation points are limited.

Algorithm 4.2.

1. Set $\boldsymbol{\tau} = \left[\tau_1, \cdots, \tau_{N-1}\right]^T$, which is a set of candidate jump points, Γ is a set to store the solution and set it empty, $AIC_c = 1000.$
2. Choosing candidate jump points $\left\{\tau_i\right\}_{i=1}^{m} \subset \boldsymbol{\tau}$ and for given spline knots θ, use the time scaling transformation (4.11) to solve ($\hat{P}$) and evaluate the corresponding AIC_c (or BIC), Let Γ' denotes the current solution which is the set of the jump points and the regression coefficients.
3. If $AIC_c^{'} \le AIC_c$, set $\Gamma = \Gamma'$, $AIC_c = AIC_c^{'}$, and go to Step 2. If there is no possible candidate jump points, stop.

4.6. Numerical Example

To assess the performance of our proposed method, some numerical examples are presented here.

For the simulated study, the data were generated by the following equation:

$$x_i = m\left(t_i\right) + \varepsilon_i, \tag{4.22}$$

with $t_i = i/n$ and ε_i sampled randomly from a normal distribution with standard deviation σ_ε. In the next numerical examples, we choose $\lambda = 0.1$.

Example 4.1. Let $n = 200,\ \sigma_\varepsilon = 0.2$, and the data is produced from the function:

$$m\left(t\right) = 2 - 2\left|t - 0.26\right|^{1/5} 1\left(t \le 0.26\right) - 2\left|t - 0.26\right|^{3/5} 1\left(t > 0.26\right) + 1\left(t \ge 0.78\right). \tag{4.23}$$

First, we use Algorithm 4.1 to detect the rough locations of the jump points. We rearrange the observation points with the given candidate jump points. Let the spline knots vector be [0.1, 0.15, 0.3, 0.5, 0.6]. We use BIC as criterion and the obtained results are that there are two jump points: 0.25225, 0.78178. The obtained BIC is -4.1056. The result is depicted in Fig. 4.2. We do the same simulation for 100 times. The

results are depicted in Fig. 4.3.

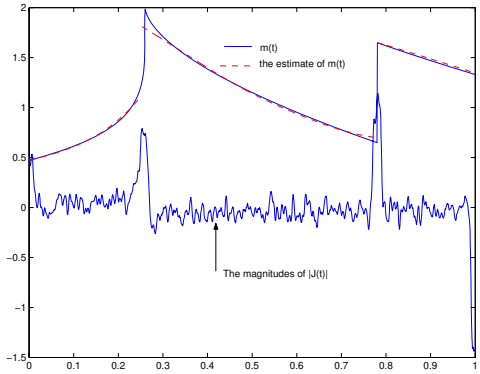

Fig. 4.2. Example 4.1. with $\lambda = 0.01$.

If we choose λ=10, then the obtained result is depicted in Fig. 4.4. From Fig. 4.4, we can see that if λ is enough, then the fitting becomes linear fitting. Thus, the parameter λ controls the gradient change rate of the splines.

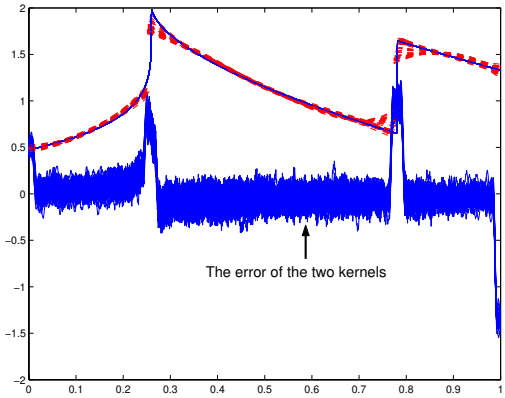

Fig. 4.3. Example 4.1. with 100 times simulation.

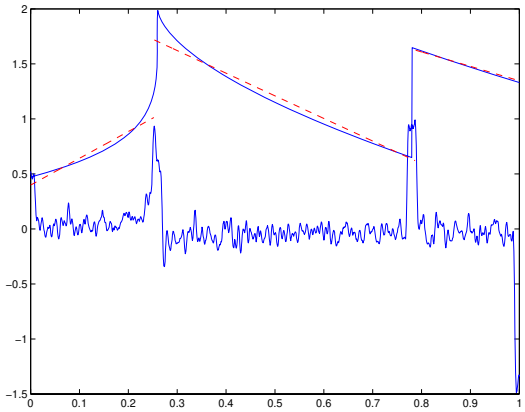

Fig. 4.4. Example 4.1. with $\lambda = 10$.

Example 4.2. We now apply our method to a real example, which contains the water levels (depths) in boreholes monitored irregularly over time. The data are taken from the database of Agriculture of Western Australia and have been analyzed by [15]. There are 49 observations. The observation points as well as its jump estimator by Algorithm 4.1 is depicted in Fig. 4.5. We can see that the kernel method cannot present an good jump estimator since the observation points is too little from the figure. Thus, we have to consider all the potential jump points and use AIC_c as criterion to choose the best model. In the process of fitting, we suppose that all of the jumps are positive since the level of the groundwater does not experience drop instantly. We re-scaling the time to the new interval [0,1]. The last obtained model has 3 jump points: 0.1050,0.2727,0.4554, $AIC_c = 4.3148$. The obtained results are depicted in Fig. 4.6.

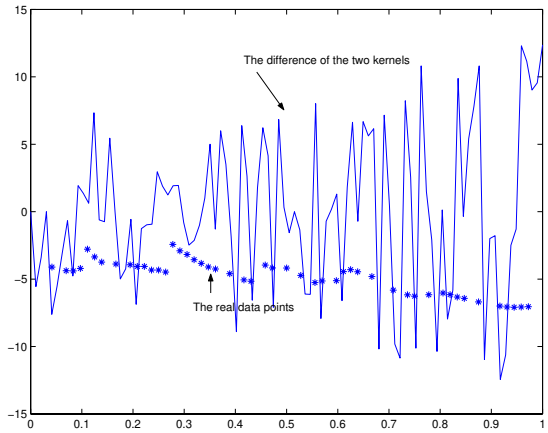

Fig. 4.5. Observation points and jump estimator of Example 4.2.

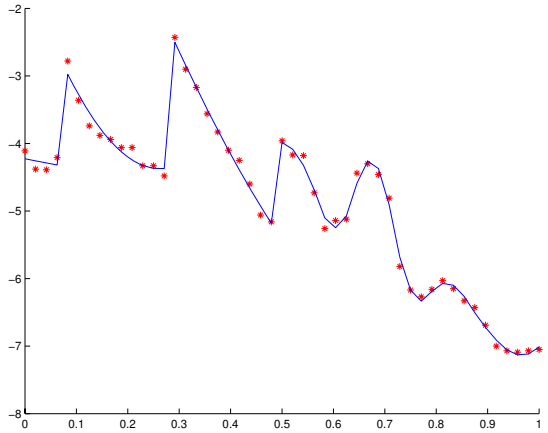

Fig. 4.6. The fitting result of Example 4.2.

4.7. Conclusion

In this chapter, a new two stage method has been proposed for solving spline regression problem with jump points. First, we detect the rough locations of jump points based on the kernel method. Then, we introduce a time scaling transformation reformulate our regression problem as a nonlinear optimization problem which is easily to be solved. Also, some numerical results are presented and which are shown that our proposed method is efficiency.

References

[1] H. Akaike, A new look at the statistical model identification, *IEEE Transaction on Automatic Control* **19**, 716-723, (1974).

[2] C. K. Chu and J. S. Marron, Choosing a kernel regression estimators, *Statistical Science* **6**, 404-419, (1991).

[3] P. Craven, and G. Wahba, Smoothing noisy data with spline functions, *Numerical Mathematics* **31**, 377-403, (1979).

[4] I. Gigbels, H. Peter and A. Kneip, On the estimation of jump points in smooth curves, *Annales Institue of Statistics and Mathematics* **51**, 231-251, (1999).

[5] M. Hurvich, and C. L. Tsai, Bias of the corrected AIC criterion for underfitted regression and time series models, *Biometrika* **78**, 499-509, (1991).

[6] S. Julious, Inference and estimation in a change-point regression problem, *Journal of Royal Statistical Society Series A* **50**, 51-61, (2001).

[7] J. Y. Koo, Spline estimation of discontinuous regression functions, *Journal of Computational and Graphical Statistics* **6**, 266-284, (1997).

[8] D. Lee, Coping with discontinuities in computer vision: their detection, classification, and measurement, *IEEE Transactions on Pattern Analysis and Machine Intelligence* **12**, 321-344, (1990).

[9] F. Lombard, Detecting change points by Fourier analysis, *Technomerics* **30**, 305-310, (1988).

[10] H. W. J. Lee, K. L. Teo, V. Rehbock and L. S. Jennings, Control parameterization enhancing transform technique for time optimal control problems. *Dynamic Systems and Applications* **6**, 243-261, (1997).

[11] A. McDonald and A. L. Owen, Smoothing with split linear fits, *Technometrics* **28**, 195-208, (1986).

[12] S. Miyata and X. Shen, Adaptive free-knot splines, *Journal of Computational and Graphical Statistics* **12**, 197-213, (2003).

[13] H. G. Müller, Change-points in nonparametric regression analysis, *Annals Statistics* **20**, 737-761, (1992).

[14] H. G. Müller and K. Song, Two-stage change-point estimators in smooth regression models, *Statistics and Probability Letters* **34**, 323-335, (1997).

[15] Q. Shao and N. Campbell, Modelling trends in groundwater levels by segmented regression with constraints. *Australian and New Zealand Journal of Statistics* **44**, 129-141, (2002).

[16] K. L. Teo, L. S. Jennings, H. W. J. Lee and V. Rehbock, The control parametrization enhancing transform for constrained optimal control problems, *Journal of Australia Mathematical Society B* **40**, 314-335, (1999).

[17] H. Tong, Threshold autoregression, limit cycles and cyclical data, with discussions, *Journal of Royal Statistical Society B* **42**, 245-292, (1980).

[18] Y. Wang, Jump and sharp cusp selection by wavelets, *Biometrika* **82**, 385-397, (1995).

[19] J. S. Wu and C. K. Chu, Kernel-type estimators of jump points and values of a regression function, *Annals Statistics* **21**, 1545-1566, (1993).

[20] Y. Yin, Detection of the number, locations and magnitudes of jumps, *Communications in Statistics-Stochastic Models* **4**, 445-455, (1988).

Section B

Control for Continuous-time Systems

Chapter 5

CHAOS CONTROL FOR CHUA'S CIRCUITS

L.A.B. Tôrres, L.A. Aguirre, R.M. Palhares and E.M.A.M. Mendes
Dept. of Electronic Engineering - DELT Universidade Federal de Minas Gerais
Email: {torres, aguirre, palhares, emmendes}@cpdee.ufmg.br

The practical implementation of Chua's circuit control methods is discussed in this chapter. In order to better address this subject, an inductorless Chua's circuit realization is first presented, followed by practical issues related to data analysis, mathematical modelling, and dynamical characterization associated to this electronic chaotic oscillator. As a consequence of the investigation of different control strategies applied to Chua's circuit, a tradeoff among control objective, control energy, and model complexity is devised, which quite naturally leads to a principle that seems to be of general nature: the Information Transmission Via Control (ITVC) for nonlinear oscillators. The main purpose of the present chapter is to serve as an introductory guide to the universe of Chua's circuit control, synchronization, and mathematical modelling.

5.1. Introduction

The so-called chaos advent was rekindled after the computer simulation carried out by Lorenz in the early sixties [56]. During the seventies some basic research took place which aimed at establishing new concepts concerning chaotic dynamics [63]. The eighties were strongly marked by the goal of developing tools to characterize chaos [32, 37]. Subjects of modeling [5, 36] control and synchronization [30, 42] of chaotic systems were mainly developed in the nineties. Of course, there is active ongoing research in these fields.

Particularly, the field of chaos control and synchronization of nonlinear oscillations has attracted much attention lately [13, 20, 21]. While much has been accomplished in the realm of theory, quite understandably much less

has been reported in terms of practical results [13]. One of the reasons for this imbalance is the obvious fact that more often than not ideas (theory) develop before actual implementation. Another possible cause is the natural difficulty to assemble a suitable setup for testing new ideas as opposed to simulating solutions on a digital computer.

From the mid-eighties considerable effort was devoted to build simple laboratory systems that could be used to produce chaotic data. An electronic circuit that has come to be known as Chua's circuit is to be found among such endeavors [57, 58]. Such a circuit has undoubtedly become a standard benchmark in the study of nonlinear dynamics and chaos [28].

In order to be able to take full advantage of the many benefits of Chua's circuit in the investigation of control and synchronization algorithms, it is important that the real circuit should include devices— called actuators— to implement the control action. In order to gain flexibility, it is usually desirable that the control law be implemented on a digital computer. This will require additional real-time I/O capabilities in order to drive the actuators [73]. The advantages of a setup that includes actuators goes beyond implementing control and synchronization algorithms. Indeed, (simulated) driven Chua's circuits are useful in a number of different ways such as, for instance, in the identification of new bifurcation scenarios [15].

The paper [73] described a laboratory setup, named Chua's Circuit Control Prototype – PCChua, with the following features: (a) composed of a Chua oscillator furnished with three actuators thus permitting mono and multi-variable control; (b) the actuators can be driven by the analog outputs of a standard I/O-board; in order to be able to actuate fast enough (c) the I/O-board is driven by a real time program written for Linux and (d) an inductorless implementation of Chua's circuit permits to slow down the original dynamics to just a few hertz. This enables implementing sophisticated control schemes without severe time restrictions in applications such as: design and verification of chaos control algorithms, practical synchronization studies, experimental chaos based information transmission systems, to mention a few.

In the present chapter, the aim is to present practical implementations of control strategies for Chua's circuit. A comprehensive account of this issue should discuss the Chua's circuit implementation itself (Sec. 5.2), together with data analysis and system identification techniques used to assess the quality of the implemented circuit and to gain insight on the peculiarities of Chua's circuit dynamics (Sec. 5.3). In addition, a sample of control strategies applied to the problem of Chua's circuit control and

synchronization are discussed in Sec. 5.4.

5.2. Chua's Circuit Implementation

This section is primarily focused on presenting a robust and reliable implementation of Chua's circuit. As it will be seen next, the circuit can be easily built, which is one of the reasons for its popularity among scientists all over the world.

5.2.1. *An Overview of Chua's Circuit*

The circuit in its standard form, built as an autonomous oscillator, is composed by a network of linear passive elements connected to a nonlinear active component called Chua's diode, as seen in Fig. 5.1.

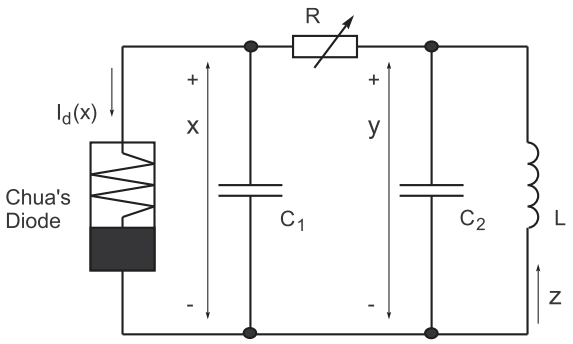

Fig. 5.1. Chua's circuit. R is a variable resistor used to change the coupling between the active and passive parts of the circuit. As a consequence variation of R leads to bifurcation phenomena.

The set of differential equations that describes the circuit behavior is obtained from Kirchhoff circuit laws, such as:

$$\begin{aligned} dx/dt &= (y - x)/(RC_1) - i_{\mathrm{d}}(x)/(RC_1); \\ dy/dt &= (x - y)/(RC_2) + z/C_2; \\ dz/dt &= -y/L - z(r_{\mathrm{L}}/L); \end{aligned} \tag{5.1}$$

where C_1, C_2, L and R are the values of the passive linear elements shown in Fig. 5.1, and r_{L}, not shown in the figure, denotes the series internal

resistance of the inductor.

The static nonlinearity of Chua's diode is the piecewise linear function given by

$$i_{\mathrm{d}}(x) = m_0 x + 0.5(m_1 - m_0)\left\{|x + B_{\mathrm{p}}| - |x - B_{\mathrm{p}}|\right\}, \tag{5.2}$$

where $m_0, m_1, B_{\mathrm{p}} \in \mathbb{R}$ are parameters. Figure 5.2 shows a measured static nonlinearity of an implemented Chua's diode.

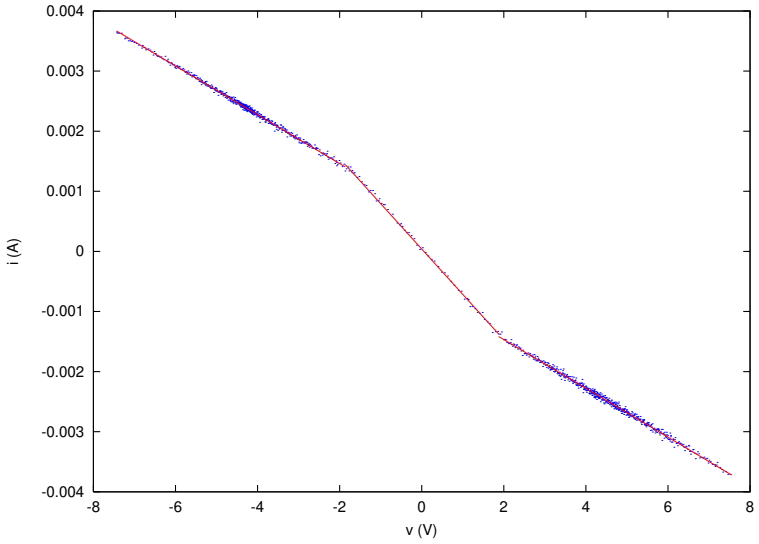

Fig. 5.2. Experimentally obtained static nonlinearity of a Chua's diode. The dots correspond to real data, and the continuous traces are the resulting linear regression applied to the measured data in order to reveal the piecewise affine structure of Chua's diode curve.

As a final remark on Chua's circuit equations, by adopting the following conventions

$$\begin{cases} t' = \frac{t}{RC_2}; \\ \tilde{z} = Rz; \\ f(x) = Ri_{\mathrm{d}}(x); \end{cases} \quad \begin{cases} p = \frac{C_2}{C_1}; \\ q = -\frac{R^2 C_2}{L}; \\ r = r_{\mathrm{L}} q; \end{cases} \tag{5.3}$$

it is possible to rewrite Eq. (5.1) in *normalized* form as:

$$\begin{aligned} \dot{x} &= p\left[y - x - f(x)\right], \\ \dot{y} &= x - y + \tilde{z}, \\ \dot{\tilde{z}} &= qy + r\tilde{z}, \end{aligned} \tag{5.4}$$

where $\dot{x} = dx/dt'$, $\dot{y} = dy/dt'$ and $\dot{\tilde{z}} = d\tilde{z}/dt'$.

There are different ways to implement the nonlinear characteristic Eq. (5.2) [46]. A robust and reliable way is by using operational amplifiers [41], as shown in Fig. 5.3.

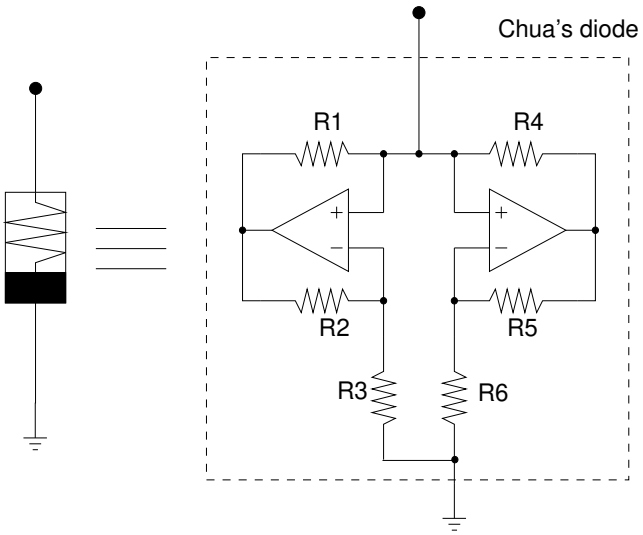

Fig. 5.3. Implementation of Chua's diode using Op.Amps. (operational amplifiers).

From the basic circuit topology shown in Fig. 5.1, many variations have been proposed in the literature, which lead to generalizations that exhibit a richer set of dynamical behaviors [19, 47].

5.2.2. *An Inductorless Version of the Circuit*

Chua's circuit exhibits a broadband spectrum, but the majority of the power density is concentrated roughly around the frequency determined by the resonant sub-circuit composed by L and C_2 in Fig. 5.1.

Very slow chaotic oscillations are desirable in many situations where computers are employed to measure data from the circuit, run sophisticated algorithms based on these data and to take some control action or to run some file or graphical output operation.

In order to slow down the chaotic oscillations, it is necessary to use larger energy storage elements, i.e. greater values for C_1, C_2 and L in Eq. (5.1).

However, despite the fact that *off-the-shelf* capacitors cover a very wide range of capacitance values, the same is not true for commercial inductors. Furthermore, the trade-off between coil size and maximum allowed inductance leads to very large and low-accuracy inductors. One possible solution to this problem is the replacement of the inductor by a circuit that simulates the behavior of an *ideal grounded inductor* over several decades of frequency [71]. This circuit is, indeed, a gyrator circuit built as an impedance transformer [14, 65] as seen in Fig. 5.4. Several other configurations of inductorless Chua circuits have been recently suggested [26, 35, 62].

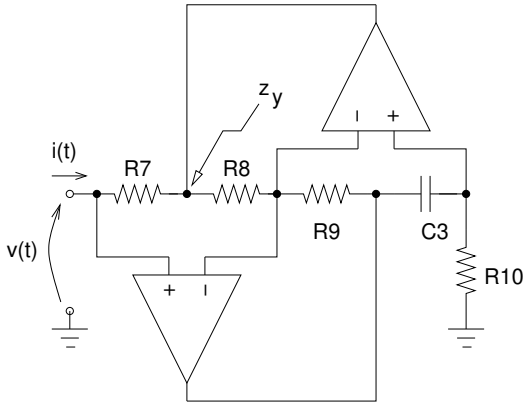

Fig. 5.4. Op-Amp realization of the inductor simulation circuit. The voltage at z_y point can be readily used to determine the "current through the realized inductor". In this type of circuit it is mandatory that one of the terminals of the realized inductor be grounded (this corresponds to grounding the terminal of R_{10}).

From Fig. 5.4, one can see that the third state; variable z in Eq. (5.1); which is the current through the inductor L shown in Fig. 5.1, can be readily determined by measuring the voltage z_y shown in Fig. 5.4 and using the expression $z = (z_y - y)/R_7$; where y is the state variable corresponding to the voltage across the capacitor C_2. Therefore the complete state vector is composed of voltages, which is in general easier to measure.

The theoretical transfer function of the simulated inductance is [65]:

$$Z(s) = \frac{\mathcal{L}\{v(t)\}}{\mathcal{L}\{i(t)\}} = \frac{V(s)}{I(s)} = \frac{R_7 R_9 R_{10} C_3}{R_8} s, \tag{5.5}$$

where $\mathcal{L}$ stands for the Laplace transform; and R_7 through R_{10} and C_3 are shown in Fig. 5.4. Obviously Eq. (5.5) suggests that the inductor is ideal since it is a pure differentiator as indicated by the zero at the origin

of the complex s-plane. In order to investigate the limits of this configuration, a realistic SPICE model was implemented and the resulting frequency response was found to be valid for almost four decades, which easily encompasses the spectral content of the measured time-series from the circuit, in chaotic and non-chaotic regimes [73].

Following the same procedure, it was also found that the assumption of nearly zero equivalent internal resistance r_{L}, associated to the realized inductor, is also valid in the same frequency range. This is a very important detail in the Chua's circuit implementation because high internal resistance r_{L} prevents the appearance of chaotic dynamics [11].

The complete circuit is shown in Fig. 5.5. A set of electronic components values that can be used in this implementation are listed in Table 5.1. For these components, in Eq. (5.1) the corresponding theoretical circuit parameters are: $0\Omega \leq R \leq 2\mathrm{k}\Omega$; $C_1 = 23,5\mu\mathrm{F}$; $C_2 = 235\mu\mathrm{F}$; $L = 42.3\mathrm{H}$; $r_{\mathrm{L}} = 0.0\Omega$; $m_0 = $ -0.409mS; $m_1 = $ -0.756mS; $B_{\mathrm{p}} = 1.86\mathrm{V}$.

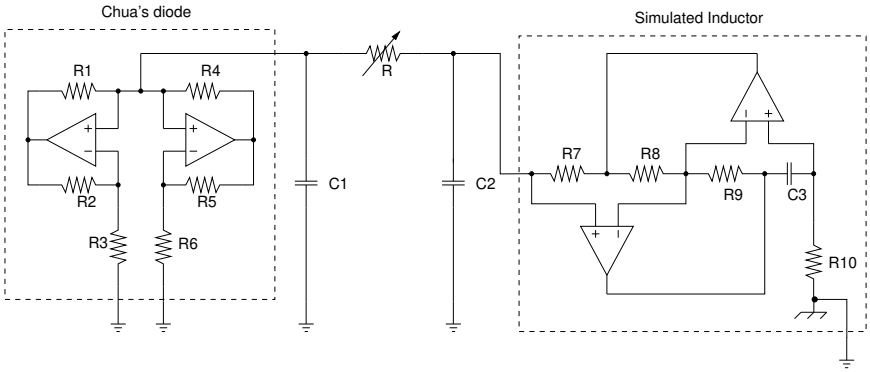

Fig. 5.5. Implemented inductorless Chua's circuit without actuators. In this case the reference point of the realized inductor is attached to the same ground reference of the rest of the circuit (see Sec. 5.2.3). The component values are shown in Table 5.1.

The main resonant frequency corresponding to the parameters in Table 5.1 is approximately 1.60 Hz. This is important in real-time applications because it enables the user to implement rather involved algorithms without being pressed too hard by computation time.

5.2.3. *PCChua – A Versatile Experimental Platform*

This section describes an experimental setup, called PCChua [73], designed to be a testbed in the study of control and synchronization schemes.

Table 5.1. Possible set of electronic components that can be used in inductorless Chua's circuit implementation.

Components	Value
R_1, R_2	220Ω
R_4, R_5	22kΩ
R_3	2.2kΩ
R_6	3.3kΩ
R_7, R_8, R_{10}	1.2kΩ
R_9	1.5kΩ
R	2kΩ (multi-turn)
C_1	23.5μF (47μF ∥ 47μF)
C_2	235μF (470μF ∥ 470μF)
C_3	23.5μF (47μF ∥ 47μF)
ICs	TL08x (4 Op.amps.)[1]

[1]Supply voltage: ±15V.

A fundamental issue in any experimental platform for control or synchronization purposes is the design and construction of devices that will actually implement the decisions made by the controller(s). Such devices are usually referred to as actuators. In the case of the PCChua platform, the following describes the built-in actuators.

The PCChua setup implements the following vector differential equation

$$\dot{\vec{x}} = \mathbf{F}(\vec{x}) + \vec{u}(t, \vec{x}), \tag{5.6}$$

where $\vec{x} = [x\ y\ z]^\top \in \mathbb{R}^3$ is the state vector, $\mathbf{F}(\cdot) : \mathbb{R}^3 \to \mathbb{R}^3$ is the Chua's circuit nonlinear vector field, and $\vec{u}(t, \vec{x}) = [u_{\mathrm{x}}\ u_{\mathrm{y}}\ u_{\mathrm{z}}]^\top \in \mathbb{R}^3$ is the vector of control inputs.

Equation Eq. (5.6) can be written in detail from Eq. (5.3) and Eq. (5.4) as

$$\begin{aligned} \dot{x} &= p\,[y - x - f(x)] + u_{\mathrm{x}}(t, \vec{x}), \\ \dot{y} &= x - y + \tilde{z} \qquad\quad + u_{\mathrm{y}}(t, \vec{x}), \\ \dot{\tilde{z}} &= -qy + r\tilde{z} \qquad\quad + u_{\mathrm{z}}(t, \vec{x}), \end{aligned} \tag{5.7}$$

where the parameters p, q and r depend on the components used, see Eq. (5.3).

From a practical point of view, the addition of the control vector $\vec{u}(t, \vec{x})$ in Eq. (5.7) can be accomplished by including in the circuit controlled voltage and current sources (actuators), as indicated in Fig. 5.6. The control

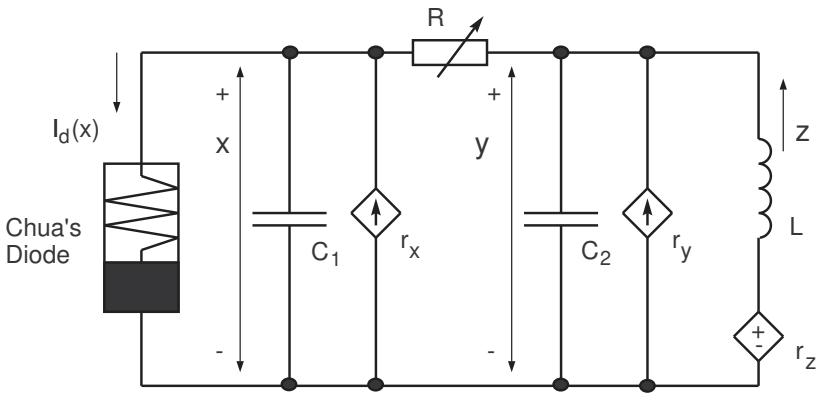

Fig. 5.6. Chua's circuit with actuators indicated.

inputs and the actuators are related by

$$\begin{aligned} r_{\mathrm{x}}(t) &= \frac{C_1}{RC_2} u_{\mathrm{x}}(t, \vec{x}), \\ r_{\mathrm{y}}(t) &= \frac{1}{R} u_{\mathrm{y}}(t, \vec{x}), \\ r_{\mathrm{z}}(t) &= \frac{L}{R^2 C_2} u_{\mathrm{z}}(t, \vec{x}). \end{aligned} \tag{5.8}$$

From Fig. 5.6 it is clear that the relative position of the voltage controlled voltage source r_z in the circuit implies that a *floating* realized inductor (gyrator circuit) is necessary. One solution to this problem is to use an independent power source to supply energy to the simulated inductor. With this modification, the realized inductor becomes a self-contained circuit with only two external terminals. However, it is important to notice that there are alternative simulated floating inductor circuit topologies that can be employed, as pointed out in [45]. An alternative is the use of a floating voltage controlled voltage source instead of a floating realized inductor.

In the PCChua, the actuators were implemented as indicated in Fig. 5.7, using the electronic components listed in Table 5.2. The current and voltage sources have fixed gains: 1V/V for the controlled voltage sources and -1mA/V for the controlled current sources.

In Fig. 5.7, the adjustable offset voltages, obtained by varying R_{14} and R_{32}, are necessary to minimize the effect of small nonzero voltage levels

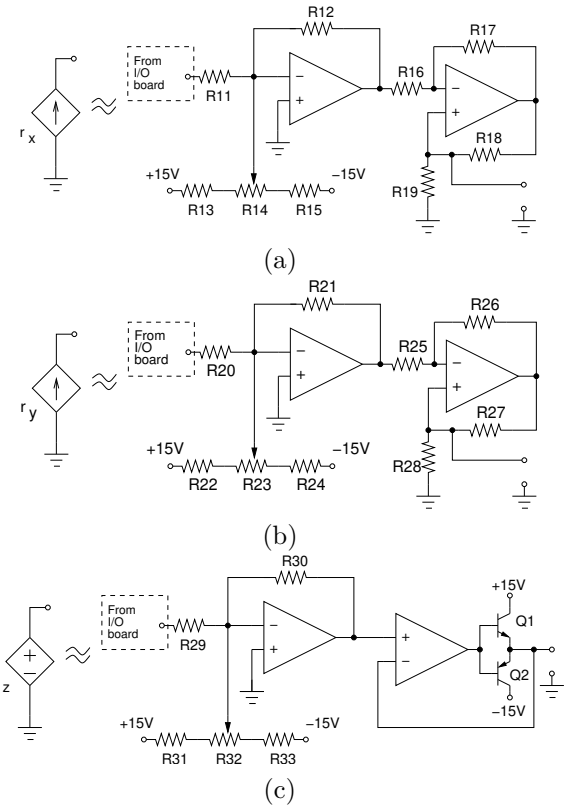

Fig. 5.7. Actuators circuits with fixed gain and offset adjustment. (a) Voltage-controlled current source r_{x} (R_{11} to R_{19}); (b) voltage-controlled current source r_{y} (R_{20} to R_{28}); and (c) voltage-controlled voltage source r_{z} (R_{29} to R_{33}).

from the external reference voltages.

The external voltage sources are actually provided by a multi-purpose data and analog output board [73], which is driven by dedicated real-time software written for a modified version of the Linux operating system, called RT-Linux, schematically represented in Fig. 5.8.

The multi-purpose board is used to measure the three voltages x, y and z_y (Fig. 5.1 and Fig. 5.4), and to issue three control signals r_{x}, r_{y} and r_{z} to the actuators in the PCChua (Fig. 5.6). The control and synchronization algorithms are executed at $f_{\mathrm{s}} = 1\mathrm{kHz}$, but the fastest rate at which data can be acquired is $f_{\mathrm{a}} = 100\mathrm{Hz}$, due to hardware limitations. Nevertheless, it is important to note that $f_{\mathrm{s}} \gg 1.6\mathrm{Hz}$, which indicates that continuous-

Table 5.2. Electronic components used in the implementation of PCChua actuators.

Components	Value
R_{11}, R_{12}, R_{13}, R_{15}	4.7kΩ
R_{16}, R_{17}, R_{18}, R_{19}	1kΩ
R_{20}, R_{21}, R_{22}, R_{24}q	4.7kΩ
R_{25}, R_{26}, R_{27}, R_{28}	1kΩ
R_{29}, R_{30}, R_{31}, R_{33}	4.7kΩ
R_{14}, R_{23}, R_{32}	5kΩ (multi-turn)
Q_1	BC547
Q_2	BC557
ICs	TL08x (6 Op.amps.)[1]

[1]Supply voltage: ±15V.

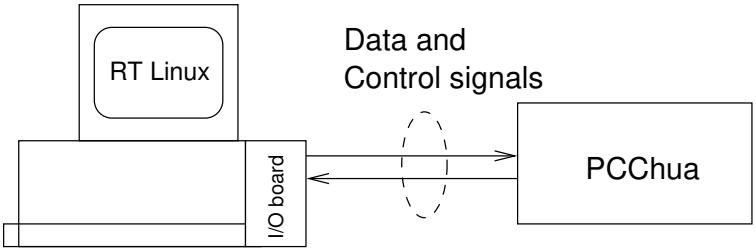

Fig. 5.8. PCChua experimental setup overview.

time versions of control and synchronization strategies can be implemented with small effort.

All the measured voltages in the PCChua are acquired using 12 bits of resolution. Two of the DACs used to issue r_x and r_y have 10 bits of resolution and the third one (used for r_z) is limited to 8 bits.

In Fig. 5.9, an example of the famous double-scroll attractor from Chua's circuit, obtained by using the PCChua experimental setup, is presented.

5.3. Chua's Circuit Data Analysis and Modeling

This section will describe a few results concerning the analysis and modeling from data of the double-scroll attractor from Chua's circuit. Further details can be found in the cited references.

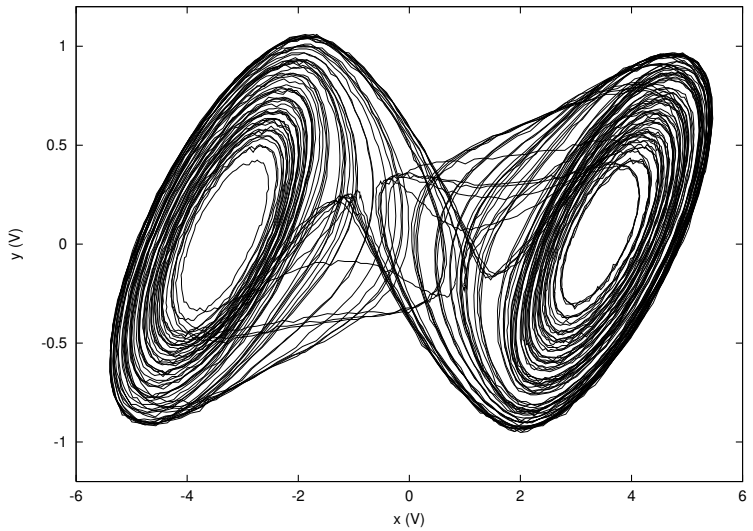

(a)

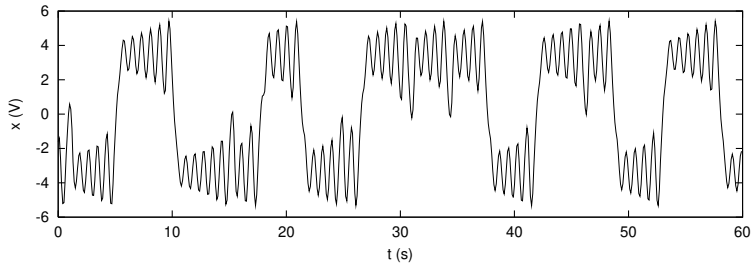

(b)

Fig. 5.9. Data collected from PCChua during 60s. (a) Measured double scroll attractor from Chua's circuit. (b) Time-series corresponding to the voltage across capacitor C_1 (x-variable) in Fig. 5.1.

5.3.1. *The Issue of Observability*

The key concept of observability is that of deciding if all the dynamical information of the full phase space $\mathbb{R}^m$ of an m-dimensional system can be retrieved by measuring one variable $s(t) = h(\mathbf{x})$, $h : \mathbb{R}^m \mapsto \mathbb{R}$, referred to as the observable and h, as the measuring function. Briefly, a system is observable if the full state can be found based on $s(t)$ only.

Let $\dot{\mathbf{x}} = \mathbf{f}(\mathbf{x})$, with $\mathbf{f} : \mathbb{R}^m \mapsto \mathbb{R}^m$, and $s(t) = h(\mathbf{x})$, with $h : \mathbb{R}^m \mapsto \mathbb{R}$ be a nonlinear system and a scalar observable, respectively. From s

a reconstructed space can be formed, for instance by taking a sufficient number of successive derivatives $\mathbf{X} = (s(t), s^{(1)}, ..., s^{(d-1)})$, where $s^{(j)}$ is the jth time derivative of s [25]. Therefore, there is Φ_s that maps the original phase space to the space reconstructed from the observable s, that is, $\Phi_s : \mathbb{R}^m(\mathbf{x}) \mapsto \mathbb{R}^d(\mathbf{X})$. Basically, $\mathbb{R}^m(\mathbf{x})$ will be observable from $s(t)$ if it is possible to go back from $\mathbb{R}^d(\mathbf{X})$ to $\mathbb{R}^m(\mathbf{x})$ on a one-to-one basis, that is, if Φ_s defines a diffeomorphism. Observability of $\mathbb{R}^m(\mathbf{x})$ from s is therefore directly related to the existence of singularities in Φ_s.

In this respect it would be interesting to answer the following question: which variable is best to observe the dynamics of Chua's circuit?

The analysis of the observability of the double scroll attractor is typically very challenging. One of the difficulties with this system is that the great difference in the velocities of convergence and divergence along the stable and unstable manifold. As a consequence, some definitions of observability indices, here denoted by the letter δ, are very small ($\approx 10^{-15}$). Another potential problem is that the application of some techniques to discontinuous systems is questionable.

Such difficulties seem to have been overcome in [4] where normalized observability indices, indicated by δ^*, were defined. The following results are obtained: $\delta_x^* = \delta_y^* = \delta_z^* = 1$, which is consistent with the fact that *locally* the system is linear almost everywhere, and we would expect to have "global" diffeomorphisms almost everywhere too. As the tolerance (a parameter used in the new definition) is increased δ_y^* quickly diminishes, whereas $\delta_x^* = \delta_z^* = 1$ remain. Increasing the tolerance even further, δ_z^* drops, thus giving the observability order $x \triangleright z \triangleright y$ (see Table 5.3).

Table 5.3. Normalized observability indices δ_s^* for the double scroll attractor for increasing values of a tolerance. These results give the observability order $x \triangleright z \triangleright y$.

p	δ_x^*	δ_y^*	δ_z^*
0.01	1	1	1
0.02	1	0.68	1
0.10	1	0	1
0.25	0.68	0	0

The results shown in Table 5.3 clearly point out that the case of the double scroll attractor is numerically badly conditioned and suggest that the best observable is x, followed by z and, finally by y. This order was confirmed by another observability test, based on data. This result, and in

particular the poorer observability properties of the observable y has been felt in the context of data sampling [2] and modeling [9] which is probably due to the fact that observing the system from y all symmetry information is lost. Analogous results for other systems can be found in [50, 51].

5.3.2. *Higher-order Spectral Analysis*

The results discussed in this section were published formerly in [33]. The main objective of higher-order spectral analysis is to assess the presence and effect of nonlinearities in the frequency domain.

5.3.2.1. *The Main Concepts*

The auto bispectrum is defined formally as the Fourier transform of the third-order correlation function of the time series. The discrete bispectrum, appropriate for sampled data, is

$$B(f_1, f_2) = E[A_{f_1} A_{f_2} A^*_{f_1+f_2}], \tag{5.9}$$

where A_{f_i} is the complex Fourier component of the time series at frequency f_i, asterisk is complex conjugation, and $E[\cdot]$ is the expected-value, or average, operator.

If the three Fourier components in the triple product on the right hand side of Eq. (5.9) are independent of each other (e.g., if they have random phase relationships such as a time series with Gaussian statistics), the bispectrum is zero. It is convenient to recast the bispectrum into its normalized (by the power at each of the three frequencies in the triad) magnitude, called the squared bicoherence, $b^2(f_1, f_2)$, which represents the fraction of the power of the triad of Fourier components $(f_1, f_2, f_1 + f_2)$ that is owing to quadratic coupling.

Similar to the bispectrum, the auto trispectrum is defined formally as the Fourier transform of the fourth-order correlation, and the discrete trispectrum is

$$T(f_1, f_2, f_3) = E[A_{f_1} A_{f_2} A_{f_3} A^*_{f_1+f_2+f_3}]. \tag{5.10}$$

The normalized magnitude of the trispectrum is called the squared tricoherence, $t^2(f_1, f_2, f_3)$, and is a measure of the fraction of the power of the quartet of Fourier components $(f_1, f_2, f_3, f_1+f_2+f_3)$ that is owing to cubic nonlinear interactions.

Higher-order spectral analysis can also be used as a means of model validation by comparing bicoherence and tricoherence functions of (measured) data and simulated data obtained by estimated models.

5.3.2.2. *The Results*

Time series of voltage v_{C_1} measured from a realization of Chua's circuit for the spiral and double-scroll attractors were used to estimate nonlinear polynomial models which can be found in [33]. The circuit parameters used during the experiments were $C_1 = 11\mu$F, $C_2 = 45\mu$F, $L = 20$H, $B_p = 1.1 \pm 0.2$ V, $m_0 = -0.37 \pm 0.04$ mS, and $m_1 = -0.68 \pm 0.04$ mS. For the spiral attractor (sampled at 12 μs) $R = 1.67\,\mathrm{k}\Omega$ and for the double scroll (sampled at 15 μs) $R = 1.64\,\mathrm{k}\Omega$. The high inductance (Sec. 5.2.2) reduces the oscillation frequency from $O(100$ kHz) to $O(1$ kHz), thus facilitating A/D conversion and recording of the data. Polynomial model parameters were estimated from 8192 values of the voltage across C_1 measured after initial transients had decayed.

Both the measured and modeled spiral attractors have a relatively narrow power spectrum dominated by a primary peak $f_p = 2.92$ Hz and its harmonics ($2f_p = 5.85$ and $3f_p = 8.78$ Hz, Fig. 5.10a). The model bicoherence (Fig. 5.10c) indicates quadratic coupling between the primary and its harmonics (e.g., the horizontal band of contours for $f_2 \approx 3$ Hz, Fig. 5.10c), similar to that observed in the measurements (Fig. 5.10b). Quadratic interactions involving Fourier components with frequencies less than f_p are significant in time series from both the data ($1 < f_2 < 3$, $f_1 \approx 3$ Hz, Fig. 5.10b) and the model (Fig. 5.10c). Tricoherence spectra for the measured time series (not shown) are similar to those from the polynomial model. Cubic interactions between quartets of Fourier components are significant for the spiral attractor, suggesting higher-order coupling between motions with frequencies f_p and its harmonics. The coupling between the primary and its harmonics, as indicated by the bicoherence (Fig. 5.10b,c) and tricoherence (not shown) spectra, suggest both quadratic and cubic interactions (as occur in the spiral attractor) are reproduced well by the polynomial model estimated from 8192 values of the voltage measured in Chua's circuit.

The higher-order spectral coherences from the model time series are slightly higher than those from the data, possibly because the model approximates the infinite-order piecewise linear current in the nonlinear resistor with a second- and third-order polynomial, leading to stronger quadratic

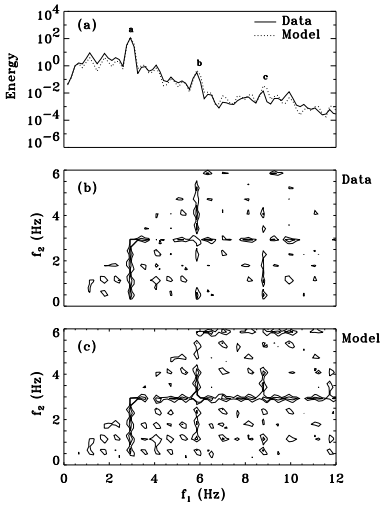

Fig. 5.10. (a) Power spectra of measured (solid curve) and modeled (dashed curve) voltage v_{c_1} from Chua's circuit when the system exhibits a spiral attractor. Contours of bicoherence of (b) measured and (c) modeled voltage v_{c_1}. The units of power are arbitrary and the frequencies of the labeled power spectral peaks (panel a) are a) 2.92, b) 5.85, and c) 8.78 Hz. The minimum contour plotted is $b = 0.85$, with additional contours every 0.1. There are 32 degrees of freedom (from [33]).

and cubic coupling than observed in the actual circuit. Noise in the measured circuit may also reduce higher-order spectral values relative to those from the model time series.

5.3.3. *Discrete-time Global Modeling*

The construction of discrete-time models from data has been thoroughly discussed in the literature. Specifically concerning the double-scroll attractor, [9] and [29] presented the case of NARMAX (nonlinear autoregressive moving average model with exogenous inputs) polynomial and rational models, respectively.

5.3.3.1. *Monovariable Polynomial Model*

The polynomial structure is very attractive because of the simplicity and insight it offers of the systems properties and therefore have been extensively used for reproducing nonlinear dynamics.

In order to identify dynamically valid models from data generated of Chua's circuit, the NARMAX model [49] was chosen. The representation

of such a model can be as follows

$$\begin{aligned} y(k) = F^{\ell}\ [\ & y(k-1),\ldots,y(k-n_y),\\ & u(k-d)\ldots u(k-d-n_u+1),\\ & e(k)\ldots e(k-n_e)]\ \ , \end{aligned} \tag{5.11}$$

where n_y, n_u and n_e are the maximum lags considered for the output, input and noise terms, respectively and d is the delay measured in sampling intervals, $T_{\rm s}$. Moreover, $u(k)$ and $y(k)$ are respectively the input and output signals. $e(k)$ accounts for uncertainties, possible noise, unmodeled dynamics, etc. and $F^{\ell}[\cdot]$ is some nonlinear function of $y(k)$, $u(k)$ and $e(k)$. The function $F^{\ell}[\cdot]$ can, of course, be a polynomial-type function with nonlinearity degree $\ell \in \mathbb{Z}^{+}$. In such a case, to estimate the parameters of this map, Eq. (5.11) should be expressed in prediction error form as

$$y(k) = \boldsymbol{\psi}^{\top}(k-1)\hat{\boldsymbol{\theta}}\ +\ \xi(k)\ \ , \tag{5.12}$$

where $\boldsymbol{\psi}(k-1)$ is the regressor vector which contains linear and nonlinear combinations of output, input and noise terms up to and including time $k-1$. The parameters corresponding to each regressor are the elements of the vector $\hat{\boldsymbol{\theta}}$. Finally, $\xi(k)$ are the residuals which are defined as the difference between the measured data $y(k)$ and the one-step-ahead prediction $\boldsymbol{\psi}^{\top}(k-1)\hat{\boldsymbol{\theta}}$. The parameter vector $\boldsymbol{\theta}$ can be estimated by orthogonal least-squares techniques [76].

One of the many advantages of such algorithms is that the Error Reduction Ratio (ERR) can be easily obtained as a by-product [17, 48].

In the particular case of Chua's circuit, one thousand data points of the output $y(k)$, the voltage over capacitor C_1, were used in the identification. The following polynomial model was obtained:

$$\begin{aligned} y(k) = {} & 3.5230y(k-1) - 4.287y(k-2) - 0.2588y(k-4) - 1.7784y(k-1)^3\\ & + 2.0652y(k-3) + 6.1761y(k-1)^2y(k-2) + 0.1623y(k-1)y(k-2)y(k-4)\\ & - 2.7381y(k-1)^2y(k-3) - 5.5369y(k-1)y(k-2)^2 + 0.1031y(k-2)^3\\ & + 0.4623y(k-4)^3 - 0.5247y(k-2)^2y(k-4) - 1.8965y(k-1)y(k-3)^2\\ & + 5.4255y(k-1)y(k-2)y(k-3) + 0.7258y(k-2)y(k-4)^2\\ & - 1.7684y(k-4)^2y(k-3) + 1.1800y(k-4)y(k-3)^2 + \boldsymbol{\psi}_{\xi}^{\top}(k-1)\hat{\boldsymbol{\theta}}_{\xi} + \xi(k)\ \ , \end{aligned} \tag{5.13}$$

where $\boldsymbol{\psi}_{\xi}^{\top}(k-1)\hat{\boldsymbol{\theta}}_{\xi}$ is the noise model composed of 20 linear terms of the form $\xi(k-j)$ used to avoid bias. This part of the model was *not* used in the simulations shown below. The identification of model Eq. (5.13) and the cluster analysis of the double-scroll and spiral attractors have been discussed in detail in [9].

Figure 5.11 show the chaotic double-scroll attractor reconstructed directly from the original data whereas Fig. 5.12 shows the chaotic double-scroll attractor reconstructed using polynomial model Eq. (5.13). For comparison purposes the analysis of the results will be postponed to next section.

5.3.3.2. *Monovariable Rational Model*

Another possibility for the function $F^{\ell}[\cdot]$ in Eq. (5.11) is a rational model defined as a ratio of two polynomials [16]

$$y(k) = \frac{a(y(k-1),\ldots,y(k-n_y),u(k-1),\ldots,u(k-n_u),e(k-1),\ldots,e(k-n_e))}{b(y(k-1),\ldots,y(k-n_y),u(k-1),\ldots,u(k-n_u),e(k-1),\ldots,e(k-n_e))} + e(k), \tag{5.14}$$

where $u(k)$ and *y(k)* are as before, n_y, n_u and n_e are the maximum lags of the output, input and noise, respectively. Moreover, such lags need not be the same in the numerator and denominator. $a(k-1)$ and $b(k-1)$ are polynomial functions nonlinear in the regressors taken up to time $k-1$. It is convenient to define the numerator and denominator polynomials in Eq. (5.14) respectively as [16]

$$a(k-1) = \sum_{j=1}^{N_{\mathrm{n}}} p_{\mathrm{n}j}\boldsymbol{\theta}_{\mathrm{n}j} = \boldsymbol{\psi}_{\mathrm{n}}^{\top}(k-1)\boldsymbol{\theta}_{\mathrm{n}} \ , \tag{5.15}$$

$$b(k-1) = \sum_{j=1}^{N_{\mathrm{d}}} p_{\mathrm{d}j}\boldsymbol{\theta}_{\mathrm{d}j} = \boldsymbol{\psi}_{\mathrm{d}}^{\top}(k-1)\boldsymbol{\theta}_{\mathrm{d}} \ , \tag{5.16}$$

where $\boldsymbol{\theta}_{\mathrm{n}j}$, $\boldsymbol{\theta}_{\mathrm{d}j}$ are the parameters of the regressors (of the numerator, $p_{\mathrm{n}j}$, and denominator, $p_{\mathrm{d}j}$,) up to time $k-1$. $N_{\mathrm{n}} + N_{\mathrm{d}}$ is the total number of parameters to be estimated.

The use of Eq. (5.14) to perform parameter estimation is not straightforward because such a function is nonlinear in the unknown parameters. An alternative solution to this problem is to multiply both sides of Eq. (5.14) by $b(k-1)$ and rearranging terms in order to yield [75]

$$
\begin{aligned}
y^*(k) &= a(k-1) - y(k)\sum_{j=2}^{N_\mathrm{d}} p_{\mathrm{d}j}\theta_{\mathrm{d}j} + b(k-1)e(k) \\
&= \sum_{j=1}^{N_\mathrm{n}} p_{\mathrm{n}j}\theta_{\mathrm{n}j} - y(k)\sum_{j=2}^{N_\mathrm{d}} p_{\mathrm{d}j}\theta_{\mathrm{d}j} + \zeta(k) \\
&= \boldsymbol{\psi}_\mathrm{n}^\top(k-1)\boldsymbol{\theta}_\mathrm{n} - \boldsymbol{\psi}_{\mathrm{d}1}^\top(k-1)\boldsymbol{\theta}_\mathrm{d} + \zeta(k) \ , \qquad (5.17)
\end{aligned}
$$

where $\boldsymbol{\psi}_\mathrm{d}^\top(k-1) = [p_{\mathrm{d}1}\ \boldsymbol{\psi}_{\mathrm{d}1}^\top(k-1)]$, $\theta_{d1} = 1$ and

$$
y^*(k) = y(k)p_{\mathrm{d}1} = \frac{a(k-1)}{b(k-1)}p_{\mathrm{d}1} + p_{\mathrm{d}1}e(k) \ , \qquad (5.18)
$$

$$
\zeta(k) = b(k-1)e(k) = \left(\sum_{j=1}^{N_\mathrm{d}} p_{\mathrm{d}j}\theta_{\mathrm{d}j}\right) e(k) \ , \qquad (5.19)
$$

where $e(k)$ is white noise. Because $e(k)$ is independent of $b(k-1)$ and has zero mean, it can be written

$$
\mathrm{E}[\zeta(k)] = \mathrm{E}[b(k-1)]\mathrm{E}[e(k)] = 0 \ . \qquad (5.20)
$$

Equation (5.18) reveals that all the terms of the form $y(k)\boldsymbol{\psi}_\mathrm{d}^\top(k-1)$, because of $y(k)$, implicitly include the noise $e(k)$ which *is* correlated with $\zeta(k)$. This, of course, results in parameter bias even if the noise $e(k)$ is white. The aforementioned correlation occurs as a consequence of multiplying Eq. (5.14) by $b(k-1)$ and should be interpreted as the price paid for turning a function which is nonlinear in the parameters to one which is linear in the parameters. Algorithms with intelligent structure selection can be found in [18] and [29], to mention a few.

Using the same data as described above and also term clustering information [8, 9], the following rational model was obtained [29]

$$
\begin{aligned}
y(k) = \frac{1}{D} \times \big(& 2.5568y(k-1) - 1.7594y(k-2) + 0.2696y(k-5) + 0.6192y(k-1)^3 \\
& - 1.0219y(k-2)^3 - 3.2455y(k-1)^2y(k-5) + 0.0735y(k-3)^3 \\
& + 0.3444y(k-1)y(k-5)^2 - 0.4401y(k-2)y(k-5)^2 \\
& + 3.4624y(k-1)y(k-2)y(k-5) + 0.1986y(k-1)^2y(k-2) \big) \\
& + \sum_{i=1}^{10} \hat{\theta}_i \xi(k-i) + \sum_{j=1}^{5} \hat{\theta}_j \xi(k-j)^2 + \xi(k) \ , \qquad (5.21)
\end{aligned}
$$

where

$$D = 1+1.5164y(k-1)y(k-2)+.5657y(k-3)y(k-5)-12.8527y(k-2)^2 \\ +0.1948y(k-1)^2+1.7662y(k-2)y(k-5)-0.1409y(k-5)^2 \\ -2.0470y(k-1)y(k-5) \ . \tag{5.22}$$

Figure 5.12 shows the chaotic double-scroll attractors reconstructed using polynomial model Eq. (5.13) and rational model Eq. (5.21). Table 5.4 shows the estimated fixed points and largest Lyapunov exponents for both the original system and the identified models.

The results suggest that both polynomial and rational models do reproduce the characteristic dynamical features of the original attractor. Such results also seem to indicate that the polynomial representation is slightly better as far as the modeling of attractors produced by Chua's circuit is concerned. This should come as no surprise because, in fact, the set of equations which describe Chua's circuit can be expressed in polynomial form.

Table 5.4. Dynamical invariants of data and identified models for Chua's Circuit

	Data	Polynomial Eq. (5.13)	Rational Eq. (5.21) – Eq. (5.22)
Fixed Points	(0,2.24,-2.24)	(0,2.24,-2.24)	(0,2.37,-2.37)
Largest Lyapunov Exponent	1.3516 ± 0.0343	1.3350 ±0.0563	1.4218 ±0.0596

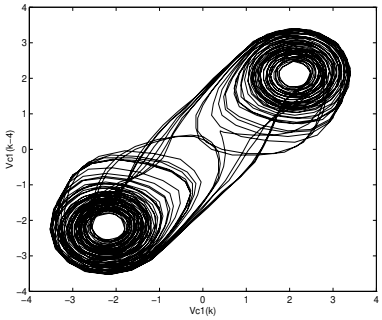

Fig. 5.11. Bi-dimensional reconstruction (2000 points) of Chua's double-scroll attractor. A window of one thousand points of these measured data were used in the identification.

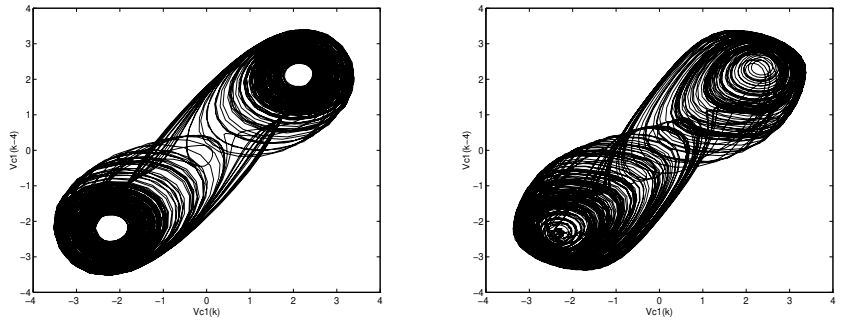

(a) (b)

Fig. 5.12. Double-scroll attractors reconstructed from (a) simulation of the polynomial model (Eq. (5.13)) and (b) simulation of the rational model (Eq. (5.21)). The x-axis is $y(k)$ and the y-axis is $y(k-4)$.

5.3.4. *Continuous-time Global Modeling*

The results of building continuous-time models from discrete-time data obtained from Chua's circuit is briefly described in this section. These results have first appeared in [6].

5.3.4.1. *The Parsimonious Models*

A 38 term model was obtained from the training time series without any structure selection, therefore, hereafter, such a model will be referred to as the *full model*. Conversely, the models obtained implementing the structure selection procedure described in [6] and references therein will be referred to as *parsimonious models* in the sense that all such models will have less than 38 terms. The parsimonious models were obtained by means of structure selection techniques.

5.3.4.2. *Topological Characterization*

The chaotic attractor is embedded in a space spanned by the successive derivatives of the experimentally recorded time series, x. Such an embedding will permit the comparison of the state portrait reconstructed from the experimental data with the portrait generated by the model. The phase space reconstructed from the recorded time series has an embedding dimension equal to 3, which coincides with the dimension of the original phase space. However, five derivative coordinates were used to obtain a global model.

Since the original dynamics can be embedded in a 3D space, only the first three coordinates will be used to characterize the topological structure of the reconstructed state space. Therefore, the first three coordinates are

$$\mathbf{x} = \begin{vmatrix} X_1 = x(t) \\ X_2 = \dot{x} \\ X_3 = \ddot{x} \ . \end{vmatrix} \tag{5.23}$$

The chaotic attractor is displayed in Fig. 5.13. Since the system presents an order two inversion symmetry, every point in the time series may have a counterpart on the opposite side of the attractor. Consequently, the reconstructed attractor should also present an inversion symmetry [53]. This information will be used at the end of this section and will prove to be useful in enhancing model quality.

The analysis of the dynamics starts with the computation of a first-return map obtained from a Poincaré section. In the case of a symmetric attractor, a fundamental map is used. This can be viewed as a first-return map to a Poincaré set defined as

$$\left\{(X_2, X_3) \in \mathbb{R}^2 \mid X_1 = 1.9, X_2 < 0\right\} \cup \left\{(X_2, X_3) \in \mathbb{R}^2 \mid X_1 = -1.9, X_2 > 0\right\}, \tag{5.24}$$

built on the absolute value of one of the two variables (X_1, X_2). The first-return map shown in Fig. 5.14 presents two critical points. The fact that this map does not exhibit any layered structure, confirms the hypothesis of symmetry.

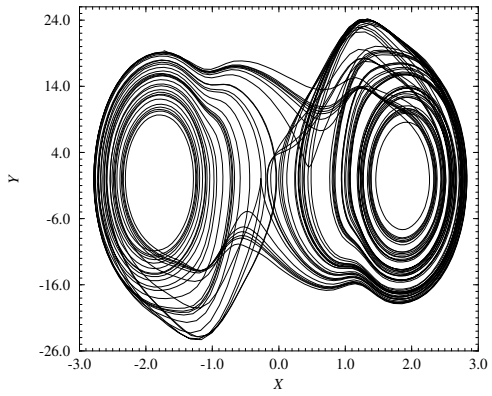

Fig. 5.13. Plane projection of the x-induced attractor generated by the experiments. $X = x$ and $Y = \dot{x}$.

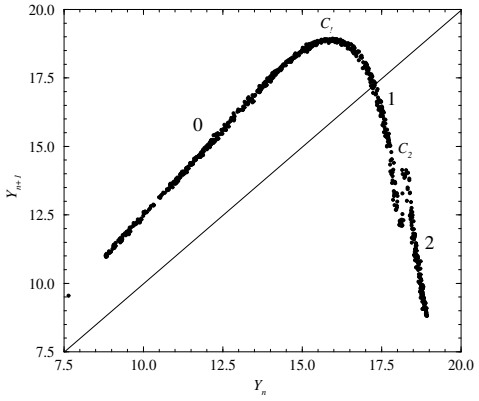

Fig. 5.14. Fundamental first-return map of the attractor reconstructed from the experimental data.

For details on this procedure, please refer to [52–54].

5.3.4.3. *Model Validation*

Figure 5.15 shows the projections of the attractors of some estimated model.

A further step was to compare the fundamental first-return map computed for attractors generated by the models with the one associated with the experimental data, as shown in Fig. 5.16. Models with 36 and 38 terms are characterized by fundamental first-return maps that have a layered structure which is not observed in the experimental data. The layered structure of the first return maps of models with 36 and 38 terms could be an indication of overparametrization [3]. As a result of this, the system becomes unsymmetrical [54].

On the other hand, the first-return maps of models with 29 and 32 terms are much closer to the experimental one and despite the differences, it seems fair to conclude that structure selection has been able to reduce the complexity of the full model resulting in parsimonious models with improved dynamics.

In order to help the algorithm account for the order two inversion, a new model was obtained using a measure which respects the symmetry of the attractor, that is for each point in the differential embedding space, a symmetrical counterpart was included in the data used to estimate the model. For instance, if the original data set had the point $\mathbf{x} = [X_1\ X_2 \ldots X_5]^T$,

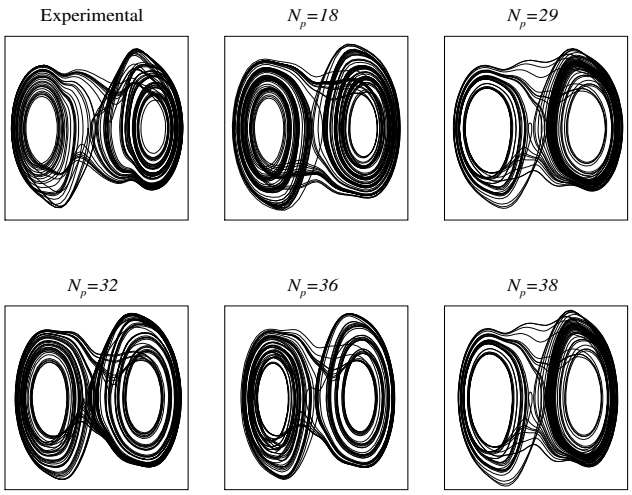

Fig. 5.15. Plane $(x \times \dot{x}) \equiv (X_1 \times X_2)$ projections of the original attractor, the four parsimonious models and the full model ($N_p = 38$).

then the mirror image of such a point, $-\mathbf{x}$, was inserted in the data set before choosing the centers. An $N_p = 20$ term model was found. The first return map of which is shown in Fig. 5.17. It should be mentioned that this model possesses an important property of the experimental flow that is not shared by the other models since all the models mentioned in Fig. 5.16 have symmetric fixed points but the related flow is *not* symmetric due to the presence of quadratic terms of the form $X_i X_j$ $(\forall i, j \neq 1)$.

Although improvement in some sense can be observed, the identified model still reveals difficulties. The first-return map does not present the layered (ghostly) structure as before. This is a signature of perfect symmetry as pointed out in [54]. Secondly, the maximum of the first return map shown in Fig. 5.17 does not coincide with the $x = y$ line as observed in other models (Fig. 5.16), this has important consequences in the resulting population of periodic orbits. As a matter of fact, for the $N_p = 20$ model the location of this maximum in relation to the $x = y$ line is very similar to that of the experimental dynamics (Fig. 5.16). Because of the third branch which is increasing, rather than decreasing, as seen in the experimental map (Fig. 5.16), the topology of part of the attractor is different. The linking numbers, that is, the half sum of oriented crossings are computed, reveal

some differences between the model and the dynamics underlying the experimental data. For instance, the pair of periodic orbits encoded by (200) and (10) are displayed for the experimental dynamics (Fig. 5.18(a)) and for the 20 term model (Fig. 5.18(b)). The linking number $lk(200, 10)$ is equal to -2 in both cases but it is noticed that the period-2 orbit of the model is a symmetric orbit, that is, it visits the two scrolls in the same way, whereas it is asymmetric and confined in to a single scroll for the dynamics underlying the experimental data. Such an example confirms that the experimental and the 20 term model attractors are not topologically equivalent although both attractors are rather difficult to distinguish by simple visual inspection. A likely reason for such a difference is the third increasing branch in the first-return map of the model, as shown in Fig. 5.17(b), which is not observed for the experimental dynamics. Interestingly, however, the first-return map of a Chua-type circuit with a smooth nonlinearity [44] also presents a similar increasing branch.

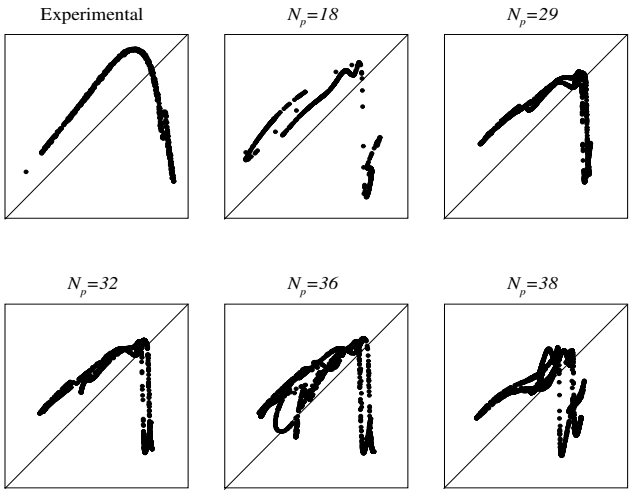

Fig. 5.16. First-return maps for the five different models.

5.3.4.4. *Multivariable Polynomial Modeling*

The following example, first presented in [10], considers data collected from PCChua, with the frequency of the main spectral peak around 1.6 Hz [73].

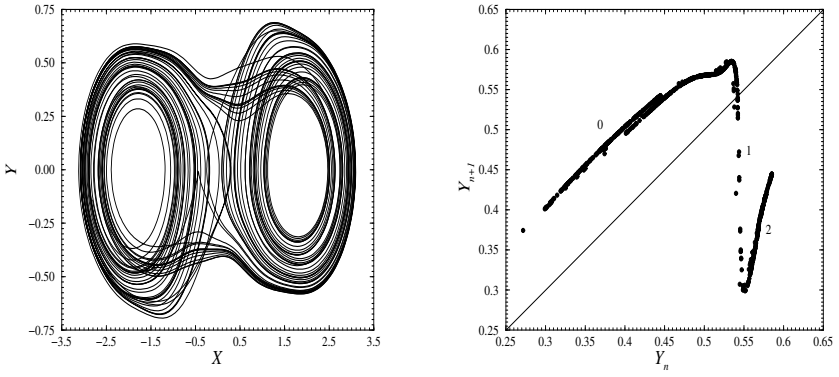

(a) (b)

Fig. 5.17. Phase portrait (a) and the corresponding first-return map (b) generated by the symmetrical model. This model has twenty terms, $N_p = 20$.

This enabled collecting the data with a sampling time of $T_\mathrm{s} = 30\,\mathrm{ms}$.

Only 1000 observations of each state variable were used to build the model. The data used to build the model are shown in Fig. 5.19. The automatic structure selection scheme followed by an orthogonal extended least squares estimation routine yielded the following model

$$
\begin{cases}
x(k) = \textit{1.21036203206}\, x(k-1) + 0.972047183733\times10^{+2}\, z(k-1) \\
\quad +0.598221283675\, y(k-1) \\
\quad -0.171315924858\times10^{-1}\, x^3(k-1) \\
\quad +0.398097703675\times10^{+5}\, y(k-1)z^2(k-1) \\
\quad +0.819593354856\times10^{+4}\, x(k-1)z^2(k-1) \\
\quad -0.111072563509\times10^{+3}\, y^2(k-1)z(k-1) \\
y(k) = \underline{\textit{0.895252009866}}\, y(k-1) - 0.223303681119\times10^{+6}\, z^3(k-1) \\
\quad +0.0837143492947\, x(k-1) \\
\quad +0.129325180333\times10^{+3}\, z(k-1) - 0.677214817432\times10^{-3}\, x^3(k-1) \\
\quad +0.181085268783\times10^{-3}\, x^2(k-1) \\
\quad -0.204050446812\times10^{+1}\, x(k-1)y(k-1)z(k-1) \\
z(k) = \textit{0.938265057186}\, z(k-1) - 0.637485684220\times10^{-3}\, y(k-1) \\
\quad -0.362134020185\times10^{-4}\, x(k-1) \\
\quad +0.315363093575\times10^{-5}\, x^2(k-1) + 0.632868345441\times10^{-5}\, y^2(k-1) \\
\quad -0.643318682312\times10^{-5}\, x(k-1)y(k-1) \\
\quad +0.187619321537\times10^{-2}\, x(k-1)z(k-1).
\end{cases}
\tag{5.25}
$$

As before (Sec. 5.3.3.1), only the deterministic part of the model is shown. It is important to notice that model Eq. (5.25) cannot produce a mathematically symmetrical attractor because it includes even parity terms [54]. When symmetry conditions were imposed during modeling, the new model did not settle unto the double scroll attractor and state estimation results did not improve.

Besides the polynomial model Eq. (5.25) multilayer perceptron (MLP)

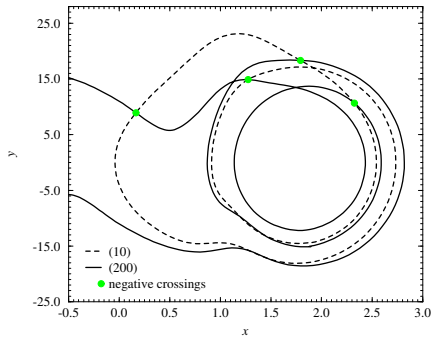

(a)

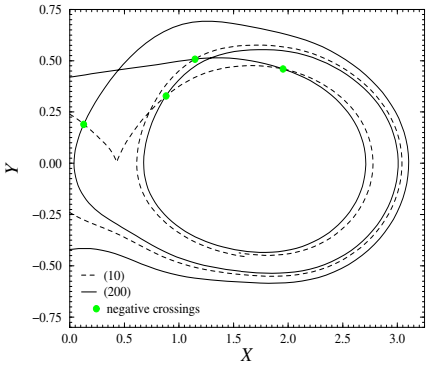

(b)

Fig. 5.18. (a) Experimental dynamics, and (b) model dynamics. The linking numbers between periodic orbits encoded by (200) and (10) is equal to -2 for both the experimental dynamics and the 20 term model dynamics. Nevertheless, the period-2 orbit does not present the same symmetry properties. See text for a possible explanation.

neural networks were trained from the same set of data. Three networks were trained, one for each state variable. The input layer in each case was the same, namely $[x(k-1), y(k-1), z(k-1)]^\top$. The activation functions of the nodes in the single hidden layer were hyperbolic tangent and the single output node was linear in all three networks. In this section we discuss the results obtained by two set of networks. The first set was composed of three fully connected networks with two nodes in the hidden layer and the second was composed of three fully connected networks with seven nodes

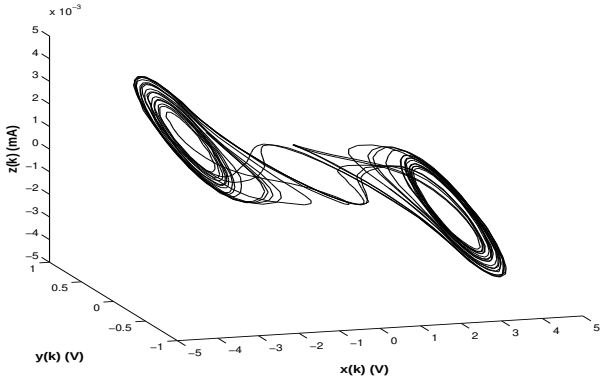

Fig. 5.19. The *measured* double scroll attractor of the implemented electronic oscillator. There are the data used to build model Eq. (5.25).

in the hidden layer. Such neural models will be referred to as MLPs2 and MLPs7, respectively. Briefly, MLPs2 also settled to limit cycle and MLPs7 showed a very long chaotic transient— consistent with the double-scroll attractor— before settling to a spiral strange attractor.

It was believed that all the estimated models— Eq. (5.25), MLPs2 and MLPs7— could be competitive in the implementation of a Unscented Kalman Filter – UKF [40]. However, it was desired to verify if models with improved global dynamics would outperform locally optimal models. In order to investigate this issue slight changes were implemented in model Eq. (5.25) *a posteriori*, as described in the following paragraph.

The free-run of model Eq. (5.25) settles to the attractor shown in Fig. 5.20(a). Such an attractor seems to be close to a genuine solution of the system in the sense that it could be the "stable version" of one of the unstable periodic orbits that compose the original attractor. When this is the case, it has been argued that the model can be perturbed (this can be done in different ways) in order to become chaotic [1]. In the present case this is achieved by slightly increasing the underlined parameter. For instance, if 0.92427441 is used, model Eq. (5.25) settles to the double-scroll attractor shown in Fig. 5.20(b)[a]. In what follows we shall refer to this as the perturbed double-scroll model.

[a]Other parameter values were tested for perturbing model Eq. (5.25) in order to obtain the double-scroll attractor. Nevertheless, the greater the disturbance (i.e. the farther from the optimal set of parameters) the worse the performance of the UKF in estimating the states, although the model might display improved global features.

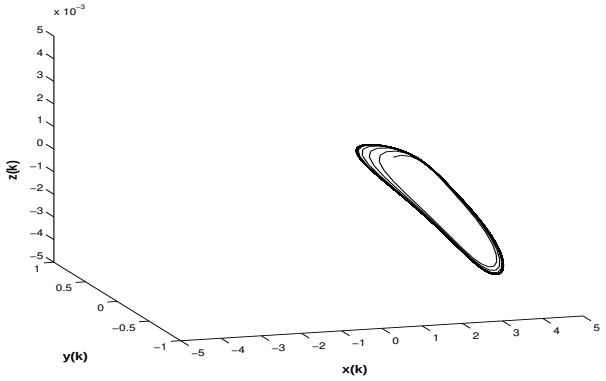

(a)

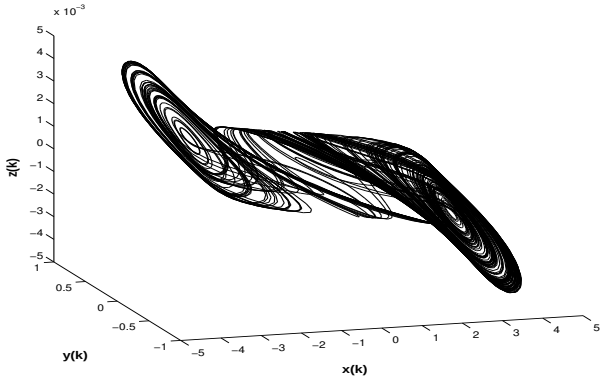

(b)

Fig. 5.20. Attractors produced by identified model (a) without and (b) with parameter perturbation, with initial conditions $x(0) = 3.2$, $y(0) = 0.37$ and -0.009. From [10].

5.3.5. *State Estimation*

The results in this section were first presented in [10]. The UKF with the identified model Eq. (5.25) was used to estimate the full state vector of the electronic circuit using only the x component to drive the filter. The following situations were tested: i) using Eq. (5.25) as obtained from the modeling step; ii) slightly perturbing the underlined parameter of Eq. (5.25) in order to approximate the resulting attractor to the original double scroll attractor; iii) using Eq. (5.25) but jointly estimating the three parameters in italic (which correspond to the terms of each equation with higher ERR index), iv) the same as in (i) but using a null process noise covariance

matrix Q.

It is important to declare that in the aforementioned situations, except in (iv), Q was taken as a diagonal matrix with elements equal to the one-step-ahead prediction error variance of the respective model[b]. In case (iii), where three parameters were also estimated, the elements of Q_θ were taken as the corresponding parameter variances obtained as a byproduct from the extended least squares estimator used during modeling step. The results are summarized in Table 5.5.

Table 5.5. Normalized root mean square (RMS) error of estimated states for the electronic system. The UKF was implemented with the identified model Eq. (5.25) — in several contexts (see text)— and with the neural models MLPs2 and MLPs7. From [10].

	situation investigated	x	y	z
(i)	model	$2.80\times10^{-7}\%$	2.58%	0.87%
(ii)	perturbed model	$3.75\times10^{-7}\%$	5.85%	2.86%
(iii)	joint parameter estimation	$3.70\times10^{-7}\%$	3.03%	1.24%
(iv)	model with $Q = 0$	88.46%	85.46%	76.46%
(v)	MLPs2	$2.57\times10^{-7}\%$	2.06%	1.18%
(vi)	MLPs7	$9.33\times10^{-7}\%$	1.27%	0.86%

The very low values of RMS for the estimation errors of the x component are a consequence of low measurement noise in PCChua experimental setup (Sec. 5.2.3) and due to the fact that the x variable is used to drive the filter.

An interesting remark that can be made based on the results of Table 5.5 is that although the perturbed model is, in a sense, closer to the original system (for instance, both have a positive Lyapunov exponent), the unperturbed model— which has a lower one-step-ahead prediction error— is better suited for use within the UKF.

When the UKF was implemented using Eq. (5.25) then, quite naturally, the UKF estimates also settled to the same attractor (possibly just a limit cycle) shown in Fig. 5.20a. This explains the very high values of RMS for situation (iv) shown in Table 5.5. This problem can be circumvented by setting a lower bound for the covariance matrix P by properly setting the process noise covariance matrix Q. Otherwise, when convergence was achieved, the trace of matrix P would tend to zero. In so doing the filter remains more active and the most recent measurements gain more weight compared to the model and as a result the UKF settles to a double-scroll attractor, see Fig. 5.21(a). In other words, there are two important sources of information in the filter: on the one hand, there is the model that

[b]Obtained by one-step-ahead simulation using each model.

propagates the sigma points and, on the other hand, there are the measurements. Suitably defining Q and R is a way of weighting differently these two sources. So as to express lack of confidence in the model, the trace of Q should be increased. Similarly, the trace of R ought to be directly related to the degree of uncertainty in the measurements.

When parameters are estimated in addition to the states, the estimated parameters converge to the values obtained during the modeling stage as indicated in Fig. 5.22. Consequently situations (i) and (iii) have close performance indices in Table 5.5.

Table 5.6 summarizes the UKF performance when extra white Gaussian noise is added to the x component in the case of polynomial and neural models. As can be seen, the UKF implemented with the neural model with 7 hidden nodes is significantly more robust to noise than the filters implemented with the other models. At first sight this could seem inconsistent with the results shown in Table 5.5 where MLPs7 has the highest error for the x variable. It should be noticed however that this weakness of MLPs7 does not appear in Table 5.6 because the filters are driven by the x variable, that is, poor performance in predicting the driving signal is not as serious as poor performance in predicting the remainder of the state vector, in which case the predictions are all we have.

Table 5.6. Normalized root mean square (RMS) error of estimated states for the electronic oscillator. The UKF was implemented with the identified model Eq. (5.25) and with the neural models MLPs2 and MLPs7. The x-component, that drives the filter, was corrupted with extra additive white Gaussian noise.

model/noise	x (%)	y (%)	z (%)
Polyn 10%	1.97	3.37	1.42
MLPs2 10%	3.48	5.63	2.55
MLPs7 10%	1.01	2.88	1.37
Polyn 25%	4.35	6.08	3.08
MLPs2 25%	8.20	12.66	5.54
MLPs7 50%	1.57	3.53	1.84
Polyn 50%	17.82	17.93	12.84
MLPs2 50%	25.56	27.20	18.13
MLPs7 50%	2.95	5.09	2.75

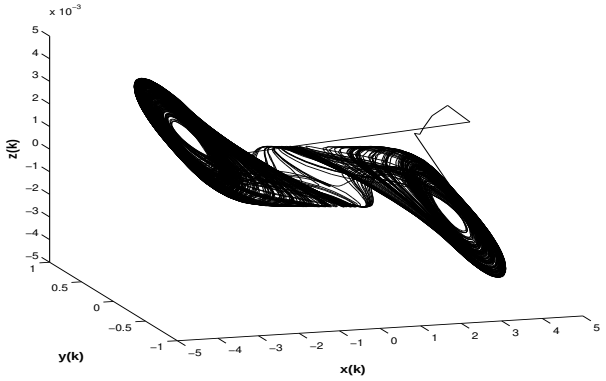

(a)

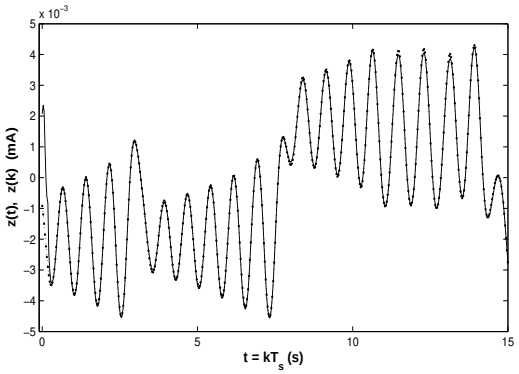

(b)

Fig. 5.21. The estimated double scroll attractor of the implemented electronic oscillator. Estimation was performed by the UKF with model Eq. (5.25) and the x component driving the filter. (a) full state vector, (b) detail of the z component (-·-) measured data, and (—) estimated component $\hat{z}(k)$. In the plot (a) the transient at the beginning was also included to give an idea of how quickly the filter settles. From [10].

5.4. Chua's Circuit Control and Synchronization

The control (and synchronization) of Chua's circuit has been chosen as a benchmark in nonlinear control of dynamical systems by many researchers around the world.

This is explained by the simultaneous conjugation, on Chua's circuit, of complex behavior, simple construction, and manageable mathematical description composed by a set of only three piecewise affine differential

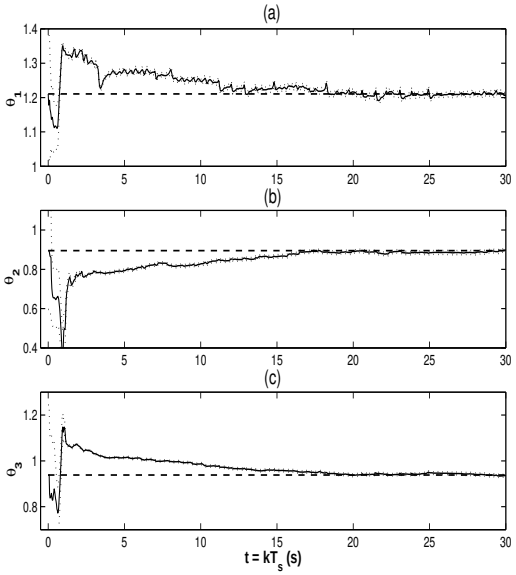

Fig. 5.22. The solid lines (—) show the results obtained from the joint estimation of the three parameters in italic in equation Eq. (5.25). The dotted lines (·) indicate plus and minus one standard deviation ($\pm\sqrt{\text{diag}\{P_\theta\}}$) of the parameters estimated by joint UKF. The dashed lines (- -) indicate the values for these parameters estimated by extended least squares during the modeling step. From [10].

equations. As a consequence, to control and/or to synchronize Chua' circuits has become a paradigm in nonlinear control systems theory.

As a sample of modern nonlinear control strategies used to control Chua circuits, or one of the many variations of this famous chaotic oscillator, it is possible to register: feedback linearization [55], backstepping [74], sliding mode [39], and fuzzy control [23], among others.

In this section, a sample of results from the application of different control and synchronization strategies to the circuit of Chua will be presented. The aim is to show how Chua's circuit can be employed to draw deep conclusions on the more general problem of controlling nonlinear systems.

5.4.1. *General Considerations – Control Objective, Available Energy and Mathematical Modelling*

The control of nonlinear dynamical systems is undoubtedly a vast field of research, which has been approached from many different points of view (see [43, 64, 66] and references therein). The lack of a universal theory, as powerful as the well known Linear System Theory [27], with which one would be capable of explaining the plethora of phenomena found in these systems, almost prevents the achievement of general results.

Despite this fact, in [12] it was possible to elaborate broader conclusions on the performance of controllers for nonlinear dynamics, by taking into account a number of aspects such as: (*i*) maximum control effort allowed (energy limits); (*ii*) the dissimilarities of the control objective (goal dynamics) when compared to the natural behavior of the uncontrolled system; and (*iii*) the controller structure complexity itself; i.e. the necessity or not of accurate models of the system to be controlled in the design of the control law. The tradeoff among these aspects can be clearly illustrated on the control and synchronization of Chua circuits.

For example, when the control objective is to force one or more state variables of the chaotic oscillator to follow an arbitrary reference; e.g. a sinusoidal signal; one expects that complex and/or high energy controllers would be necessary, as it will be presented in Sec. 5.4.4.

On the other hand, if the reference signal is constant at a specific value such that the problem becomes one of stabilization of unstable fixed points of Chua's circuit, the demanded energy could be reduced, and the controller could be made simpler than the one used in the former case, as it will be seen in Sec. 5.4.2.

Another example is the stabilization of unstable periodic orbits (UPO); which are the fundamental bricks in the system chaotic attractor, and therefore are close to the natural behavior of the uncontrolled system. In this case, one expects that simple and low energy controllers would suffice. This is indeed verified in the famous OGY chaos control method [61], whose variations have been applied to Chua's circuit in [23] and [34].

Similarly, although not obvious, in the problem of synchronization of unidirectionally coupled identical nonlinear oscillators, if one considers that this is indeed a control problem where the reference signal is the trajectory produced by the so-called *master* system, such that a *slave* system has to be controlled in order to follow it, simple and/or low energy controllers could be employed. This is a consequence of the fact that the control

objective is to force the slave system follow one of its natural trajectories after synchronization has been attained. If the goal trajectory belongs to the library of natural behaviors of the slave then, after synchronization has been reached, the control effort should vanish in the absence of noise and perturbations. This will be discussed in the next section.

5.4.1.1. *The ITVC Principle*

Interesting considerations naturally arise from the close relationship between control and synchronization of nonlinear oscillators. In [72] for continuous-time systems, and in [69] for discrete-time systems, a general principle called *Information Transmission Via Control* – ITVC was presented and proved, which relates the control effort $u(t)$, demanded to keep the systems synchronized, to the perturbation (or information) $p(t)$ signal injected at the master oscillator, as shown in Fig. 5.23.

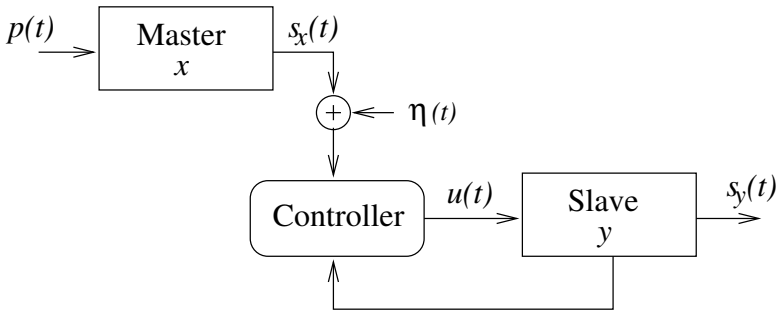

Fig. 5.23. Unidirectionally coupled systems or master-slave configuration. $p(t)$ and $u(t)$ are the perturbation and the control signals, respectively; $x(t)$ and $y(t)$ are the state vectors of the master and the slave nonlinear oscillators, which tend to synchronize by means of the control action $u(t)$. $s_x(t)$ and $s_y(t)$ are measured signals from the oscillators. The Information Transmission Via Control principle [72] states that $u(t) \to p(t)$, in the absence of noise $\eta(t)$, as long as $y(t) \to x(t)$.

Consider the following information transmission system based on additively perturbed nonlinear oscillators:

$$\dot{x} = f(x) + p(t), \tag{5.26}$$

$$\dot{y} = \hat{f}(y) + u(t), \tag{5.27}$$

$$s_x = h(x) + \eta(t), \tag{5.28}$$

where $x \in \mathbb{R}^n$ is the master oscillator state vector, $f : \mathbb{R}^n \to \mathbb{R}^n$, $p(t) = [p_1(t) \;\; p_2(t) \;\; \ldots \;\; p_n(t)]$ is a vector of information signals, where it is allowed

to have $p_k(t) = 0$ for some values of $k \in \{1, 2, \ldots, n\}$; $s_x \in \mathbb{R}^q$ is the vector of transmitted signals, such that $q \leq n$; $h : \mathbb{R}^n \to \mathbb{R}^q$ is a general mapping; $\eta(t) = [\eta_1(t) \ \ \eta_2(t) \ \ldots \ \eta_q(t)]$ is a vector of noise signals; $y \in \mathbb{R}^n$ is the slave oscillator state vector; $\hat{f} : \mathbb{R}^n \to \mathbb{R}^n$, and $u(t) = [u_1(t) \ \ u_2(t) \ \ldots \ u_n(t)]$ is a vector of control signals, also represented as continuous functions of time. In this case, the following can be established:

Theorem 5.1. *(ITVC – Information Transmission Via Control Principle). Define the synchronization error vector as*

$$e = x - y. \tag{5.29}$$

Suppose that the systems Eq. (5.26) and Eq. (5.27) have $\mathcal{C}^0$ (continuous) vector fields $f(x)$ and $\hat{f}(y)$, respectively. In addition, $f(x) = \hat{f}(x), \forall x \in \mathbb{R}^n$, i.e. the two autonomous oscillators are identical. Under these assumptions, one has the following result:

$$\lim_{t\to\infty} \|e\| = 0 \Rightarrow \lim_{t\to\infty} \|p(t) - u(t)\| = 0, \tag{5.30}$$

where $\|\cdot\|$ denotes the Euclidean norm.

An important fact, concerning the general result of the ITVC principle, was also proved in [72]. In practice, identical synchronization ($\|e\| \to 0$) is not possible due to unavoidable noise and parameters mismatch, such that the synchronization error does not go to zero, but instead it remains limited: $0 \leq \|e\| \leq \mathcal{E} < \infty$. When this occurs, high-energy controllers should not be used to recover $p(t)$, as can be deduced from the following result:

Theorem 5.2. *(Information recovery when both systems are not identically synchronized). Suppose that $f : \mathbb{R}^n \to \mathbb{R}^n$ is a $\mathcal{C}^\omega$ (analytic) function representing the vector fields of both master Eq. (5.26) and slave Eq. (5.27) oscillators ($f(x) = \hat{f}(x), \forall x \in \mathbb{R}^n$). In addition, suppose that $0 \leq \|e\| \leq \mathcal{E} < \infty$. Considering the recovering error defined as*

$$e_{\mathrm{d}} = p(t) - u(t),$$

then

$$\|e_{\mathrm{d}}(t)\| \to \|\dot{e}\|, \tag{5.31}$$

as long as $\mathcal{E} \to 0$. More specifically, it is possible to write that

$$\begin{cases} \|e_{\mathrm{d}}(t)\| \leq \|\dot{e}(t)\| + \rho(y)\mathcal{E} + \phi(\mathcal{E}^2) \\ \|e_{\mathrm{d}}(t)\| \geq \|\dot{e}(t)\| - \rho(y)\mathcal{E} - \phi(\mathcal{E}^2) \end{cases} \tag{5.32}$$

where $\rho(y) = \|D_f^y\|$ *is the norm of the Jacobian matrix* D_f^y *of* $f(e+y)$ *evaluated around* $e = e_0 = 0$*, which depends on the value of* y*.*

The function $\phi(\mathcal{E}^2) : \mathbb{R} \to \mathbb{R}^+$ *represents high order terms in* $\mathcal{E}$ *that vanish when* $\mathcal{E} \to 0$*, i.e.* $\lim_{\mathcal{E}\to 0} \phi(\mathcal{E}^2)/\mathcal{E} = 0$*.*

By applying the above theorem, one sees that the error $e_{\rm d}(t)$ in recovering the perturbation (information) approaches the derivative of the synchronization error e. Therefore, the theorem clearly establishes that it is possible to achieve a dynamic condition arbitrarily close to the identical synchronization ($\|e\| \approx 0$), and still do not recover accurately the original perturbation signal $p(t)$, if the controller structure is such that it results in $\|\dot{e}\| \gg 0$.

Such controllers; i.e. the control laws that lead to the condition

$$\|\dot{e}\| = \left\| \left[f(x) - \hat{f}(y) \right] + [p(t) - u(t)] \right\| \gg 0;$$

are called in this context "high-energy controllers", because usually it is observed negligible mismatch between master and slave oscillators ($\|f(x) - \hat{f}(y)\| \approx 0$); and the perturbation signal is generally kept small ($\|p(t)\| \approx \|e\|$) in order to not destabilize the master oscillator. Under these assumptions, it follows that $\|\dot{e}\| \gg 0 \Rightarrow \|u(t)\| \gg 0$. In Sec. 5.4.4.2 an example of this situation will be discussed.

The ITVC principle, as stated in [69], has also been used as the basis for model validation procedures that rely on the control effort spent to synchronize identified discrete-time models with the corresponding acquired data set from a real system [7]. Similar remarks concerning the fact that low-energy controllers should be used in this validation approach (due to the impossibility of achieving perfect synchronization between real data and identified model) were also proved in [69].

5.4.2. *Linear State Feedback*

In this section, the control and synchronization of Chua's chaotic oscillator is investigated based on the design of linear state feedback controllers.

A method for selecting the controller gain matrix is proposed based on the use of the optimization technique known as the ellipsoid algorithm [31]. The formulation presented here can be viewed as an extension of the work in [70] where the focus was the controller structure design. The objective is to provide a more general method to determine the non zero elements in the controller gain matrix in order to issue stable controlled systems.

The connection between the control and synchronization problems is explored in detail. It is shown that the synchronization problem is similar to the equilibrium point stabilization problem concerning the linear controller design requirements.

Consider the controlled circuit of Chua (Fig. 5.6, page 105) described by the set of differential equations Eq. (5.7), repeated here, but substituting $\tilde{z}$ by z for clarity purposes:

$$\begin{aligned} \dot{x} &= p\,[y - x - f(x)] + u_{\mathrm{x}}(t, \vec{x}), \\ \dot{y} &= x - y + z \qquad\quad + u_{\mathrm{y}}(t, \vec{x}), \\ \dot{z} &= -qy + rz \qquad\quad + u_{\mathrm{z}}(t, \vec{x}), \end{aligned} \tag{5.33}$$

where $p = C_2/C_1$ and $q = -R^2C_2/L$. Note that the derivatives were taken relative to the normalized time variable $t = t'/RC_2$, where t' represents the actual time (Sec. 5.2.1). The nonlinear function $f(x) = Ri_{\mathrm{d}}(x)$ in Eq. (5.33) is proportional to the current through the Chua's diode, which is given by Eq. (5.2), page 100.

The control inputs $u_{\mathrm{x}}(t)$, $u_{\mathrm{y}}(t)$ and $u_{\mathrm{z}}(t)$ in Eq. (5.33), assuming linear state feedback control, can be rewritten in vector form as

$$\vec{u}(t) = [u_{\mathrm{x}}\ u_{\mathrm{y}}\ u_{\mathrm{z}}]^{\top} = K(\vec{x} - \vec{x}_{\mathrm{ref}}(t)), \tag{5.34}$$

where $\vec{x} = [x\ y\ z]^{\top}$ is the state vector, the reference vector is denoted by $\vec{x}_{\mathrm{ref}}(t) = [x_{\mathrm{ref}}(t)\ y_{\mathrm{ref}}(t)\ z_{\mathrm{ref}}(t)]^{\top}$ and $K \in R^{3\times 3}$ is the controller gain matrix. Using the Chua's diode characteristic Eq. (5.2) together with Eq. (5.34), it is possible to rewrite Eq. (5.33) in matrix form as

$$\dot{\vec{x}} = A_x\vec{x} + \vec{b}_x + K\,(\vec{x} - \vec{x}_{\mathrm{ref}}) \tag{5.35}$$

where

$$A_x = \begin{cases} A_1 \in R^{3\times 3}, \text{ if } x \in [-B_{\mathrm{p}}, +B_{\mathrm{p}}], \\ A_2 \in R^{3\times 3}, \text{ if } x < -B_{\mathrm{p}} \text{ or } x > +B_{\mathrm{p}}, \end{cases} \tag{5.36}$$

$$\vec{b}_x = \begin{cases} \vec{b}_1 = pR[B_{\mathrm{p}}(m_0 - m1)\ 0\ 0]^{\top}, & \text{if } x < -B_{\mathrm{p}}, \\ \vec{b}_2 = [0\ 0\ 0]^{\top}, & \text{if } x \in [-B_{\mathrm{p}}, +B_{\mathrm{p}}], \\ \vec{b}_3 = pR[B_{\mathrm{p}}(m_1 - m_0)\ 0\ 0]^{\top}, & \text{if } x > +B_{\mathrm{p}}. \end{cases} \tag{5.37}$$

Actually, the matrix A_x is the Jacobian matrix of the nonlinear vector field of the autonomous chaotic oscillator.

Defining the error vector as

$$\vec{e} = \vec{x} - \vec{x}_{\mathrm{ref}},$$

it is possible to derive the following differential equation describing the error dynamics as a linear time-variant non-autonomous system represented by

$$\frac{d\vec{e}}{dt} = A_x(\vec{e} + \vec{x}_{\text{ref}}) + \vec{b}_x + K\vec{e} - \frac{d\vec{x}_{\text{ref}}}{dt};$$

$$\dot{\vec{e}} = A_k\vec{e} + \vec{\eta}(t), \tag{5.38}$$

$$A_k = A_x + K, \tag{5.39}$$

$$\vec{\eta}(t) = A_x\vec{x}_{\text{ref}}(t) + b_x - \dot{\vec{x}}_{\text{ref}}(t). \tag{5.40}$$

Assuming that it is possible to adequately choose the gain matrix K in Eq. (5.39) so that the instantaneous eigenvalues of A_k have negative real parts, the time evolution of the error vector inside each linear region is given by [27]

$$\vec{e}(t) = \exp\left[A_k(t-t_0)\right]\vec{e}(t_0) + \text{conv}\left[\vec{\eta}(t)\,,\,\exp\left[A_k(t-t_0)\right]\right] \tag{5.41}$$

where t_0 corresponds to the time instant when the system enters the linear region, and $\text{conv}\left[\cdot\,,\,\cdot\right]$ denotes the linear convolution operator. Note that, despite the complexity in Eq. (5.41), from the above assumption of asymptotic stability, the error behavior can be approximated by

$$\vec{e}\left(t \gg |\lambda_c|^{-1}\right) \approx \text{conv}\left[\vec{\eta}(t)\,,\,\vec{h}(t)\right], \tag{5.42}$$

$$\vec{h}(t) = \exp\left[A_k(t-t_0)\right],$$

$$\lambda_c = \min|\text{real}\{\lambda(A_k)\}|,\ \ \lambda_c < 0,$$

Moreover, the greater the value of $|\lambda_c|$ the faster the decay of the components in the vector function $\vec{h}(t)$, in such a way that the expression Eq. (5.42) becomes similar to

$$\vec{e}(t > T) \approx \text{conv}\left[\vec{\eta}(t)\,,\,\vec{\delta}(t)\right], \tag{5.43}$$

where $\vec{\delta}(t)$ is a vector of impulsive functions whose magnitudes are proportional to the areas under the graphs of the $\vec{h}(t)$ components, which in turn become smaller for greater values of $|\lambda_c|$. This qualitative analysis was carried out to stress that the larger the absolute values of the real parts of the instantaneous eigenvalues of A_k in Eq. (5.39), the smaller the maximum steady-state error, as can be seen from Eq. (5.43). This effect can be obtained by means of gain augmentation, e.g. through the use of large values in a diagonal matrix K; which is a well known result from linear control theory.

Assuming that the matrix K was appropriately chosen, reducing the error vector norm in order to guarantee that the state vector $\vec{x}$ and the reference state $\vec{x}_{\text{ref}}$ will be in the same affine region after a time interval T, the Eq. (5.40) can be rewritten as

$$\vec{\eta}(t > T) = A_{x_{\text{ref}}}\vec{x}_{\text{ref}}(t) + b_{x_{\text{ref}}} - \dot{\vec{x}}_{\text{ref}}(t). \tag{5.44}$$

Note that the first two terms in Eq. (5.44) constitutes the very nonlinear vector field of an autonomous Chua's circuit whose state vector is $\vec{x}_{\text{ref}}$.

Suppose that the control objective is to stabilize an equilibrium point $\vec{p}_{\text{eq}}$ of the chaotic oscillator. In this case, Eq. (5.44) becomes

$$\left.\begin{array}{l} \vec{x}_{\text{ref}} = \vec{p}_{\text{eq}} = [x_{\text{eq}}\ y_{\text{eq}}\ z_{\text{eq}}]^{\top}, \\ \dot{\vec{x}}_{\text{ref}} = 0, \\ A_{x_{\text{eq}}}\vec{p}_{\text{eq}} + \vec{b}_{x_{\text{eq}}} = 0, \end{array}\right\} \Rightarrow \vec{\eta}(t > T) = 0. \tag{5.45}$$

A similar result can be derived when the reference trajectory is generated by another Chua's oscillator with the same parameters, i.e. a master-slave synchronization problem,

$$\dot{\vec{x}}_{\text{ref}} = A_{x_{\text{ref}}}\vec{x}_{\text{ref}} + \vec{b}_{x_{\text{ref}}} \Rightarrow \vec{\eta}(t > T) = 0. \tag{5.46}$$

The above result reveals that there exists a strong similarity between the Chua's circuit equilibrium point stabilization and synchronization problems. In both cases, the requirement on providing larger absolute values for the instantaneous eigenvalues of A_k in Eq. (5.39) can be softened due to the nature of the control objective.

The most important requirement concerning the matrix K selection is to guarantee an asymptotically stable matrix A_k in Eq. (5.38) for all $t \geq 0$.

Clearly, from Eq. (5.36) and Eq. (5.39), at any instant, only one of two possible characteristic polynomials will be relevant in the stability analysis. Applying the Routh criterion [27] on the coefficients of the characteristic polynomials

$$\begin{array}{l} \det\left[(A_1 + K) - \lambda I\right] = 0 \Rightarrow \lambda^3 + \alpha_2\lambda^2 + \alpha_1\lambda + \alpha_0 = 0, \\ \det\left[(A_2 + K) - \lambda I\right] = 0 \Rightarrow \lambda^3 + \beta_2\lambda^2 + \beta_1\lambda + \beta_0 = 0, \end{array} \tag{5.47}$$

where $I \in R^{3\times 3}$ is the identity matrix and $\det[\cdot]$ denotes matrix determi-

nant, issues the following set of restrictions

$$\Omega : \begin{cases} g_1 : & \alpha_0 & > 0, \\ g_2 : & \alpha_1\alpha_2 - \alpha_0 & > 0, \\ g_3 : & \alpha_2 & > 0, \\ g_4 : & \beta_0 & > 0, \\ g_5 : & \beta_1\beta_2 - \beta_0 & > 0, \\ g_6 : & \beta_2 & > 0. \end{cases} \tag{5.48}$$

Note that the coefficients α_n and β_n, $n = 0, 1, 2$; are, in general, nonlinear functions of the elements k_{ij}; $i, j = 1, 2, 3$; in matrix K.

The great complexity exhibited in Eq. (5.48) can be reduced using simpler control structures. For example, assuming that $u_{\rm x}(t) = u_{\rm y}(t) = 0$ in Eq. (5.33) so that, the circuit is controlled only by the voltage source in series with the inductor L shown in Fig. 5.6, page 105, the matrix K becomes

$$K = \begin{bmatrix} 0 & 0 & 0 \\ 0 & 0 & 0 \\ k_1 & k_2 & k_3 \end{bmatrix}, \tag{5.49}$$

and there will be only two nonlinear restrictions in Eq. (5.48), namely g_2 and g_5. Clearly, other control structures can be tested based on the same approach, and the set of restrictions Eq. (5.48) bounds a region Ω in the m-dimensional controller parameter space for which the matrix A_k in Eq. (5.39) is asymptotically stable; where m is the number of non zero elements in the matrix K.

Concerning the control problem, an additional requirement is to maximize the minimum absolute eigenvalue of A_k in Eq. (5.39), in order to achieve a better tracking performance. This means that there exists an optimal set of control parameters $\vec{k}^*$ inside the region Ω. On the other hand, when dealing with the synchronization problem, the requirement on the minimum absolute eigenvalue of A_k is not critical, as discussed previously on the similarity between the synchronization and the equilibrium point stabilization problems.

Considering only the restrictions g_i in Eq. (5.50) and using the center-cut ellipsoid algorithm described in [31], examining the restrictions in a cyclical order, it is possible to select a viable matrix K that leads to asymptotic stability in the synchronization problem.

In the case of the general control problem; i.e. arbitrary reference signal $\vec{x}_{\rm ref}(t)$; note that the coefficients α_2 and β_2 in Eq. (5.47) are the negative sum of the stable eigenvalues of (A_1+K) and (A_2+K), respectively. Hence,

a possible way to maximize the minimum absolute eigenvalue of A_k is to solve the following optimization problem

$$\begin{aligned} &\max\{\alpha_2 + \beta_2\} \\ &\text{s. t.} \quad g_i > 0; i = 1, 2, \ldots, 6; \end{aligned} \tag{5.50}$$

where the restrictions g_i were defined in Eq. (5.48). The use of the ellipsoid algorithm on Eq. (5.50), issues a gain matrix K well suited for control purposes.

A simulation procedure was carried out using the following set of Chua's circuit parameters: $C_1 = 23.5\mu$F, $C_2 = 235\mu$F, $L = 43.43$H, $R = 1.8$kΩ (see Fig. 5.6, page 105); and $m_0 = -0.36$mS, $m_1 = -0.68$mS and $B_{\rm p} = 1.0$V as Chua's diode parameters; Eq. (5.2), page 100. The results are shown in Fig. 5.24 to Fig. 5.26 for the control structure represented by the gain matrix K shown in Eq. (5.49) with $k_1 = -19.00$, $k_2 = -46.47$ and $k_3 = -3.40$.

The objective is to demonstrate that a badly designed linear controller, exhibiting large error signal as shown in Fig. 5.24 and Fig. 5.25, can still efficiently synchronize two circuits of Chua as shown in Fig. 5.26. Note that the gain and offset distortions for a reference signal completely inside one affine region of Eq. (5.35) is different from the signal distortion observed for a reference signal inside another affine region, as shown in Fig. 5.24 and Fig. 5.25 respectively. This is a result of different sets of eigenvalues for $(A_1 + K)$ and $(A_2 + K)$ in Eq. (5.38) that leads to different temporal behaviors for the state vector $\vec{x}$ in each corresponding region described by Eq. (5.35).

The above results indicate that the synchronization problem is quite similar to the equilibrium point stabilization problem concerning the stability requirements on the gain matrix controller selection, and that the nature of the control objective is indeed crucial in the controller performance evaluation.

5.4.3. *Robust Control and Synchronization via Linear Matrix Inequalities*

The synchronization problem of two Chua's circuits via state feedback can also be addressed using optimization techniques based on the so called linear matrix inequalities (LMIs). The main advantage of this kind of strategy is that the control law can be derived in a systematic way if the system model is available.

As shown in the previous section, the nonlinear Chua's circuit can be modelled as a piecewise linear framework. Roughly the idea is that Chua's

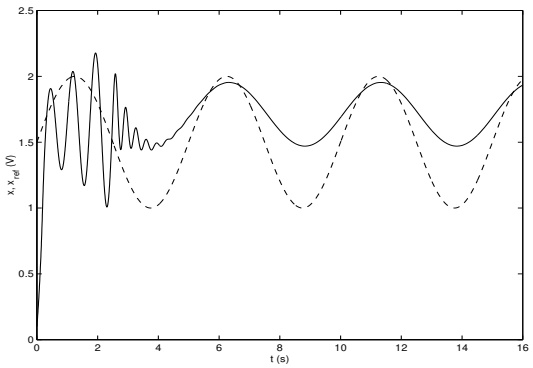

(a)

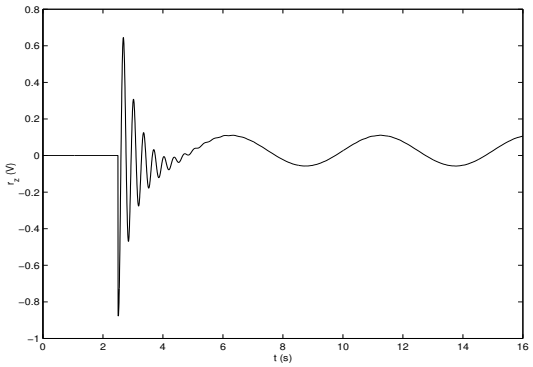

(b)

Fig. 5.24. Chua's circuit linear control using only a voltage source in series with inductor L (see Fig. 5.6. Control activated at $t = 2.5$s. (a) (—) Voltage across capacitor C_1; $(--)$ Reference signal: $x_{\rm ref}(t) = 1.5 + 0.5\sin(0.4\pi t)$, $y_{\rm ref}(t) = 0$, $z_{\rm ref}(t) = 0$. (b) Applied control signal.

circuit can be represented by a set of "local" systems. With such modelling procedure, diffused techniques from the robust $\mathcal{H}_\infty$ control theory can be easily applied to these systems. Section 5.4.3.1 presents the LMI based formulation to obtain the control gain to synchronize a master-slave scheme. To evaluate the synchronization control performance, the information transmission problem is addressed in Sec. 5.4.3.2 using the PCChua (Sec. 5.2.3); i.e. the information signal can be recovered in the slave system using a coherent demodulation technique, if the robust synchronization is established.

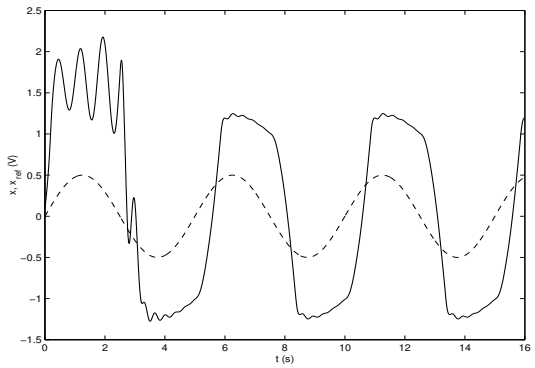

(a)

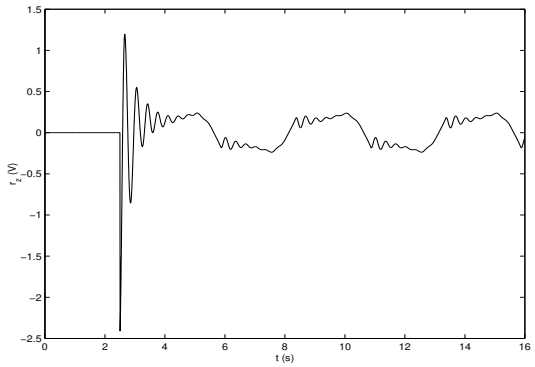

(b)

Fig. 5.25. Chua's circuit linear control using only a voltage source in series with inductor L. Control activated at $t = 2.5$s. (a) (—) Voltage across capacitor C_1; $(--)$ Reference signal: $x_{\mathrm{ref}}(t) = 0.5\sin(0.4\pi t)$, $y_{\mathrm{ref}}(t) = 0$, $z_{\mathrm{ref}}(t) = 0$. (b) Applied control signal.

Notice that other robust $\mathcal{H}_\infty$ synchronization strategies for coupled Chua's circuits based on LMIs have been reported in the recent literature; e.g. a fuzzy control based approach [60] and a time-delay feedback control [67].

5.4.3.1. *Robust $\mathcal{H}_\infty$ Synchronization*

Consider a synchronization scheme of nonlinear discrete time systems with state and output transitions described as:

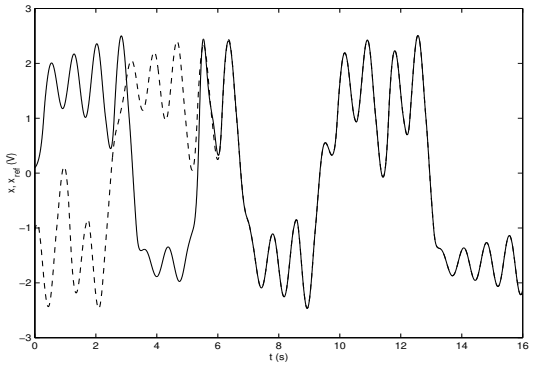

(a)

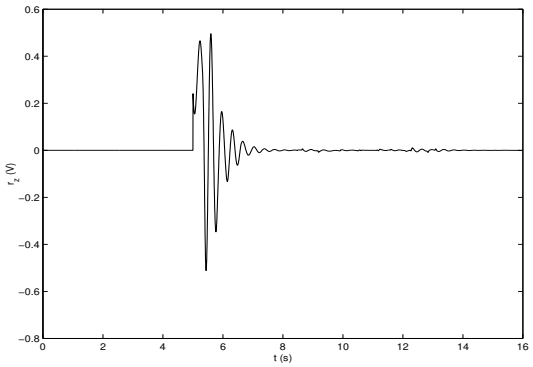

(b)

Fig. 5.26. Chua's circuit synchronization using only a voltage source in series with inductor L. Control activated at $t = 5.0$s. (a) (—) Voltage across capacitor C_1; $(--)$ Genuine chaotic trajectory: $\dot{\vec{x}}_{\rm ref} = A_{x_{\rm ref}}\vec{x}_{\rm ref} + \vec{b}_{x_{\rm ref}}$. (b) Applied control signal.

$$\text{Master} \begin{cases} x^{\rm m}_{k+1} = A(\rho_k)x^{\rm m}_k + B(\rho_k) \\ y^{\rm m}_k = Cx^{\rm m}_k \end{cases} \tag{5.51}$$

$$\text{Slave} \begin{cases} x^{\rm s}_{k+1} = A(\rho_k)x^{\rm s}_k + B(\rho_k) + u_k \\ y^{\rm s}_k = Cx^{\rm s}_k \end{cases} \tag{5.52}$$

where $x^{m,s}_k \in \mathbb{R}^n$ and $x^{m,s}_{k+1} \in \mathbb{R}^n$ denote the state vectors in the discrete

time instants k and $k+1$, respectively[c], $y_k^{m,s} \in \mathbb{R}^m$ denotes the measured output vectors, $u_k \in \mathbb{R}^n$ denotes the synchronization control vector, $A(\rho_k) \in \mathbb{R}^{n\times n}$ represents the dynamic matrix of the system, $B(\rho_k) \in \mathbb{R}^n$ is the affine term, $C \in \mathbb{R}^{m\times n}$ is the output matrix and $\rho_k \in \mathbb{R}^p$ is a parameter vector that depends on time k. The synchronism is achieved when dynamical systems simultaneously describe a common trajectory on the state space.

By defining the synchronization error as the difference between the master and slave states, $\varepsilon_k = x_k^{\mathrm{m}} - x_k^{\mathrm{s}}$, and assuming a control law $u_k = L(\rho_k)(y_k^{\mathrm{m}} - y_k^{\mathrm{s}})$, where $L(\rho_k) \in \mathbb{R}^{n\times m}$ is the matrix of synchronization control gains, the synchronism of the master and slave systems can be investigated by checking the synchronization system error given by:

$$\varepsilon_{k+1} = (A(\rho_k) - L(\rho_k)C)\varepsilon_k \tag{5.53}$$

Global synchronization of the master and slave systems means that, for any initial state x_0^{s} of the slave, and any initial state x_0^{m} of the master, the convergence condition presented below is verified

$$\lim_{k\to\infty} \| \varepsilon_k \| \to 0, \quad \forall \varepsilon_0 \in \mathbb{R}^n \tag{5.54}$$

where $\| \cdot \|$ is the Euclidean norm.

The difficulty to establish the general conditions for the synchronization of global chaotic systems has led many researchers to consider particular classes of nonlinear systems. In the literature, a class of systems commonly investigated is the so-called Lur'e systems. Numerous approaches such as those ones given in [22, 38, 68] deal with the synchronization of this class of systems.

This section focus on the synchronization of a class of Lur'e discrete time systems represented by local descriptions in the state space. The nonlinear systems are then modelled in a piecewise linear framework with the state space partitioned into N regions R_i with $\bigcup_{i=1}^{N} R_i \subseteq \mathbb{R}^n$. At each discrete time instant k, the state vector x_k visits a unique region R_i of the state space associated to a set of constant matrices A_i, B_i e L_i. Notice that such a modelling procedure allows to apply some techniques borrowed from the robust control theory.

Consider a scenario where the master system is disturbed by exogenous signals $w_k \in \mathbb{R}^q$ in their state and measured output:

[c] 'm' and 's' denote the systems *master* and *slave*, respectively.

$$\text{Master} \begin{cases} x_{k+1}^{\mathrm{m}} = A_i x_k^{\mathrm{m}} + B_i + E_i w_k \\ y_k^{\mathrm{m}} = C_i x_k^{\mathrm{m}} + D_i w_k \end{cases} \tag{5.55}$$

where $E_i \in \mathbb{R}^{n\times q}$ and $D_i \in \mathbb{R}^{m\times q}$ are weighting matrices.

In this noisy context the synchronization of the master and slave systems could suffer a performance degradation and, in the worst case, the synchronization could be completely lost. The determination of a control law u_k that guarantees a robust (insensible to the presence of noise) synchronization of the master and slave systems becomes fundamental.

The results stated in the sequel deal with the problem of chaotic system synchronization in a noise environment. The main result is based on the concept of robust $\mathcal{H}_\infty$ stability of the error system Eq. (5.53) rewritten as:

$$\text{Error} \quad \begin{cases} \varepsilon_{k+1} = (A_i - L_i C)\varepsilon_k + (E_i - L_i D_i) w_k \\ z_k = \tilde{C}\varepsilon_k + \tilde{D} w_k \end{cases} \tag{5.56}$$

where $z_k \in \mathbb{R}^r$ denotes a weighing vector of the synchronization error and $\tilde{C} \in \mathbb{R}^{r\times n}$ and $\tilde{D} \in \mathbb{R}^{r\times q}$ are weighting matrices.

The robust $\mathcal{H}_\infty$-norm performance index can be guaranteed to obtain the upper bound γ to the induced ℓ_2 gain defined as:

$$\sup_{\|w\|_2 \neq 0} \frac{\| z \|_2}{\| w \|_2} < \gamma \tag{5.57}$$

where $\| \cdot \|_2$ represents the ℓ_2-norm.

Notice that the induced ℓ_2 gain is the rate between the energy of the weighting synchronization error signal 'z' and the energy of the exogenous disturbing signal 'w'. Therefore the synchronization problem can be formulated as a $\mathcal{H}_\infty$ robust stability problem of the synchronization error system given in Eq. (5.56).

To solve this synchronization problem, namely to determine the synchronization control gain matrices L_i, it is sufficient to find a feasible solution to the following LMI optimization problem:

$$\begin{cases} \min_{\delta,S_i,S_j,F_i,V} \ \delta \\ \\ s.t. \qquad \begin{bmatrix} S_j - V^T - V & VA_i - F_iC_i & VE_i - F_iD_i \\ A_i^TV^T - C_i^TF_i^T & -S_i + \tilde{C}^T\tilde{C} & \tilde{C}^T\tilde{D} \\ E_i^TV^T - D_i^TF_i^T & \tilde{D}^T\tilde{C} & -\delta\mathbf{I} + \tilde{D}^T\tilde{D} \end{bmatrix} \prec 0, \end{cases} \tag{5.58}$$

$\forall (i,j) \in \{1 \cdots N\}$; where the unknowns are the symmetric definite positive matrices $S_i, S_j \in \mathbb{R}^{n\times n}$, $i = 1,\ldots,N$, $j = 1,\ldots,N$, any matrices $V \in \mathbb{R}^{n\times n}$ and $F_i \in \mathbb{R}^{n\times r}$, and the scalar $\gamma \triangleq \sqrt{\delta} > 0$. The synchronization gain is given by $L_i = V^{-1}F_i$. Moreover, the minimum $\mathcal{H}_\infty$ disturbance attenuation level from the input w_k to the weighting synchronization error output 'z_k' corresponds to the optimal solution of the minimization problem, i.e., $\gamma = \sqrt{\delta}$. Proof details for this result can be found in [24].

5.4.3.2. *Experimental Results with Information Transmission*

A practical implementation of the Chua oscillator to achieve the robust $\mathcal{H}_\infty$ synchronization is considered. Further, the information transmission problem is investigated in the light of the information transmission via control principle – ITVC discussed in Sec. 5.4.1.1. The information transmission test is used as a performance index to validate the proposed approach for robust synchronization. All the experiments were performed in the laboratory setup PCCHUA described in Sec. 5.2.3.

Consider the information transmission scheme exhibited in Fig. 5.27. This scheme shows the Chua's oscillator circuits on a unidirectional coupling.

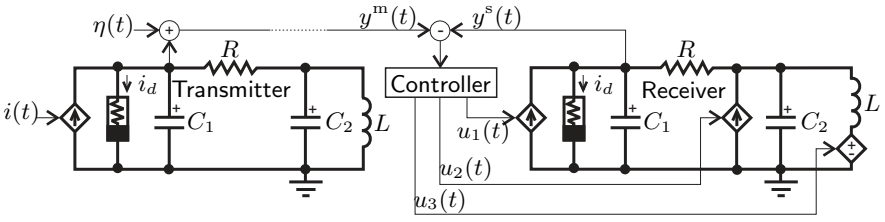

Fig. 5.27. Unidirectional communication system. It is interesting to note that the use of the voltage across C_1, which is the x-variable, has been found to be the best scalar variable trhrough which the dynamics of Chua's circuit can be observed, see Sec. 5.3.1.

The information to be transmitted $i(t)$ is injected on the master Chua's

chaotic oscillator (*transmitter*) as a perturbation only in the direction of $v_{C_1}(t)$. Mathematically this perturbation corresponds to a modification on the differential equations that govern the motion of the oscillator in the direction of $v_{C_1}(t)$. Then a scalar signal $y^{\mathrm{m}}(t)$ is used to carry the information and to serve as a reference signal to allow the synchronization of the slave oscillator (*receiver*). This signal can be corrupted by noise interferences $\eta(t)$ on the transmission channel.

Despite the fact that the information signal must be of very low amplitude in order to keep the master oscillator in the chaotic regime, the oscillator unperturbed dynamical behavior is considerably altered, as can be seen by comparing Fig. 5.9(a), page 108, with Fig. 5.28.

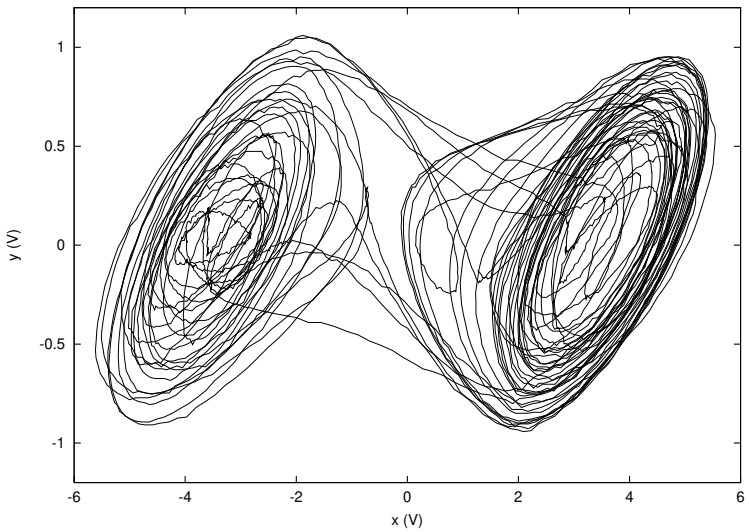

Fig. 5.28. Typical information perturbed double scroll attractor exhibited by the master oscillator – real data. This figure should be compared to Fig. 5.9, page 108. The information signal is injected using a voltage controlled current source in parallel with capacitor C_1, shown in Fig. 5.6, page 105.

The transmitter system can be represented by the set of differential equations

$$\begin{cases} C_1 \frac{dv_{C_1}(t)}{dt} = \frac{v_{C_2}(t)-v_{C_1}(t)}{R} - i_d(v_{C_1}(t)) + i(t) \\ C_2 \frac{dv_{C_2}(t)}{dt} = \frac{v_{C_1}(t)-v_{C_2}(t)}{R} + i_L(t) \\ L \frac{di_L(t)}{dt} \quad = -v_{C_2}(t) - r_L i_L(t) \\ i_d(v_{C_1}) \quad = m_0 v_{C_1} + \frac{(m_1-m_0)(|v_{C_1}+B_p|-|v_{C_1}-B_p|)}{2} \\ y^{\mathrm{m}}(t) \quad = v_{C_1}(t) + \eta(t) \end{cases} \tag{5.59}$$

where C_1, C_2, L, R, rL, m_0, m_1 e B_p are the circuit's parameters; $i(t)$ is the scalar information signal; $y^{\mathrm{m}}(t)$ is the transmitted signal and $\eta(t)$ is the noise signal on transmission channel. By construction, the receiver oscillator is fully controllable by the controller signals $u(t)$.

Analogous to the transmitter the receiver system has its motion governed by the set of differential equations

$$\begin{cases} C_1^* \frac{dv_{C_1^*}(t)}{dt} = \frac{v_{C_2^*}(t)-v_{C_1^*}(t)}{R^*} - i_d(v_{C_1^*}(t)) + u_1(t) \\ C_2^* \frac{dv_{C_2^*}(t)}{dt} = \frac{v_{C_1^*}(t)-v_{C_2^*}(t)}{R^*} + i_L^*(t) + u_2(t) \\ L^* \frac{di_L^*(t)}{dt} \quad = -v_{C_2^*}(t) - r_L^* i_L^*(t) + u_3(t) \\ i_d(v_{C_1^*}) \quad = m_0^* v_{C_1^*} + \frac{(m_1^*-m_0^*)(|v_{C_1^*}+B_p^*|-|v_{C_1^*}-B_p^*|)}{2} \\ y^{\mathrm{s}}(t) \quad = v_{C_1^*}(t) \end{cases} \tag{5.60}$$

where C_1^*, C_2^*, L^*, R^*, rL^*, m_0^*, m_1^* e B_p^* are the receiver circuit's parameters; $u_1(t)$, $u_2(t)$ and $u_3(t)$ are scalar control signals and $y^{\mathrm{s}}(t)$ is the receiver output measured signal.

The ITVC principle (Sec. 5.4.1.1) states that any controller that guarantees an identical, or quasi-identical, master-slave synchronization can actually perform as a demodulator and thus recovering the transmitted information. In this way, the control signal $u_1(t)$ corresponds to the demodulated information signal $i(t)$.

To carry out the proposed approach the parameters of the Chua oscillator (or the communication system) shown in Fig. 5.27 have to be estimated. This was done by using real data acquired from PCChua, together with the Kalman filter like algorithm known as UKF [40], to estimate the parameters shown in Table 5.7.

Further, as the PCChua is implemented in a digital platform and the approach has been proposed in discrete-time setting, the transmitter

Table 5.7. Estimated parameters of the PCChua oscillator circuit

Parameter	Value	Parameter	Value
R	1673Ω	r_L	0Ω
C_1	30.14μF	m_0	-0.365mS
C_2	185.66μF	m_1	-0.801mS
L	52.28H	B_p	1.74V

Eq. (5.59) and receiver Eq. (5.60) were discretized and the resulting communication scheme similar to the one shown in (Fig. 5.27) (now in the discrete domain) is represented as a robust master-slave synchronization scheme. By applying the discretization approach presented in [59], a piecewise linear representation for the transmitter and receiver systems was obtained that describes the motion of Chua oscillator circuits by means of three linear local models:

$$\begin{aligned} \text{Transmitter} &\begin{cases} x^{\mathrm{m}}_{k+1} = A_i x^{\mathrm{m}}_k + B_i + \underbrace{E_i w_k}_{\iota(k)} \\ y^{\mathrm{m}}_k = C_i x^{\mathrm{m}}_k + D_i w_k \end{cases} \\ \text{Receiver} &\begin{cases} x^{\mathrm{s}}_{k+1} = A_i x^{\mathrm{s}}_k + B_i + u_k \\ y^{\mathrm{s}}_k = C_i x^{\mathrm{s}}_k \end{cases} \end{aligned} \tag{5.61}$$

with the following matrices describing the local motion

$$A_1 = \begin{bmatrix} 1 - T/(RC_1) - Tm_0/C_1 & T/(RC_1) & 0 \\ T/(RC_2) & 1 - T/(RC_2) & T/C_2 \\ 0 & -T/L & 1 - Tr_L/L \end{bmatrix}$$

$$A_2 = \begin{bmatrix} 1 - T/(RC_1) - Tm_1/C_1 & T/(RC_1) & 0 \\ T/(RC_2) & 1 - T/(RC_2) & T/C_2 \\ 0 & -T/L & 1 - Tr_L/L \end{bmatrix}$$

$$A_3 = \begin{bmatrix} 1 - T/(RC_1) - Tm_0/C_1 & T/(RC_1) & 0 \\ T/(RC_2) & 1 - T/(RC_2) & T/C_2 \\ 0 & -T/L & 1 - Tr_L/L \end{bmatrix}$$

$$B_1 = \begin{bmatrix} \frac{+TB_p(m_1-m_0)}{C_1} \\ 0 \\ 0 \end{bmatrix},\ B_2 = \begin{bmatrix} 0 \\ 0 \\ 0 \end{bmatrix},\ B_3 = \begin{bmatrix} \frac{-TB_p(m_1-m_0)}{C_1} \\ 0 \\ 0 \end{bmatrix}$$

$$E_i = \begin{bmatrix} 0.001 \\ 0 \\ 0 \end{bmatrix},\ C_i = \begin{bmatrix} 1 \\ 0 \\ 0 \end{bmatrix}^T,\ D_i = 0.0001$$

$$\tilde{C}_i = \begin{bmatrix} 1\ 0\ 0 \\ 0\ 1\ 0 \\ 0\ 0\ 1 \end{bmatrix},\ \tilde{D}_i = \begin{bmatrix} 0 \\ 0 \\ 0 \end{bmatrix}$$

By solving the optimization problem in Eq. (5.58) and considering the discretized master-slave synchronization scheme with the parameters shown in Table 5.7, sampling time $T = 10\,\text{ms}$, and a unique synchronization gain ($L_i = G$, $\forall i \in \{1, 2, 3\}$), the following result can be obtained:

$$G = \begin{bmatrix} 99.45 \times 10^{-3} & 2.93 \times 10^{-3} & 51.50 \times 10^{-9} \end{bmatrix}^T \tag{5.62}$$

that guarantee a level $\gamma = 9.70 \times 10^{-4}$ of disturbance attenuation $\mathcal{H}_\infty$. By doing $L_i = G$ for $i \in \{1, 2, 3\}$ in Eq. (5.58), the implementation of the proposed approach for robust $\mathcal{H}_\infty$ synchronization of the chaotic systems, represented by piecewise linear models, was simplified and the transmission of index model 'i' to the receiver system is no longer necessary.

The weighting matrices E_i and D_i were defined based on the amplitudes of the information signal $i(t)$ and the noise signal $\eta(t)$, respectively. The entry term $\iota(k) = E_i w_k$ assumes an equivalence of the information signal at discrete time instants k, i.e., $\iota(k) \equiv \frac{T}{C_1} i(kT)$. In the context of communication, the performance index $\mathcal{H}_\infty$-norm appears as a criterium that ensures a better information reconstruction. This argument is based on that the robust $\mathcal{H}_\infty$ stabilization of the error system Eq. (5.56) tends to minimize the effect of the exogenous entry 'w_k' over the weighting synchronization error vector 'ε_k' and, consequently, the information signal $i(t)$ has its influence minimized over the transmitted signal $y^{\text{m}}(t)$.

The weighting matrices $\tilde{C}$ and $\tilde{D}$ were conveniently defined in order to establish the directions and intensities of the weighting synchronization

error vector.

Notice that synchronization gain G in Eq. (5.62) must be transformed in order to include the effect of the zero-order hold actuators and to generate compensation signals compatible to the receiver system Eq. (5.60). The synchronization gain considered in the PCChua implementation becomes

$$G^{PCchua} = \begin{bmatrix} 2.99 \times 10^{-3} \\ 0.54 \times 10^{-3} \\ 2.69 \times 10^{-3} \end{bmatrix} \quad \equiv \quad \begin{bmatrix} C_1 G_1/T \\ C_2 G_2/T \\ L G_3/T \end{bmatrix} \tag{5.63}$$

In order to emphasize the effectiveness of the proposed methodology and to validate its implementation two information transmission experiments were performed in the PCChua platform.

In the first experiment, a sinusoidal signal $i(t)$ of amplitude of 0.12 mA and frequency of 0.3 Hz is used as the information signal to be transmitted, as shown in Fig. 5.29. The information signal starts to perturb the natural behavior of the transmitter oscillator at 30 sec and stop at 90 sec.

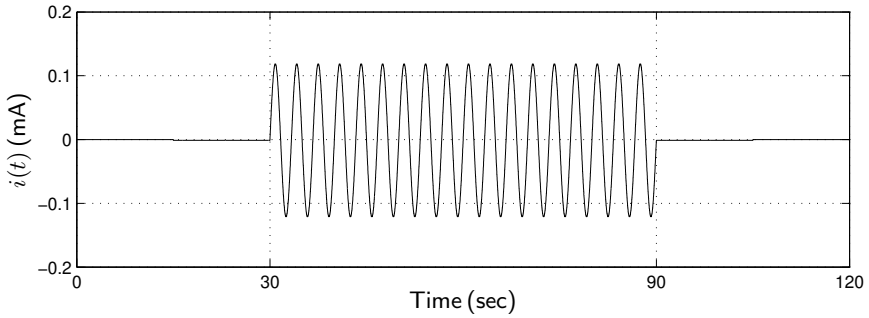

Fig. 5.29. [E1] Information signal: $i(t) = 0.12\sin(2\pi 0.3t)$ mA

Figure 5.30 depicts the signal $y^{\mathrm{m}}(t)$ transmitted by the master oscillator (transmitter) that serves as a reference signal to the synchronization of the slave oscillator (receiver). The transmission occurs in the time interval from 15 sec to 105 sec.

The synchronization error signal $\varepsilon(t)$ corresponding to the difference between the transmitted signal $y^{\mathrm{m}}(t)$ and the measured slave signal $y^{\mathrm{s}}(t)$ is shown in Fig. 5.31. Outside the time span from 15 sec to 105 sec the controller is inactive and the synchronization error signal corresponds to the natural behavior of the free running receiver oscillator.

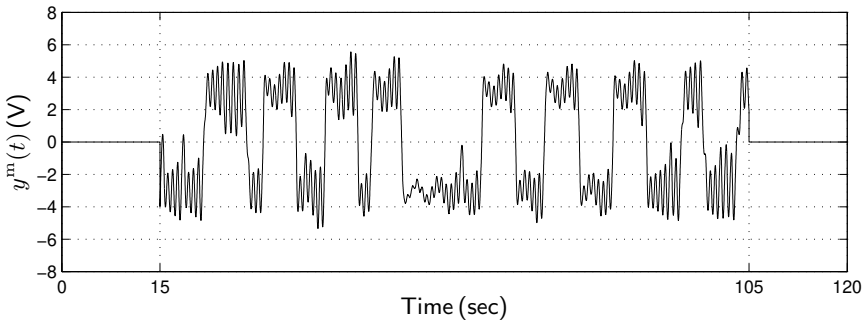

Fig. 5.30. [E1] Transmitted signal

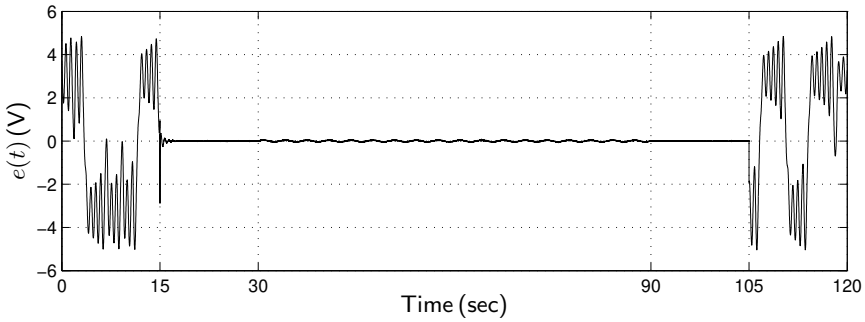

Fig. 5.31. [E1] Error signal: $e(t) = y^{\mathrm{m}}(t) - y^{\mathrm{s}}(t)$ V

Figure 5.32 shows the control action $u_1(t)$ and Fig. 5.33 shows a close comparison between the transmitted information $i(t)$ and the recovered information represented by the control action $u_1(t)$.

In the second experiment an information signal $i(t)$ with a more complex behavior is considered. This information signal is the summation of a sinusoidal signal (0.4 Hz), a square signal (1.0 Hz) and a sawtooth signal (1.5 Hz). All signals have the same amplitude, that is, 0.12 mA.

Figure 5.34 shows the transmitted signal $y^{\mathrm{m}}(t)$. The synchronization error $\varepsilon(t)$ signal and the control signal $u_1(t)$ are depicted in Fig. 5.35 and Fig. 5.36, respectively. In Fig. 5.37, it can be readily noticed that the information from 75 sec to 95 sec is recovered via ITVC principle.

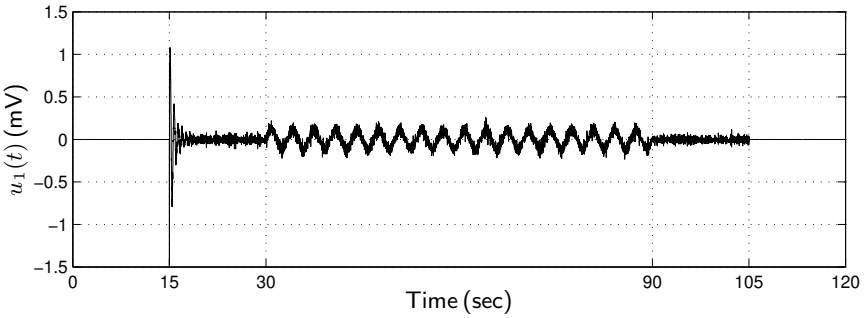

Fig. 5.32. [E1] Control signal: component $u_1(t)$

5.4.4. *Nonlinear State Feedback*

In this section, two different control structures will be used to control and synchronize connected Chua circuits, in order to send information from the master to the slave oscillator, similarly to what was presented in Sec. 5.4.3.2. However, in this section the control action will be restricted to the first equation in Eq. (5.60); i.e. $u_2(t) = u_3(t) = 0$; such that

$$\begin{cases} C_1^* \frac{dv_{C_1^*}(t)}{dt} = \frac{v_{C_2^*}(t) - v_{C_1^*}(t)}{R^*} - i_d(v_{C_1^*}(t)) + u(t) \\ C_2^* \frac{dv_{C_2^*}(t)}{dt} = \frac{v_{C_1^*}(t) - v_{C_2^*}(t)}{R^*} + i_L^*(t) \\ L^* \frac{di_L^*(t)}{dt} = -v_{C_2^*}(t) - r_L^* i_L^*(t) \\ i_d(v_{C_1^*}) = m_0^* v_{C_1^*} + \frac{(m_1^* - m_0^*)(|v_{C_1^*} + B_p^*| - |v_{C_1^*} - B_p^*|)}{2} \\ y^{\mathrm{s}}(t) = v_{C_1^*}(t) \end{cases} \tag{5.64}$$

where C_1^*, C_2^*, L^*, R^*, rL^*, m_0^*, m_1^* e B_p^* are the slave system parameters; $u(t)$ is a scalar control signal, and $y^{\mathrm{s}}(t)$ is the receiver output measured signal. The objective is to synchronize both oscillators; the master Eq. (5.59), page 146, and the slave Eq. (5.64), by means of the scalar control signal $u(t)$ at the receiver, and to recover the original information signal $i(t)$ as a byproduct of the synchronization process.

The design of the following control structures will highlight the tradeoff between control energy, control objective, and controller complexity, as briefly presented in Sec. 5.4.1, and detailed in [12].

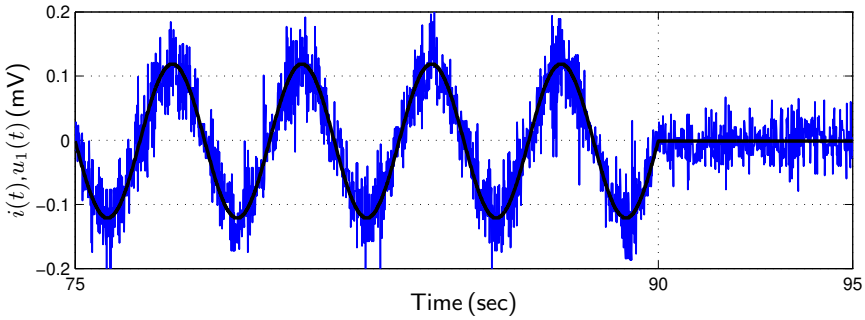

(a) Information signal $i(t)$ - black; Control signal $u_1(t)$ - blue

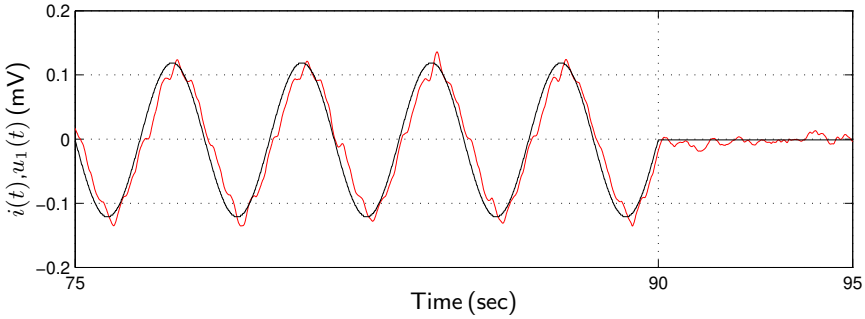

(b) Information signal $i(t)$ - black; Control signal filtered $u_1(t)$ - red

Fig. 5.33. [E1] Recovered information without filtering (a) and with filtering (b) (Butterworth filter: 2th order; $f_c = 2\,\mathrm{Hz}$)

5.4.4.1. *Low Energy Adaptive Proportional Controller*

In this section a nonlinear controller designed with no prior knowledge of the system dynamics is presented. The only consideration is that, from the results obtained in the previous Sec. 5.4.2 and Sec. 5.4.3, it is known that a low energy controller should be implemented (see also Sec. 5.4.1).

The proposed controller structure is quite general, as can be verified by the following set of equations:

$$\begin{aligned} e_{\mathrm{T}}(t) &= y^{\mathrm{s}}(t) - v_{C_1^*}(t), \\ k_{\mathrm{p}}(t) &= k_{\mathrm{p}}^1 + k_{\mathrm{p}}^2 \left(1 - \frac{1}{1 + \delta_{\mathrm{p}} e_{\mathrm{T}}^2(t)}\right), \\ u(t) &= k_{\mathrm{p}}\left(e_{\mathrm{T}}\right) e_{\mathrm{T}}(t), \end{aligned} \tag{5.65}$$

where k_{p}^1, k_{p}^2 and δ_{p} are parameters of this adaptive proportional controller,

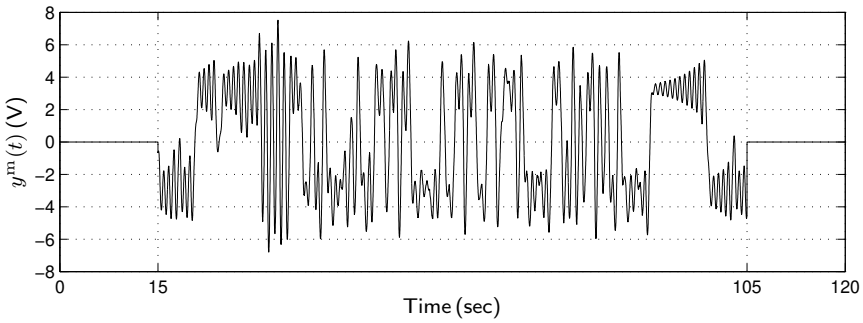

Fig. 5.34. [E2] Transmitted signal

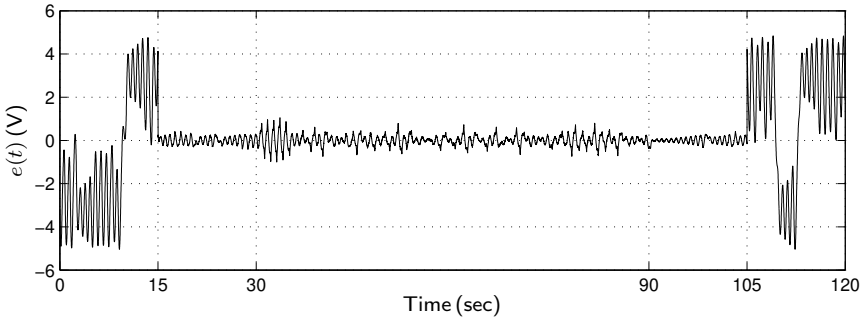

Fig. 5.35. [E2] Error signal: $e(t) = y^{\mathrm{m}}(t) - y^{\mathrm{s}}(t)\,\mathrm{V}$

for which the static characteristic curve is shown in Fig. 5.38.

The rationale for the control law Eq. (5.65) is that, when the circuits are almost synchronized, the slave oscillator is following a trajectory that is very close to its natural behavior, and therefore a minimum control effort is necessary to keep the synchronization condition. At the same time, as discussed in Sec. 5.4.1.1, a low energy controller should be used as demodulator for master-slave connected nonlinear oscillators, and therefore the proportional gain is reduced when $|e_{\mathrm{T}}| \approx 0$ (Fig. 5.38), in order to fulfill this requirement.

It is important to note that in Eq. (5.65) *there are no assumptions about the master oscillator structure* and, at a first sight, it is far from obvious that the control action can actually synchronize both Chua circuits, and at the same time it will be able to approximate the original information signal after the synchronization takes place. This shows again that the knowledge

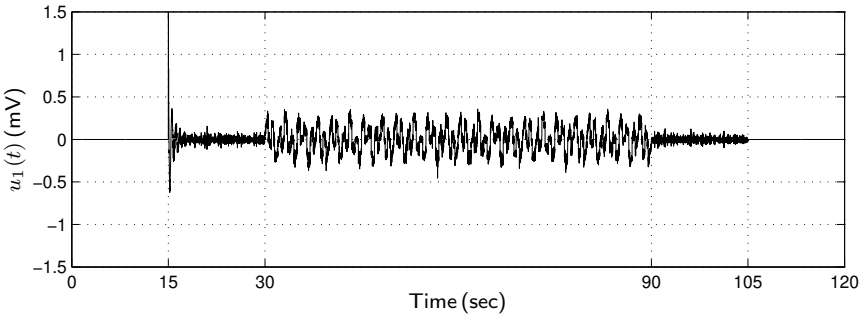

Fig. 5.36. [E2] Control signal: component $u_1(t)$

of the dynamical system model is useful in designing the controllers, but its importance is weighted by the nature of the problem under consideration.

Measured results using control Eq. (5.65) are shown in Fig. 5.39 and Fig. 5.40. In Fig. 5.40 one can see that the *filtered* recovered information signal is worse than those obtained with the $\mathcal{H}_\infty$ state feedback controller (Sec. 5.4.3.2), as it can be seen by comparison with the result shown in Fig. 5.33, page 152.

The slight attenuation of the recovered signal, depicted in Fig. 5.40(b), is mainly related to the strong nonlinear character of Eq. (5.65). Such attenuation becomes more evident during the peaks of the recovered signal. The same phenomenon does not occur with information signals that have smaller amplitudes. In addition, it is worth noting that the delay time between the original and the recovered information signal observed in Fig. 5.40(b), is due to the phase lag introduced by the low-pass Butterworth filter.

5.4.4.2. *High Energy Sliding Mode Controller*

Following the approach of minimal controller complexity of the previous section; i.e. designing a nonlinear controller for Chua's circuit without relying on accurate knowledge of system model; a simple sliding mode controller will be proposed that is capable of synchronizing two Chua circuits to an arbitrary precision.

Consider the following set of equations representing a sliding mode con-

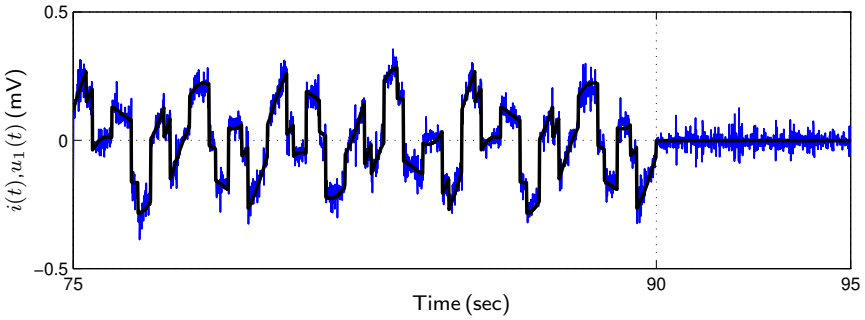

(a) Information signal $i(t)$ - black; Control signal $u_1(t)$ - blue

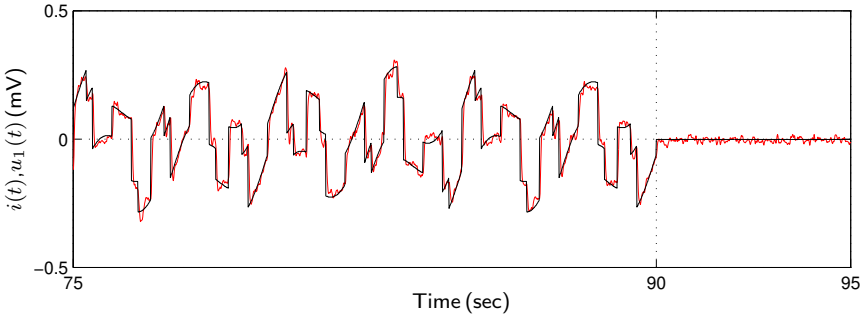

(b) Information signal $i(t)$ - black; Control signal filtered $u_1(t)$ - red

Fig. 5.37. [E2] Recovered information without filtering (a) and with filtering (b) (Butterworth filter: 2nd order; $f_c = 10\,\mathrm{Hz}$)

troller applied to the slave oscillator Eq. (5.64):

$$e_{\mathrm{T}}(t) = y^{\mathrm{s}}(t) - v_{C_1^*}(t),$$
$$u(t) = \begin{cases} \mathrm{u_{max}},\ e_{\mathrm{T}}(t) > \delta_{\mathrm{s}}; \\ \mathrm{u_{min}},\ e_{\mathrm{T}}(t) < -\delta_{\mathrm{s}}; \end{cases} \tag{5.66}$$

where $\mathrm{u_{max}} = -\mathrm{u_{min}} = 0.5\mathrm{mA}$ and $\delta_{\mathrm{s}} > 0$. Moreover, the control action is switched according to the hysteresis behavior depicted in Fig. 5.41.

In this case, by choosing appropriately the value of δ_{s} in Eq. (5.66), it is possible synchronize both Chua circuits with arbitrarily small synchronization error. The case $\delta_{\mathrm{s}} = 0.4$, simulated using normalized equations (Sec. 5.2.1, Eq. (5.4), page 100, is shown in Fig. 5.42.

What is relevant in this example is the fact that it is possible to have both oscillators in a quasi-identical synchronization condition and the control action will still be composed only by positive and negative

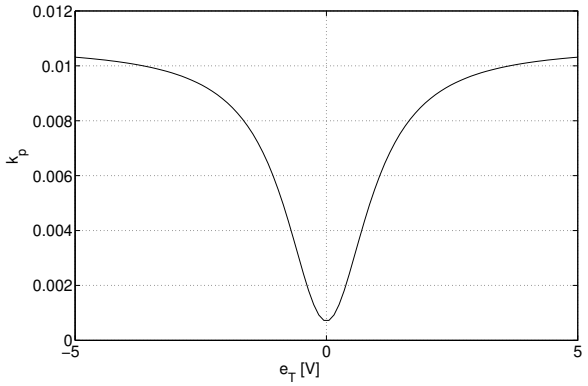

Fig. 5.38. Adaptive proportional controller characteristic curve for $k_{\mathrm{p}}^1 = 0.0007$, $k_{\mathrm{p}}^2 = 0.01$, $\delta_{\mathrm{p}} = 1.0$.

saturation levels $\mathrm{u_{max}}$ and $\mathrm{u_{min}}$, no matter the waveform of the information/perturbation signal injected at the transmitter. And this is true even in the case when the strong assumptions of identical vector fields and absence of noise in the transmission channel are considered to be valid.

Therefore, despite the fact that the circuit can be made to follow arbitrary reference signals; which includes the synchronization of Chua circuits in master-slave configuration as a special case; the ITVC principle cannot be realized due to the high energy nature of the sliding mode controller.

5.5. Conclusions

This chapter has focused on chaos control for Chua circuits. In order to properly address this involved theme, an account of various published works on Chua's circuit implementation, data analysis, mathematical modeling, dynamical characterization, control and synchronization was presented.

Chua's circuit is undoubtedly a paradigmatic nonlinear oscillator that is capable of exhibiting many interesting dynamical behaviors. In addition, it remains as one of the most robust and easily built chaotic circuits, specially when realized by using simulated inductors (Sec. 5.2.2). With this peculiar construction, one is able to obtain Chua circuits that exhibit very slow oscillations appropriate to digital analysis and control [71].

This path has been followed in the implementation of the so-called PCChua experimental setup (Sec. 5.2.3), which comprises a complete computer based system flexible enough to investigate chaos control through the

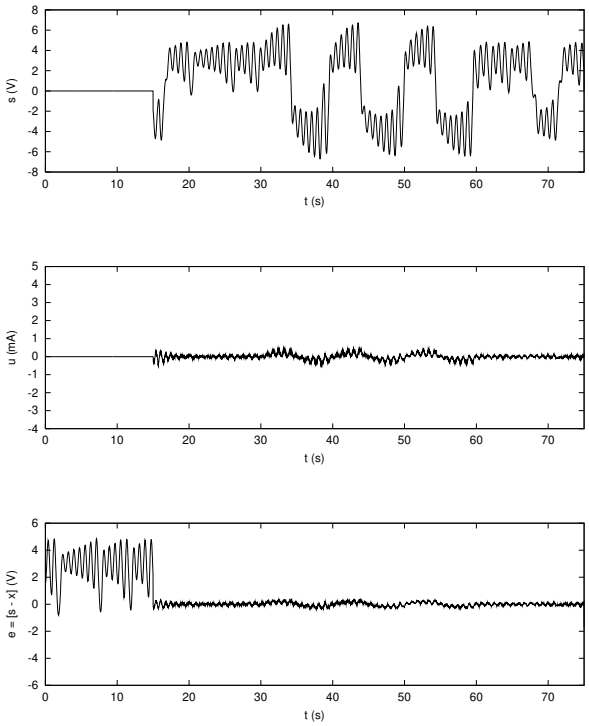

Fig. 5.39. Synchronization between the perturbed master oscillator and the slave oscillator. Control law as in Eq. (5.65) with $k_{\mathrm{p}}^{\mathrm{min}} = 0.0007$, $k_{\mathrm{p}}^{\mathrm{max}} = 0.01$, $\delta_{\mathrm{p}} = 1.0$. (a) Transmitted signal $s(t)$. Information signal perturbation starts at $t = 30$s. (b) Control action at the receiver. Controller activated at $t = 15$s. (c) Synchronization error $[s(t) - y_1(t)]$.

realization of any control method that can be represented mathematically by Eq. (5.6), page 104. As a consequence of this flexibility, the PCChua can also be used to simulate parametric variations in Chua's circuit, so that the system bifurcation diagram can be easily obtained from real data, as shown in [73].

One of the most interesting Chua's circuit dynamical behaviors – the chaotic regime – which is usually represented by the so-called double scroll attractor; was thoroughly investigated in Sec. 5.3 through different attempts of data analysis and mathematical modeling. As a byproduct of such effort, many dynamical properties associated to the circuit of Chua, and also topological characteristics of the double scroll attractor, were revealed such as observability indices, symmetry, higher-order spectral coher-

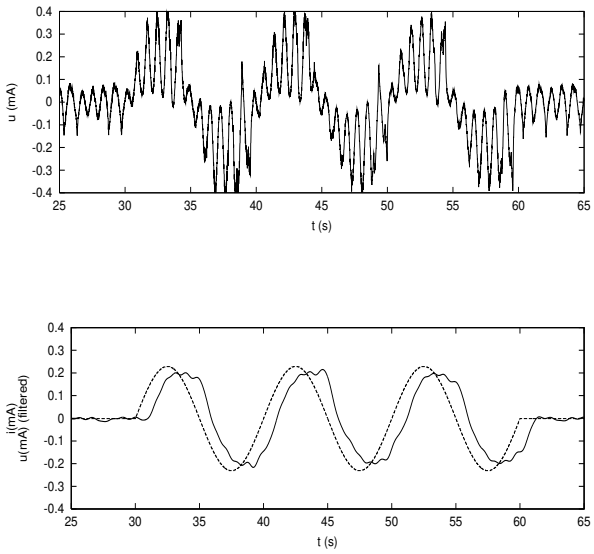

Fig. 5.40. Recovered information signal. Control law as in Eq. (5.65) with $k_{\mathrm{p}}^{\min} = 0.0007$, $k_{\mathrm{p}}^{\max} = 0.01$, $\delta_{\mathrm{p}} = 1.0$. (a) Control signal at the receiver. (b) $(-)$ Control signal after applying an order 4 Butterworth low-pass filter ($f_{\mathrm{c}} = 0.5$Hz); $(\cdots)$ Original information signal: $i(t) = [0.23\sin(2\pi(0.1)t)]$mA.

ence, etc.

Concerning the problem of controlling Chua's circuit, in Sec. 5.4 a broad discussion took place in order to show how intertwined are the control of nonlinear dynamical systems with specific properties of control methods such as control energy, control objective and control law complexity (Sec. 5.4.1). One of the key results of such endeavor is the principle called Information Transmission Via Control – ITVC (Sec. 5.4.1.1), that was extensively used on various control and synchronization strategies discussed in this chapter.

Linear and nonlinear state feedback based control techniques, together with robust control and synchronization design methods, were applied to the master-slave configuration of two unidirectionally connected Chua circuits (Sec. 5.4.2, Sec. 5.4.3 and Sec. 5.4.4). These examples were aimed to highlight that in the synchronization of chaotic oscillators; usually viewed as a trajectory tracking control problem; one should consider the interesting fact that to follow a chaotic reference, that is similar to the signal produced by the uncontrolled nonlinear system, is easier to accomplish than following

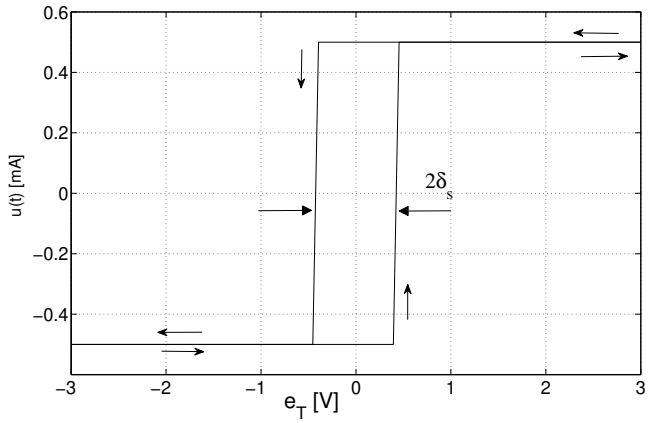

Fig. 5.41. Switching law Eq. (5.66).

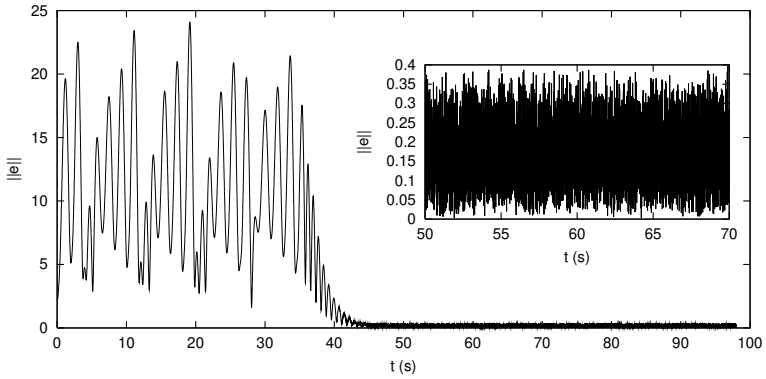

Fig. 5.42. Synchronization error norm for the oscillators coupled via switching control law Eq. (5.66). Control activated at $t = 35$s.

a simple, but unnatural, sinusoidal signal.

It is hoped that this chapter can serve as a starting point for investigating Chua's circuit dynamical characterization, data analysis, mathematical modeling, control and synchronization. The long list of cited references reflects the authors desire to provide an adequate introduction to these subjects.

Acknowledgments

The authors are grateful to financial support from Brazilian governmental research-funding agencies *Conselho Nacional de Desenvolvimento Cientfico e Tecnológico* – CNPq and Fundação de Amparo à Pesquisa do Estado de Minas Gerais – FAPEMIG.

References

[1] L.A. Aguirre, J. Maquet, and C. Letellier, Induced one-parameter bifurcations in identified nonlinear dynamical models, *Int. J. Bifurcation and Chaos* **12**, 1, pp. 135-145, (2002).
[2] L.A. Aguirre, A nonlinear correlation function for selecting the delay time in dynamical reconstructions, *Phys. Lett.* **203A**, 2,3, pp. 88-94, (1995).
[3] L.A. Aguirre, Recovering map static nonlinearities from chaotic data using dynamical models, *Physical D* **100**, 1,2, pp. 41-57, (1997).
[4] L.A. Aguirre, S.B. Bastos, M.A. Alves, and Letellier C, Observability of nonlinear dynamics: normalized indices and a time series approach, *Submitted*, (2008).
[5] L.A. Aguirre and S.A. Billings, Retrieving dynamical invariants from chaotic data using NARMAX models, *Int. J. Bifurcation and Chaos* **5**, 2, pp. 449-474, (1995).
[6] L.A. Aguirre, U.S. Freitas, C. Letellier, and J. Maquet, Structure-selection techniques applied to continuous-time nonlinear models, *Physical D* **158**, 1-4, pp. 1-18, (2001).
[7] L.A. Aguirre, E.C. Furtado, and L.A.B. Tôrres, Evaluation of dynamical models: Dissipative synchronization and other techniques, *Phys. Rev. E* **74**, 6, (2006).
[8] L.A. Aguirre and C.R.F. Jácome, Cluster analysis of NARMAX models for signal-dependent systems, *IEE Proc. Control Theory Appl.* **4**, 145, pp. 409-414, (1998).
[9] L.A. Aguirre, C.G. Rodrigues, and E.M.A.M. Mendes, Nonlinear identification and cluster analysis of chaotic attractors from a real implementation of Chua's circuit, *Int. J. Bifurcation and Chaos* **6**, 7, pp. 1411-1423, (1997).
[10] L.A. Aguirre, B.O.S. Teixeira, and L.A.B. Tôrres, Using data-driven discrete-time models and the unscented Kalman filter to estimate unobserved variables of nonlinear systems, *Phys. Rev. E* **72**, 026226, pp. 1-12, (2005).
[11] L.A. Aguirre and L.A.B. Tôrres, Fixed point stability analysis of Chua's circuit: A case study with a real circuit, *International Journal of Circuits, Systems and Computers* **7**, 2, pp. 111-115, (1997).
[12] L.A. Aguirre and L.A.B. Tôrres, Control of nonlinear dynamics: Where do models fit in?, *Int. J. Bifurcation and Chaos* **10**, 3, pp. 667-681, (2000).
[13] B.R. Andrievskii and A.L. Fradkov, Control of chaos: Methods and appli-

cations. I. Methods, *Automation and Remote Control* **64**, 5, pp. 673-713, (2003).

[14] A. Antoniou, Realisation of gyrators using OpAmps and their use in RC-active network synthesis, *Proceedings IEE* **116**, 11, pp. 1838-1850, (1969).

[15] M.S. Baptista and I.L. Caldas, Phase-locking and bifurcations of the sinusoidally-driven double scroll circuit, *Nonlinear Dynamics* **17**, 2, pp. 119-139, (1998).

[16] S.A. Billings and S. Chen, Extended model set, global data and threshold model identification of severaly nonlinear systems, *International Journal of Control* **50**, 5, pp. 1897-1923, (1989).

[17] S.A. Billings, S. Chen, and M.J. Korenberg, Identification of mimo nonlinear systems using a forward-regression orthogonal estimator, *International Journal of Control* **49**, 6, pp. 2157-2189, (1989).

[18] S.A. Billings and Q.M. Zhu, Rational model identification using an extended least-squares algorithm, *International Journal of Control* **54**, 3, pp. 529-546, (1991).

[19] E. Bilotta, P. Pantano, and F. Stranges, A gallery of Chua attractors. Part I, *Int. J. Bifurcation and Chaos* **17**, 1, pp. 1-60, (2007).

[20] S. Bocaletti, C. Grebogi, Y.C. Lai, H. Mancini, and D. Maza, The control of chaos: theory and applications, *Physics Reports* **329**, 3, pp. 103-197, (2000).

[21] S. Bocaletti, J. Kurths, G. Osipov, D.L. Valadares, and C.S. Zhou, The synchronization of chaotic systems, *Physics Reports* **366**, pp. 1-101, (2002).

[22] S. Bowong, F.M.M. Kakmeni, and R. Koina, A new synchronization principle for a class of Lur'e systems with applications in secure communication, *Int. J. Bifurcation and Chaos* **14**, 7, pp. 2477-2491, (2004).

[23] O. Calvo and J.H.E. Cartwright, Fuzzy Control of Chaos, *Int. J. Bifurcation and Chaos* **8**, 8, pp. 1743-1747, (1998).

[24] C.D. Campos, R.M. Palhares, E.M.A.M. Mendes, L.A.B. Tôrres, and L.A. Mozelli, Experimental Results on Chua's Circuit Robust Synchronization via LMIs, *Int. J. Bifurcation and Chaos* **17**, 9, pp. 3199-3209, (2007).

[25] M. Casdagli, S. Eubank, J.D. Farmer, and J. Gibson, State space reconstruction in the presence of noise , *Physical D* **51**, pp. 52-98, (1991).

[26] U. Çam and R. Kiliç, Inductorless realization of nonautonomous MLC chaotic circuit using current-feedback operational amplifiers, *Journal of Circuits, Systems and Computers* **14**, 1, pp. 99-107, (2005).

[27] C.-T. Chen, *Linear System Theory and Design,* 3rd edn. (Oxford Univ. Press, 1998).

[28] L.O. Chua, Chua Circuit: An Overview 10 years later, *Journal of Circuits, Systems and Computers* **4**, 2, pp. 117-159, (1994).

[29] M.V. Corrêa, E.M.A.M. Mendes, and L.A. Aguirre, Modeling chaotic dynamics with discrete nonlinear rational models, *Int. J. Bifurcation and Chaos* **10**, 5, pp. 1019-1032, (2000).

[30] W.L. Ditto and K. Showalter, Focus Issue: Control and synchronization of chaos, *Chaos* **7**, 4, Guest Editors, (1997).

[31] S.T. Dziuban, J.G. Ecker, and M. Kupferschmid, Using deep cuts in an ellipsoid algorithm for nonlinear programming, *Mathematical Programming*

Study **25**, pp. 93-107, (1985)

[32] J.P. Eckmann and D. Ruelle, Ergodic-Theory of Chaos and Strange Attractors, *Reviews of Modern Physics* **57**, 3, pp. 61-656, (1985).

[33] S. Elgar, B. Vanhoff, L.A. Aguirre, U.S. Freitas, and V. Chandran, Higher-Order Spectra of Nonlinear Polynomial Models for Chua's Circuit, *Int. J. Bifurcation and Chaos* **12**, 8, pp. 2425-2431, (1998).

[34] Z. Galias, New Method for Stabilization of Unstable Periodic Orbits in Chaotic Systems, *Int. J. Bifurcation and Chaos* **5**, 1, pp. 281-295, (1995).

[35] G. Ghandi, An improved Chua's circuit and its use in hyperchaotic circuit, *Analog Integrated Circ. and Signal Processing* **46**, 2, pp. 173-178, (2006).

[36] G. Gouesbet and C. Letellier, Global vector field reconstruction by using a multivariate polynomial L_2 approximation on nets, *Phys. Rev. E* **49**, 6, pp. 4955-4972, (1994).

[37] P. Grassberger and I. Procaccia, Measuring the Strangeness of Strange Attractors, *Physica D* **9**, 1-2, pp. 189-208, (1983).

[38] H. Huang, H.X. Li, and J. Zhong, Master-slave synchronization of general Lur'e systems with time-varying delay and parameter uncertainty, *Int. J. Bifurcation and Chaos* **16**, 2, pp. 281-294, (2006).

[39] M.-J. Jang, C.-L. Chen, and C.-K. Chen, Sliding mode control of chaos in the cubic Chua's circuit system, *Int. J. Bifurcation and Chaos* **12**, 6, pp. 1437-1449, (2002).

[40] S.J. Julier and J.K. Uhlmann, Unscented filtering and nonlinear estimation, *Proceedings of the IEEE* **92**, 3, pp. 401-422, (2004).

[41] M.P. Kennedy, Robust OP Amp realization of Chua's circuit, *Frequenz* **46**, 3-4, pp. 66-80, (1992).

[42] M.P. Kennedy and M.J. Ogorzalek, Special issue on chaos synchronization and control: Theory and applications, *IEEE Transactions on Circuits and Systems Part I* **44**, 10, Guest Editors, (1997).

[43] H.K. Khalil, *Nonlinear Systems.* (Prentice Hall, 2002).

[44] A.I. Khibnik, D. Roose, and L.O. Chua, On periodic orbits and homoclinic bifurcations in Chua's circuit with a smooth nonlinearity, *Int. J. Bifurcation and Chaos* **3**, 2, pp. 363-384, (1993).

[45] R. Kiliç, A comparative study on realization of Chua's circuit: hybrid realizations of Chua's circuit combining the circuit topologies proposed for Chua's diode and inductor elements, *Int. J. Bifurcation and Chaos* **13**, 6, pp. 1475-1493, (2003).

[46] R. Kiliç, On current feedback operational amplifier-based realizations of Chua's circuit, *Circuits Systems and Signal Processing* **22**, 5, pp. 475-491, (2003).

[47] R. Kiliç, O.G. Saracoglu, and F. Yildirim, A new nonautonomous version of Chua's circuit: Experimental observations, *J. of the Franklin Institute – Engineering and Applied Mathematics* **343**, 2, pp. 191-203, (2006).

[48] M.J. Korenberg, S.A. Billings, Y. Liu, and P.J. McIlroy, Orthogonal parameter estimation algorithm for nonlinear stochastic systems, *International Journal of Control* **48**, 1, pp. 193-210, (1989).

[49] I.J. Leontaritis and S.A. Billings, Input-output parametric models for non-

linear systems part II: stochastic nonlinear systems, *International Journal of Control* **41**, 2, pp. 329-344, (1985).

[50] C. Letellier and L.A. Aguirre, Investigating nonlinear dynamics from time series: the influence of symmetries and the choice of observables, *Chaos* **12**, 3, pp. 549-558, (2002).

[51] C. Letellier, L.A. Aguirre, and J. Maquet, Relation between observability and differential embeddings for nonlinear dynamics, *Phys. Rev. E* **71**, 066213, pp. 1-8, (2005).

[52] C. Letellier and R. Gilmore, Covering dynamical systems: Two-fold covers , *Phys. Rev. E* (**in press**), (2000).

[53] C. Letellier and G. Gouesbet, Topological characterization of reconstructed attractors modding out symmetries, *Journal de Physique II* **6**, pp. 1615-1638, (1996).

[54] C. Letellier, G. Gouesbet and N. Rulkov, Topological analysis of chaos in equivariant electronic circuits, *Int. J. Bifurcation and Chaos* **6**, 12, pp. 2531-2555, (1996).

[55] T.-L. Liao and F.-W. Chen, Control of Chua's circuit with a cubic nonlinearity via nonlinear linearization technique, *Circuits, Systems and Signal Processing* **17**, 6, pp. 719-731, (1998).

[56] E. Lorenz, Deterministic Nonperiodic Flows, *Journal of Atmospheric Sciences* **20**, pp. 131-140, (1963).

[57] R.A. Madan, Special issue on Chua's circuit: a paradigm for chaos, *Journal of Circuits, Systems and Computers* **3**, 1, (1993)

[58] T. Matsumoto, A chaotic attractor from Chua's circuit, *IEEE Transactions on Circuits and Systems Part I* **33**, 12, pp. 1055-1058, (1984).

[59] E.M.A.M. Mendes and S.A. Billings, A note on discretization of nonlinear differential equations, *Chaos* **12**, 1, pp. 66-71, (2002).

[60] L.A. Mozelli, C.D. Campos, R.M. Palhares, L.A.B. Tôrres, and E.M.A.M. Mendes, Chaotic synchronization and information transmission experiments: A fuzzy relaxed $\mathcal{H}_\infty$ control approach, *Circuits, Systems and Signal Processing* **26**, 4, pp. 427-449, (2007).

[61] E. Ott, C. Grebogi, and J.A. Yorke, Controlling Chaos, *Physical Review Letters* **64**, 11, pp. 1196-1199, (1990).

[62] A.G. Radwan, A.L. Soliman, and A.M. El-Sedeek, An inductorless CMOS realization of Chua's circuit, *Chaos, Solitons and Fractals* **18**, pp. 149-158, (2003).

[63] D. Ruelle and F. Takens, Nature of Turbulence, *Communications in Mathematical Physics* **23**, 4, (1971).

[64] S. Sastry, *Nonlinear Systems: analysis, stability and control.* (Springer-Verlag New York, Inc., 1999).

[65] A.S. Sedra and K.C. Smith, *Microelectronic Circuits.* (Oxford University Press, USA, 2003).

[66] J.-J. Slotine and W. Li, *Applied Nonlinear Control.* (Prentice Hall, 1990).

[67] F.O. Souza, R.M. Palhares, E.M.A.M. Mendes, and L.A.B. Tôrres, Robust $\mathcal{H}_\infty$ control for master-slave synchronization of Lur'e systems with time-delay feedback control, *Int. J. Bifurcation and Chaos* **To appear**, (2008).

[68] J.A.K. Suykens, P.F. Curran, and L.O. Chua, Robust synthesis for master-slave synchronization of Lur'e systems, *IEEE Transactions on Circuits and Systems Part I* **46**, 7, pp. 841-850, (1999).
[69] L.A.B. Tôrres, Discrete-time dynamic systems synchronization: Information transmission and model matching, *Physica D* **228**, 1, pp. 31-39, (2007).
[70] L.A.B. Tôrres and L.A. Aguirre, An extended chaos control method applied to the Chua's circuit, *Electronics Letters* **35**, 10, pp. 768-770, (1999).
[71] L.A.B. Tôrres and L.A. Aguirre, Inductorless Chua's circuit, *Electronics Letters* **36**, 23, pp. 1915-1916, (2000).
[72] L.A.B. Tôrres and L.A. Aguirre, Transmitting information by controlling nonlinear oscillators, *Physica D* **196**, 3-4, pp. 387-406, (2004).
[73] L.A.B. Tôrres and L.A. Aguirre, PCCHUA – A laboratory setup for relatime control and synchronization of chaotic oscillations, *Int. J. Bifurcation and Chaos* **15**, 8, pp. 2349-2360, (2005).
[74] T. Wu and M.-S. Chen, Chaos control of modified Chua's System, *Physica D* **164**, pp. 53-58, (2002).
[75] Q.M. Zhu and S.A. Billings, Recursive parameter estimation for nonlinear rational models, *J. Syst. Eng.* **1**, pp. 63-76, (1991).
[76] Q.M. Zhu and S.A. Billings, Fast ortogonal identification of nonlinear stochastic models and radial basis functions, *International Journal of Control* **64**, 5, pp. 871-886, (1996).

Chapter 6

CHAOS CONTROL FOR A PWM H-BRIDGE INVERTER

B. Robert[*], M. Feki[*] and H.H.C. Iu[**]

[*]*Department of Electronics, Electrotechnics and Automatic,*
University of Reims-Champagne-Ardenne, France.
E-mail: {bruno.robert, moez.feki}@univ-reims.fr
[**]*School of Electrical, Electronic and Computer Engineering,*
The University of Western Australia, Perth, Australia.
E-mail: herbert@ee.uwa.edu.au

Pulse width modulation (PWM) current-mode single phase inverters are known to exhibit bifurcations and chaos when parameters vary or if the gain of the proportional controller is arbitrarily increased. Our aim in this chapter is to show, using control theory and numerical simulations, how to apply a method to stabilize the desired periodic orbit for larger values of the proportional gain. To accomplish this aim, a time-delayed feedback controller (TDFC) is used in conjunction with the proportional controller in its simple form as well as in its extended form (ETDFC). The main advantages of those methods are the robustness and ease of construction because they do not require the knowledge of an accurate model but only the period of the target unstable periodic orbit (UPO). Moreover, to improve the dynamical performances, an optimal criterion and an adaptive law are defined to determine the control parameters.

6.1. Introduction

Power electronics is a discipline that has emerged from the need to convert electrical energy. Its field of application is wide and concerns industrial, commercial, residential and also aerospace environments. Power converters are basic switching circuits that are modeled by a number of linear differential equations corresponding to different topologies. The toggling between different topologies can either be done

naturally due to switching characteristics or done under the force of a feedback control system. Due to the existence of various operating modes and control saturations, the overall operation is compared to a piecewise smooth nonlinear dynamical system. Early studies by Hamill and coworkers [6, 11] have shown that switching power converters can exhibit several nonlinear phenomena. These include subharmonic oscillations, quasi-periodic operations, bifurcations and chaos.

Chaos in power electronics have been observed by many researchers [8, 11, 19]. In fact, engineers have frequently encountered chaos in power electronics systems, but more often than not this phenomenon was considered as strange and undesirable, hence engineers usually attempted to avoid chaos. During the last two decades, tools of analyzing bifurcations and chaos have been well developed. Therefore, the investigation of nonlinear dynamics in power electronics has become popular.

Actually, much work has focused on bifurcation and chaos due to parameter variations [1, 4, 7]. Recently it has been shown by [19] that control parameters themselves may lead to bifurcation and chaos if they are not properly selected.

Since the seminal paper [15] (OGY), control of chaos has been the focus of a growing literature. Knowing that a chaotic attractor contains infinitely many UPO, the OGY methods take advantage of the great sensitivity of chaotic orbits to stabilize a UPO by appropriately perturbing an accessible parameter [9, 10]. These methods suffer from lack of robustness to imprecise measurements and to uncontrolled parameter variations.

To overcome this deficiency, the TDFC has been proposed as an alternative method [16, 17]. TDFC is known for its robustness and simplicity of construction. Besides, the system model need not be known but only the length τ of the UPO to be stabilized is essential. The control signal is proportional to the difference between the current state and the τ -delayed state. Once the desired UPO is stabilized the control signal vanishes. This method has been successfully applied to the control of duffing equations [2], discrete chaotic systems [14] and to the control of power converters [3, 12, 20].

In this chapter we propose to control a PWM current-mode H-bridge inverter using TDFC [13] and ETDFC methods in conjunction with the proportional controller. A discrete model describing the behavior of the converter is developed and digital controllers are designed. Using the Jury criteria a stability zone in the parameter space is defined. In this study we show the effect of the TDFC and ETDFC on the bifurcation diagrams and we present two-dimensional bifurcation diagrams.

Our work will be outlined as follows. In section 6.2 we present the discrete model of an H-bridge converter circuit. Section 6.3 gives an overview on the effect of the variation of the proportional gain and boosting of the chaotic behavior. Sections 6.4 and 6.5 will be devoted to the presentation of the TDFC and ETDFC controllers and their results, respectively. In section 6.4 we show a two-degree of freedom design procedure and the resulting two-dimensional bifurcation diagram. The ETDFC controller presented in section 6.5 leads to a three-degrees of freedom design and improves the results obtained in the preceding sections. Section 6.6 includes results on sinusoidal output tracking. Finally, our conclusions and remarks are stated in section 6.7.

6.2. H-Bridge Model

In order to increase dynamical performances, a growing number of applications in the field of electrical engineering require that they be fed by a precise current generator. However, all industrial power sources are voltage generators. It therefore follows that converters are necessary to adapt voltage sources to loads. Indeed, owing to the presence of many windings in electrical machines, most of them are naturally inductive and are deemed to be current sources. A convenient way to adapt sources is to add a current control to a voltage converter. In this section, we describe the converter structure and its running mode before setting up its sampled data model.

With the goal to increase the efficiency of the power stages, static converters operate by switching the load between several voltage sources. There is a wide range of conversion structures, more or less complex, whose choice depends on many parameters. By controlling the switching pattern over the operating period, it is possible to vary the

average output voltage. This technique, called Pulse Width Modulation (PWM), is very widespread.

A well-known structure, used in most variable speed drives, is the H-Bridge. Fig. 6.1 illustrates the circuit of this voltage inverter i.e. a DC/AC converter. A switch is realized in this bridge by combining a bipolar transistor and an anti-parallel diode. The inverter is fed by a voltage source E and it supplies a resistive and inductive load (L, R). The output current is controlled by a current loop. The four equivalent switches, named S1, S2, S3 and S4, are shared among two pairs (S1, S2) and (S3, S4). Pairs are controlled by the PWM modulator in a complementary way. States of the switches define two distinct topologies of the inverter, T1 (S1, S2 on and S3, S4 off) and T2 (S1, S2 off and S3, S4 on), and yield to two opposite voltages across the load. For example, topology T1 implies that the voltage across the load $v = E$.

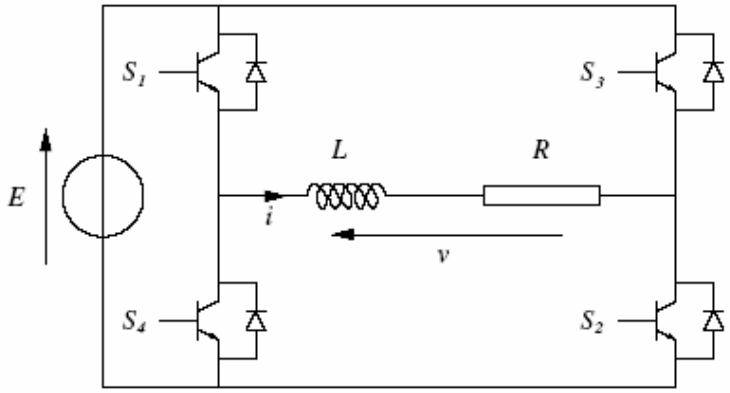

Fig. 6.1. H-bridge.

The PWM modulator defines the switching period T. It generates a high state ($C = 1$), centered in the period, whose duration is defined by the current controller acting on the duty ratio d. dn denotes the duty cycle on the nth functioning period. The low state ($C = 0$) is split into two parts at the beginning and the end of the period. So the normal running mode of the converter involves a sequence of three topologies: T2 −T1 −T2. Then the voltage v evolves as depicted in Fig. 6.2 and $v = -(-1)^C E$. This

pattern avoids switchings and interferences at the sampling times because the digital controller samples current at the beginning of the switching period. At that point the sampling frequency is equal to the fundamental PWM frequency.

Fig. 6.2 also shows different possible waveforms of the output current under a normal periodic operating mode. As explain before, it is important to reduce the current ripple within a period. For that aim (see the dashed curve), the inverter period is chosen much smaller than the electric time constant *L/R*. This figure assumes also that the reference current *In* is constant. In fact, it is possible to track a sinusoidal current reference (see section 6.6).

Due to the sampled nature of the current controller, a nonlinear map will be required as a model of the converter instead of a usual linear averaged state space model. For the sake of generality, the current is scaled with respect to the maximum output current *E/R* and the voltage is scaled to *E*. On each interval, the one-dimensional model is described by a single linear differential equation.

$$-\frac{1}{2\delta}\frac{di}{dt} = i + (-1)^C, \tag{6.1}$$

where $\delta = RT/2L << 1$ in order to reduce the ripple current. By integrating on the three intervals and stacking up the solutions, the model becomes a nonlinear discrete time map.

$$i_{n+1} = \alpha i_n + \beta(2\sinh(\delta d_n) - \sinh(\delta)), \tag{6.2}$$

where $\alpha = e^{-2\delta}$ and $\beta = 2e^{-\delta}$.

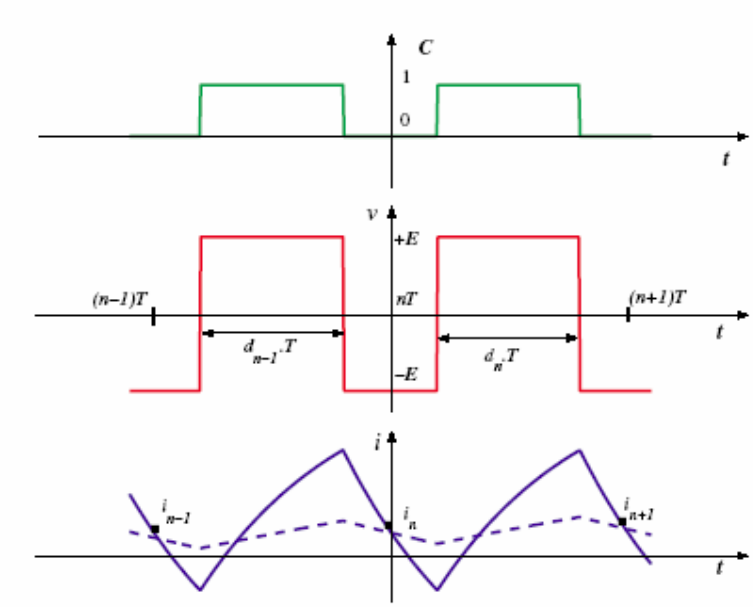

Fig. 6.2. Centered PWM voltage and current waveform.

For the sake of clarity, it is important to note that due to boundedness of the duty cycle d, the PWM modulator introduces saturations to limit too much wandering i.e. to keep the duty cycle d inside the interval [0, 1]. Saturated running modes are characterized by a unique topology over T namely T1 or T2. Saturation of the modulator requires in fact a piecewise model and can be studied in an analytical way by the normal form theory. Saturations lead to the emergence of border collision bifurcations when controller parameters vary. These phenomena have been thoroughly investigated in previous works [18, 19]. Because our goal in this chapter is to define a new controller stabilizing the normal running mode over a wide range, we focus on the standard model (6.2).

With the objective of the design of an experimental prototype, the constants are chosen in order to make it easier with a power that does not exceed a few *kW* and to satisfy the frequency condition presented above. To maintain the ripple current at a low level, we set L/R = 0.5ms and T = 0.2ms, hence parameters were chosen as follows:

$$R = 40\Omega,\ L = 20\text{mH},\ E = 400\text{V},$$

leading to the following constants:

$$\delta = 0.2,\ \alpha = 670.32 \times 10^{-3},\ \beta = 1.6375.$$

6.3. Current-programmed Inverter

Fig. 6.3 depicts an H-Bridge current-programmed single phase inverter. The proportional corrector is the main controller used to control the switching process and is given by:

$$\gamma_n = \gamma_{Pn} = k(I_n - i_n), \tag{6.3}$$

where k is a proportional gain and I_n is the reference current. In this case, the PWM modulator generates the duty cycle:

$$d_n = \frac{1}{2} + \gamma_{Pn} = \frac{1}{2} + k(I_n - i_n). \tag{6.4}$$

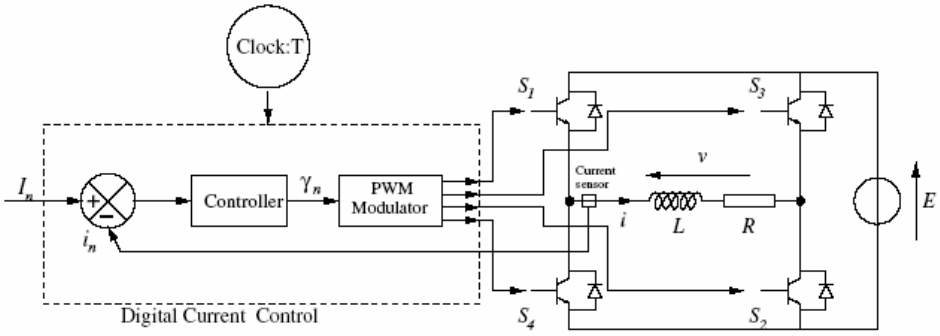

Fig. 6.3. Current-programmed single phase inverter.

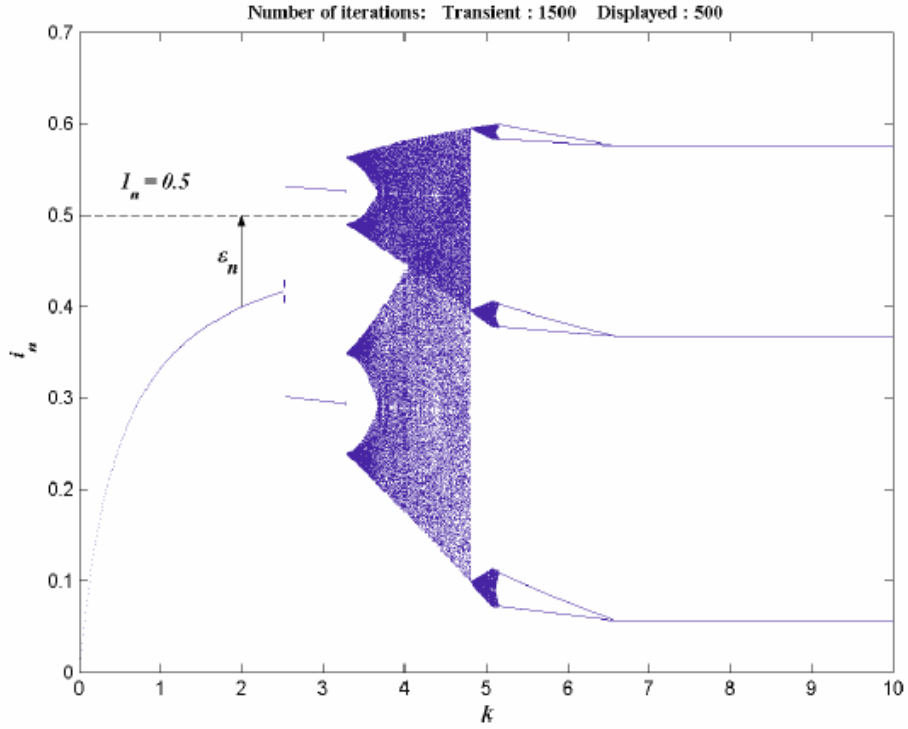

Fig. 6.4. Bifurcation diagram with proportional corrector.

With the objective of the design of an experimental prototype, the constants are chosen in order to make it easier with a power that does not exceed a few *kW* and to satisfy the frequency condition presented above. To maintain the ripple current at a low level, we set L/R = 0.5ms and T = 0.2ms, hence parameters were chosen as follows: As a matter of fact, when static converters are driven by a T-periodic clock, it is important to have a T-periodic output current. Using the discrete-time map given by (6.2) and (6.4), the T-periodic output corresponds to a fixed point of order one. The local stability of the T-periodic mode is analyzed by deriving the Jacobian of the discrete-time map in the neighborhood of the fixed points. By solving $i_{n+1} = i_n$ we obtain the fixed point denoted by i^* as a function of k, and thereby we can determine the loci of the

eigenvalues when k varies. By combining the inverter model (6.2) and the proportional controller (6.4) we obtain a first-order closed loop iteration with a unique eigenvalue λ_P given by:

$$\lambda_P = \alpha - 2\beta\delta k \cosh(\delta d^*), \tag{6.5}$$

where d^* is the solution of:

$$\begin{cases} (\alpha - 1)i^* + \beta(2\sinh(\delta d^*) - \sinh(\delta)) = 0, \\ d^* = \dfrac{1}{2}k(I_n - i^*). \end{cases} \tag{6.6}$$

When k varies the eigenvalue crosses the unit circle at $\lambda_0 = -1$ with $k = k_0$. Using the fact that $\delta d^* << 1$ it follows that $\cosh(\delta d^*) \approx 1$ and

$$k_0 \approx \frac{\alpha + 1}{2\beta\delta} = 2.55. \tag{6.7}$$

Therefore, for $k > k_0$ the T-periodic mode becomes unstable. The bifurcation diagram depicted in Fig. 6.4 was obtained by iterating (6.2) and (6.4) and the exact value of $k_0 = 2.52$ is obtained. It has been shown in [19] that the fixed point of order one (corresponding to T-periodic orbit) continues to exist but becomes unstable.

6.4. Time-delayed Feedback Controller

6.4.1. Controller Design

The TDFC controller is similar to a proportional corrector but referenced to the same state delayed by a time τ equal to the length of the UPO to be stabilized. The aim of this section is to stabilize the UPO of length T. Using the discrete-time notation, this corresponds to stabilizing the fixed point of order one for higher values of k thus the TDFC expression is given by:

$$\gamma_{Dn} = \eta(i_n - i_{n-1}), \tag{6.8}$$

where η is the TDFC gain to be adjusted. Fig. 6.5 shows the block diagram of the TDFC controller. The whole control signal and the duty cycle become:

$$\gamma_n = \gamma_{Pn} + \gamma_{Dn},$$

$$d_n = \frac{1}{2} + k(I_n - i_n) + \eta(i_n - i_{n-1}). \tag{6.9}$$

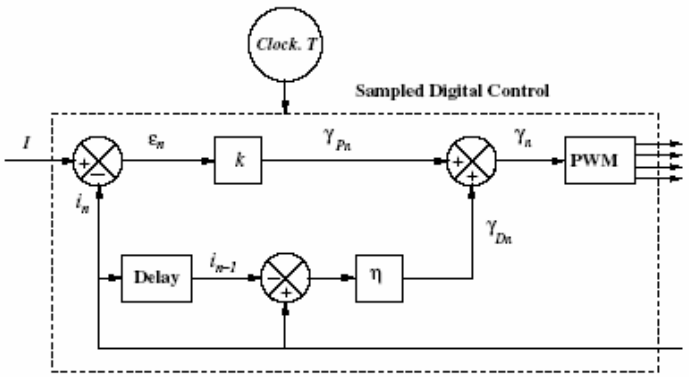

Fig. 6.5. TDFC controller.

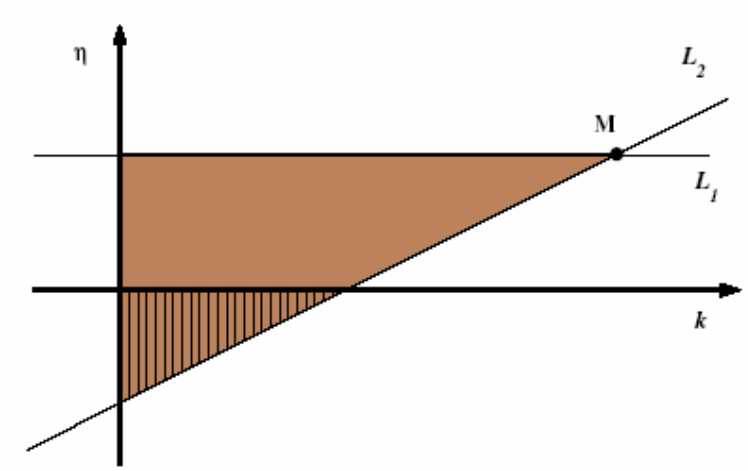

Fig. 6.6. Stability zone in the k-η space.

6.4.2. Stability Analysis

When TDFC is applied, the discrete system defined by (6.2) and (6.8) becomes second order since it involves i_n and i_{n-1}. Let us define $x_n = i_{n-1} - i^*$ and $y_n = i_n - i^*$, using x_n and y_n as the new state variables and combining (6.2) and (6.8) yields

$$\begin{aligned} x_{n+1} &= y_n, \\ y_{n+1} &= \alpha y_n + (\alpha - 1)i^* + \beta(2\sinh(\delta d_n) - \sinh(\delta)). \end{aligned} \tag{6.10}$$

We investigate the local stability by deriving the Jacobian evaluated at the origin:

$$J(d^*) = \begin{bmatrix} 0 & 1 \\ J_1(\eta, d^*) & J_2(\eta, k, d^*) \end{bmatrix}. \tag{6.11}$$

Since at equilibrium we have $i_n = i_{n-1}$ then TDFC signal is null. Thus d^* is again the solution of (6.6) and it follows that

$$J_1(\eta, d^*) = -2\beta\eta\delta\cosh(\delta d^*),$$
$$J_2(\eta, k, d^*) = \alpha + 2\beta\delta(\eta - k)\cosh(\delta d^*).$$

The characteristic equation is given by:

$$z^2 - J_2 z - J_1 = 0. \tag{6.12}$$

The Jury criterion is used to evaluate the stability domain in terms of k and η. According to the Jury criterion, the system is stable if the following conditions are satisfied:

$$\left|-J_1\right| < 1, \tag{6.13}$$
$$\left|1 - J_2 - J_1\right| > 0, \tag{6.14}$$
$$\left|1 + J_2 - J_1\right| > 0. \tag{6.15}$$

(6.13) yields to an upper limit on η

$$\eta < \frac{1}{2\beta\delta\cosh(\delta d^*)}, \tag{6.16}$$

(6.14) yields to a lower limit on k

$$k > \frac{\alpha - 1}{2\beta\delta\cosh(\delta d^*)}. \tag{6.17}$$

We should note that $\alpha - 1 < 0$, then it is sufficient to choose $k > 0$, in order to satisfy condition (6.17) as well as the positiveness of the proportional corrector gain. The last of Jury's conditions (6.15) leads to an affine relation between η and k:

$$\eta > \frac{k}{2} - \frac{\alpha + 1}{4\beta\delta\cosh(\delta d^*)}. \tag{6.18}$$

Using conditions (6.16)–(6.18), a stability zone in the parameters space $k - \eta$ is defined and depicted in Fig. 6.6.

The shaded zone has a special interest if we assume that the reference is constant. Indeed, (6.9) can be written in the following form:

$$\gamma_n = k(I_n - i_n) - \eta((I_n - i_n) - (I_n - i_{n-1})).$$

Denote $\varepsilon_n = I_n - i_n$ the steady state error, then the control signal is similar to a Proportional-Derivative (P.D.) controller:

$$\gamma_n = K_P \varepsilon_n + K_D(\varepsilon_n - \varepsilon_{n-1}),$$

where $K_P = k$ and $K_D = -\eta$. Ordinarily we have $K_P > 0$ and $K_D < 0$, then the conjunction of the proportional and the TDFC controllers can be assimilated to a P.D. controller inside the shaded zone of Fig. 6.6. It is known from linear control theory that the larger the proportional gain k the less is the steady state error ε. In view of Fig. 6.6, k is maximized when η is maximized and the limit of stability is the point **M** which is the intersection of boundary lines

$$L_1: \quad \eta = \frac{1}{2\beta\delta} \quad \text{and} \quad L_2: \quad \eta = \frac{k}{2} - \frac{1+\alpha}{4\beta\delta}$$

obtained from (6.16) and (6.18) with the approximation $\cosh(\delta d^*) \approx 1$. The coordinates of **M** are:

$$\eta_{\max} \approx \frac{1}{2\beta\delta} = 1.5, \tag{6.19}$$

$$k_{\max} \approx \frac{3+\alpha}{2\beta\delta} = 5.6. \tag{6.20}$$

6.4.3. Results

The two-dimensional bifurcation diagram depicted in Fig. 6.7 indicates in brown the zone of the period one mode and this matches the stability

zone shown in Fig. 6.6. Zones of higher periods as well as chaotic zones are also shown as parameters k and η vary. Particularly, when $\eta = 0$ we observe that as k increases the output current is of period one then becomes period two and for a short interval of k becomes period four before it goes into chaotic mode. As k increases further the output becomes period six and finally arrives at period three mode and this matches very well with the one-dimensional bifurcation diagram shown in Fig. 6.4. We also notice that as η increases and a TDFC controller is acting then the period one mode extends for higher values of k as expected (see also Fig. 6.8). Fig. 6.8 shows that the fixed point of order one that was embedded in a zone of period two mode $(2.5 \le k \le 3.3)$ and in a chaotic attractor $(3.3 \le k \le 5.0)$ has been stabilized by the application of the TDFC in conjunction with the proportional controller.

6.4.4. Optimality Criterion

The main concern of the previous design was to obtain stability of the fixed point of order one for larger values of k which reduces the steady state error ε_n. In this section, we show that a drawback of TDFC is to degrade the dynamical response by increasing the settling time. Fig. 6.9 shows the sampled and hold output current resulting from a step reference from $I_n = 0$ to $I_n = 0.5$ with $k = 2$ and different values of η. We note that the transient time is increased when the TDFC is applied. When η tends to $\eta_{\max}$, the transient time becomes too large.

To overcome this problem we present an adaptive law to calculate a value of η that leads to a fast response for each value of k. The linearization of system (6.10) gives

$$\begin{bmatrix} x_{n+1} \\ y_{n+1} \end{bmatrix} = J \begin{bmatrix} x_n \\ y_n \end{bmatrix} = J^{n+1} \begin{bmatrix} x_0 \\ y_0 \end{bmatrix}.$$

This implies that [5]

$$\left\| \begin{matrix} x_{n+1} \\ y_{n+1} \end{matrix} \right\| = \left\| J^{n+1} \right\| \left\| \begin{matrix} x_0 \\ y_0 \end{matrix} \right\| \le \pi(n)\sigma(J)^{n+1} \left\| \begin{matrix} x_0 \\ y_0 \end{matrix} \right\|. \tag{6.21}$$

where $\pi(n) \geq 0$ is a positive polynomial in n and $\sigma(J)$ is the spectral radius of J. To obtain a fast response we should choose k and η that minimize $\sigma(J)$. In case of complex eigenvalues $\sigma(J) = \sqrt{-J_1}$, thus η should be as small as possible. When η is less than or equal to a critical value η_c (i.e. $\eta \leq \eta_c$), the eigenvalues become real and the spectral radius is minimum if both eigenvalues are equal, that is when the discriminant is equal to zero,

$$J_2^2(\eta_c, k, d^*) + 4J_1(\eta_c, d^*) = 0.$$

Solving for η_c we obtain

$$\eta_c = k + \frac{2 - \alpha - 2\sqrt{2\beta\delta k + 1 - \alpha}}{2\beta\delta}. \tag{6.22}$$

Fig. 6.10 shows the loci of the eigenvalues when η varies for different values of k. Fig. 6.11 depicts the effect of adapting the TDFC gain η according to the value of the proportional gain k. Indeed, for $k = 4$ the proportional gain on its own leads to a chaotic output as shown in Fig. 6.4. However, if the TDFC is arbitrarily added ($\eta = 1.3$) the fixed point of order one is stabilized and the step reference is tracked with a certain static error. Nevertheless, the settling time equal to 50 cycles (10ms) is significantly long. Eventually, the adapted TDFC ($\eta = 0.86$) yields to the stability of the fixed point with a considerably shorter settling time equal to 7 cycles (1.4ms).

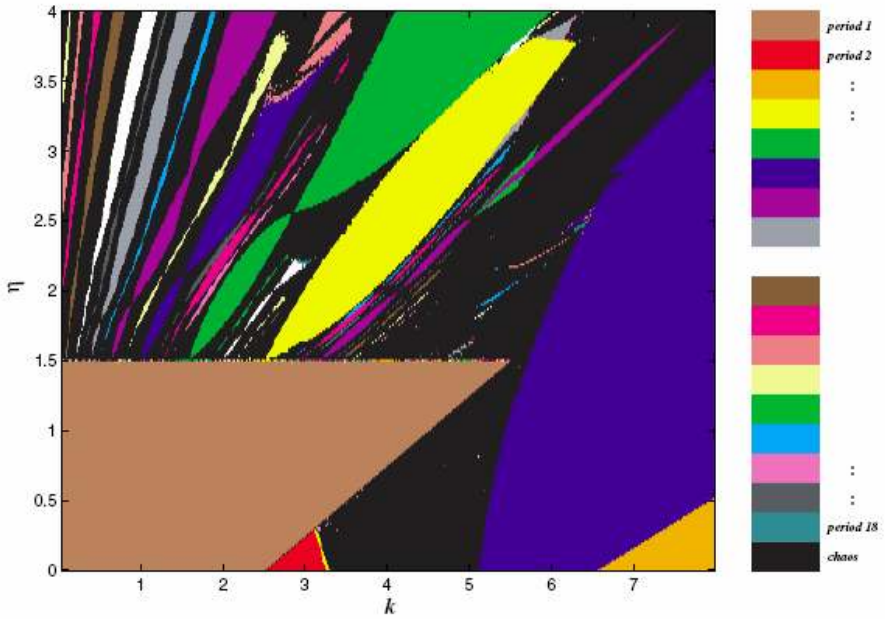

Fig. 6.7. 2-D bifurcation diagram.

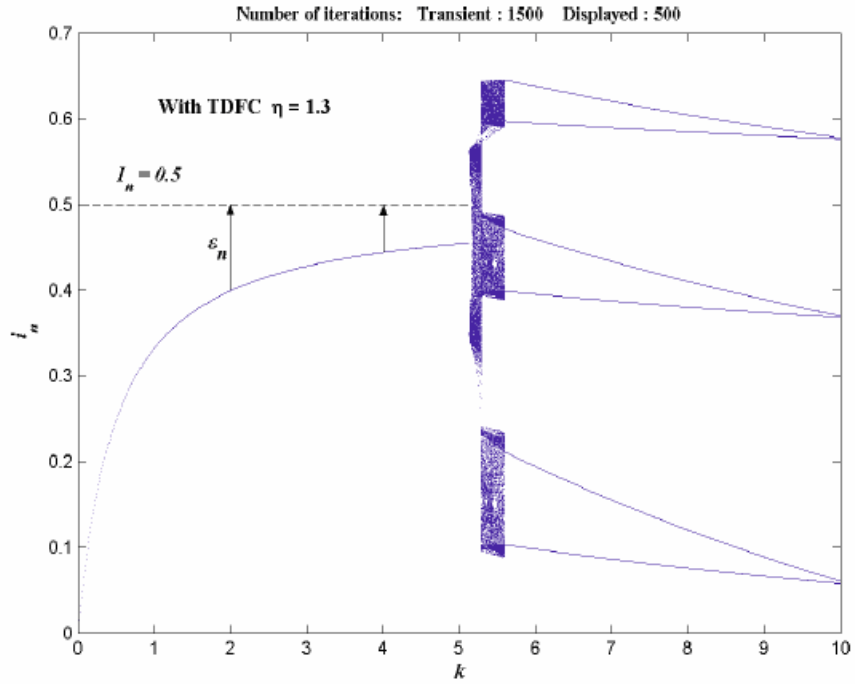

Fig. 6.8. 1-D bifurcation diagram with TDFC controller.

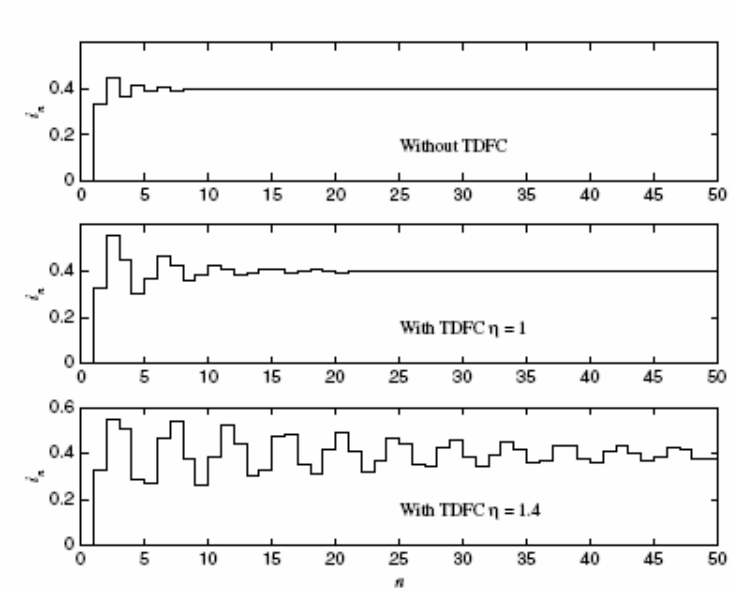

Fig. 6.9. Dynamic responses to step with k=2.

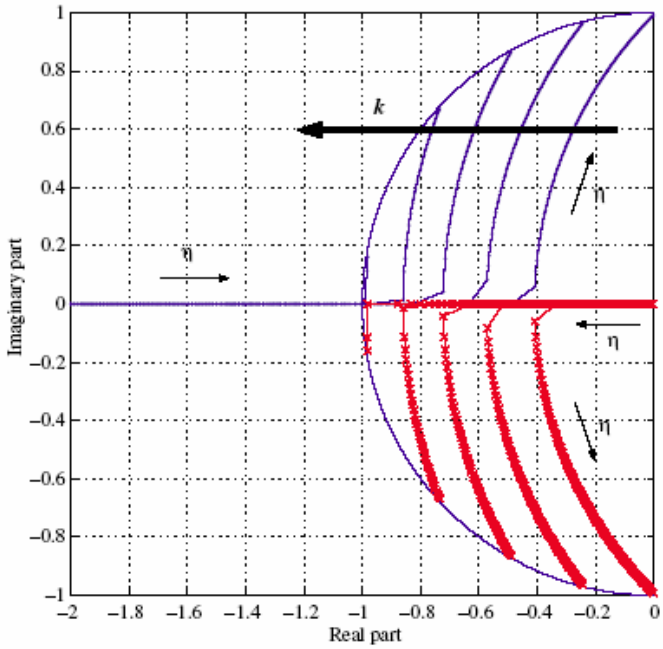

Fig. 6.10. Eigenvalues loci for different values of η and *k*.

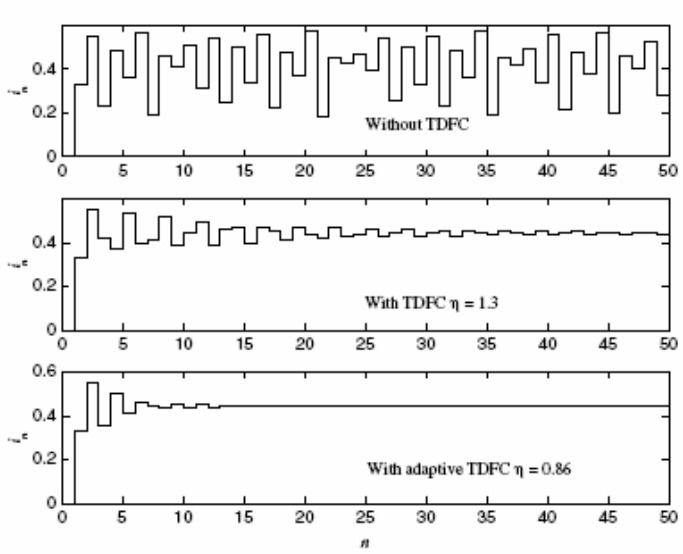

Fig. 6.11. Dynamic responses to the step with k=4.

6.5. Extended Time-delayed Feedback Controller

6.5.1. Controller Design

The ETDFC is a generalization of the TDFC and provides the designer with a third parameter r hence one more degree of freedom. The ETDFC extends the effect of earlier states to the present output with a decaying weight as we go further in the past. The output signal of the ETDFC is given by:

$$\gamma_{En} = \eta\left(i_n - (1-r)\sum_{m=1}^{n} r^{m-1} i_{n-m} \right), \tag{6.23}$$

where k, η and $0 \leq r < 1$ are control parameters to be fixed to guarantee stability of the fixed point of order one. We clearly notice that (6.23) is equivalent to (6.8) if $r = 0$. The block diagram realization of the ETDFC

is shown in Fig. 6.12. The overall control signal and the duty cycle are expressed as:

$$\gamma_n = \gamma_{Pn} + \gamma_{En},$$

$$d_n = \frac{1}{2} + k(I_n - i_n) + \eta\left(i_n - (1-r)\sum_{m=1}^{n} r^{m-1} i_{n-m}\right). \qquad (6.24)$$

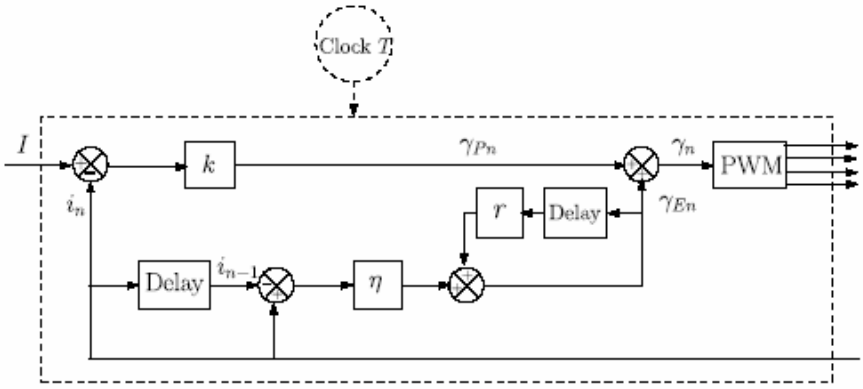

Fig. 6.12. ETDFC controller.

6.5.2. Stability Analysis

To derive necessary conditions for local stability of the fixed point of order one, we start by finding the Jacobian matrix of the discrete-time map. Let us first denote

$$z_{n+1} = \eta\left(i_n - (1-r)\sum_{m=1}^{n} r^{m-1} i_{n-m}\right),$$

and notice that $z_{n+1} = \eta(i_n - i_{n-1}) + rz_n$. Thus the discrete-time inverter model can be described as follows:

$$i_{n+1} = \alpha i_n + \beta(2\sinh(\delta d_n) - \sinh(\delta)),$$

$$d_n = \frac{1}{2} + k(I_n - i_n) + \eta(i_n - i_{n-1}) + rz_n,$$

$$z_{n+1} = \eta(i_n - i_{n-1}) + rz_n. \tag{6.25}$$

Since at equilibrium ETDFC vanishes then again we can define $x_n = i_{n-1} - i^*$ and $y_n = i_n - i^*$ where i^* and d^* are the solutions of (6.6). Using x_n, y_n and z_n as the new state variables, system (6.25) becomes

$$x_{n+1} = y_n,$$

$$y_{n+1} = \alpha y_n + (\alpha - 1)i^* + \beta(2\sinh(\delta d_n) - \sinh(\delta)),$$

$$z_{n+1} = \eta(y_n - x_n) + rz_n. \tag{6.26}$$

Hence the Jacobian matrix is

$$J = \begin{bmatrix} 0 & 1 & 0 \\ J_1 & J_2 & J_3 \\ -\eta & \eta & r \end{bmatrix}$$

where

$$J_1 = -2\beta\eta\delta\cosh(\delta d^*),$$

$$J_2 = \alpha + 2\beta(\eta - k)\delta\cosh(\delta d^*),$$

$$J_3 = 2\beta r\delta\cosh(\delta d^*).$$

The characteristic equation of the linearized system is:

$$z^3 - (J_2 + r)z^2 + (rJ_2 - \eta J_3 - J_1)z + \eta J_3 + rJ_1 = 0. \tag{6.27}$$

Using the system description (6.26), the aim is to stabilize the origin of the system hence we obtain $i_n = i_{n-1} = i^*$ and ETDFC becomes zero. The Jury stability criteria yields to conditions on control parameters k, η and r:

$$k > \frac{\alpha - 1}{2\beta\delta \cosh(\delta d^*)}. \tag{6.28}$$

$$\eta > (1+r)\left(\frac{k}{2} - \frac{1+\alpha}{4\beta\delta \cosh(\delta d^*)}\right). \tag{6.29}$$

$$\eta < rk + \frac{1 - r\alpha}{2\beta\delta \cosh(\delta d^*)}. \tag{6.30}$$

$$\eta > rk - \frac{1 + r\alpha}{2\beta\delta \cosh(\delta d^*)}. \tag{6.31}$$

We recall that since $\delta = 0.2$ and $0 \leq d^* \leq 1$ then we have $\cosh(\delta d^*) \approx 1$ and $\alpha < 1$. A proportional gain is usually considered positive, thus condition (6.28) reduces to $k > 0$. Let us now define three lines ($\eta = L(k)$)

$$L_3: \quad \eta = (1+r)\left(\frac{k}{2} - \frac{1+\alpha}{4\beta\delta}\right).$$

$$L_4: \quad \eta = rk + \frac{1 - r\alpha}{2\beta\delta}.$$

$$L_5: \quad \eta = rk - \frac{1 + r\alpha}{2\beta\delta}.$$

We notice that L_4 and L_5 have the same slopes (i.e. r) therefore they are parallel. We further see that since $r < 1$ then L_3 is above L_5 when $k > 0$.

$$(1+r)\left(\frac{k}{2}-\frac{1+\alpha}{4\beta\delta}\right)-\left(rk-\frac{1+r\alpha}{2\beta\delta}\right)=\frac{1-r}{2}\left(k+\frac{1-\alpha}{2\beta\delta}\right)>0.$$

Thus, it follows that condition (6.31) is obviously satisfied when condition (6.29) is satisfied and that as r tends to 1 condition (6.31) tends to condition (6.29). Moreover, we notice that when r tends to zero $L4 \equiv L1$ and $L3 \equiv L2$. Fig. 6.13 sketches the stability zone in the parameters space for a fixed value of r.

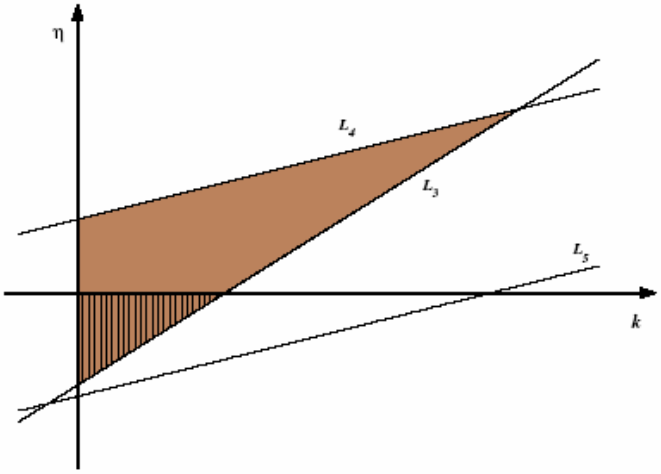

Fig. 6.13. Stability zone in the parameter space.

6.5.3. Results

Figs. 6.14–6.16 show two-dimensional bifurcation diagrams. It is worth noting that the period one zone shown in brown in Fig. 6.14 matches the zone depicted in Fig. 6.13. Moreover, we see that the fixed point of order one can be stabilized for higher values of k when η and r increase. However, we notice that for large values of η and r, small values of k no longer lead to stability but to different other modes, this is clearly depicted in Fig. 6.14 as well as in Fig. 6.17.

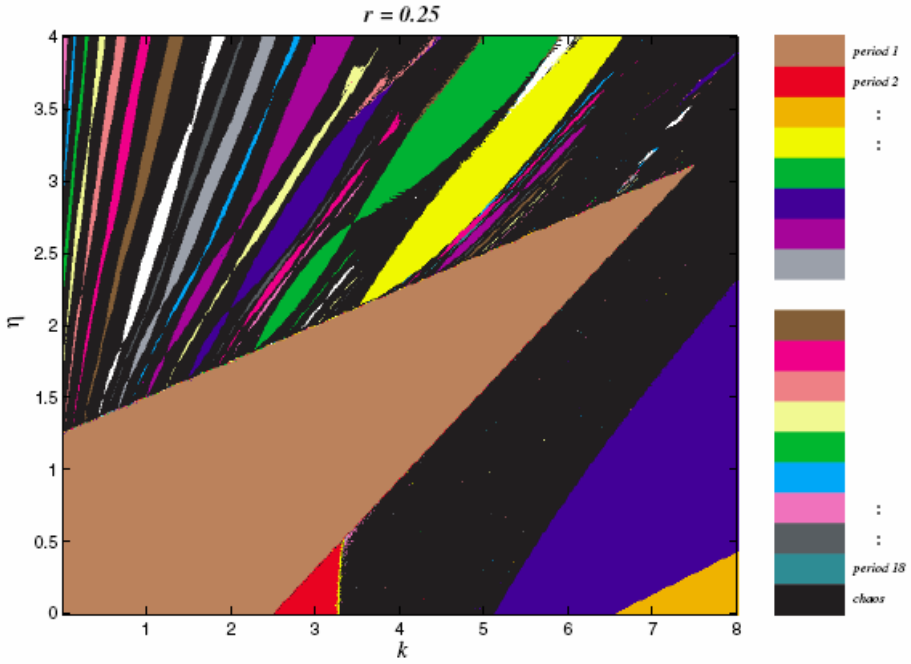

Fig. 6.14. 2-D bifurcation diagram (k-η).

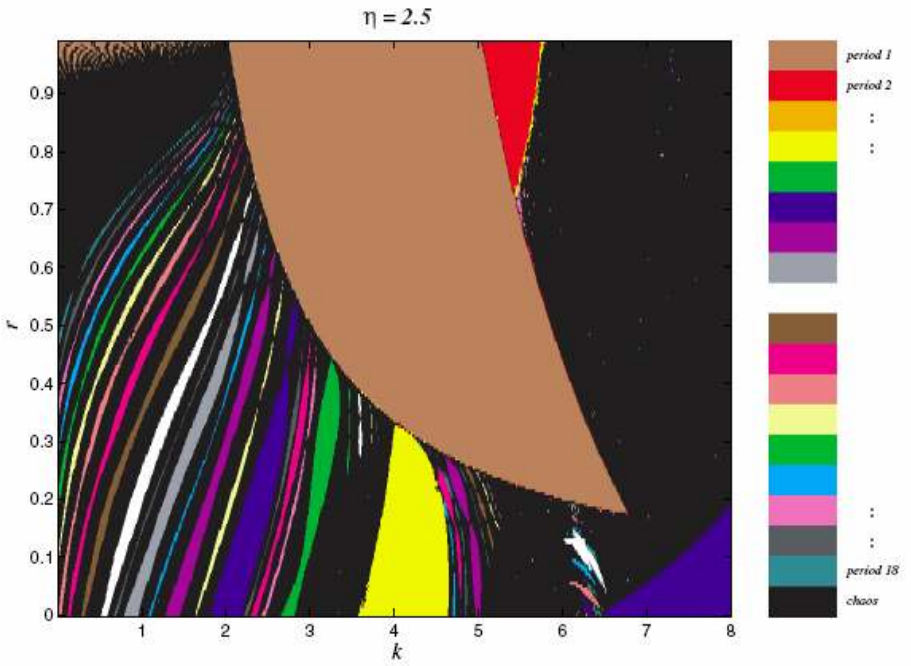

Fig. 6.15. 2-D bifurcation diagram (*k*-*r*).

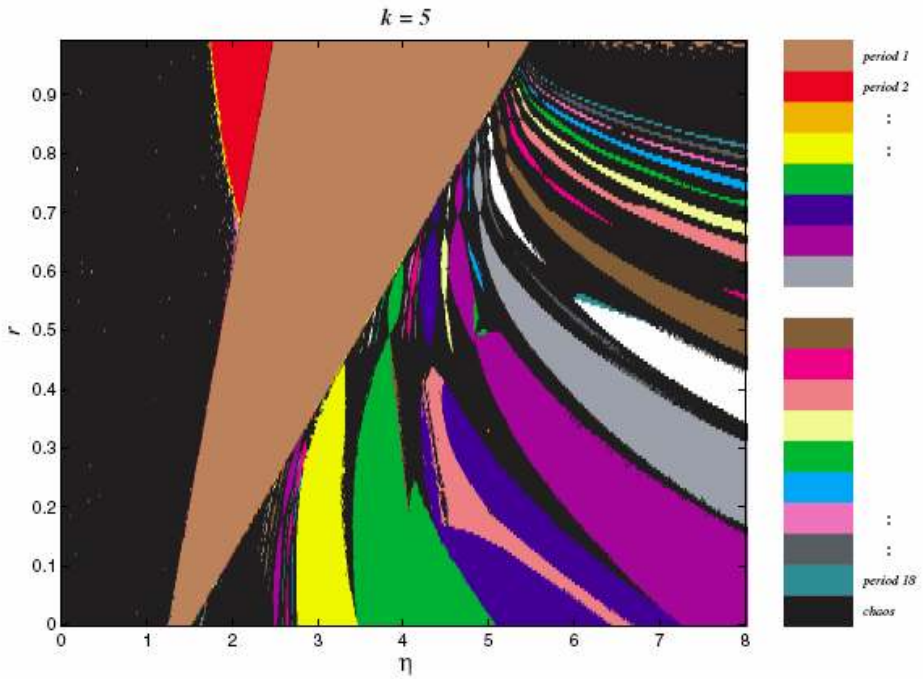

Fig. 6.16. 2-D bifurcation diagram (η-*r*).

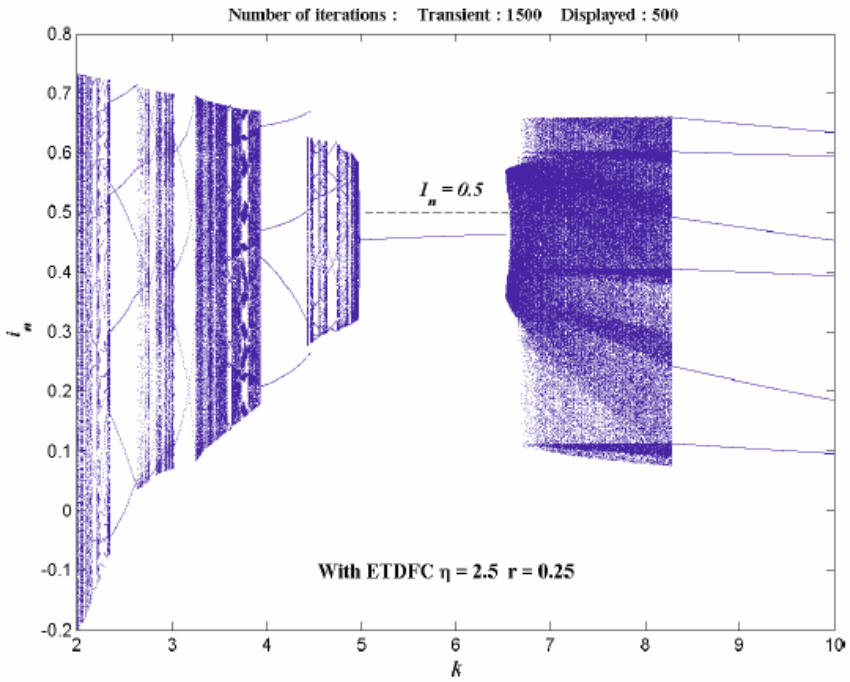

Fig. 6.17. 1-D bifurcation diagram with ETDFC controller.

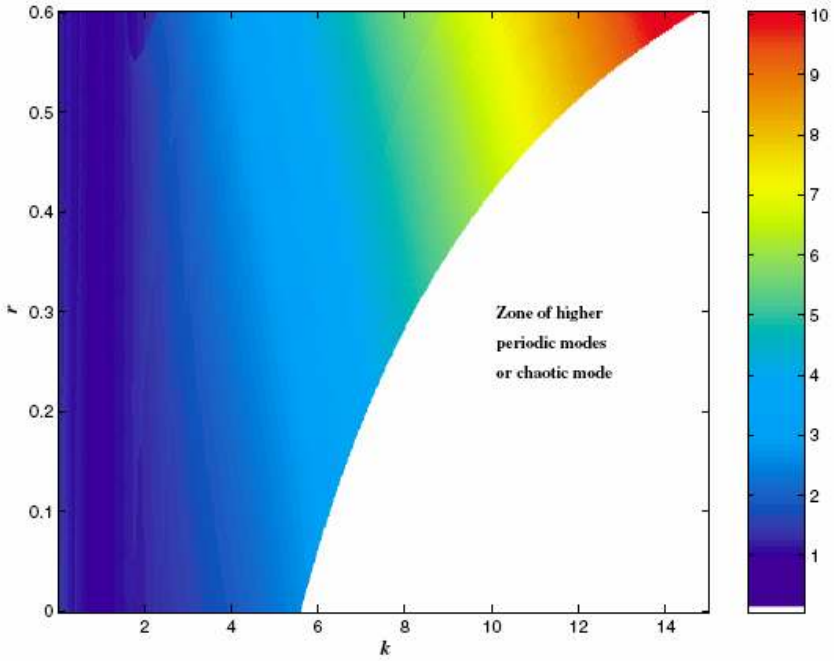

Fig. 6.18. Optimal values of η for different values of *k* and *r*.

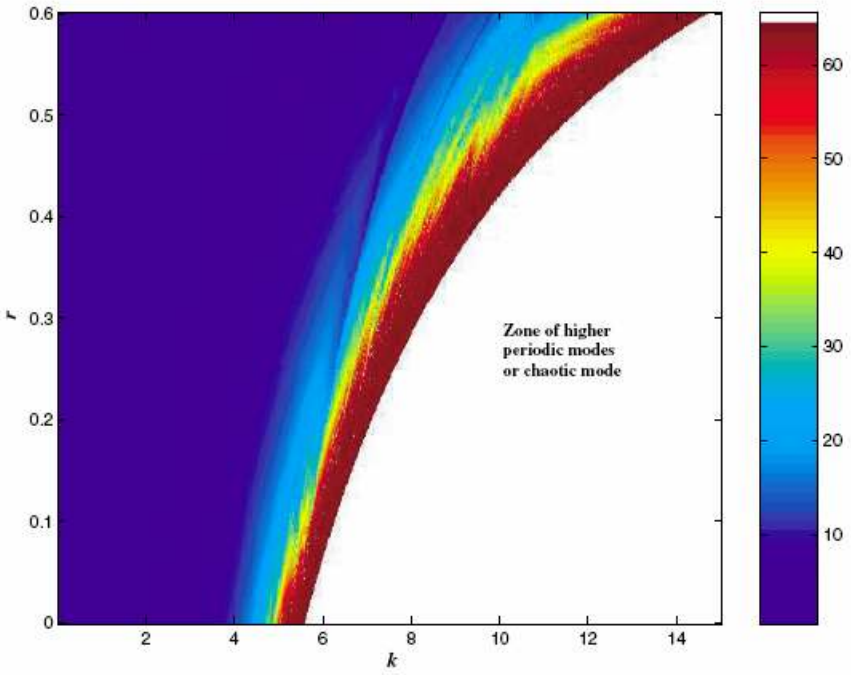

Fig. 6.19. Settling time shown in number of periods *T*.

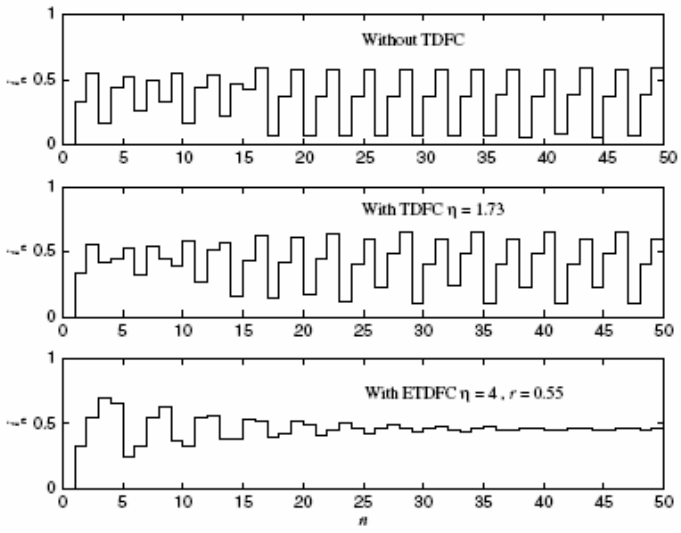

Fig. 6.20. Dynamic responses to the step with k=6.

6.5.4. Optimality Criterion

Similarly to the case of TDFC, the ETDFC may induce significantly slow dynamic response if the parameters are not properly chosen. In this section we present numerical simulations results to find optimal parameters values that lead to a fast response. The criterion considered herein is to find the shortest settling time to be within an interval of 5% around the fixed point.

For different values of k and r, Fig. 6.18 shows the optimal value of η necessary to minimize the settling time. The optimum value η_{opt} is coded on the colorbar and we see that it increases when both k and r increase. Fig. 6.19 depicts the settling time in the number of periods. We notice that as we move to the boundary of the stability zone the settling time gets longer. Moreover, we can notice that for small values of r the settling time increases rapidly as we move towards the stability boundary, whereas for large values of r the settling time increases gradually. Fig. 6.20 sketches the sampled and hold output current for k = 6. When no TDFC is applied the response is period 6 as shown in Fig.

6.4. When TDFC with adaptive value η is applied the response is again period 6. However, the ETDFC stabilizes the fixed point of order one.

6.6. Results on Sinusoidal Output Tracking

When considering an industrial application, we should think of a sinusoidal mode functioning. In the foregoing sections we have considered a constant reference current for simplicity of the analysis. In that case, a new frequency condition has to be met: the reference frequency must be much smaller than the inverter's in order to guarantee a variation of the current close to a sinusoid (as shown in Fig. 6.21).

T has to be small enough for obtaining an output current close to a sinusoid, besides T has to be sufficiently large to allow the application of a digital control and to limit the losses to an acceptable level. Considering a reference frequency ranging from zero to 100Hz and a minimal switching frequency to reference frequency ratio equal to 50, the switching period is upper limited to $T = 0.2$ms.

In Fig. 6.22 we compare in the case of $k = 2$ the performance of the proportional, TDFC and ETDFC controllers. The sampled and hold current is sketched, and we see that when the adaptive TDFC or ETDFC is applied the performance is almost unchanged. We have seen in section 6.4 that when the proportional gain is raised to $k = 4.5$, TDFC should be applied to obtain stability of the period one mode. Although, we apply adaptive TDFC, Fig. 6.23 shows that the settling time can be further minimized with the action of ETDFC. In Fig. 6.24 we present sinusoidal reference tracking when $k = 7.2$ which can only be obtained with ETDFC. We note that a suitable choice of the parameters leads to faster settling time. In Fig. 6.25 the continuous time-domain waveform of the output current is depicted to show how the ripple is minimized in the periodic mode compared to the chaotic mode.

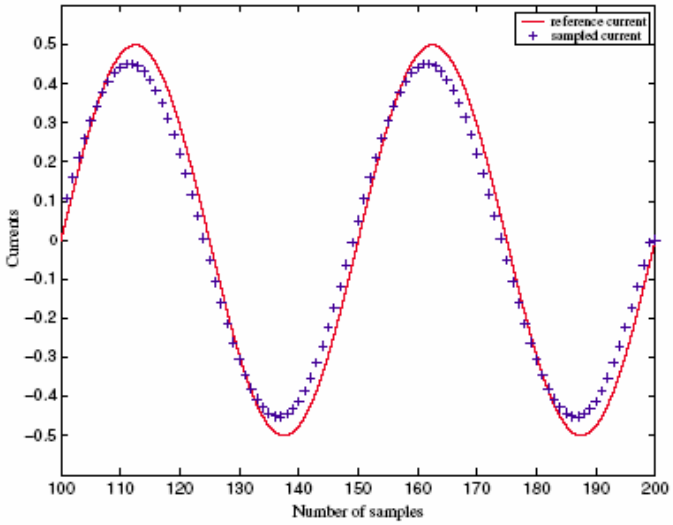

Fig. 6.21. Input reference current and controlled current in the load.

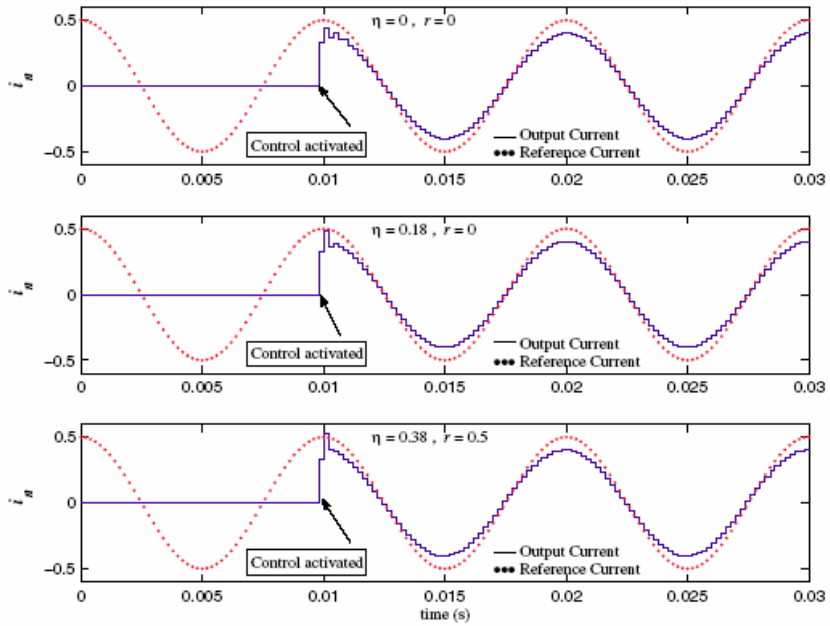

Fig. 6.22. Sinusoidal reference tracking with k=2.

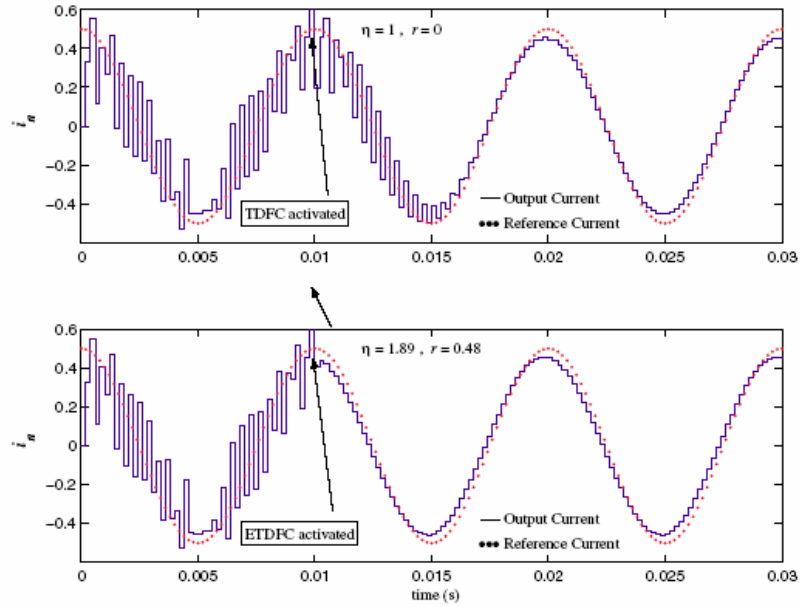

Fig. 6.23. Sinusoidal reference tracking with k=4.5.

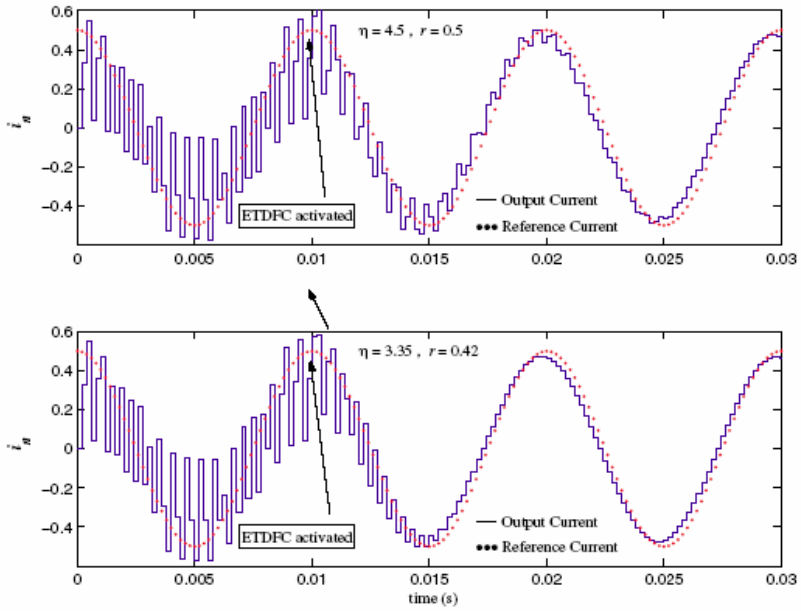

Fig. 6.24. Sinusoidal reference tracking with k=7.2.

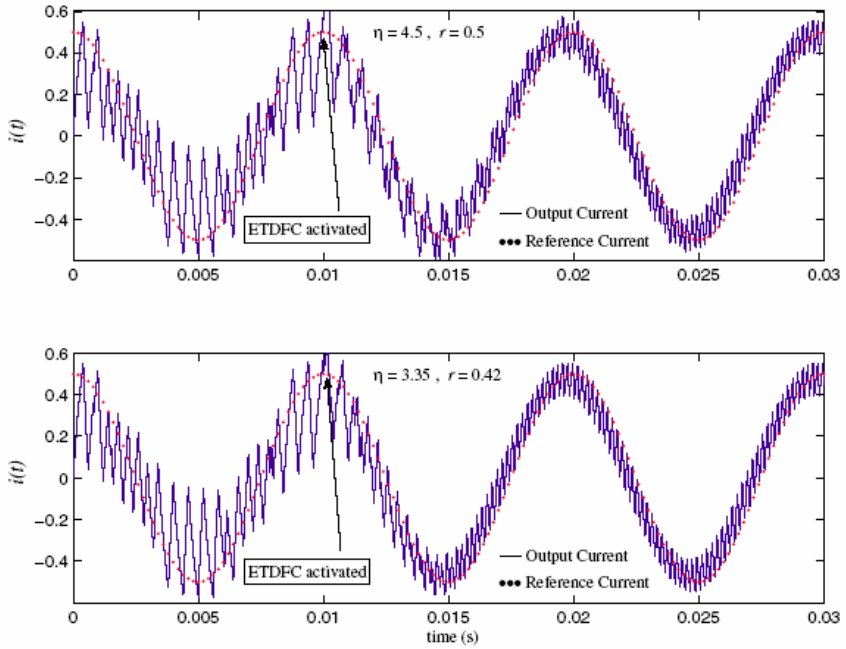

Fig. 6.25. Time-domain waveform for sinusoidal reference tracking with k=7.2.

6.7. Conclusion

By modeling power electronic converters using nonlinear discrete time maps, it is possible to predict and control chaotic behaviors. The Extended Time-Delayed Feedback Control is an efficient method to stabilize unstable periodic orbits. In this work TDFC presented in section 6.4 and ETDFC presented in section 6.5 have been applied to stabilize a current-programmed PWM single phase inverter. By analyzing the Jacobian matrix of the map, we have determined the stability domain of the T-periodic running mode. For each controller, we have presented 2-D bifurcation diagrams (see Figs. 6.7, 6.14–6.16) corresponding to different control parameters. We have also presented the stability zones in the parameters space (see Figs. 6.6 and 6.13). It may be worthwhile to study the effect of the system parameters variations on these stability zones.

It has been found that the TDFC and ETDFC induce longer settling time if parameters are not appropriately chosen (see Figs. 6.9 and 6.19). To tackle this problem, an adaptive TDFC has been proposed [see (6.22)] and numerical analysis of ETDFC has been presented to give the optimal parameters that lead to minimum settling time (see Fig. 6.18). The range of the stable *T*-periodic mode of the inverter is widened and the dynamical performances are improved. Results on tracking sinusoidal reference have been presented (see Figs. 6.22–6.24) with the perspective of an experimental realization of the presented control methods.

Acknowledgement

This work is supported in part by ARC Discovery Projects Grant (No. DP0559109).

References

[1] S. Banerjee and K. Chakrabarty, Nonlinear modeling and bifurcations in the boost converter, *IEEE Trans. Power Electron.* **13**, 252–260, (1998).

[2] M. Basso, R. Genesio and A. Tesi, Stabilizing periodic orbits of forced systems via generalized Pyragas controllers, *IEEE Trans. Circuits Syst.-I* **44**, 1023–1027, (1997).

[3] C. Batle, E. Fossas and G. Olivar, Stabilization of periodic orbits of the buck converter by time-delayed feedback, *Int. J. Circuit Th. Appl.* **27**, 617–631, (1999).

[4] L. Benadero, A. El Aroudi, G. Olivar, E. Toribio and E. Gomez, Two-dimensional bifurcation diagrams background pattern of fundamental DC-DC converters with PWM control, *Int. J. Bifurcation and Chaos* **13**, 427–451, (2003).

[5] F. Callier and C. Desoer, *Linear System Theory* (Springer-Verlag 1991).

[6] J. Deane and D. Hamill, Instability, subharmonics and chaos in power electronic systems, *IEEE Trans. Power Electron.* **5**, 260–268, (1990).

[7] M. Di Bernardo and F. Vasca, On discrete time maps for the analysis of bifurcations and chaos in dc/dc converters, *IEEE Trans. Circuits Syst.-I* **47**, 130–143, (2000).

[8] M. Di Bernardo and C. K. Tse, Chaos in power electronics: An overview, *Chaos in Circuits and Systems* **11**, eds. G. Chen and T. Ueta, (World Scientific, Singapore, Chap. 16, 317–340, 2002).

[9] W. Ditto, M. Spano and J. Linder, Techniques for the control of chaos, *Physica D* **86**, 198–211, (1995).

[10] C. Grebogi and Y. C. Lai, Controlling chaos in high dimension, *IEEE Trans. Circuits Syst.-I* **44**, 971–975, (1997).

[11] D. Hamill and D. Jefferies, Subharmonics and chaos in a controlled switched-mode power converter, *IEEE Trans. Circuits Syst.-I* **35**, 1059–1061, (1988).

[12] H. Iu and B. Robert, Control of chaos in a PWM current-mode H-bridge inverter using time-delayed feedback, *IEEE Trans. Circuits and Syst.-I* **50**, 1125–1129, (2003).

[13] H. Iu and B. Robert, Control of chaos in a PWM inverter using time-delayed feedback, *Proc. of Shanghai Int. Symp. Nonlinear Sciences and Applications* Shanghai, China, (2003.

[14] K. Konishi and H. Kokame, "Observer-based delayed-feedback control for discrete-time chaotic systems, *Phys. Lett. A* **248**, 359–368, (1998).

[15] E. Ott, C. Grebogi and J. A. Yorke, Controlling chaos, *Phys. Rev. Lett.* **64**, 1196–1199, (1990).

[16] K. Pyragas, Continuous control of chaos by self-controlling feedback, *Phys. Lett. A* **170**, 421–428, (1992).

[17] K. Pyragas, Control of chaos via extended delay feedback, *Phys. Lett. A* **206**, 323–330, (1995).

[18] B. Robert and C. Robert, Border collision bifurcations in a chaotic PWM H-bridge single phase inverter, *Proc. 10th Int. Power Electronics and Motion Control Conf. EPE-PEMC* Dubrovnik, Croatia, (2002).

[19] B. Robert and C. Robert, Border collision bifurcations in a one-dimensional piecewise smooth map for a PWM current-programmed H-bridge inverter, *Int. J. Contr.* **75**, 1356–1367, (2002).

[20] B. Robert, H. Iu and M. Feki, Adaptive time-delayed feedback for chaos control in a PWM single phase inverter, *J. Circuits Syst. Comput.* **13**, 519–534, (2004).

CHAPTER 7

CHAOS CONTROL OF EPILEPTIFORM BURSTING IN THE BRAIN

M.W. Slutzky*, P. Cvitanovic** and D.J. Mogul***

*Department of Neurology,
Northwestern Memorial Hospital,
251 East Huron Street, Chicago, IL 60611, USA
E-mail: mslutzky@md.northwestern.edu
**School of Physics,
Georgia Institute of Technology,
837 State Street, Atlanta, GA 30332, USA
E-mail: Predrag.cvitanovic@physics.gatech.edu
***Department of Biomedical Engineering,
Illinois Institute of Technology,
10 West 32nd Street, Room 116, Chicago, IL 60616, USA
E-mail: mogul@iit.edu

Epilepsy, defined as recurrent seizures, is a pathological state of the brain that afflicts over one percent of the world's population. Seizures occur as populations of neurons in the brain become overly synchronized. Although pharmacological agents are the primary treatment for preventing or reducing the incidence of these seizures, over 30% of epilepsy cases are not adequately helped by standard medical therapies. Several groups are exploring the use of electrical stimulation to terminate or prevent epileptic seizures. One experimental model used to test these algorithms is the brain slice where a select region of the brain is cut and kept viable in a well-oxygenated artificial cerebrospinal fluid. Under certain conditions, such slices may be made to spontaneously and repetitively burst, thereby providing an *in vitro* model of epilepsy. In this chapter, we discuss our efforts at applying chaos analysis and chaos control algorithms for manipulating this seizure-like behavior in a brain slice model. These techniques may provide a nonlinear control pathway for terminating or potentially preventing epileptic seizures in the whole brain.

7.1. Introduction

More than 60 million people worldwide are afflicted with epilepsy, and over 30% of these people are not sufficiently helped by medications [1]. Some of these patients have the option of surgically removing the seizure-generating part of the brain (the focus). While surgery is often successful in preventing seizures, it can have serious side effects such as memory loss –in up to 35% of patients [2] – or speech deficits, not to mention adverse events such as infections and hemorrhage [3]. Therefore, many groups are working to develop less-invasive alternatives to surgery for treating drug-resistant epilepsy [4]. Some currently available therapies use electrical stimulation of either the vagus nerve [5], the centromedian thalamic nucleus [6], the anterior thalamic nucleus [7], or the hippocampus [8] to stop seizures with modest success. Vagus nerve stimulators reduce the number of seizures by 50% or more in approximately 35-40% of patients [9]. However, their mechanism of action is uncertain and they have several adverse effects [5]. These stimulators have only been available for a few years, so their long-term effects are unclear. Long-term stimulation of the brain at a tonic high frequency could potentially create new epileptic foci in those areas. Moreover, the goal of invasive therapies is now to render patients seizure-free, not just reduce seizure frequency, since studies have shown that a reduction in seizure frequency alone does not remove their psychosocial issues (i.e. anxiety and depression) that come from having seizures. Existing stimulators most often succeed in reducing seizure frequency, but do not often prevent all seizures; thus there is a great deal of room for improvement. Schiff *et al.* [10] suggested that chaos control techniques might be used to prevent or stop seizures with intermittent electrical stimuli. These techniques possess the advantage of requiring relatively infrequent stimulation of the tissue. This would reduce the likelihood of inducing new epileptic seizures and decrease power requirements, both important considerations for an implanted device. However, prior to using chaos control techniques, one should first demonstrate that the system is indeed chaotic.

7.2. Searching for Evidence of Chaos in the Brain

A seizure is an abnormal, excessive, synchronous discharge of one or several groups of neurons in the brain. One of the hallmarks of epilepsy is the presence of spikes in the electroencephalogram (EEG, recorded from the scalp) during this interictal period. While the precise role of interictal spikes in epileptogenesis is not currently certain [11-13], it is plausible that developing a method to control them could provide a way to control seizure activity as well. Complex partial seizures are the most common type of seizures in adults and are the most likely to be refractory to medical treatment. Most complex partial seizures arise in the temporal lobe, particularly in the hippocampus or amygdala; thus, the hippocampal slice is a frequently used in vitro model for investigating seizures. The hippocampus is buried deep within the temporal lobe of the brain and makes up part of the limbic system. On an EEG, the period during which a seizure takes place is referred to as the ictal period; the period between seizures is thus the interictal period. Bursts are the in *vitro* analogues of these spikes and can be induced to occur spontaneously in the transverse rat hippocampal slice providing an *in vitro* model of epilepsy.

Significant efforts have been made to try to characterize the system behavior in epilepsy. Several studies of EEG voltage have focused on calculating the correlation dimension [14, 15] which can be misleading in practice because of the need for many assumptions and the prevalence of false positive results. Some have searched for chaos by calculating Lyapunov exponents of EEG seizure activity [16, 17], and found evidence both supporting [16, 18] and contradicting [17] the existence of nonlinear determinism. However, the algorithms used perform poorly in systems with a substantial stochastic component in addition to determinism, and thus have not proven very reliable in characterizing biological systems [17, 19]. Other measures have shown evidence either for the presence of determinism in experimental data, [20-23] or against it [24-26]. However, most of these methods rely on either very long, stationary time series or low noise; it is difficult to achieve either of these conditions in a neurophysiological system. Our laboratory used a combination of new [27] and old techniques to characterize epileptiform behavior [28].

7.2.1. Transforming Brain Signals into State Space

Our laboratory investigated epileptiform behavior in the *in vitro* hippocampal slice. Epileptiform bursting was induced by bathing the slices in artificial cerebrospinal fluid (ACSF) containing either relatively high potassium concentration ($[K^+]_o$=10.5 mM), zero magnesium, or the neurotransmitter gamma-aminobutyric acid ($GABA_A$) antagonists bicuculline and picrotoxin. Fig. 7.1a shows the setup used to record and manipulate bursts. A typical burst is shown in Fig. 7.1b. Both morphology and burst duration were consistent for all three induction protocols.

The system state variable was interburst intervals (IBIs). IBIs were recorded at one point in space, thus producing a one-dimensional time series. Using time-delay embedding, scalar data can be converted into vectors which form a more complete representation of the system in state space and preserve the geometric and dynamical properties of the system [29]. IBIs were first embedded into two-dimensional vectors consisting of the current and next IBIs (e.g., see Fig. 7.1c). Such IBI embeddings have also been shown to be sufficient to characterize most of the original system's dynamical behavior [30].

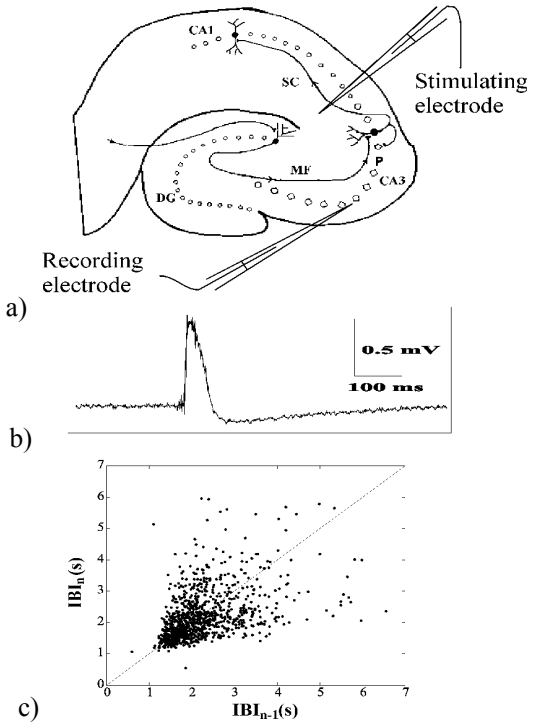

Fig. 7.1. Bursting in the hippocampal slice. a) Schematic of hippocampal slice organization. The recording electrode was placed in the pyramidal cell body layer (P) of the CA3 region. The stimulating electrode was placed in the Schaffer collateral (SC) axons to the CA1 region. b) Example of a spontaneous burst recorded extracellularly in the CA3 pyramidal layer. c) A return map of 1000 interburst intervals (IBIs) recorded during spontaneous bursting. Fixed points lie along the identity (45°) line.

7.2.2. Global Measure of Chaos: Lyapunov Exponent Estimates and Short-time Expansion

Exponential divergence of two nearly identical points in state space can be quantified by the Lyapunov exponents of a system. If the largest exponent in a deterministic system is positive, this signifies exponential expansion and thus chaos. For small and noisy data sets, the

computation of Lyapunov exponents can be very difficult. Most algorithms, in particular Kantz' method [31], look at the expansion rates of small neighborhoods of points localized in state space and average them out as time evolves. However, in our previous experiments, this method did not provide meaningful information for short time series with a great deal of noise or extremely rapid expansion [28]. In the case of short data sets recorded from *in vitro* bursting experiments in rat hippocampi, it was necessary to use larger initial neighborhoods to obtain enough initial points for the method to work correctly. These larger neighborhoods then expanded to the size of the entire attractor so quickly that it was impossible to calculate an accurate average expansion rate.

To overcome these obstacles, we developed a new method of detecting determinism, *short-time expansion (STE)*, which measured the rate of spread among nearby points in state space after only one time step [27]. It averaged this rate of spread over the entire "attractor" (i.e., all the points in the data set) which reduced the effects of local noise on the computations. Thus, it was a global measure of the mean expansion rate over the entire state space. While the resulting measure of expansion was not a Lyapunov exponent, it would converge to the largest Lyapunov exponent in a noiseless system. The global expansion rate of the data was then compared with that of randomized surrogates of the data. Since a deterministic system should expand at a slower rate than a stochastic systems (if the amplitude of the noise was comparable to the size of the attractor), this comparison enabled us to identify the presence of determinism in the data.

For each point in the data set, a given number of nearest neighbors was found and was then fit to an ellipse using principal components analysis (PCA). The square root of the largest principal component component (i.e., the standard deviation) was used as a measure of the initial spread between the points. The points in the neighborhood were then evolved one iterate into the future. PCA was again performed on the evolved neighborhood, and the square root of the ratio of the two largest principal components then provided a measure of the one-step expansion rate. The local Lyapunov exponent could be estimated by the

natural logarithm of this rate. The global expansion rate (L_{ave}) was then obtained by averaging the local estimates. That is,

$$L_{ave} = \sum_{i=1}^{B} \frac{\lambda_i \cdot n_i}{n_{total}}, \qquad \lambda_i = \ln\left(\sqrt{\frac{p_1}{p_0}}\right), \tag{7.1}$$

where p_0 and p_1 were the largest principal components of the initial and iterated clouds of points, respectively; n_i was the number of points in each box; n_{total} was the total number of points; B was the number of boxes; and λ_i was the local expansion rate. It was expected that after only one time step small neighborhoods of points would not spread out as quickly in deterministic systems as they would in strongly stochastic systems. If the system contained a large stochastic component, the points would likely spread out over most if not all of the attractor after only one time step. Also, additive (extrinsic) noise should average out in this calculation leaving primarily the deterministic component. Therefore, L_{ave} should be smaller for a deterministic system than for a stochastic system.

In order to test for determinism in the short-time expansion rate analysis, we generated surrogate data by randomly shuffling the order of the IBIs [19]. The surrogate data represented the null hypothesis that the experimental data could be explained by a linear stochastic process. If the L_{ave} vs. nearest neighbor (NN) curve for the original data was significantly different from the average curve computed for the surrogates, then the likelihood of determinism being present would be strengthened.

This method was used to analyze 12 sets of IBI data from high-$[K^+]_o$ and zero-$[Mg^{2+}]_o$ experiments and 5 surrogates of each data set. The curve in Fig. 7.2 shows the experiment with the biggest difference between data and corresponding surrogate average. Even in this case, there was no noticeable flattening of the data curve; it was almost parallel with the surrogate mean curve. Other data curves displayed even greater similarity to their surrogates' curves. However, the curve in this case was displaced from the surrogates, which may mean that it is not quite as disordered as the surrogates. Thus, the results of this analysis suggest that globally the bursting data contain a great deal of stochastic

noise with no determinism detectable by our measure of the global expansion rate. This suggested that chaos control might be difficult to achieve in practice, especially if the amplitude of the noise were larger than the region in which control was desired.

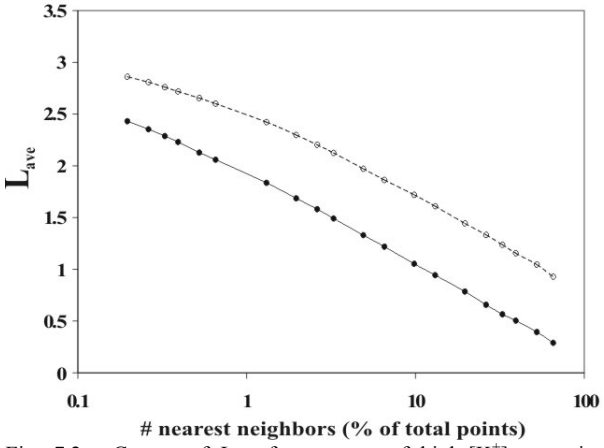

Fig. 7.2. Curves of L_{ave} for one set of high-$[K^+]_o$ experimental data (M) and corresponding surrogates (F) both decline logarithmically to zero with increasing NN. No plateaus are evident which indicates that the data are stochastic.

7.2.3. Local Measure of Chaos: Unstable Periodic Orbits

A chaotic attractor can be described by a skeleton of unstable periodic orbits (UPOs) [32]. These UPOs are periodic paths in state space to and from which the system recurrently approaches and recedes. The presence of UPOs in a system implies the presence of determinism and suggests chaos. Furthermore, the presence of UPOs strengthens the rationale for using chaos control techniques to manipulate bursting, since UPOs are the points around which control can be applied [10]. Le Van Quyen *et al.* [33] found evidence of a few period-1 orbits in epileptic EEG recordings from three human subjects. So *et al.* [34] found several period-1 orbits in both the high-$[K^+]_o$ *in vitro* model and in human epileptic EEG recordings as well as a few orbits of periods 2 and 3 in intracellular recordings from CA1 neurons in normal ACSF. More

recently, another group found period-1 orbits in guinea pig hippocampal slices induced to burst using soman and 4-aminopyridine [35]. Our group used the method of So *et al.* [13] to search for low-period orbits. This technique uses a transformation to concentrate data around UPOs thus creating peaks in the histogram of the transformed data that correspond to the locations of the UPOs. The significance of these peaks was assessed using surrogate data.

For period-1 orbits, the transformation was defined as

$$\hat{\mathbf{z}} \equiv [\mathbf{I} - \mathbf{S}(\mathbf{z}, \mathbf{R})]^{-1} \cdot [\mathbf{F}(\mathbf{z}) - \mathbf{S}(\mathbf{z}, \mathbf{R}) \cdot \mathbf{z}], \tag{7.2}$$

where **x** was the d-dimensional time-delay vector of IBIs, **I** was the identity matrix, **F(x)** was a vector of the next iterate of **x**, and **S(x,R)** was a d×d matrix function of **x** and a d×d×d random tensor **R** given by

$$\mathbf{S}(\mathbf{z}, \mathbf{R}) = \nabla \mathbf{F}(\mathbf{z}) + \mathbf{R} \cdot [\mathbf{F}(\mathbf{z}) - \mathbf{z}]. \tag{7.3}$$

Here **∇F(x)** was the d×d Jacobian matrix of **F(x)**, which was calculated using a least-squares fit of 3 nearest neighbors in state space. This transform was applied to every point **x** in the set and summarized in a spatial distribution function of the experimental data approximated by a histogram with a bin size of 0.02 seconds. The transformation shifted all points in the linear region of a fixed point **x*** even closer to **x***, thus creating a peak in the distribution function ($\hat{x}$). Fifty surrogate data sets were generated and transformed, and their corresponding probability distributions were calculated and averaged together. A cumulative histogram of the maximum deviation of each surrogate from the surrogate mean at each point was used to estimate the probability that ZW a peak in the transformed data was due to the presence of a true UPO at that point. To account for nonstationarity of the data (i.e., drifting of the mean IBI length) due to factors such as fatigue of the neurons, network plasticity, or fluctuations in temperature and pressure, each set of data was divided into windows of 256 IBIs and then analyzed.

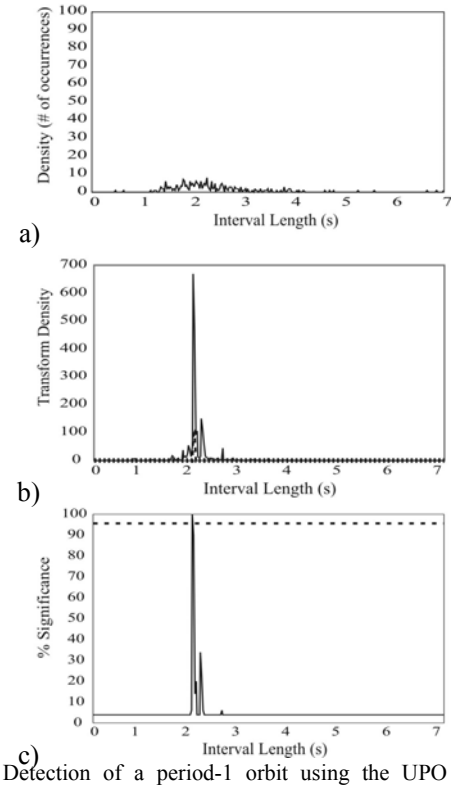

Fig. 7.3. Detection of a period-1 orbit using the UPO transform. a) Histogram of the raw IBI data. b) Histogram of transformed data (solid) and mean of transformed surrogates (dotted). c) A fixed point is found at the location of the peak (1.98 s) with $p<0.04$ (dashed line represents 96% significance line).

A histogram of one window of the original (untransformed) IBIs from a high-$[K^+]_o$ experiment is shown in Fig. 7.3a. Note that no discernible peak is shown at the location of the period-1 orbit. After the transform is performed on the data (Fig. 7.3b), a sharp peak in the data (solid line) is seen at the corresponding location of the period-1 orbit (1.98 s). The dashed line shows the histogram of the mean of the transformed surrogates. Note that the peak for the surrogates is much lower than that for the transformed IBI data. A UPO was declared statistically significant if the peak in the distribution function of the data (minus the surrogate mean) was greater than 96% of the maximal peaks of the

transformed surrogates (minus the surrogate mean). Since the peak in Fig. 7.3c is above the 96% significance line, it marks the location of a true period-1 orbit at 1.98 s. Period-1 orbits were found in 71% of the 17 high-$[K^+]_o$ experiments, 25% of the eight zero-$[Mg^{2+}]_o$ preparations, and 75% of the eight $GABA_A$ blockade experiments. Due to nonstationarity, period-1 orbits emerged, drifted, and disappeared over the course of an experiment.

The case for chaos is made even stronger when orbits of higher periods are considered. UPOs of period 2 (Fig. 7.4a) and period-3 (Fig. 7.4b) were found in more than 35% of the high-$[K^+]_o$ experiments, 50% of the zero-$[Mg^{2+}]_o$ experiments, and 50% of the $GABA_A$ antagonist experiments. The significance in this three-dimensional representation of a two-dimensional histogram is coded by color and height. Thus strong evidence of determinism was found using UPO analysis. While these results seem to present conflicting evidence, they might suggest that *in vitro* epileptiform bursting may contain local islands of determinism (UPO detection) within a globally stochastic sea (Lyapunov analysis). It is possible that the noise level of the system was so high that it drowned out the determinism even using global averages.

7.3. Chaos Control of Epileptiform Bursting

The property of sensitive dependence on initial conditions would lead one to believe that chaotic systems cannot be controlled. However, it has been shown [36] that it is indeed possible to control chaotic behavior – i.e., to move the system from a chaotic orbit to a periodic orbit. The basic principle is that all saddle fixed points have at least one stable and one unstable manifold associated with them, and these manifolds can be linearly approximated within a small radius (hereafter referred to as the control radius). Ott, Grebogi, and Yorke [37] showed that chaos can be controlled using relatively small perturbations to system parameters (a.k.a. OGY control). Another, simpler method was developed by Hunt [38] and successfully applied to a nonlinear diode circuit. Modifications to these two techniques have subsequently been developed. Other control schemes using artificial neural networks have also been proposed [39-41]. Since then, many chaos control algorithms have been advanced

[42-45]. A variant of OGY called proportional perturbation feedback (PPF) [43] modified the system state point (viz., the interburst interval) instead of a system parameter. Schiff *et al.* [10] were the first to control epileptiform bursting in the hippocampal slice using PPF. However, their results did not reveal how many of the bursts were "stimulated" vs. how many were "spontaneous." Thus our laboratory set out to control bursting using a more rigorous approach. We used a modification of PPF called stable manifold placement (SMP) [46] which is simpler and more robust than PPF because it requires less assumptions to be made about system parameters.

In this section, we explore in detail the modification of bursting behavior using techniques from chaos control. Accurate fixed point estimation is crucial to the success of chaos control. Therefore, in addition to SMP control, we implemented for the first time in a biological system a method of continuously refining the fixed point and stable manifold estimates, developed by Christini and Kaplan [47]. We also describe a novel protocol, *state-point forcing*, that helps determine the validity of fixed point estimates and assesses the feasibility of chaos control.

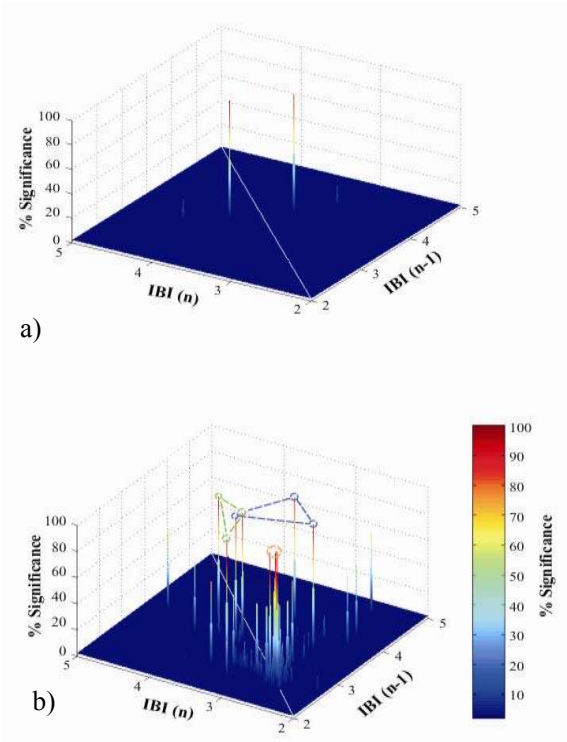

Fig. 7.4. Period-2 and period-3 orbits in 3-D representations of 2-D state space. a) Significance plot of a period-2 orbit (red peaks) in a high-$[K^+]_o$. Significance is shown by the color bar at right and by the height. b) Two period-3 orbits from a zero-$[Mg^{2+}]_o$ model. The two sets of three red peaks (circled in green and blue) manifest the three points along two period-3 orbits. A fixed point is circled in orange.

7.3.1. Slice Electrophysiology

A real-time data acquisition processor recorded the IBIs, calculated when a stimulus needed to be delivered, and sent out the stimulus signal. A bipolar tungsten stimulating electrode was placed in the Schaffer collaterals (Fig. 7.1a). Stimuli consisted of single, 80 μs square-wave current pulses with amplitudes 0.1-0.3 mA. The host computer ran the control software that performed fixed point detection (using the algorithm described above [34, 38] with 10 surrogates used for significance testing), adaptive control techniques, data storage and display, and enabled changes to system parameters and control techniques in real time.

7.3.2. SMP Control

In SMP control, instead of moving the stable manifold to the state point, the state point was moved onto the stable manifold. Thus, when the state

point fell outside of the control radius, a stimulus was sent to the slice to trigger a burst at the exact time needed to shift the state point onto the stable manifold. The advantage of using SMP was that the calculation of the desired IBI did not require estimation of the next "natural" IBI (as PPF does); instead, it was obtained through simple algebra. That is, the desired IBI value was given by

$$x_{n+1} = \lambda_s (x_n - x^*) + x^*, \tag{7.4}$$

where x_n was the current IBI, x^* was the fixed point, and λ_s was the eigenvalue (slope) of the stable manifold. The displayed IBIs were marked as stimulated or unstimulated. This assisted our assessment of the quality of control attained.

Using the SMP algorithm, the variance of IBIs was reduced compared to uncontrolled bursting, but tight control was not achieved (Fig. 7.5). There were several parameters that could affect the performance of this algorithm, including several parameters in the UPO detection algorithm. The number of nearest neighbors used to fit the Jacobian matrix for the UPO transform was optimized to 4, the same number for the Hénon map, since there was no notable effect of changing it. The control algorithm also had to account for the delay between the stimulus and the recorded burst due to finite conduction velocity in the tissue. This stimulus-burst delay was varied from 15-50 ms depending on the properties of each slice. It was kept constant during each experiment. Since the linear approximation of the stable manifold was only accurate within a small distance of the fixed point, we also tried applying control only when the previous state point was within a set radius (R_{UPO}) of the fixed point. R_{UPO} was varied from 0.5-10 s, but there was no noticeable improvement in control quality. When R_{UPO} was small (0.5-1 s) and there were several long IBIs, sometimes it would take a long time before the system state would get close enough to the fixed point for control to resume.

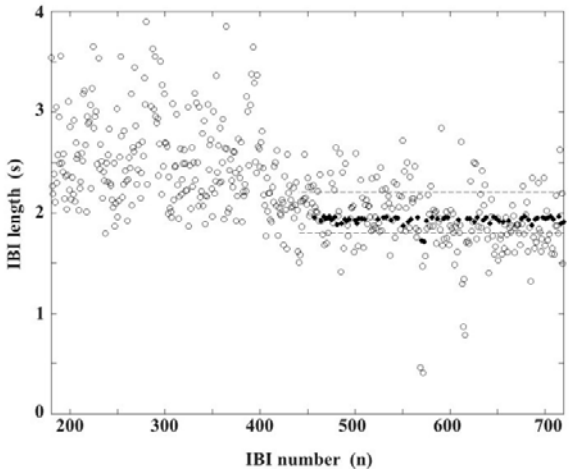

Fig. 7.5. SMP control in a bursting experiment. Beginning of control and control radius marked by dashed lines. IBIs were stimulated (●) vs. natural (○). Variance of IBIs did decrease modestly with control.

7.3.3. Effect of Control Radius (R_c) and Synaptic Plasticity on Control Efficacy

Previous work [49] suggested that stimulating the Schaffer collaterals at low frequencies (~1 Hz) could sometimes cause a form of synaptic plasticity called long term depression (LTD), which could cause IBIs to lengthen over time. To assess whether some of the nonstationarity and impediments to control were due to this form of synaptic plasticity, the NMDA-receptor antagonist AP-5 was used. While LTD might occur using other receptors besides the NMDA type, AP-5 should block the majority of LTD via this pathway. Slices were bathed in high-$[K^+]_o$ ACSF for 20 minutes, and then in high-$[K^+]_o$ ACSF containing 50 μM AP-5. The AP-5 solution was washed in for 5 minutes before starting the same control sequence used above with high-$[K^+]_o$. R_c was again decreased in stepwise fashion. The effect of the size of R_c on control efficacy was investigated both with and without AP-5. Six experiments were done with high-$[K^+]_o$ only, and four were done using high-$[K^+]_o$ plus AP-5. Fig. 7.6 shows examples of experiments in which R_c was varied using high-$[K^+]_o$ only (Fig. 7.6a) or high-$[K^+]_o$ with AP-5 (Fig. 7.6b). As R_c decreased, variance decreased but the proportion of IBIs that were stimulated increased. This conclusion was true for both the standard high-$[K^+]_o$ experiments and for experiments using AP-5. This similarity of results suggested that synaptic plasticity does not

significantly influence the quality of control obtained. We found that the control radius that optimally balanced variance vs. number of stimuli was usually 50-100 ms depending on the initial variance of the bursting.

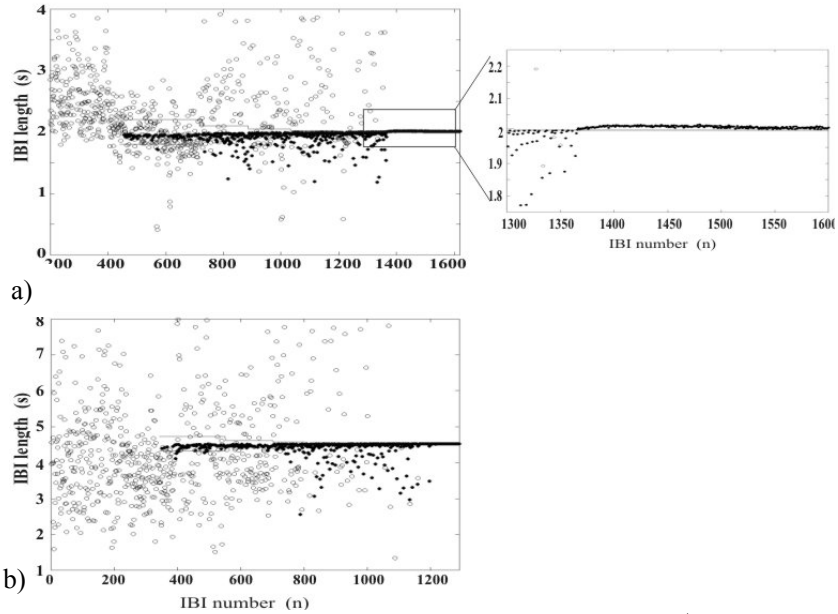

Fig. 7.6. Experiments varying R_c using basic SMP control. a) A high-$[K^+]_o$ experiment varying control radius (R_c, solid lines). As R_c decreased, the variance also decreased, but the ratio of stimulated (●) to unstimulated (○) IBIs increased. The magnification (right) of the boxed area shows the demand pacing phenomenon: all of the IBIs after IBI 1370 are stimulated, since the system never can get within the tiny R_c. b) Similar results were found in experiments using AP-5. Thus, there did not appear to be any effects from LTD.

At extremely small control radii, nearly every IBI was stimulated (see inset in Fig. 7.6a). This occurred because R_c was smaller (2 ms) than the precision of the stimulus-burst interval. That is, the interval from when the stimulus was applied to when the burst was detected fluctuated by a few milliseconds from burst to burst, and therefore the estimate could be off by as much as 5 ms. Thus, the control algorithm kept stimulating but could not get the IBI within the control region. In this case, the system performed almost identically to demand pacing. Interestingly, the results

looked very similar to those obtained by Schiff *et al*. [10], as well as Christini and Collins [44], especially if the IBIs were not designated as stimulated or natural. Since their work did not make this distinction, it could be possible that their control algorithm was constantly stimulating due to a very small control radius. This could explain why our control of bursting did not seem as striking as those reported earlier.

7.3.4. Adaptive Control Techniques

Accurate estimates of the fixed point location and stable manifold slope were the two key elements needed to achieve good control. Nonstationarity is a significant obstacle in both estimates, especially in fixed point location. One way of overcoming this obstacle is to dynamically refine the approximation of these parameters. This *adaptive tracking* method, adapted from Christini and Kaplan [47] fitted data to linear approximations of the dynamics in the neighborhood of the fixed point to re-estimate the fixed point and stable manifold slope. Assuming that the data were in the neighborhood of a UPO, the unperturbed system dynamics could be approximated by the linear equation $x_{n+1} = ax_n + bx_{n-1} + c$, where the current state point was (x_{n-1}, x_n). Rewritten in terms of the fixed point parameters, this equation became

$$x_{n+1} = \left(\lambda_s + \lambda_u\right)x_n - \lambda_s\lambda_u\, x_{n-1} + x^*\left(1 + \lambda_s\lambda_u - \lambda_s - \lambda_u\right) \tag{7.5}$$

where x* was the fixed point and λ_s and λ_u were the stable and unstable eigenvalues, respectively. When a control stimulus was applied, the system dynamics were described by

$$x_{n+1} = \hat{\lambda}_s(x_n - \hat{x}^*) + \hat{x}^* \tag{7.6}$$

where $\hat{}$ signifies that λ_s and x^* were estimates. That is, when control stimuli were applied, they circumvented the normal fixed point dynamics. Therefore, the natural values of λ_s and x^* could not be estimated from stimulated bursts. However, when unstimulated bursts occurred, the system would behave according to (7.5). The parameters x^*, λ_s, and λ_u could then be estimated by a least-squares fit of the data

triplets (x_{n+1}, x_n, x_{n-1}). Only "natural triplets" – those where x_{n+1} was an unstimulated IBI, but the preceding two points could be stimulated or unstimulated – were used. This regression was performed after every new natural triplet (or, equivalently, natural IBI).

Adaptive tracking noticeably improved control over basic SMP alone [48]. The algorithm successfully adjusted for the drift of the system (Fig. 7.7a). Our refinements of the tracking algorithm and its parameters produced small but incremental improvements in control quality. Several parameters had to be carefully adjusted. The least-squares fit itself had several notable caveats. The number of natural triplets used for the fit (NT) varied from 4-20. Too few triplets could cause poor fits and result in volatile fluctuations of the parameter values. Too many would not allow the algorithm to track the system quickly enough. Also, the fit would sometimes not accurately represent the natural fixed point dynamics. If most of the IBIs were stimulated, and then control was turned off, the state point tended to jump out from the fixed point along the unstable manifold. In this case, the stable manifold could not be estimated accurately since the state point would not approach the fixed point at all. If the majority of the NT triplets behaved this way, the fit would be very poor. Therefore, singular value decomposition (SVD) was used to perform the least-squares fit. If the ratio between the fit's largest and smallest singular values were very large ($>10^6$), then the fit would be poor (ill-conditioned). In that case, the parameter estimates would not be adjusted.

In all of the later experiments, NT was set to 10, but the fixed point estimates still often fluctuated. Therefore, we limited the distance by which the fixed point estimate could change from the current estimate in any one fit. This parameter, called the fixed point adjustment maximum (FAM), was optimized and normally set in the range of 0.5-1s, in proportion to the initial variance of the system. This adjustment reduced variability substantially, but if FAM was set too small, the algorithm wouldn't adapt well. Another modification allowed the algorithm to remove outliers by including only natural triplets in the fit if the natural IBIs were within a certain radius (R_{NT}) of the current fixed point location. Improving the fit also reduced fluctuations in the fixed point estimates. The optimal range for R_{NT} was about 0.4-1 s, depending on the variance

of all the data. While the results using this technique were not dramatic, they were a definite improvement over basic SMP control. At first, the tracking algorithm produced some fluctuations in the fixed point estimates which inhibited control. After adding regulating parameters such as the FAM and R_{NT}, the fixed point estimate tracked with the system smoothly over time. Even with these modifications, triplet regression would still occasionally make "illogical" adjustments to the fixed point location. For example, when all the natural IBIs were greater than the fixed point, the new fixed point estimate would still sometimes be set smaller than the current estimate. We therefore required that the new estimate move in the same direction as most of the natural IBIs are located relative to the current fixed point. This modification helped stabilize control.

On several occasions in tracking experiments, the system briefly remained in a period-2 or period-3 orbit for approximately 6-12 IBIs, as seen in Fig. 7.7b. We also observed a few shorter encounters where the system stayed in a period-1 orbit (i.e., extremely close to the fixed point) for a few IBIs. These encounters provided tantalizing hints that control was indeed possible, at least for short periods of time. These "close encounters" were seen in different experiments, but recurrence to the same period-2 orbit later in the experiment was not usually seen probably due to nonstationarity. The fact that higher-period orbits were attained more often than period-1 orbits suggests that the fixed point estimate was close but still not accurate enough.

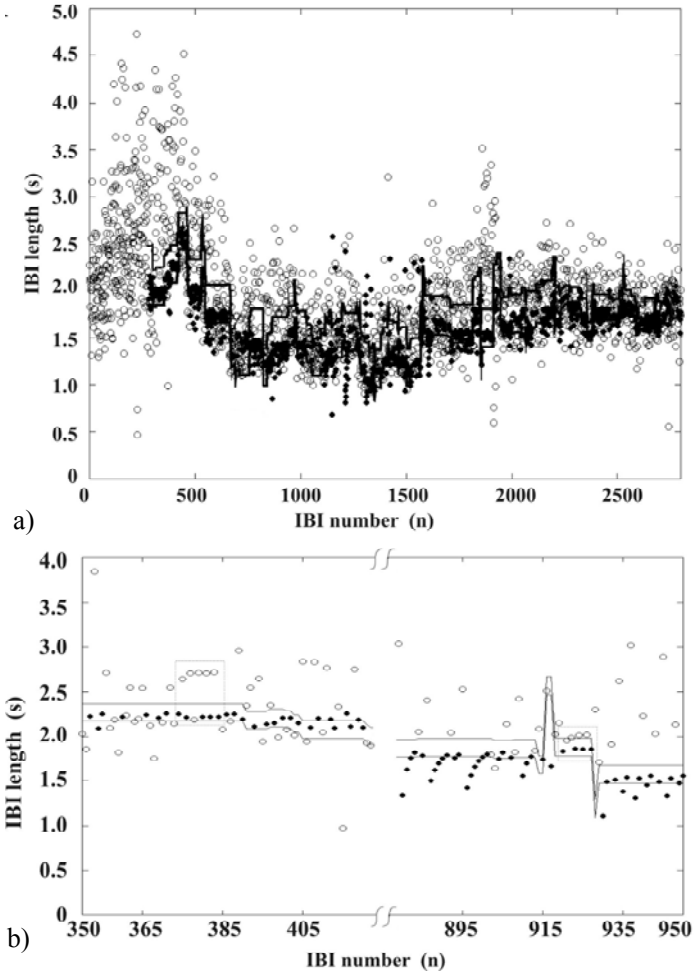

Fig. 7.7. Adaptive tracking control of bursting. A) An example of a tracking experiment. The fixed point estimate and control region (solid lines) tracks along well with the system. Variance is relatively low, but a large amount of stimulated IBIs (●) are still needed. b) Two brief encounters with possible period-2 orbits in one experiment, shown in the dashed boxes near IBIs 375 and 920.

7.4. Feasibility of Control and Fixed Point Detection by State-point Forcing

To help ascertain exactly what were the obstacles to control, we developed a novel control protocol called *state point forcing*. Previously, the control algorithm only applied a single stimulus that placed the state point on the stable manifold estimate and let the system drift in to the fixed point on its own. In contrast, the new approach kept stimulating until the state point was on (or very close to) the fixed point in two dimensions. (Due to limitations in stimulus-burst interval precision, the state point could not always be forced exactly onto the fixed point, so it merely had to be within 40 ms of the fixed point.) The stable manifold slope estimate was set to zero to minimize the amount of stimuli needed. If the fixed point estimate were accurate, then the state point should remain close to the fixed point on the next iterate. However, if the fixed point estimate were not accurate (or no fixed point existed at that time) then the state point could end up anywhere on the next iterate. We therefore hypothesized that if we first forced the state point onto the fixed point and then forced it onto some other arbitrary point in the system attractor, the subsequent iterates should in general stay closer to the fixed point than to the arbitrary point. If there were a significant difference between the two cases, it would imply that the fixed point estimate was relatively accurate.

To quantify these differences, we used the change in the center of mass (ΔX_{cm}) of the cluster of points around the forced point and after an iterate If the system state were forced onto a true fixed point, then ΔX_{cm} should be small, while if it were forced onto an arbitrary point (or an inaccurate fixed point estimate), then ΔX_{cm} should be relatively big. When a significant fixed point was found, the state point was alternately forced onto the fixed point or the arbitrary point for 30-40 IBIs each,. The forcing point switched between the fixed point and the arbitrary point several times, until the fixed point seemed to be drifting due to nonstationarity.

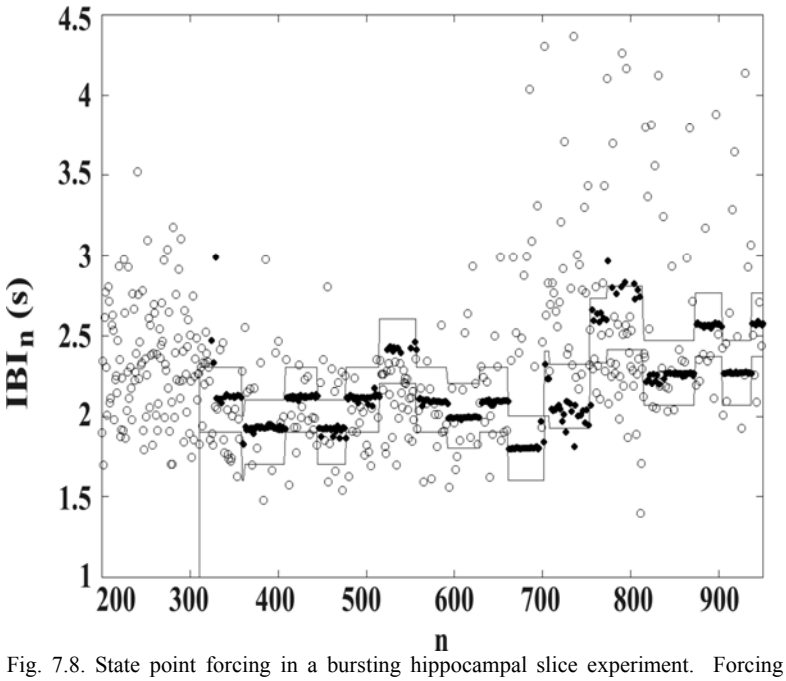

Fig. 7.8. State point forcing in a bursting hippocampal slice experiment. Forcing alternated between the fixed point and arbitrary points 4 times (counted as 4 fixed point trials in analysis). Then tracking was turned on (at n~700) until a new fixed point was found at n=820. Tracking was then turned off and forcing turned back on. Natural IBIs stayed closer to fixed points than to arbitrary points.

At this point, state-point forcing was turned off and the fixed point was relocated using adaptive tracking . If a suitable fixed point estimate was found (i.e., tracking seemed to be working and had stabilized at one location after a while), then tracking was turned off, λ_s was set to 0, and state-point forcing resumed. An example of a state-point forcing experiment is shown in Fig. 7.8.

The value of ΔX_{cm} was computed for each fixed point and its corresponding arbitrary forcing point. The fixed point trials were evenly split (51 each) between those detected with the UPO transform (UPOT) and those found with the adaptive tracking algorithm (AT). Statistical comparisons of ΔX_{cm} were made with the paired t-test or the Wilcoxon signed rank test. The data were first compared for both UPO types

combined, and ΔX_{cm} was significantly smaller when forcing to the fixed points than to the arbitrary points (median values 0.258 s vs. 0.404 s, $P<0.004$, signed rank test). The UPOT fixed points alone did not show a significant difference in ΔX_{cm}, but the AT fixed points did have significantly smaller ΔX_{cm} when forcing to the fixed vs. arbitrary point.

We designed the state-point forcing protocol to ascertain whether control was at all feasible and to help identify the obstacles in detail. Specifically, we sought to verify that our fixed point estimates were valid. Also, if the system state would not stay close to the fixed point for a few iterates even when placed directly onto the fixed point, then no control short of pacing (tonic stimulation) would have much chance of working. The results of the forcing experiments suggested that the fixed point estimates were indeed valid, since forcing onto the fixed points produced significantly less divergence in the subsequent iterate than did forcing onto the arbitrary points.

More detailed analysis revealed that forcing to fixed points found with adaptive tracking (AT) produced significant results whereas those found with the UPO transform (UPOT) did not. This suggested that perhaps the adaptive tracking algorithm provided better estimates of the fixed point than did the UPO transform algorithm. When the UPO transform was applied offline (using 50 surrogates to test significance) to state-point forcing data, only 23% of the fixed points detected online (using 10 surrogates) were found to be statistically significant offline. This could be the reason that the forcing protocol did not produce significant results for UPO-transformed fixed points. Moreover, it is possible that much of the difficulty we had with control was due to inaccurate or false fixed point estimates. Another notable result was that when the arbitrary forcing point was shorter than the fixed point, the difference in ΔX_{cm} was strongly significant ($P<0.0001$), whereas when the arbitrary forcing point was longer than the fixed point, the difference in ΔX_{cm} was not significant ($P=0.8$). This result could be explained in two ways. The first is artifactual: when the arbitrary point was shifted up, the neurons often burst spontaneously before stimuli could be applied, and thus there were fewer points that could be used in the calculation of ΔX_{cm}. Alternatively, when the arbitrary point was shifted down, the stimuli would be occurring more quickly, thus giving the neurons less

time to recover, and therefore the next spontaneous bursts could have been longer simply because the neurons were refractory. We tried to avert this second possibility by shifting the arbitrary point by different amounts, in a range from 0.1 s to 0.4 s.

7.5. Obstacles to Chaos Control

The implications of these results for the feasibility of control were not as clear. The next IBIs (after a stimulated burst) stayed relatively close to the fixed points, although not as close as would be required to obtain tight control. This may have been due to the high levels of stochastic dynamical noise that were also present in the system. A high level of noise certainly would have hindered attempts to control the system – especially if the amplitude were on the order of the control radius – since the system state would often bounce out of the control region as soon as it was placed within it. It would have also impaired the fixed point and stable manifold estimates. Unfortunately, there was no way of empirically determining the level of noise in the system, so we could not determine whether noise was the biggest impediment to control.

Estimation of the stable manifold was itself a very difficult task. Even with a low-noise system, the method of fitting local neighbors of the fixed point using a linear least-squares algorithm was a simplification. It is far from certain that the manifolds were linear, so any linear approximation would only be accurate within a very small radius of the fixed point. It is possible (due to small sample size) that the four neighbors used for the Jacobian were often outside of this linear region. With the addition of high-level noise, fitting the stable manifold could become problematic because there are too few natural triplets that approach the fixed point.

Several necessary assumptions were made that may have had an effect on the quality of control achieved. The use of IBIs as the state variable was somewhat arbitrary; mainly made to stay consistent with prior studies [10, 44]. The use of IBIs may have contributed to noise and nonstationarity since they vary on a long time scale and thus many factors can change in between each measurement. Perhaps using a variable such as the raw extracellular voltage could have improved the

results. However, it would have been extremely difficult to precisely control extracellular voltage levels using a point-source electrode. Also, a two-dimensional embedding may have been too small to capture the entire system's dynamics. We used it because it greatly simplified the calculations and because it was the same dimension used as previously reported by Schiff *et al.*[10]. Moreover, all of these studies [10, 43, 44, 48] have used only one spatial dimension; it is possible that increasing the spatial dimensionality of the state variable may help control the system. All of these assumptions were necessary to make but also could have compromised control efficacy if they were inaccurate.

Finally, the phenomenon of nonstationarity was a large obstacle to control. There were many potential sources for drift of IBI values. Fluctuations in flow rate and temperature could easily have altered the system behavior by system metabolism. There also could have been intrinsic nonstationarity in the bursting itself. Synaptic plasticity did not appear to have a significant effect, but it is possible that the slice became "fatigued" or refractory. We attempted to control for fatigue by ensuring that burst amplitudes remained constant throughout the experiment, since burst amplitude is an indicator of neurotransmitter supply [49].

7.6. Conclusion

Chaos control techniques showed modest success at controlling spontaneous epileptiform bursting. Adaptive tracking noticeably improved control over non-adaptive methods and seemed to counter nonstationarity, but intrinsic randomness may have prevented us from obtaining precise control. The process of slicing the hippocampus itself severs many regulatory connections, both extrinsic and intrinsic. It is possible that the intact brain could be less noisy or more stationary than the *in vitro* hippocampal slice, and hence easier to control.

It is still not known whether controlling interictal bursts or spikes (or anticontrolling, i.e., making them more disordered [50]) could prevent a seizure. Nor is it known how tightly the spikes would have to be controlled to be successful. However, if one could maneuver the system from a chaotic to a periodic state, then it is likely that one could also convert it from a periodic to a chaotic one. Once the ability to

manipulate the system is established, one could then determine whether a chaotic or periodic rhythm would be desirable to stop or prevent seizure activity. Thus, continued exploration, and extension of analysis algorithms into multiple spatiotemporal dimensions, should help reveal whether chaos control is a practical solution for preventing epileptic seizures.

References

[1] P. Kwan and M. J. Brodie, Early identification of refractory epilepsy, *N Engl J Med* **342**(5), 314-319, (2000).

[2] G. D. Cascino, Improving quality of life with epilepsy surgery: The seizure outcome is the key to success, *Neurology* **68**(23), 1967-1968, (2007).

[3] E. Behrens, J. Schramm and J. Zentner et al., Surgical and neurological complications in a series of 708 epilepsy surgery procedures, *Neurosurgery* **41**(1), 1-9, (1997).

[4] B. J. Gluckman, H. Nguyen and S. L. Weinstein et al., Adaptive electric field control of epileptic seizures, *J Neurosci* **21**(2), 590-600, (2001).

[5] G. L. Morris and W. M. Mueller, Long-term treatment with vagus nerve stimulation in patients with refractory epilepsy, *Neurology* **53**(8), 1731-1735, (1999).

[6] F. Velasco, M. Velasco and A. L. Velasco et al., Electrical stimulation of the centromedian thalamic nucleus in control of seizures: long-term studies, *Epilepsia* **36**(1), 63-71, (1995).

[7] S. N. Lim, S. T. Lee and Y. T. Tsai, Electrical stimulation of the anterior nucleus of the thalamus for intractable epilepsy: A long-term follow-up study, *Epilepsia* **48**(2), 342-347, (2007).

[8] K. P. B. Vonck, E. Achten, J. de Reuck and J. Caemaert, Long-term amygdalohippocampal stimulation for refractory temporal lobe epilepsy, *Annals of Neurology* **52**(5), 556-565, (2002).

[9] J. I. Sirven, M. Sperling and D. Naritoku et al., Vagus nerve stimulation therapy for epilepsy in older adults, *Neurology* **54**(5), 1179-1182, (2000).

[10] S. J. Schiff, K. Jerger and D. H. Duong et al., Controlling chaos in the brain, *Nature* **370**(6491), 615-620, (1994).

[11] J. Gotman and M. G. Marciani, Electroencephalographic spiking activity, drug levels, and seizure occurrence in epileptic patients, *Ann Neurol* **17**(6), 597-603, (1985).

[12] S. F. Traynelis and R. Dingledine, Potassium-induced spontaneous electrographic seizures in the rat hippocampal slice, *J Neurophysiol* **59**(1), 259-276, (1988).

[13] M. Barbarosie and M. Avoli, CA3-driven hippocampal-entorhinal loop controls rather than sustains in vitro limbic seizures, Characterizing nonlinearity in invasive EEG recordings from temporal lobe epilepsy, *J Neurosci* **17**(23), 9308-9314, (1997).

[14] M. C. Casdagli, L. D. Iasemidis and J. C. Sackellares et al., Characterizing nonlinearity in invasive EEG recordings from temporal lobe epilepsy, *Physica D* **99**(2-3), 381-399, (1996).
[15] I. Yaylali, H. Kocak and P. Jayakar, Detection of seizures from small samples using nonlinear dynamic system theory, *IEEE Transactions on Biomedical Engineering* **43**(7), 743-751, (1996).
[16] J. Sarnthein, H. D. I. Abarbanel and H. Pockberger, Nonlinear analysis of epileptic activity in rabbit neocortex, *Biological Cybernetics* **78**(1), 37-44, (1998).
[17] J. Theiler, On the Evidence for low-dimensional chaos in an epileptic electroencephalogram, *Physics Letters A* **196**(5-6), 335-341, (1995).
[18] J. P. Pijn, J. Vanneerven and A. Noest et al., Chaos or noise in EEG signals - Dependence on state and brain site, *Electroencephalography and Clinical Neurophysiology* **79**(5), 371-381, (1991).
[19] J. Theiler, S. Eubank and A. Longtin et al., Testing for nonlinearity in time-series - The method of surrogate data, *Physica D* **58**(1-4), 77-94, (1992).
[20] D. T. Kaplan, Exceptional events as evidence for determinism, *Physica D* **73**(1-2), 38-48, (1994).
[21] P. G. Aitken, T. Sauer, and S. J. Schiff, Looking for chaos in brain slices, *J Neurosci Methods* **59**(1), 41-48, (1995).
[22] S. Pueyo, The study of chaotic dynamics by means of very short time series, *Physica D* **106**(1-2), 57-65, (1997).
[23] P. Grassberger, T. Schreiber, and C. Schaffrath, Nonlinear time sequence analysis, *International Journal of Bifurcations and Chaos* **1**, 521-547, (1991).
[24] T. Chang, S. J. Schiff and T. Sauer et al., Stochastic versus deterministic variability in simple neuronal circuits: I. Monosynaptic spinal cord reflexes, *Biophys J* **67**(2), 671-683, (1994).
[25] D. Petracchi, The search for periodic unstable orbits in periodically driven spike trains, *Chaos Solitons and Fractals* **8**(3), 327-334, (1997).
[26] S. J. Schiff, K. Jerger and T. Chang et al., Stochastic versus deterministic variability in simple neuronal circuits: II. Hippocampal slice, *Biophys J* **67**(2), 684-691, (1994).
[27] M. W. Slutzky, P. Cvitanovic and D. J. Mogul, Identification of determinism in noisy neuronal systems, *J Neurosci Methods* **118**(2), 153-161, (2002).
[28] M. W. Slutzky, P. Cvitanovic and D. J. Mogul, Deterministic chaos and noise in three in vitro hippocampal models of epilepsy, *Ann Biomed Eng* **29**(7), 607-618, (2001).
[29] F Takens, *Detecting Strange Attractors in Turbulence, Lecture Notes in Mathematics* **898**, (Springer-Verlag, New York, 1981).
[30] T. Sauer, Interval embedding of chaotic signals, *Chaos* **5**(1), 127-132, (1995).
[31] H. Kantz, A robust method to estimate the maximal Lyapunov exponent of a time-series, *Physics Letters A* **185**(1), 77-87, (1994).
[32] D. Auerbach, P. Cvitanovic and J. P. Eckmann et al., Exploring chaotic motion through periodic orbits, *Phys Rev Lett* **58**(23), 2387-2389, (1987).
[33] J. Martinerie, C. Adam and M. Le Van Quyen et al., Epileptic seizures can be anticipated by non-linear analysis, *Nature Medicine* **4**(10), 1173-1176, (1998).

[34] P. So, J. T. Francis and T. I. Netoff et al., Periodic orbits: a new language for neuronal dynamics, *Biophys J* **74**(6), 2776-2785, (1998).
[35] P. K. Harrison, J. E. H. Tattersall and R. A. Clement, Periodic orbit analysis reveals subtle effects of atropine on epileptiform activity in the guinea-pig hippocampal slice, *Neuroscience Letters* **357**(3), 183-186, (2004).
[36] T. Shinbrot, Progress in the control of chaos, *Advances in Physics* **44**(2), 73-111, (1995).
[37] E. Ott, C. Grebogi and J. A. Yorke, Controlling chaos, *Physical Review Letters* **64**(11), 1196-1199, (1990).
[38] E. R. Hunt, Stabilizing high-period orbits in a chaotic system - The diode resonator, *Physical Review Letters* **67**(15), 1953-1955, (1991).
[39] P. M. Alsing, A. Gavrielides and V. Kovanis, Using neural networks for controlling chaos, *Physical Review E* **49**(2), 1225-1231, (1994).
[40] M. Funke, M. Herrmann and R. Der, Controlling low-dimensional chaos: Determination and stabilization of unstable periodic orbits by Kohonen neural nets, *International Journal of Adaptive Control and Signal Processing* **11**(6), 489-499, (1997).
[41] C. T. Lin and C. P. Jou, Controlling chaos by GA-based reinforcement learning neural network, *IEEE Transactions on Neural Networks* **10**(4), 846-859, (1999).
[42] K. Pyragas, Continuous control of chaos by self-controlling feedback, *Physics Letters A* **170**(6), 421-428, (1992).
[43] A. Garfinkel, M. L. Spano and W. L. Ditto et al., Controlling cardiac chaos, *Science* **257**(5074), 1230-1235, (1992).
[44] D. J. Christini and J. J. Collins, Controlling nonchaotic neuronal noise using chaos control techniques, *Phys Rev Lett* **75**(14), 2782-2785, (1995).
[45] M. Z. Ding, W. M. Yang and V. In et al., Controlling chaos in high dimensions: Theory and experiment, *Physical Review E* **53**(5), 4334-4344, (1996).
[46] D. J. Christini and J. J. Collins, Control of chaos in excitable physiological systems: A geometric analysis, *Chaos* **7**(4), 544-549, (1997).
[47] D. J. Christini and D. T. Kaplan, Adaptive estimation and control method for unstable periodic dynamics in spike trains, *Physical Review E* **61**(5), 5149-5153, (2000).
[48] M. W. Slutzky, P. Cvitanovic and D. J. Mogul, Manipulating epileptiform bursting in the rat hippocampus using chaos control and adaptive techniques, *IEEE Trans Biomed Eng* **50**(5), 559-570, (2003).
[49] J. S. Bains, J. M. Longacher and K. J. Staley, Reciprocal interactions between CA3 network activity and strength of recurrent collateral synapses, *Nature Neuroscience* **2**(8), 720-726, (1999).
[50] K. Gupta, H. P. Singh and B. Biswal et al., Adaptive targeting of chaotic response in periodically stimulated neural systems, *Chaos* **16**(2), (2006).

Section C

Control for Discrete-time Systems

CHAPTER 8

CHAOS CONTROL FOR PHASE LOCK LOOP

A.M. Harb[*] and B.A. Harb[**]

[*]*Department of Electrical Engineering,*
Jordan University of Science and Technology, Irbid, Jordan
E-mail: aharb@just.edu.jo
[**]*Department of Electrical Engineering,*
Yarmouk University, Irbid, Jordan
E-mail: bharb@yu.edu.jo

Previous study showed that a third-order phase locked loop (PLL) with sinusoidal phase detector characteristics experienced a Hopf bifurcation point as well as chaotic behavior. As a result, this behavior drives the PLL to the out-of-lock (unstable) state. The analysis was based on a modern nonlinear theory such as bifurcation and chaos. The main goal of this chapter is to control this chaotic behavior. A nonlinear controller based on the theory of backstepping is designed. The study showed the effectiveness of the designed nonlinear controller in controlling the undesirable unstable behavior and pulling the PLL back to the in-lock state.

8.1. Introduction

8.1.1. The Concept of Phased Lock Loop

Phase locked loops (PLLs) are an important part of modern electronic communication and control systems due to its accuracy, controllability, and capability of providing high power and frequency [1, 2]. They play a major role in electronic synchronization circuits. Its ability on tracking phase-varying signal makes it very attractive to be used in systems where

it is necessary to estimate the phase of a received signal. Also, they are used extensively in applications requiring the synthesis of highly stable sinusoidal signals. In such systems, it is often necessary to estimate the instantaneous phase of a received signal which has been contaminated by random noise/or other type of interference. Often, one is supplied with a sinusoidal reference voltage, and it is necessary to produce a second sinusoidal voltage having a frequency which is an integer multiple of the reference's frequency. PLLs offer a practical method of performing these tasks. The basic configuration of a PLL is shown in Fig. 8.1. It consists of three building blocks; a phase detector, a time-invariant loop filter and a voltage controlled oscillator (VCO) [3]. The PLL is considered to be phase locked when the loop's phase error is constant ϕ_o and the loop is in stable equilibrium state [4, 5]. This means that small perturbation from ϕ_o, in the phase error will eventually dampen out as a result of the closed loop dynamic. Equivalently, ϕ_o is an asymptotically stable solution of the autonomous, nonlinear differential equation describing the closed loop phase error. The PLL can be false locked [4-7] where a periodic orbit exists for a certain loop parameter. It is known that the PLL under consideration exhibits a chaotic behavior preceded by a series of period doubling for the periodic orbit associated with false lock state of the PLL.

Chaos in phase-locked loops has been investigated by many researchers for at least two decades. Phase locked loops like many chaotic systems such as Chua's circuit family [8], Josephson junctions [9] and Van der Pol oscillator [10] have been studied extensively in the literature. Recently, research on chaos in phase-locked loop has extended beyond analysis of chaotic behavior. The idea of chaos synchronization was utilized to build communication systems to ensure the security of information been transmitted [11].

The PLL under consideration is considered as a chaos generator for such systems. This kind of response is undesirable for other communication systems. For example, when the PLL is used to demodulate an FM signals, the output of the VCO may become chaotic for certain loop parameters. This behavior drives the PLL to the out-of-lock state [12]. In both cases, chaos prediction and controlling (when it is undesirable) are of a great importance for the designer.

Endo and Watada [13] determined the bifurcation sets of the Shilinkov-type homoclinic orbits for a third-order autonomous PLL with a symmetric periodic triangular phase detector having a second order loop filter. It was shown that this kind of PLL has a chaotic attractor. Harb and Harb [14] showed that a third order PLL with sinusoidal phase detector characteristics experienced chaos through Hopf bifurcation. In other word, the PLL is unlocked after the Hopf bifurcation point. The analysis was based on modern nonlinear theory such as bifurcation and chaos theory. The method of multiple scales, perturbation method, has been used to find the normal form at the vicinity of the Hopf bifurcation point. The point was found to be supercritical one. That means, a small periodic solutions, limit cycles, are borned at the Hopf bifurcation point. As the control parameter was increased, the limit cycles deformed and at the end culminating to chaos.

Recently, great attention is been paid to chaos and bifurcation control. Bifurcation control deals with using a control input to modify the characteristics of a parameterized nonlinear system. The control can thus be static or dynamic feedback control, or open loop control. The objective can be stabilization and reduction of the amplitude of bifurcation orbital solutions, optimization of a performance index near bifurcation, reshaping of the bifurcation diagram or a combination of these.

Bifurcation control are used in [15], these controllers are designed to control the bifurcation route that leads to chaos. Many researchers are proposed other methods to control chaos, Ott [16] and Ott *et. al*.[17]. In Hubler [18], Hubler and Luscher [19], and Jackson [20] the methods are based on classical control. Abed *et. al.* [21] and Nayfeh and Balachandran [15] designed state feedback nonlinear controllers. Ikhouane [22], Harb *et. al.* [23], and Zaher *et. al*. [24-27] used the backstepping recursive nonlinear controller. Calvo and Cartwright [28], and Mann *et. al.* [29] introduced the use of fuzzy theory control in chaotic systems. Harb and Abdel-Jabbar [30] introduced a model-based control strategy based on global state feedback linearization (GLC) to control the chaotic behavior in a power system. In this chapter, a controlling scheme is proposed to stabilize the chaotic behavior and drive the PLL under consideration to the steady state (in-lock-state). A

nonlinear controller based on backstepping recursive theory is designed to control the chaotic oscillation in a third order PLL.

8.2. Mathematical Model

After Harb and Harb [14], the basic configuration of a PLL is shown in Fig. 8.1. It consists of three building blocks; a phase detector, a time-invariant loop filter and a voltage controlled oscillator (VCO). The VCO's instantaneous frequency is given by

$$\frac{d\theta_v}{dt} = \omega_o + k_v e(t) \quad \text{rad/sec}, \tag{8.1}$$

where ω_O is called the VCO quiescent or center frequency and k_V is the VCO gain which has units of (rad/sec-volt). The output of the phase detector is given by

$$x(t) = k_1\left[\sin(\theta_i - \theta_v) + \sin(\theta_i + \theta_v)\right]. \tag{8.2}$$

The term $\sin(\theta_i + \theta_v)$ contains higher fundamental frequency components which are eliminated by the loop filter. Then, the output of the loop filter becomes

$$e(t) = e_o(t) + \int_0^t x(t-u) f(u) du\,,\ t \geq 0\,, \tag{8.3}$$

where $f(t)$ is the impulse response of the filter, and $e_O(t)$ is the filter's zero-input response which depends only on the initial conditions existing in the filter at t = 0. If the filter is stable, $e_O(t) \to 0$ as $t \to \infty$ for any set of initial conditions. The loop filter which will be considered in this chapter has the form

$$F(s) = \frac{1+\tau_{z1}s}{1+\tau_{p1}s} \cdot \frac{1+\tau_{z2}s}{1+\tau_{p2}s} = F_1(s)\ .\ F_2(s), \tag{8.4}$$

where $F_1(s)$ and $F_2(s)$ are two cascade lag-lead filters. Equations (8.1), (8.2), and (8.3) can be combined to obtain

$$\frac{d\theta_v}{dt} = \omega_o + k_v \int_0^t x(u) f(t-u) du = \omega_o + k_1 k_v \int_0^t f(t-u) \sin\left(\theta_i(u) - \theta_v(u)\right) du\,. \tag{8.5}$$

Define the closed loop phase error as

$$\phi \equiv \theta_i - \theta_v , \tag{8.6}$$

and the closed loop gain as

$$k = k_1 k_v . \tag{8.7}$$

The results which follow are simplified by defining

$$\theta_1 = \theta_i - \omega_o t , \tag{8.8}$$

and

$$\theta_2 = \theta_v - \omega_o t . \tag{8.9}$$

These quantities can be used with equations (8.5), (8.6) and (8.7) to write

$$\frac{d\phi}{dt} = \frac{d\theta_1}{dt} - Ak\int_0^t f(t-u)\sin(\phi(u))du \quad \text{for } t \geq 0 . \tag{8.10}$$

The differential equation that describes the closed loop phase error in the PLL is given by

$$\frac{d\phi}{dt} = \frac{d\theta}{dt} - k\left[\frac{1+\tau_{z1}\,d/dt}{1+\tau_{p1}\,d/dt}.\frac{1+\tau_{z2}\,d/dt}{1+\tau_{p2}\,d/dt}\right]\sin(\phi), \tag{8.11}$$

where τ_{p1} , τ_{p2} , $\tau_{z1,}$ and τ_{z2} are the loop filters time constants. After simplifications, the above equation becomes

$$\frac{d^3\phi}{dt^3}+\frac{d^2\phi}{dt^2}\left(\frac{\tau_{p1}+\tau_{p2}}{\tau_{p1}\tau_{p2}}+\frac{k\tau_{z1}\tau_{z2}\cos\phi}{\tau_{p1}\tau_{p2}}\right)+\frac{d\phi}{dt}\left(\frac{1}{\tau_{p1}\tau_{p2}}+\frac{k(\tau_{z1}+\tau_{z2})\cos\phi}{\tau_{p1}\tau_{p2}}\right) \tag{8.12}$$

$$-\frac{k\tau_{z1}\tau_{z2}\sin\phi}{\tau_{p1}\tau_{p2}}\left(\frac{d\phi}{dt}\right)^2+\frac{k\sin\phi}{\tau_{p1}\tau_{p2}}=\frac{d^2\theta_1}{dt^2}+\frac{\tau_{p1}+\tau_{p2}}{\tau_{p1}\tau_{p2}}\frac{d^2\theta_1}{dt^2}+\frac{1}{\tau_{p1}\tau_{p2}}\frac{d\theta_1}{dt}$$

If the input frequency is constant, then

$$\theta_1(t) = (\omega_i-\omega_o)\, t + \theta_o, \tag{8.13}$$

and by normalizing the time variable using $t' = (k/\tau_{p1}\tau_{p2})^{1/3}\, t$, equation (8.12) becomes

$$\dddot{\phi} + a\ddot{\phi} + b\cos(\phi)\ \ddot{\phi} + c\dot{\phi} + d\cos(\phi)\,\dot{\phi} - e\sin(\phi)\,\dot{\phi}^2 + \sin(\phi) = \delta , \tag{8.14}$$

where $\dot{} = d/dt'$, $s = (k/\tau_{p1}\tau_{p2})^{1/3}$, $a = \left(\tau_{p1} + \tau_{p2}\right)s^2 / k$, $b = \tau_{z1}\tau_{z2}\, s^2$, $c = s/k$, $d = (\tau_{z1} + \tau_{z2})\, s$, $e = \tau_{z1}\, \tau_{z2}\, s^2$, $\delta = \omega_{os} / k$ and $\omega_{os} = \omega_i - \omega_o$. The above equation can be written as:

$$\dot{\phi} = x \,, \tag{8.15a}$$

$$\dot{x} = y \,, \tag{8.15b}$$

and

$$\dot{y} = -ay - b\cos(\phi)y - cx - d\cos(\phi)x + e\sin(\phi)x^2 - \sin(\phi) + \delta \,. \tag{8.15c}$$

8.3. Equilibrium Solution

The equilibrium solution of the system of equations (8.15a)-(8.15c) corresponding to $\dot{\phi} = \ddot{\phi} = \dddot{\phi} = 0$. Setting the right hand sides of equations (8.15a)-(8.15c) equal to zero, we end up with a nonlinear algebraic equation. The solution of this equation as a function of one of the control parameters are defined by using a continuation scheme. The stability of an equilibrium solution depends on the eigenvalues of the Jacobian matrix of equations (8.15a)-(8.15c) evaluated at the equilibrium point. In this chapter we write our own program for calculating the fixed points and their bifurcations rather than use an available bifurcation software package, such as BIFOR2 and AUTO94.

To this end, we follow Watada, Endo and Seishi [13] and consider the case of the sinusoidal phase detector. In Fig. 8.2, we show the bifurcation diagram, which is the variation of the control parameter *K* with the state variable $\dot{\phi}$. The solid line denotes stable nodes, while the dashed line denotes unstable foci. There is only one Hopf bifurcation point *H* at *Ko* = 7299.01. Using the normal form near the Hopf bifurcation point *H*, we find that *H* is a supercritical point. So, as *K* was increased above 7299.01, a sequence of deformed (asymmetric) periodic solutions was observed, leading to chaos at the control parameter *K*= 85299 as shown in Fig. 8.3.

8.4. Backstepping Recursive Nonlinear Controller

Appendix 8A gives more details about the methodology of backstepping control theory. First, let $x_1 = \phi, x_2 = x,$ and $x_3 = y$. Second, a designed control signal *u* is added to equation (8.15c). Therefore, one can rewrite the system as follows

$$\dot{x}_1 = x_2, \tag{8.16}$$

$$\dot{x}_2 = x_3, \tag{8.17}$$

and

$$\dot{x}_3 = -Ax_3 - Bx_3\cos(x_1) - Cx_2 - Dx_2\cos(x_1) + Ex_2{}^2\sin(x_1) - \sin(x_1) + \delta + u. \tag{8.18}$$

Design Methods. Let

$$e_1 = x_1 + \sin^{-1}(\delta), \tag{8.19a}$$

$$e_2 = x_2 - x_{2_{des}} = x_2 - c_1 e_1, \tag{8.19b}$$

and

$$e_3 = x_3 - x_{3_{des}} = x_3 - c_2 e_1 - c_3 e_2. \tag{8.19c}$$

Thus,

$$\dot{e}_1 = c_1 e_1 + e_2, \tag{8.20a}$$

$$\dot{e}_2 = e_3 + c_2 e_1 + c_3 e_2 - c_1(e_2 + c_1 e_1), \tag{8.20b}$$

and

$$\begin{aligned}\dot{e}_3 = {} & -A(e_2 + c_1 e_1) - B(e_3 + c_2 e_1 + c_3 e_2)\cos(e_1 - \sin^{-1}(\delta)) - C(e_2 + c_1 e_1) \\ & - D(e_2 + c_1 e_1)\cos(e_1 - \sin^{-1}(\delta)) + E(e_2 + c_1 e_1)^2\sin(e_1 - \sin^{-1}(\delta)) - \\ & \sin(e_1 - \sin^{-1}(\delta)) + \delta + u - c_2(e_2 + c_1 e_1) - c_3(e_3 + c_2 e_1 + c_3 e_2 \\ & - c1(e_2 + c_1 e_1))\end{aligned} \tag{8.20c}$$

Let

$$V = \frac{1}{2}\sum_{i=1}^{3} k_i e_i^2 \ , \ k_i > 0, \tag{8.21}$$

then

$$\dot{V} = \sum_{i=1}^{3} k_i e_i \dot{e}_i = k_1 e_1 \dot{e}_1 + k_2 e_2 \dot{e}_2 + k_3 e_3 \dot{e}_3. \tag{8.22}$$

Substituting equations (8.16)-(8.21) into equation (8.22), and

1- choose c_i and k_i such that the first and second terms in $\dot{V}$ are equal to zero, $i=1,2,3$.
2- For $c_1 = c_2 = 0 = c_3 = 0, k_1 = 0 = k_2 = 0,$ and $k_3 = 1$, choose u such that:

$$u = -e_3 + Be_3 \cos(e_1 - \sin^{-1}(\delta)) + Ce_2 + De_2 \cos(e_1 - \sin^{-1}(\delta)) - Ee_2{}^2 \sin(e_1 - \sin^{-1}(\delta)) + \sin(e_1 - \sin^{-1}(\delta)) - \delta \quad (8.23)$$

to make sure that the system is stable. Substituting the control signal equation (8.23) into the original system of equations (8.15a, 8.15b, and 8.15c), and integrate the new system, one obtain the simulation results as shown in Fig. 8.4. But the system without any control action is experiencing chaotic behavior via Hopf bifurcation. Fig. 8.3 shows the uncontrolled system. It so clear that, for the value of control parameter Ko = 85299, the chaotic oscillations appear via period doubling rout to chaos. As a result, the PLL is driven to the out-of-lock state and it will not achieve phase lock (stable equilibrium state). As we mentioned, the main objective of this chapter is control and to get red of the chaotic behavior. So, by comparing the uncontrolled system shown in Fig. 8.3 (Figs. 8.3a and 8.3b) to the controlled system shown in Fig. 8.4 (Figs. 8.4a and 8.4b), on can see that the system is recovered from its chaotic behavior and exhibits a stable equilibrium solution. This means that the phase locked-loop is (in-lock-state). Fig. 8.5 (Figs. 8.5a and 8.5b) show the error signals e_2 and e_3. In order to see the effectiveness of the designed controller, we apply the designed control signal after 50 second of the integration time. Fig. 8.6 (Figs. 8.6a and 8.6b) show how the controller brings the system to the equilibrium solution or in-lock-state. The results were achieved by using one control signal.

8.4. Conclusions

In the existing literature, it was showed that a third-order phase locked loop (PLL) with sinusoidal phase detector characteristics experienced a Hopf bifurcation point as well as chaotic behavior. This behavior drives the PLL to the out-of-lock (unstable) state. In this chapter, a nonlinear controller based on the theory of backstepping has been designed to control this chaotic behavior. The study showed the effectiveness of the designed nonlinear controller in controlling the undesirable unstable

(chaotic) behavior and pulling the PLL back to the in-lock state, i.e, it drives the chaotic oscillation into an equilibrium constant behavior (phase lock state).

Appendix 8A—Methodology of Backstepping

To explain the methodology of the backstepping controller, let me start from a special case that has been taken from Khalil's book [31]. It is the integrator backstepping, as shown in Fig. 8.7a. Let

$$\dot{\eta} = f(\eta) + g(\eta)\xi, \tag{8.A1}$$

and

$$\dot{\xi} = u, \tag{8.A2}$$

where η and ξ are the state variables and u is the control signal. If the component of equation (8.A1) can be stabilized by a smooth state feedback control law $\xi = \phi(\eta)$, with $\phi(0) = 0$, then, the origin of $\dot{\eta} = f(\eta) + g(\eta)\phi(\eta)$, is asymptotically stable. Suppose that we know a smooth and positive definite Lyapunov function $V(\eta)$ that satisfies the inequality

$$\frac{\partial V}{\partial \eta}[f(\eta) + g(\eta)\phi(\eta)] \le -W(\eta), \tag{8.A3}$$

where $W(\eta)$ is positive definite. Adding and subtracting $g(\eta)\phi(\eta)$ on the right hand side of equation (8.A1), one obtain the equivalent representation shown in Fig. 8.7b and Fig. 8.7c and mathematically as follows:

$$\dot{\eta} = [f(\eta) + g(\eta)\phi(\eta)] + g(\eta)[\xi - \phi(\eta)], \tag{8.A4}$$

and

$$\dot{\xi} = u, \tag{8.A5}$$

or

$$\dot{\eta} = [f(\eta) + g(\eta)\phi(\eta)] + g(\eta)z, \tag{8.A6}$$

and

$$\dot{z} = v, \tag{8.A7}$$

where $z = \xi - \phi(\eta)$ and $v = u - \dot{\phi}$. Equations (8.A4) and (8.A5) are similar to equations (8.A1) and (8.A2), except that now the first component has an asymptotically stable origin when the input is zero. This feature will be exploited in the design of *v* to stabilize the overall system. Using the following Lyapunov function as

$$V_c(\eta, \xi) = V(\eta) + \tfrac{1}{2} z^2 , \tag{8.A8}$$

then

$$\dot{V}_c = \frac{\partial V}{\partial \eta}[f(\eta) + g(\eta)\phi(\eta)] + \frac{\partial V}{\partial \eta} g(\eta) z + zv \le -W(\eta) + \frac{\partial V}{\partial \eta} g(\eta) z + zv . \tag{8.A9}$$

Choosing $v = -\dfrac{\partial V}{\partial \eta} g(\eta) - kz,$ where $k>0$, one obtain, $\dot{V}_c \le -W(\eta) - kz^2$, which shows that the origin ($\eta=0$, $z=0$) is asymptotically stable. Since $\phi(0) = 0,$ so, the origin ($\eta=0$, $\xi=0$) is also asymptotically stable. Substituting for *v*, *z*, and $\dot{\phi}$, one obtain the state feedback control law

$$u = \frac{\partial \phi}{\partial \eta}[f(\eta) + g(\eta)\xi] - \frac{\partial V}{\partial \eta} g(\eta) - k[\xi - \phi(\eta)] . \tag{8.A10}$$

If all the assumptions hold globally, and $V(\eta)$ is radial unbounded, we can conclude that the origin is globally asymptotically stable.

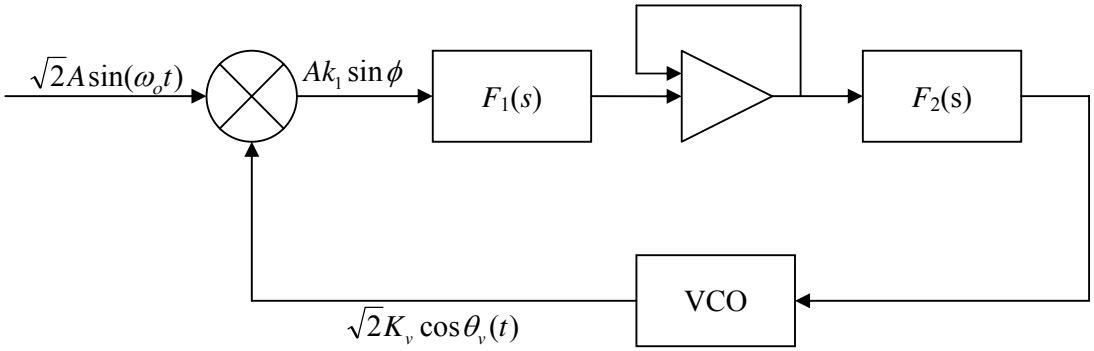

Fig. 8.1. Block diagram of a phase-locked loop with second-order loop filter.

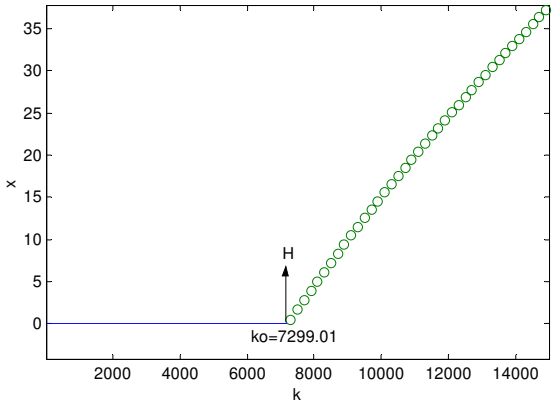

Fig. 8.2. Bifurcation diagram (Variation of state variable versus the control parameter *K*).

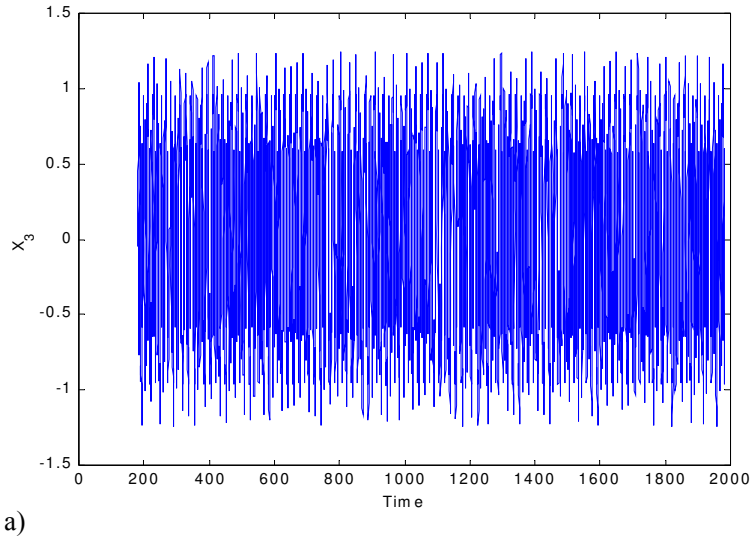

a)

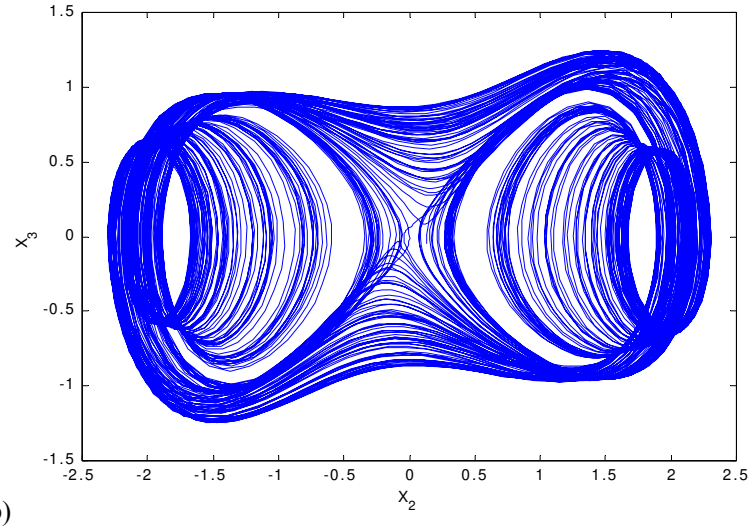

b)

Fig. 8.3. Uncontrolled simulations, a) The chaotic time response and b) state-plane of the state variables X_2 and X_3 at Ko = 85299.

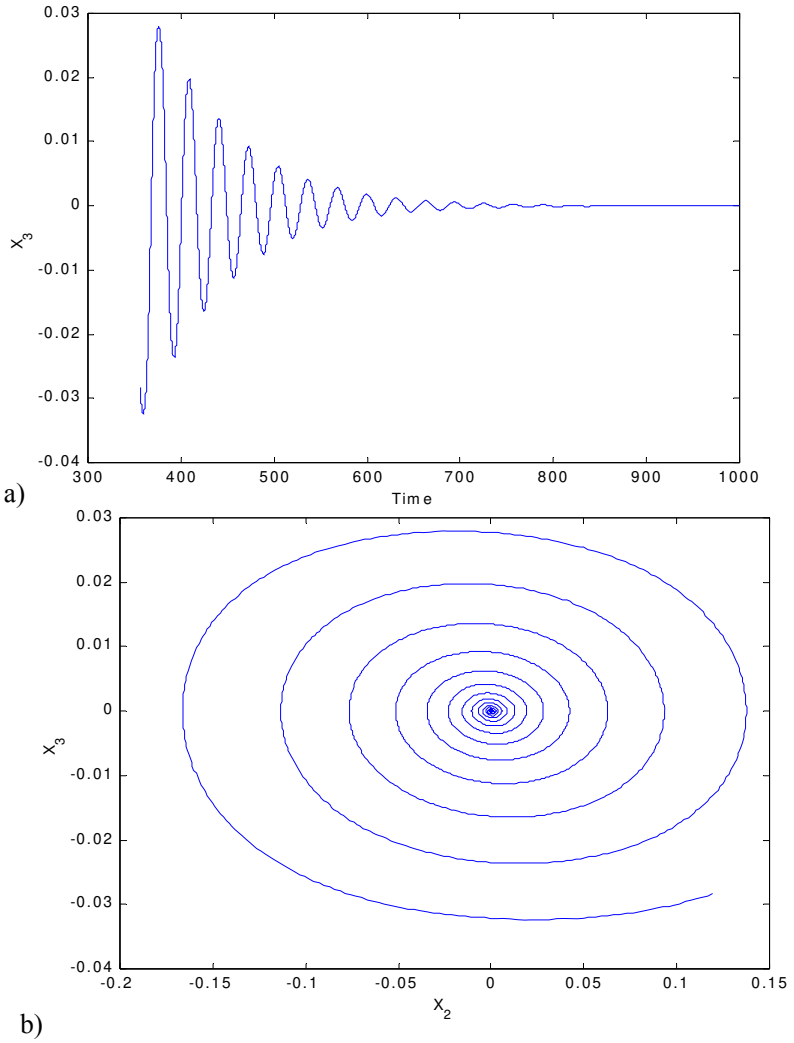

Fig. 8.4. Controlled simulations: a) Time history and b) state-plane of the state variables X_2 and X_3 , at Ko = 85299.

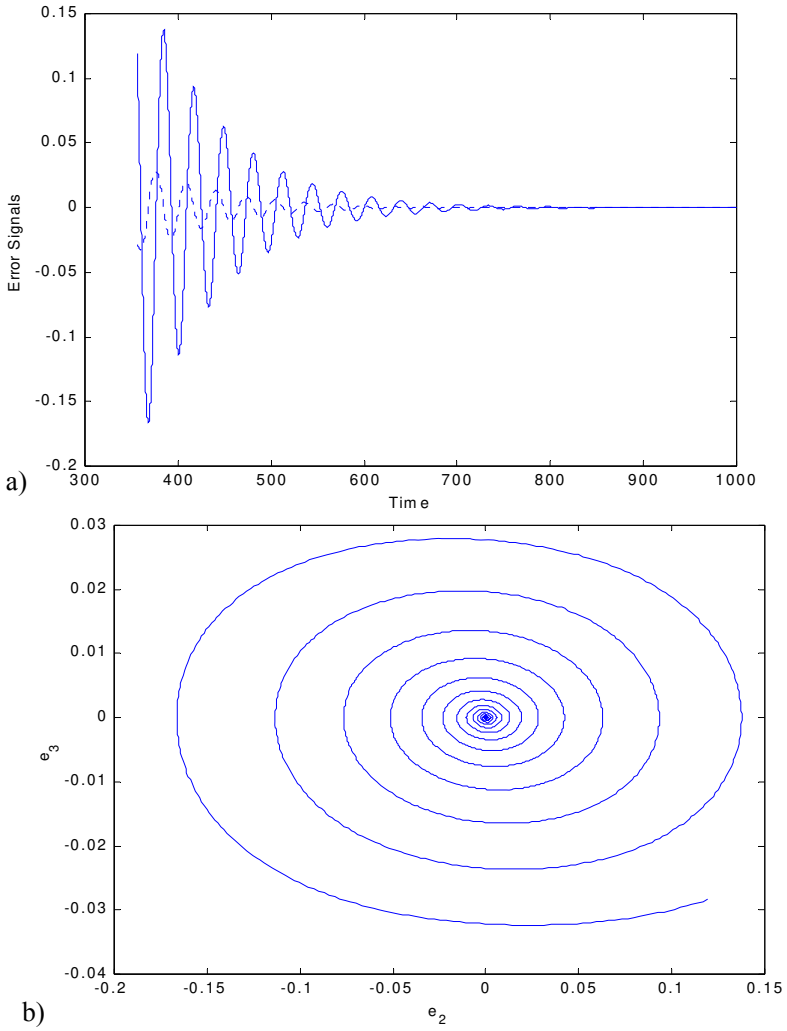

Fig. 8.5. Controlled simulations: a) Time history and b) state-plane) of the error signals e_2 and e_3, at Ko = 85299.

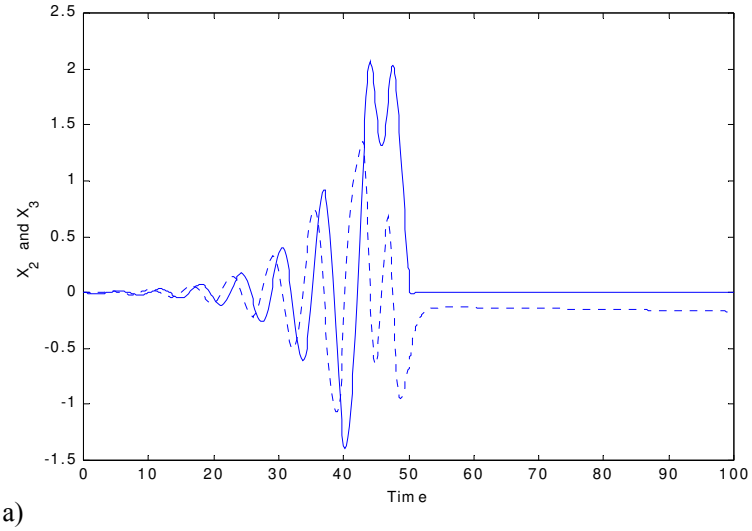

a)

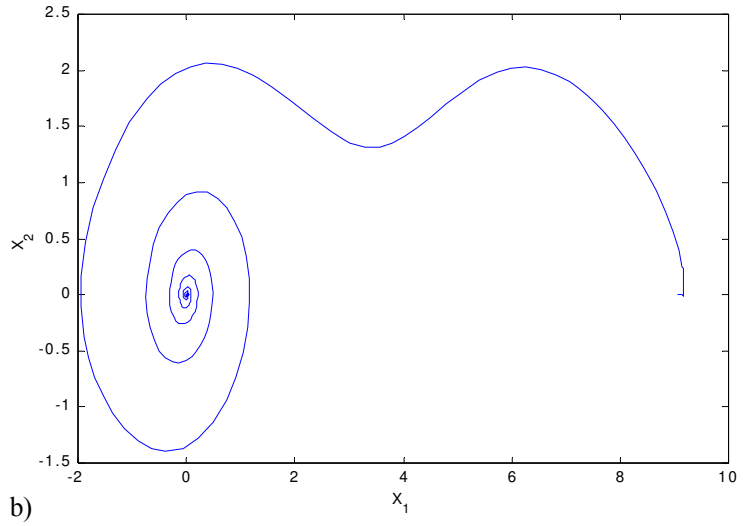

b)

Fig. 8.6. Applying the control signal after 50 seconds, a) the time history and b) the state-plane of state variables X_2 and X_3 , at Ko = 85299.

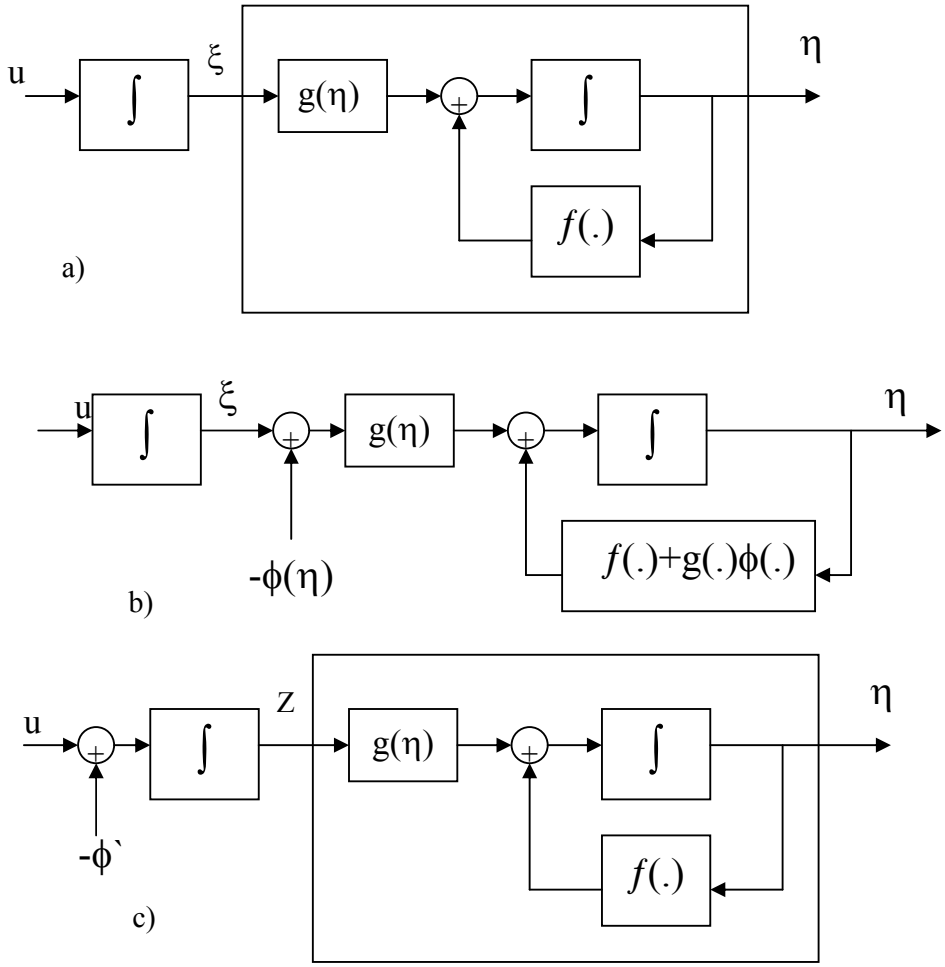

Fig. 8.7. a) The block diagram of the system, b) Introducing φ(η), c) backstepping -φ(η) through the integrator.

References

[1] A. J. Viterbi, *Principle of Coherent Communications* (New York: McGraw Hill, 1966).
[2] A. Blanchard, *Phase-Locked Loops* (New York: John Wiley 1976).
[3] F. M. Gardner, *Phase Lock Techniques* (New York: John Wiley 1979).

[4] J. L. Stensby, Saddle node bifurcation at a nonhyperbolic limit cycle in a phase locked loop, *Journal of Franklin Institute* **330**(5), 775-786, 1993.
[5] B. Harb and J. L. Stensby, The half-plane pull-in range of a second-order phase locked loop, *Journal of Franklin Institute* **333B**(2), 191-199, (1996).
[6] C. Piccardi, Bifurcations of limit cycles in periodically forced nonlinear systems: The harmonic balance approach, *IEEE Trans. Circuits Syst. I* **41**, 315-320, (1994).
[7] J. L. Stensby and B. Harb, Computing the half-plane pull-in range in a second-order phase locked loop, *IEE Electronics Letters* 1995.
[8] S. Wu, Chua's circuit family, *Proceedings of the IEEE* **75**, 1022-1032, (1987).
[9] F. Salam and S. Sastry, Dynamics of the forced Josephson junction circuit: The region of chaos, *IEEE Transactions on Circuit and Systems* **32**, 784-795, (1980).
[10] M. P. Kennedy and L. O. Chua, Van der Pol and chaos, *IEEE Transactions on Circuits and Systems* **33**, 974-980, (1981).
[11] T. Endo and L. O. Chua, Synchronization of chaos in phase- locked loops, *IEEE Transactions on Circuits and Systems* **38**, 1580-1588, (1991).
[12] T. Endo and L. O. Chua, Chaos from phase- locked loops, *IEEE Transactions on Circuits and Systems* **35**, 987-1003, (1988).
[13] K. Watada, T. Endo and H. Seishi, Shilnikov orbits in an autonomous third-order chaotic phase-locked loop, *IEEE Transactions on Circuits and Systems–I: Fundamental Theory and Applications* **45**, 979-983, (1998).
[14] B. Harb and A. Harb, Chaos and bifurcation in third-order phase locked loop, *Chaos, Solitons and Fractals* **19**(3), 667-672, (2004).
[15] A. H. Nayfeh and B. Balachandran, *Applied Nonlinear Dynamics* (John Wiley, New York, 1994).
[16] E. Ott, *Chaos in Dynamical Systems* (Cambridge University Press, Cambridge, England, 1993).
[17] E. Ott, C. Grebogi and J. A. Yorke, Controlling chaotic dynamical systems, *CHAOS* (Soviet-American Perspectives on Nonlinear Science, D. K. Campbell, ed., 153-172, 1992a).
[18] A. Hubler, An adaptive control of chaotic systems, *Helv, Phys. Acta* **62**, 343-346, (1989).
[19] A. Hubler and E. Luscher, Resonant stimulation and control of nonlinear oscillators, *Naturwissenschaften* **76**, 67-69, (1989).
[20] E. A. Jackson, Control of dynamic flows with attractors, *Phys. Rev. A* **44**, 4839-4853, (1991).
[21] E. H. Abed and J. H. Fu, Local feedback stabilization and bifurcation control, I. Hopf bifurcation, *Systems and control letters* **7**, 11-17, (1986).
[22] F. Ikhouane and M. Krstic, Robustness of the tuning functions adaptive backstepping design for linear systems, *IEEE Trans. on Aut. Control* **43**(3), 431-437, (1998).
[23] A. Harb, A. Zaher and M. Zohdy, Nonlinear recursive chaos control, *Proc. of ACC* Alaska, USA, (2002).
[24] A. Zaher and M. Zohdy, Robust control of biped robots, *Proc. of ACC* 1473-1478, Chicago IL, USA, (2000).

[25] A. Zaher, M. Zohdy, F. Areed and K.Soliman, Real-time model-reference control of non-linear processes, *2nd Int. Conf. on Computers in Industry* Manama Bahrain, (2000).
[26] A. Zaher, M. Zohdy, F. Areed and K. Soliman, Robust model-reference control for a class of non-linear and piece-wise linear systems, *Proc. of ACC* 4514-4519, Arlington VA, USA, (2001).
[27] A. Zaher, M. Zohdy, F. Areed and K. Soliman, Robust estimation-based design for uncertain plants, *AMSE conference* Dearborn, MI, USA, (2001).
[28] O. Calvo and J. Cartwright, Fuzzy control of chaos, *International Journal of Bifurcation and Chaos* **8**(8), (1998).
[29] G. K. I. Mann, B. G. Hu and R. G. Gosine, Analysis of direct action fuzzy PID controller structures, *IEEE Trans. System and Cybernetics* **29**(3), (1999).
[30] A. Harb and N. Abedl-Jabbar, Controlling Hopf bifurcation and chaos in a small power system, *Chaos, Solitons and Fractals* **18**(5), 1055-1063, (2003).
[31] H. Khalil, *Nonlinear Systems* (Prentice Hall, 2nd Edition, 1996).

CHAPTER 9

CONTROL OF SIGMA DELTA MODULATORS VIA FUZZY IMPULSIVE APPROACH

B.W.K. Ling,[*] C.Y.F. Ho[**] and J.D. Reiss[***]

[*]*Department of Electronic Engineering, Division of Engineering,*
King's College London, WC2R 2LS, United Kingdom
E-mail: wing-kuen.ling@kcl.ac.uk
[**]*School of Mathematical Sciences,*
Queen Mary College London,
Mile End Road, London, E1 4NS, United Kingdom
E-mail: c.ho@qmul.ac.uk
[***]*Department of Electronic Engineering,*
Queen Mary College London,
Mile End Road, London, E1 4NS, United Kingdom
E-mail: josh.reiss@elec.qmul.ac.uk

In this chapter, a fuzzy impulsive control strategy is applied to high order interpolative lowpass sigma delta modulators. The state vectors that the impulsive controller resets to are determined so that the state vectors of interpolative lowpass sigma delta modulators (SDMs) are bounded within any arbitrary nonempty region no matter what the input step size, the initial condition and the filter parameters are, the occurrence of limit cycle behaviors and the effect of audio clicks are minimized, as well as the state vectors are close to the invariant set if it exists. To work on this problem, first, the local stability criterion and the condition for the occurrence of limit cycle behaviors are derived. Second, based on the derived conditions, as well as a practical consideration based on the boundedness of the state variables and a heuristic measure on the strength of audio clicks, fuzzy membership functions and a fuzzy impulsive control law are formulated. The controlled state vectors are then determined by solving the fuzzy impulsive control law. One of the advantages of the fuzzy impulsive control strategy over the existing linear control strategies is the

robustness to the input signal, the initial condition and the filter parameters, and that over the existing nonlinear control strategy are the efficiency and the effectiveness in terms of lower frequency of applying the control force and higher signal-to-noise ratio (SNR) performance.

9.1. Introduction

Because of the advance in electronic technology, the implementation cost of sigma delta modulators (SDMs) could be very low [2] and nowadays SDMs are very popular in analog-to-digital (A/D) and digital-to-analog (D/A) conversions [1]. Many systems, such as in the consumer and professional audio processing systems [2], communication systems [3], and precision measurement devices [4], etc, employ SDMs in their A/D and D/A conversions.

The working principles of sigma delta modulation are based on the oversampling and the noise shaping techniques. It is well known that when the input signals are critically sampled, that is, the signals are sampled with the frequencies equal to twice of their bandwidths, then the signals can be perfectly reconstructed and the signals are spread over the whole frequency band. When the input signals are oversampled, that is, the signals are sampled with the frequencies greater than twice of their bandwidths, then the signal bands are decreased and the bandwidths of the signals are inversely proportional to the oversampling ratios. By applying simple lowpass filtering, noises outside the signal bands are filtered and good signal-to-noise ratios (SNR) could be achieved. Noise shaping technique is further to shape the noise in the signal band to the noise band by applying a negative feedback. By a proper design of a loop filter, the magnitudes of the signal transfer function in the signal band and in the noise band are approximately equal to one and zero, respectively, and that of the noise transfer function in the signal band and in the noise band are approximately equal to zero and one, respectively. Hence, signals and noises are separated and better SNR could be further achieved.

However, in order to achieve good noise shaping characteristics, SDMs are suffered from instability problems. This is because the magnitude of the loop filter response at the signal band has to be tended to an infinity in order to achieve the magnitude of the signal transfer function equal to one and that of the noise transfer function equal to zero.

This implies that the loop filter is unstable or marginally stable. Consequently, control is required. Although there are many existing linear control strategies for stabilizing interpolative SDMs, such as variable structure compensation (sliding mode control strategy) [5] and time delay feedback control strategy [6], etc, these linear control strategies stabilize the loop filter by changing the effective poles of the loop filter. Since the loop filter is usually designed to have a very noise shaping characteristics, it is not guaranteed that the SNR of the controlled SDMs is still maintained or even improved if the effective poles of the loop filter are changed. Moreover, the parameters in the controller depend on the loop filter parameters, so it is not guaranteed that a particular class of controllers can stabilize all types of interpolative SDMs. Furthermore, the controlled SDMs may still be unstable when the magnitude of the input signal is increased. In addition, it cannot be guaranteed that the controlled SDMs are stable for all initial conditions in the state space.

In order to control the SDMs without changing the effective poles of the loop filter, nonlinear control strategy, such as the clipping control strategy, was employed [2]. For the clipping control strategy, as the state variables are always reset to the *same* values, periodic output sequences may result and this periodic behavior is known as limit cycle behavior. This situation is found very frequently when the input signal is very slow time varying or the clipped level is set at very low value. For audio applications [2], the occurrence of limit cycle behaviors results to the annoying audio tones, which should be avoided. Besides, there may be a large jump between the unclipped and clipped state levels. As a result, audio clicks may be observed, which should also be avoided. Furthermore, as the set of the state vectors under the clipping control strategy is usually not the same as the invariant set, the clipping force may be applied very frequently.

In order to solve these problems, an impulsive control strategy is discussed in this chapter, in which it is to reset the state vectors to *different* positions in the state space whenever the control force is applied. Hence, the occurrence of limit cycle behaviors and the effect of audio clicks can be minimized with the guarantee of the bounded state variables. Moreover, if the invariant set exists, then we only need to reset the state variables of the loop filter once and the state vectors of the SDMs are guaranteed to be within the invariant set forever if the effects of limit cycle behaviors and audio clicks do not consider. As there are

usually an infinite number of state vectors in the invariant set, this chapter suggests a method to determine the state vectors that the impulsive controller resets to. Since the SDMs consist of a quantizer, nonlinear behaviors, such as fractal and chaotic behaviors, combined with the practical consideration on the boundedness of the state variables and a heuristic measure on the strength of audio clicks, cause a difficulty to solve the state vectors analytically. To solve this problem, a fuzzy approach is employed because employing fuzzy approach can simplify the complicated problems and can capture heuristic knowledge in the system in an easy manner.

The outline of this chapter is as follows. In Section 9.2, we introduce the notations which appear throughout this chapter. In Section 9.3, the conditions for the occurrence of limit cycle behaviors and the local stability criterion of the SDMs are derived, which are used for the formulation of fuzzy membership functions and fuzzy impulsive control law. In Section 9.4, a fuzzy impulsive control strategy is discussed. In Section 9.5, some simulation results are presented to illustrate the effectiveness of the fuzzy impulsive control strategy. Finally, a conclusion is summarized in Section 9.6.

9.2. Notations

The block diagram of an interpolative SDM is shown in Fig. 9.1. The input to the SDM and the output of the loop filter are denoted as, respectively, $u(k)$ and $y(k)$. We assume that the loop filter is a single input single output real system and the input is also real, that is, $u(k) \in \Re$, so $y(k) \in \Re$. The transfer function of the loop filter is denoted as $F(z)$. $F(z)$ is assumed to be causal, rational and proper with the order of the polynomial of z^{-1} in the numerator being equal to that in the denominator and there is a delay in the numerator. We make those assumptions because this type of SDMs is commonly used in the industry [2]. Denote the coefficients in the denominator and numerator of $F(z)$ as, respectively, a_i for $i = 0,1,\cdots,N$ and b_j for $j = 1,\cdots,N$, where N is the order of the loop filter. Then

$$F(z)=\frac{\sum_{j=1}^{N} b_j z^{-j}}{\sum_{i=0}^{N} a_i z^{-i}}. \tag{9.1}$$

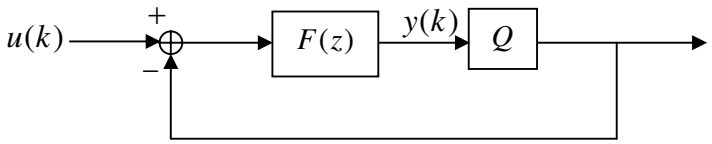

Fig. 9.1. The block diagram of an interpolative SDM.

Since this chapter is based on the feedforward structure of the SDMs, without loss of generality, we assume that the loop filter is realized via the direct form because the expressions will be much simplified. For other minimal realizations, they can be converted to the direct form realization using simple transformations. Hence, the SDMs can be described by the following state space equation:

$$\mathbf{x}(k+1)=\mathbf{A}\mathbf{x}(k)+\mathbf{B}(\mathbf{u}(k)-\mathbf{s}(k)) \tag{9.2}$$

for $k \geq 0$, where

$$\mathbf{x}(k)\equiv[x_1(k), \quad \cdots, \quad x_N(k)]^T \equiv [y(k-N), \quad \cdots, \quad y(k-1)]^T \tag{9.3}$$

is the state vector of the SDMs,

$$\mathbf{u}(k)\equiv[u(k-N), \quad \cdots, \quad u(k-1)]^T, \tag{9.4}$$

$$\mathbf{s}(k)\equiv[s_1(k), \quad \cdots, \quad s_N(k)]^T \equiv [Q(y(k-N)), \quad \cdots, \quad Q(y(k-1))]^T, \tag{9.5}$$

$$\mathbf{A}\equiv\begin{bmatrix} 0 & 1 & 0 & \cdots & 0 \\ \vdots & \ddots & \ddots & \ddots & \vdots \\ \vdots & & \ddots & \ddots & 0 \\ 0 & \cdots & \cdots & 0 & 1 \\ -\frac{a_N}{a_0} & \cdots & \cdots & \cdots & -\frac{a_1}{a_0} \end{bmatrix} \text{ and } \mathbf{B}\equiv\begin{bmatrix} 0 & \cdots & \cdots & \cdots & 0 \\ \vdots & & & & \vdots \\ \vdots & & & & \vdots \\ 0 & \cdots & \cdots & \cdots & 0 \\ \frac{b_N}{a_0} & \cdots & \cdots & \cdots & \frac{b_1}{a_0} \end{bmatrix}, \tag{9.6}$$

in which Q is a one bit quantizer defined as follows:

$$Q(y)\equiv\begin{cases} 1 & y \geq 0 \\ -1 & otherwise \end{cases}. \tag{9.7}$$

Since the oversampling ratio of the SDM is usually very high, the input can be approximated as a step signal. Hence, we further assume that $\mathbf{u}(k) = \overline{\mathbf{u}}$ for $k \geq 0$.

In many practical situations, the magnitude of the state variables of the SDM should not be larger than certain values. For the direct form realization, since all the state variables are the delay versions of the output of the loop filter, we denote the desired bound on the state variables as V_{cc}. That is, $|x_i(k)| < V_{cc}$ for $i = 1,2,\cdots,N$ and $k \geq 0$. Otherwise, the SDM is guaranteed to yield an unwanted behavior. Denote B_o as the set of the desired state vectors. That is, $B_o \equiv \{\mathbf{x} : |x_i| < V_{cc} \text{ for } i = 1,2,\cdots,N\}$.

9.3. Conditions for Occurrence of Limit Cycle Behaviors and Local Stability Criterion

As discussed in Section 9.1, limit cycle behaviors should be avoided. Hence, before we suggest the fuzzy impulsive control strategy, the conditions for exhibiting limit cycle behavior are discussed below. This is essential for formulating a fuzzy membership function for avoiding the occurrence of limit cycle behavior.

Suppose the eigen decomposition of matrix $\mathbf{A}$ exists. That is, there exists a full rank matrix $\mathbf{T}$ and a diagonal matrix $\mathbf{D}$ which consist of the eigenvectors and eigenvalues of matrix $\mathbf{A}$, respectively, such that $\mathbf{A} = \mathbf{TDT}^{-1}$. We make this assumption because it is satisfied for most of SDMs employed in the industry [2]. Denote λ_i and ξ_i for $i = 1,2,\cdots,N$ be the eigenvalues and the corresponding eigenvectors of the matrix $\mathbf{A}$. Let n_d be the number of eigenvalues of matrix $\mathbf{A}$ on the unit circle with their phases are integer multiples of $\frac{2\pi}{P}$, that is, $\lambda_{i+N-n_d} = e^{\frac{j2\pi k_i}{P}}$ for $k_i \in Z$ and $i = 1,2,\cdots,n_d$. Denote L_i for $i = 1,2,\cdots,N$ be the i^{th} row of

$$\sum_{j=0}^{P-1} \mathbf{A}^{P-1-j}\mathbf{B}(\mathbf{u}(k_0 + j) - \mathbf{s}(k_0 + j)), \tag{9.8}$$

where $P \in Z^+$ and $k_0 \geq 0$. Let $\mathbf{r}_j$ for $j = 1,2,\cdots,N$ be the j^{th} row of $\mathbf{I} - \mathbf{A}^P$, where $\mathbf{I}$ is an $N \times N$ identity matrix. Denote

$$\Psi_P \equiv \{\mathbf{x}(0) : \mathbf{r}_i\mathbf{x}(k_0) = L_i \text{ for } i = 1,2,\cdots,N - n_d\}. \tag{9.9}$$

Lemma 9.1. The number of linearly independent rows in the matrix $\mathbf{I}-\mathbf{A}^P$ is $N-n_d$, that is, $\exists c_{i,n}\in\Re$ for $i=1,2,\cdots,N-n_d$ and $n=1,2,\cdots,n_d$ such that $\sum_{i=1}^{N-n_d} c_{i,n}\mathbf{r}_i=\mathbf{r}_{N-n_d+n}$. If $\Psi_P\neq\emptyset$, where Ø denotes the empty set, and $\sum_{i=1}^{N-n_d} c_{i,n}L_i=L_{N-n_d+n}$ for $n=1,2,\cdots,n_d$, then the SDMs exhibit limit cycle behavior with period P, and Ψ_P is the corresponding nonempty set of initial condition. If $\Psi_P=\emptyset$ or $\exists n\in\{1,2,\cdots,n_d\}$ such that $\sum_{i=1}^{N-n_d} c_{i,n}L_i\neq L_{N-n_d+n}$, then there will not exist any fixed point or periodic state sequence.

Proof. Denote $\mathbf{Q}\equiv\mathbf{I}-\mathbf{A}^P$. Since $\mathbf{A}=\mathbf{TDT}^{-1}$ and $\lambda_{i+N-n_d}=e^{\frac{j2\pi k_i}{P}}$ for $k_i\in Z$ and $i=1,2,\cdots,n_d$, we have:

$$\mathbf{QT}=\left[\left(1-\lambda_1^P\right)\xi_1,\ \cdots,\ \left(1-\lambda_{N-n_d}^P\right)\xi_{N-n_d},\ \mathbf{0},\ \cdots,\ \mathbf{0}\right] \tag{9.10}$$

and

$$rank(\mathbf{QT})=rank\left(\left[\left(1-\lambda_1^P\right)\xi_1,\ \cdots,\ \left(1-\lambda_{N-n_d}^P\right)\xi_{N-n_d},\ \mathbf{0},\ \cdots,\ \mathbf{0}\right]\right). \tag{9.11}$$

Since $\mathbf{T}$ is a full rank matrix, $\{\xi_1,\cdots,\xi_{N-n_d}\}$ are linearly independent. As $1-\lambda_i^P\neq 0$ for $i=1,2,\cdots,N-n_d$, $rank(\mathbf{QT})=N-n_d$. However, $rank(\mathbf{QT})\le rank(\mathbf{Q})$. Hence, $rank(\mathbf{Q})\ge N-n_d$. Since

$$\mathbf{Q}=\left[\left(1-\lambda_1^P\right)\xi_1,\ \cdots,\ \left(1-\lambda_{N-n_d}^P\right)\xi_{N-n_d},\ \mathbf{0},\ \cdots,\ \mathbf{0}\right]\mathbf{T}^{-1}, \tag{9.12}$$

$rank(\mathbf{Q})\le N-n_d$. Hence, $rank(\mathbf{Q})=N-n_d$. As a result, the number of linearly independent rows in the matrix $\mathbf{I}-\mathbf{A}^P$ is $N-n_d$.

Since $\Psi_P\neq\emptyset$, $\exists\mathbf{x}(0)\in\Re^N$ such that $\mathbf{r}_i\mathbf{x}(k_0)=L_i$ for $i=1,2,\cdots,N-n_d$. As $\sum_{i=1}^{N-n_d} c_{i,n}L_i=L_{N-n_d+n}$ for $n=1,2,\cdots,n_d$, $\sum_{i=1}^{N-n_d} c_{i,n}\mathbf{r}_i\mathbf{x}(k_0)=L_{N-n_d+n}$ for $n=1,2,\cdots,n_d$. Since $\sum_{i=1}^{N-n_d} c_{i,n}\mathbf{r}_i=\mathbf{r}_{N-n_d+n}$ for $n=1,2,\cdots,n_d$, $\mathbf{r}_{N-n_d+n}\mathbf{x}(k_0)=L_{N-n_d+n}$ for $n=1,2,\cdots,n_d$. Hence, $\mathbf{r}_i\mathbf{x}(k_0)=L_i$ for $n=1,2,\cdots,N$. This implies that

$$\left(\mathbf{I}-\mathbf{A}^{P}\right)\mathbf{x}\left(k_0\right)=\sum_{j=0}^{P-1}\mathbf{A}^{P-1-j}\mathbf{B}\left(\mathbf{u}\left(k_0+j\right)-\mathbf{s}\left(k_0+j\right)\right). \tag{9.13}$$

As a result, we have $\mathbf{x}\left(k_0\right)=\mathbf{x}\left(k_0+P\right)$. Hence, the SDMs exist limit cycle behaviors with period P for $k \geq k_0$. Obviously, Ψ_P is the corresponding nonempty set of initial condition.

When $\Psi_P=\emptyset$ or $\exists n \in \left\{1,2,\cdots,n_d\right\}$ such that $\sum_{i=1}^{N-n_d} c_{i,n} L_i \neq L_{N-n_d+n}$, then there does not exist $\mathbf{x}(0)$ such that $\mathbf{x}\left(k_0+P\right)=\mathbf{x}\left(k_0\right)$. Hence, there will not exist any fixed point or periodic state sequence, and this completes the proof. ■

The importance of this Lemma is to characterize the set of initial condition that corresponds to the limit cycle behaviors with period P for $k \geq k_0$. This set of initial condition will be used for the formulation of fuzzy rules shown in Section 9.4.

This result is a generalization of [2]. In [2], it mainly considers the DC pole cases, that is $k_i=0$ for $i=1,2,\cdots,n_d$. However, we reveal that even though there is not DC pole, but if there exist some poles on the unit circle with their phases are nonzero integer multiple of $\frac{2\pi}{P}$, then the matrix $\mathbf{Q}$ will also drop rank. Besides, when there are more than one DC poles in the loop filter transfer function, if the degeneracy is equal to the multiplicity of the eigenvalues of matrix $\mathbf{A}$, then the eigen decomposition of matrix $\mathbf{A}$ exists and Lemma 9.1 is still applied.

As discussed in Section 9.1 and 9.2, stability is an important issue. Hence, the stability analysis is performed before the fuzzy impulsive control strategy is suggested. Although the global stability of the SDMs is usually preferred because global stability implies local stability, sometimes global stability cannot be achieved. Only local stability can be achieved and local stability may be enough for some applications, such as for audio applications [2].

The local stability is discussed as follows. Define the forward dynamics and one of the possible backward dynamics of the system as $\aleph_{\mathrm{f}}:\Re^N \to \Re^N$ and $\aleph_{\mathrm{b}}:\Re^N \to \Re^N$, respectively. That is:

$$\mathbf{x}\left(k+1\right) \equiv \aleph_{\mathrm{f}}\left(\mathbf{x}\left(k\right)\right) \text{ in which } \mathbf{x}\left(k+1\right)=\mathbf{A}\mathbf{x}\left(k\right)+\mathbf{B}\left(\overline{\mathbf{u}}-Q\left(\mathbf{x}\left(k\right)\right)\right) \tag{9.14}$$

and

$$\mathbf{x}\left(k-1\right) \equiv \aleph_{\mathrm{b}}\left(\mathbf{x}\left(k\right)\right) \text{ in which } \mathbf{x}\left(k\right)=\mathbf{A}\mathbf{x}\left(k-1\right)+\mathbf{B}\left(\overline{\mathbf{u}}-Q\left(\mathbf{x}\left(k-1\right)\right)\right), \tag{9.15}$$

respectively. Denote

$$x'(k) \equiv b_N \bar{u} + \sum_{i=1}^{N-1} b_{N-i}(\bar{u} - Q(x_i(k))) - \sum_{i=1}^{N} a_{N-i} x_i(k) \tag{9.16}$$

and

$$\hat{\mathbf{x}}(k) \equiv \left[\frac{x'(k) - Q(x'(k)a_N)b_N}{a_N}, \quad x_1(k), \quad \cdots, \quad x_{N-1}(k) \right]^T. \tag{9.17}$$

Then

$$\mathbf{A}\hat{\mathbf{x}}(k) + \mathbf{B}(\bar{\mathbf{u}} - Q(\hat{\mathbf{x}}(k))) =$$

$$\left[x_1(k), \quad \cdots, \quad x_{N-1}(k), \quad x_N(k) + \frac{b_N}{a_0} \left(Q(x'(k)a_N) - Q\left(\frac{x'(k) - Q(x'(k)a_N)b_N}{a_N} \right) \right) \right]^T. \tag{9.18}$$

If $|x'(k)| > |b_N|$, then

$$Q(x'(k) - Q(x'(k)a_N)b_N) = Q(x'(k)). \tag{9.19}$$

Hence,

$$Q(x'(k)a_N) - Q\left(\frac{x'(k) - Q(x'(k)a_N)b_N}{a_N} \right) = Q(x'(k)a_N) - Q(x'(k)a_N) = 0 \tag{9.20}$$

and

$$\mathbf{A}\hat{\mathbf{x}}(k) + \mathbf{B}(\bar{\mathbf{u}} - Q(\hat{\mathbf{x}}(k))) = [x_1(k), \quad \cdots, \quad x_N(k)]^T = \mathbf{x}(k). \tag{9.21}$$

If $|x'(k)| < |b_N|$, then

$$Q(x'(k) - Q(x'(k)a_N)b_N) = -Q(x'(k)a_N)Q(b_N) \tag{9.22}$$

and

$$Q(x'(k)a_N) - Q\left(\frac{x'(k) - Q(x'(k)a_N)b_N}{a_N} \right) = Q(x'(k)a_N) + Q(x'(k)a_N)Q(a_N b_N). \tag{9.23}$$

If $Q(a_N b_N) = -1$, then

$$Q(x'(k)a_N) - Q\left(\frac{x'(k) - Q(x'(k)a_N)b_N}{a_N} \right) = 0 \tag{9.24}$$

and

$$\mathbf{A}\hat{\mathbf{x}}(k) + \mathbf{B}(\bar{\mathbf{u}} - Q(\hat{\mathbf{x}}(k))) = \mathbf{x}(k). \tag{9.25}$$

Hence, if $|x'(k)| > |b_N|$ or $|x'(k)| < |b_N|$ and $Q(a_N b_N) = -1$, then the one of the possible backward dynamics of the SDMs can be defined as

$$\aleph_b(\mathbf{x}(k)) = \left[\frac{x'(k) - Q(x'(k)a_N)b_N}{a_N}, \quad x_1(k), \quad \cdots, \quad x_{N-1}(k) \right]^T. \tag{9.26}$$

Suppose the above conditions are satisfied $\forall k \in Z$. Denote

$$\wp \equiv \{ \mathbf{x}(0) : \aleph_{\mathrm{f}}(\mathbf{x}(k)) \in \wp \quad \text{for } k \geq 0, \quad \text{and} \quad \aleph_{\mathrm{b}}(\mathbf{x}(k)) \in \wp \quad \text{for } k \leq 0 \} \tag{9.27}$$

and a map $\Im : \wp \to \wp$ such that

$$\Im(\mathbf{x}) \equiv \mathbf{A}\mathbf{x} + \mathbf{B}(\bar{\mathbf{u}} - Q(\mathbf{x})). \tag{9.28}$$

Lemma 9.2. If $|x'(k)| > |b_N|$ or $|x'(k)| < |b_N|$ and $Q(a_N b_N) = -1$, then $\wp$ is an invariant set under $\Im$. That is, $\Im(\wp) = \wp$. Hence, if $\exists k_0 \in Z$ such that $\mathbf{x}(k_0) \in \wp$, then $\mathbf{x}(k) \in \wp \ \ \forall k \in Z$.

Proof. The result follows directly from the definition. ■

Although it was reported in [7] that if the invariant set exists and there exists an initial condition in the invariant set, then the local stability is guaranteed. However, the conditions on the existence of the invariant map are not explored and this relationship is explored in Lemma 9.2.

It is worth noting that if $\exists k_0 \in Z$ such that $\mathbf{x}(k_0) \in \Re^N \setminus \wp$, then $\mathbf{x}(k) \in \Re^N \setminus \wp \ \ \forall k \in Z$, and $\mathbf{x}(k)$ may diverge. Hence, it is not sufficient to conclude the global stability of the SDMs.

The importance of Lemma 9.2 is that it provides information for formulating a fuzzy membership function to achieve local stability.

9.4. Fuzzy Impulsive Control Strategy

9.4.1. Fuzzy Impulsive Control Strategy

Fig. 9.2 shows the block diagram of how the fuzzy impulsive controller influenced the SDMs. As discussed in Section 9.1, the fuzzy impulsive controller determines the controlled state vectors and reset the state variables of the loop filter to the controlled state variables via a reset circuit. To determine the controlled state vectors, two step procedures are employed. The first step of the procedure is the training phase in which the invariant set and the set of state vectors that exhibits limit cycle behaviors are learnt through training. By generating a set of DC signals inputted to the system with different initial condition, the state vectors are tested if they form an invariant set and exhibit limit cycle behaviors or not. The second step of the procedure is the control phase in which the controlled state vectors are determined and the state variables are reset to the corresponding values. The details are discussed in below.

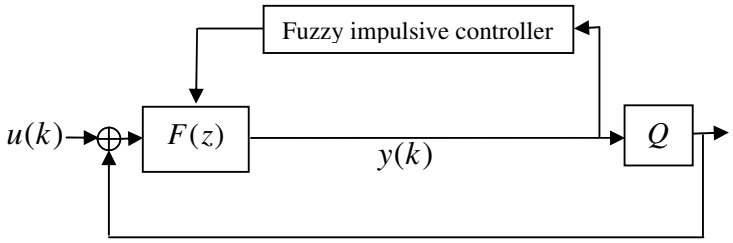

Fig. 9.2. The block diagram of the interpolative SDM under the fuzzy impulsive control strategy.

As discussed in Section 9.1, we want to minimize the effect of audio clicks. To achieve this goal, we want to minimize the distance between the original state vectors $\mathbf{x}(k_0+1)$ and the controlled state vectors $\mathbf{x}^c(k_0+1)$. However, $\mathbf{x}(k_0+1)$ may be outside the desired bounded region B_0, so we define a vector $\mathbf{x}^r \in B_0$ such that $\left\|\mathbf{x}(k_0+1)-\mathbf{x}^r\right\|_2$ is minimum and our goal is to minimize the distance between $\mathbf{x}^c(k_0+1)$ and $\mathbf{x}^r$ via a triangular fuzzy membership function as follows:

$$\mu_{\text{continuous}}\left(\mathbf{x}^c(k_0+1)\right) \equiv \left(\prod_{i=1}^{N} f_i\left(\mathbf{x}^c(k_0+1), \mathbf{x}^r\right)\right)^{\frac{1}{N}}, \tag{9.29}$$

where

$$f_i\left(\mathbf{x}^c(k_0+1), \mathbf{x}^r\right) \equiv \begin{cases} \dfrac{x_i^c(k_0+1)-V_{cc}}{x_i^r-V_{cc}} & x_i^r \le x_i^c(k_0+1) \le V_{\text{cc}} \\ \dfrac{x_i^c(k_0+1)+V_{cc}}{x_i^r+V_{cc}} & -V_{\text{cc}} \le x_i^c(k_0+1) \le x_i^r \\ 0 & \text{otherwise} \end{cases}. \tag{9.30}$$

Since a triangular fuzzy membership function is employed and $\mathbf{x}^r \in B_0$, $\mu_{\text{continuous}}\left(\mathbf{x}^c(k_0+1)\right)=1$ when $\mathbf{x}^c(k_0+1)=\mathbf{x}^r$, $\mu_{\text{continuous}}\left(\mathbf{x}^c(k_0+1)\right)=0$ when $\mathbf{x}^c(k_0+1) \in \Re^N \setminus B_0$, and $0 \le \mu_{\text{continuous}}\left(\mathbf{x}^c(k_0+1)\right) \le 1$ $\forall \mathbf{x}^c(k_0+1) \in \Re^N$. Hence, $\mu_{\text{continuous}}\left(\mathbf{x}^c(k_0+1)\right)$ force the new state vectors $\mathbf{x}^c(k_0+1)$ to be within B_0. Note that if $\mathbf{x}(k_0+1) \in B_0$, then $\mathbf{x}^r = \mathbf{x}(k_0+1)$

and there will be no audio click effect by setting $\mathbf{x}^c(k_0+1)=\mathbf{x}^r$. Since $\mu_{\text{continuous}}(\mathbf{x}^c(k_0+1))$ captures the knowledge on the closeness between $\mathbf{x}^c(k_0+1)$ and $\mathbf{x}^r$, and the effect of audio clicks is minimized if $\mathbf{x}^c(k_0+1)$ is closed to $\mathbf{x}^r$, this fuzzy membership function can minimize the effect of audio clicks.

As discussed in Section 9.1 and 9.2, the local stability criterion is an important issue. According to Lemma 9.2, if $|x'(k)|>|b_N|$ or $|x'(k)|<|b_N|$ and $Q(a_N b_N)=-1$, then $\mathbf{x}(k)\in\wp\ \ \forall k\in Z$ if $\exists k_0\in Z$ such that $\mathbf{x}(k_0)\in\wp$. However, the trajectory may not be inside B_0 because $\wp$ is usually not equal to B_0. In order to guarantee that the trajectory is bounded within B_0, we want the controlled state vectors to be inside $\wp\cap B_0$, that is, $\mathbf{x}^c(k_0+1)\in\wp\cap B_0$. Supposing that $\wp\cap B_0\neq\emptyset$. This implies that there exist state vectors that achieve local stability within the set of the desired bounded state variables. Denote $\mathbf{x}^p\in\wp\cap B_0$ such that $\left\|\mathbf{x}(k_0+1)-\mathbf{x}^p\right\|_2$ is minimum. If $\wp\cap B_0\neq\emptyset$, $|x'(k)|>|b_N|$ or $|x'(k)|<|b_N|$ and $Q(a_N b_N)=-1$, then we define the following triangular fuzzy membership function:

$$\mu_{\text{stable}}(\mathbf{x}^c(k_0+1))\equiv\left(\prod_{i=1}^{N} f_i(\mathbf{x}^c(k_0+1),\mathbf{x}^p)\right)^{\frac{1}{N}}. \tag{9.31}$$

Since a triangular fuzzy membership function is employed and $\mathbf{x}^p\in B_0$, $\mu_{\text{stable}}(\mathbf{x}^c(k_0+1))=0$ when $\mathbf{x}^c(k_0+1)\in\Re^N\setminus B_0$, $\mu_{\text{stable}}(\mathbf{x}^c(k_0+1))=1$ when $\mathbf{x}^c(k_0+1)=\mathbf{x}^p$ and $0\le\mu_{\text{stable}}(\mathbf{x}^c(k_0+1))\le 1\ \ \forall\mathbf{x}^c(k_0+1)\in\Re^N$. Hence, $\mu_{\text{stable}}(\mathbf{x}^c(k_0+1))$ force the new state vectors $\mathbf{x}^c(k_0+1)$ to be within B_0. If $\mathbf{x}(k_0+1)\in\wp\cap B_0$, then $\mathbf{x}^p=\mathbf{x}(k_0+1)$. By setting $\mathbf{x}^c(k_0+1)=\mathbf{x}^p$, the local stability criterion is satisfied. Since $\mu_{\text{stable}}(\mathbf{x}^c(k_0+1))$ captures the knowledge on the closeness between $\mathbf{x}^c(k_0+1)$ and $\mathbf{x}^p$, which also reflects the closeness between $\mathbf{x}^c(k_0+1)$ and the set of state vectors that achieved local stability within the desired bounded region, this fuzzy membership function can capture the local stability criterion into the system.

However, if $\wp \bigcap B_0 = \emptyset$, then $\mathbf{x}^p$ does not exist. Or if $\exists k' \in Z$ such that $|x'(k)| < |b_N|$ and $Q(a_N b_N) = 1$, then the local stability criterion is not guaranteed. In this case, the SDM may suffer from an instability problem. In order to avoid this case to be happened, if $\wp \bigcap B_0 = \emptyset$, or if $\exists k' \in Z$ such that $|x'(k)| < |b_N|$ and $Q(a_N b_N) = 1$, then we define

$$\mu_{\text{stable}}\left(\mathbf{x}^c(k_0+1)\right) \equiv \begin{cases} \delta_{\text{stable}} & \mathbf{x}^c(k_0+1) \in B_0 \\ 0 & \mathbf{x}^c(k_0+1) \in \Re^N \setminus B_0 \end{cases}, \tag{9.32}$$

where $1 \geq \delta_{\text{stable}} > 0$ and δ_{stable} is very closed to zero. The reasons why small value of δ_{stable} can avoid the instability problem are discussed in Section 9.4.2. Since the fuzzy membership value of the state vectors outside B_0 is exactly equal to zero, this fuzzy membership function will force the new state vectors $\mathbf{x}^c(k_0+1)$ to be within B_0.

As discussing in Section 9.1, the occurrence of limit cycle behaviors should be avoided. Since $\bigcup_{\forall P>0} \Psi_P$ is the set of state vectors that exhibiting limit cycle behavior, we do not want to move the new state vectors $\mathbf{x}^c(k_0+1)$ into $\bigcup_{\forall P>0} \Psi_P$. Moreover, we do not want to move $\mathbf{x}^c(k_0+1)$ into $\bigcup_{\forall k \leq k_0} \{\mathbf{x}(k)\}$ too. This is because after a certain number of iterations, the state vectors may go to the same points in the state space and cause limit cycle behaviors to occur. Define

$$PER(k_0) \equiv \left(\bigcup_{\forall P>0} \Psi_P \right) \cup \left(\bigcup_{\forall k \leq k_0} \{\mathbf{x}(k)\} \right). \tag{9.33}$$

If $PER(k_0) \bigcap B_0 = B_0$, then all the state vectors in B_0 may result limit cycle behaviors and this situation should be avoided. On the other hand, if $PER(k_0) \bigcap B_0 = \emptyset$, then we cannot find a state vector $\mathbf{x}^q \in B_0 \bigcap PER(k_0)$ such that $\left\| \mathbf{x}(k_0+1) - \mathbf{x}^q \right\|_2$ is minimum. Hence, if $PER(k_0) \bigcap B_0 = B_0$ or $PER(k_0) \bigcap B_0 = \emptyset$, we define the fuzzy membership function as

$$\mu_{\text{aperiodic}}\left(\mathbf{x}^c(k_0+1)\right) \equiv \begin{cases} \delta_{\text{aperiodic}} & \mathbf{x}^c(k_0+1) \in B_0 \\ 0 & \mathbf{x}^c(k_0+1) \in \Re^N \setminus B_0 \end{cases}, \tag{9.34}$$

where $1 \geq \delta_{\text{aperiodic}} > 0$ and $\delta_{\text{aperiodic}}$ is also very closed to zero. Similarly, the reason why small value of $\delta_{\text{aperiodic}}$ can avoid the occurrence of limit cycle behaviors is discussed in Section 9.4.2. Otherwise, we define the fuzzy membership function as

$$\mu_{\text{aperiodic}}\left(\mathbf{x}^c\left(k_0+1\right)\right) \equiv \begin{cases} 1-\left(\prod_{i=1}^{N} f_i\left(\mathbf{x}^c\left(k_0+1\right), \mathbf{x}^q\right)\right)^{\frac{1}{N}} & \mathbf{x}^c\left(k_0+1\right) \in B_0 \\ 0 & \mathbf{x}^c\left(k_0+1\right) \in \Re^N \setminus B_0 \end{cases} \quad .(9.35)$$

Since f_i is a triangular fuzzy membership function and $\mathbf{x}^q \in B_0$, $\mu_{\text{aperiodic}}\left(\mathbf{x}^c\left(k_0+1\right)\right) = 0$ when $\mathbf{x}\left(k_0+1\right) \in B_0 \cap PER\left(k_0\right)$ because $\mathbf{x}^q = \mathbf{x}\left(k_0+1\right)$ when $\mathbf{x}\left(k_0+1\right) \in B_0 \cap PER\left(k_0\right)$, $\mu_{\text{aperiodic}}\left(\mathbf{x}^c\left(k_0+1\right)\right) = 0$ when $\mathbf{x}^c\left(k_0+1\right) \in \Re^N \setminus B_0$ and $0 \leq \mu_{\text{aperiodic}}\left(\mathbf{x}^c\left(k_0+1\right)\right) \leq 1 \quad \forall \mathbf{x}^c\left(k_0+1\right) \in \Re^N$. Hence, $\mu_{\text{aperiodic}}\left(\mathbf{x}^c\left(k_0+1\right)\right)$ force the new state vectors $\mathbf{x}^c\left(k_0+1\right)$ to be within B_0. Since $\mu_{\text{aperiodic}}\left(\mathbf{x}^c\left(k_0+1\right)\right)$ captures the knowledge on the separation between $\mathbf{x}^c\left(k_0+1\right)$ and $B_0 \cap PER\left(k_0\right)$, which also reflects the separation between $\mathbf{x}^c\left(k_0+1\right)$ and the set of state vectors within the desired bounded region that exhibits limit cycle behaviors, $\mu_{\text{aperiodic}}\left(\mathbf{x}^c\left(k_0+1\right)\right)$ can be used to avoid the occurrence of limit cycle behaviors.

Once the fuzzy membership functions are defined, we can define the fuzzy impulsive control law as follows:

If $\mathbf{A}\mathbf{x}\left(k_0\right) + \mathbf{B}\left(\overline{\mathbf{u}} - Q\left(\mathbf{x}\left(k_0\right)\right)\right) \in \Re^N \setminus B_0$, then the fuzzy impulsive controller will reset the state variables of the loop filter to $\mathbf{x}^c\left(k_0+1\right)$ where $\mathbf{x}^c\left(k_0+1\right)$ is the state vector such that the following function is maximized,

$$\mu_{\mathbf{x}^c\left(k_0+1\right)}\left(\mathbf{x}^c\left(k_0+1\right)\right) \equiv \max_{\mathbf{x}^c\left(k_0+1\right) \in \Re^N} \left(\mu_{\text{stable}}\left(\mathbf{x}^c\left(k_0+1\right)\right) \mu_{\text{aperiodic}}\left(\mathbf{x}^c\left(k_0+1\right)\right) \mu_{\text{continuous}}\left(\mathbf{x}^c\left(k_0+1\right)\right)\right)^{1/3} \quad .(9.36)$$

Otherwise, no control force is applied to the SDMs.

Lemma 9.3. $\forall \overline{u} \in \Re$, $\forall \mathbf{x}\left(0\right) \in \Re^N$, $\forall a_i \in \Re$ for $i = 0,1,\cdots,N$ and $\forall b_j \in \Re$ for $j = 1,\cdots,N$, $\mathbf{x}^c\left(k\right) \in B_0$ for $k > 0$.

Proof. It can be seen that $\forall \bar{u} \in \Re$, $\forall \mathbf{x}(0) \in \Re^N$, $\forall a_i \in \Re$ for $i = 0,1,\cdots,N$, $\forall b_j \in \Re$ for $j = 1,\cdots,N$, $\forall k_0 \geq 0$ and $\forall \mathbf{x}^c(k_0+1) \in B_0$, $\mu_{\text{continuous}}(\mathbf{x}^c(k_0+1)) > 0$ and $\mu_{\text{stable}}(\mathbf{x}^c(k_0+1)) > 0$. If $PER(k_0) \cap B_0 = B_0$ or $PER(k_0) \cap B_0 = \emptyset$, then $\mu_{\text{aperiodic}}(\mathbf{x}^c(k_0+1)) > 0$. Although $\mu_{\text{aperiodic}}(\mathbf{x}^c(k_0+1)) = 0$ if $PER(k_0) \cap B_0 \neq B_0$, $PER(k_0) \cap B_0 \neq \emptyset$ and $\mathbf{x}(k_0+1) \in B_0 \cap PER(k_0)$, since $PER(k_0) \cap B_0 \neq B_0$, $\exists \mathbf{x}^c(k_0+1) \in B_0 \setminus PER(k_0)$ such that $\mu_{\text{aperiodic}}(\mathbf{x}^c(k_0+1)) > 0$. Hence, $\exists \mathbf{x}^c(k_0+1) \in B_0 \setminus PER(k_0)$ such that $\mu_{\mathbf{x}^c(k_0+1)}(\mathbf{x}^c(k_0+1)) > 0$. As a result, if $\mathbf{A}\mathbf{x}(k_0) + \mathbf{B}(\bar{\mathbf{u}} - Q(\mathbf{x}(k_0))) \in \Re^N \setminus B_0$, then the fuzzy impulsive controller will reset the state vector of the loop filter to $\mathbf{x}^c(k_0+1)$ where $\mathbf{x}^c(k_0+1) \in B_0 \setminus PER(k_0)$. If $\mathbf{A}\mathbf{x}(k_0) + \mathbf{B}(\bar{\mathbf{u}} - Q(\mathbf{x}(k_0))) \in B_0$, since no control force is applied to the SDM, $\mathbf{x}^c(k_0+1) = \mathbf{x}(k_0+1) \in B_0$. Hence, $\mathbf{x}^c(k) \in B_0$ for $k > k_0$. Thus, $\forall k_0 \geq 0$, $\mathbf{x}^c(k) \in B_0$ for $k > 0$. And this completes the proof. ■

It is worth noting that different values of $\bar{u}$, $\mathbf{x}(0)$, a_i for $i = 0,1,\cdots,N$ and b_j for $j = 1,\cdots,N$, will affect the existence of $\wp$ and $\bigcup_{\forall P>0} \Psi_P$. However, Lemma 9.3 is still applied even though $\wp = \emptyset$ or $\wp = B_0$, and $\bigcup_{\forall P>0} \Psi_P = \emptyset$ or $\bigcup_{\forall P>0} \Psi_P = B_0$. Hence, Lemma 9.3 guarantees that the controlled trajectory is bounded within B_0 no matter what the input step size, the initial condition and the filter parameters are. This is very important because we do not want the trajectory of the SDM to be unbounded if the input step size is increased, or the initial condition or the loop filter of the SDMs are changed. Another advantage of this fuzzy impulsive control strategy is that we can alter the maximum bound of the state variables easily by setting the value of V_{cc} appropriately, which is independent of the input step size, the initial condition and the filter parameters.

Lemma 9.4. $\forall \bar{u} \in \Re$, $\forall \mathbf{x}(0) \in \Re^N$, $\forall a_i \in \Re$ for $i = 0,1,\cdots,N$ and $\forall b_j \in \Re$ for $j = 1,\cdots,N$, $\left\| \mathbf{x}^c(k+1) - \mathbf{x}^r \right\|_2 \leq 2V_{\text{cc}}\sqrt{N}$ for $k > 0$.

Proof. Since $\forall \overline{u} \in \Re$, $\forall \mathbf{x}(0) \in \Re^N$, $\forall a_i \in \Re$ for $i = 0,1,\cdots,N$ and $\forall b_j \in \Re$ for $j = 1,\cdots,N$, $\mathbf{x}^c(k) \in B_0$ for $k > 0$, the result follows directly. ■

The importance of this Lemma is that it guarantees the norm of the difference between $\mathbf{x}^r$ and $\mathbf{x}^c(k+1)$ being bounded by $2V_{cc}\sqrt{N}$, no matter what the input step size, the initial condition and the filter parameters are. As discussed in above, we do not want the norm of the difference between $\mathbf{x}^r$ and $\mathbf{x}^c(k+1)$ to be too large because the effect of audio clicks may be too large for these situations.

Lemma 9.5. If $\exists k_0 \in Z$ such that $PER(k) \bigcap B_0 \neq B_0$ for $k \geq k_0$, and $\mathbf{A}\mathbf{x}(k_0) + \mathbf{B}(\overline{\mathbf{u}} - Q(\mathbf{x}(k_0))) \in \Re^N \setminus B_0$, then $\exists M > 0$ such that $\mathbf{x}^c(k) = \mathbf{x}^c(k+M)$ for $k > k_0$.

Proof. The proof follows directly from Lemma 9.3. ■

The importance of this Lemma is that it states the condition that limit cycle behaviors do not occur when the fuzzy impulsive control strategy is applied at once. We will show the contrast in Section 9.5 that the clipping control strategy usually results in the limit cycle behaviors, while our approach will minimize the occurrence of limit cycle behaviors.

9.4.2. Parameters in the Fuzzy Impulsive Controller

There are only three parameters in the fuzzy impulsive control strategy. They are V_{cc}, $\delta_{\text{aperiodic}}$ and δ_{stable}. V_{cc} is the maximum allowable bound on each state variable and this value is determined based on the real situations, such as the hardware constraints and the safety specifications, etc. For example, if the hardware operates normally in a safe condition only when the state variables are bounded by 20V, then V_{cc} may be set accordingly. For the parameters $\delta_{\text{aperiodic}}$ and δ_{stable}, the fuzzy impulsive controller works properly $\forall \delta_{\text{aperiodic}} \in (0,1]$ and $\forall \delta_{\text{stable}} \in (0,1]$. However, since $\delta_{\text{aperiodic}}$ represents the fuzzy membership value of how to avoid the occurrence of limit cycle at $\mathbf{x}^c(k_0+1)$ when $PER(k_0) \bigcap B_0 = B_0$ or $PER(k_0) \bigcap B_0 = \emptyset$, and all the state vectors in B_0 may cause the trajectory to exhibit limit cycle behaviors if $PER(k_0) \bigcap B_0 = B_0$, we suggest the

SDM control designers to set this value as a small number closed to zero, such as 10^{-3}. For δ_{stable}, since it represents the fuzzy membership value of the local stability of the SDM at $\mathbf{x}^c(k_0+1)$ when $\wp \cap B_0 = \emptyset$, or if $\exists k' \in Z$ such that $|x'(k)| < |b_N|$ and $Q(a_N b_N) = 1$, and in this case, the SDM may exhibit divergent behavior if the fuzzy impulsive control strategy is not applied, we recommend the SDM control designers to set this value as a small number closed to zero too, for example, 10^{-3}.

9.4.3. Complexity Issue

Although more fuzzy rules and sophisticated fuzzy engine will improve the performance of the SDMs, this will increase the complexity of the system and may cause real time processing problems, particular for audio applications [2]. The Nyquist rate for audio signal is 44.1kHz [2], since the input signals are typically oversampled at 64 or 128 [2], the number of samples inputted to the SDM per second is 2.8224M or 5.6448M. Because several megasamples are needed to process per second, only three basic fuzzy rules are captured and only a simple fuzzy engine is used to reduce the complexity for processing. According to the simulation results shown in Section 9.5, these three basic rules and a simple fuzzy engine is enough for achieving the objectives.

9.4.4. Implementation of the Fuzzy Impulsive Controller

As discussed in the above, the fuzzy impulsive controller resets the state variables of the loop filter to the controlled state variables of $\mathbf{x}^c(k_0+1)$ if $\mathbf{A}\mathbf{x}(k_0) + \mathbf{B}(\overline{\mathbf{u}} - Q(\mathbf{x}(k_0))) \in \Re^N \setminus B_0$, and $\mathbf{x}^c(k_0+1)$ is calculated based on equation (9.36). Numerical solvers, such as MATLAB or MATCAD, can be employed for solving equation (9.36). To reset the state variables of the loop filter, many existing reset circuits can be employed [8].

9.5. Simulation Results

To illustrate our results, a fifth order SDM with loop filter transfer function

$$\frac{20z^{-1}-74z^{-2}+103.0497z^{-3}-64.0015z^{-4}+14.9584z^{-5}}{1-5z^{-1}+10.0025z^{-2}-10.0075z^{-3}+5.0075z^{-4}-1.0025z^{-5}} \quad (9.37)$$

is illustrated. This fifth order SDM is commonly employed in the industry [2]. The SDM can be implemented via the Jordan form [2] and can be realized as the following state space equation

$$\tilde{\mathbf{x}}(k+1)=\tilde{\mathbf{A}}\tilde{\mathbf{x}}(k)+\tilde{\mathbf{B}}(u(k)-y(k)) \quad (9.38)$$

for $k \geq 0$, where

$$y(k)=Q(\tilde{\mathbf{C}}\tilde{\mathbf{x}}(k)), \quad (9.39)$$

$$\tilde{\mathbf{A}} \equiv \begin{bmatrix} 1 & 0 & 0 & 0 & 0 \\ 1 & 1 & -0.0018 & 0 & 0 \\ 0 & 1 & 1 & 0 & 0 \\ 0 & 0 & 1 & 1 & -0.000685 \\ 0 & 0 & 0 & 1 & 1 \end{bmatrix}, \tilde{\mathbf{B}} \equiv \begin{bmatrix} 1 \\ 0 \\ 0 \\ 0 \\ 0 \end{bmatrix} \text{ and } \tilde{\mathbf{C}} \equiv \begin{bmatrix} 20 \\ 6 \\ 1 \\ 0.09375 \\ 0.00589 \end{bmatrix}^T . \quad (9.40)$$

Assume that the initial condition of this SDM is zero, that is, $\tilde{\mathbf{x}}(0)=[0,\ 0,\ 0,\ 0,\ 0]^T$. By using a simple transformation, this SDM can be realized by the direct form and the corresponding initial condition is $\mathbf{x}(0)=[0,\ -5,\ 28.5,\ 32.25,\ 35.9793]^T$ when $u=0.75$. We can check that the trajectory of this SDM is bounded for this initial condition ($\tilde{\mathbf{x}}(0)=[0,\ 0,\ 0,\ 0,\ 0]^T$) if the input step size is approximately between -0.71 and 0.75, and may diverge if the input step size is outside this range. The relationship between the maximum absolute value of the state variables (realized in the direct form) and the input step size is plotted in Fig. 9.3. From the simulation result, we can see that even though the trajectory is bounded for this range of input step size, the maximum absolute value of the state variables is between 20.0523 and 59.4633, which may be too large for some practical applications [2]. Fig. 9.3 also shows the plot of the maximum absolute value of the state variables (also realized in the direct form) for $k>0$ versus the input step size when the fuzzy impulsive control strategy is applied at $V_{cc}=20$. According to Lemma 9.3, the maximum absolute value of the state variables of the controlled SDM is bounded by V_{cc} for $k>0$ and $\forall \overline{u} \in \Re$, even though $|\overline{u}| \geq V_{cc}$. Hence, we can guarantee that the state variables are bounded by 20.

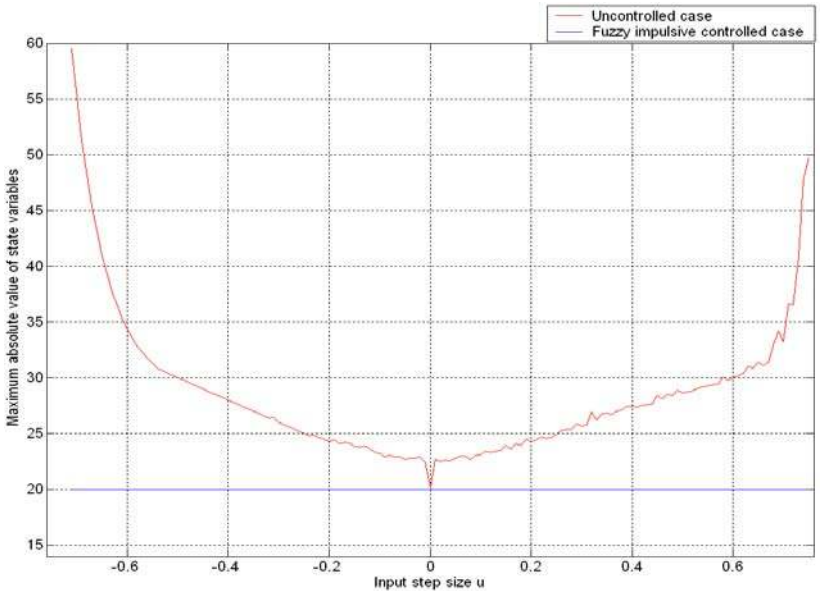

Fig. 9.3. Plot of the maximum absolute value of the state variables (realized in direct form) against the input step size when $\tilde{\mathbf{x}}(0)=[0,\ 0,\ 0,\ 0,\ 0]^T$.

This SDM is not globally stable. That means, $\exists\tilde{\mathbf{x}}(0)\in\Re^N$ such that the trajectory is unbounded. For example, when $\bar{u}=0.75$, Fig. 9.4a and Fig. 9.4b show the responses of $x_1(k)$ with $\tilde{\mathbf{x}}(0)=[0,\ 0,\ 0,\ 0,\ 0]^T$ and $\tilde{\mathbf{x}}(0)=[0.001,\ 0,\ 0,\ 0,\ 0]^T$, respectively. It can be seen from Fig. 9.4a and Fig. 9.4b that even though the SDM exhibits acceptable behavior when $\tilde{\mathbf{x}}(0)=[0,\ 0,\ 0,\ 0,\ 0]^T$ and the difference between these two initial conditions is very small, the SDM exhibits divergent behavior when $\tilde{\mathbf{x}}(0)=[0.001,\ 0,\ 0,\ 0,\ 0]^T$ and the behaviors of the SDM for these two different initial conditions are very different. On the other hand, according to Lemma 9.3, the maximum absolute value of the state variables is always bounded by V_{cc} for $k>0$ and $\forall\mathbf{x}(0)\in\Re^N$ if the fuzzy impulsive control strategy is applied. Fig. 9.4c and Fig. 9.4d show the corresponding state responses when the fuzzy impulsive control strategy is applied at $V_{cc}=40$. From the simulation result, we see that the

SDM exhibits acceptable behavior with the state variables bounded by V_{cc} for both of these two initial conditions.

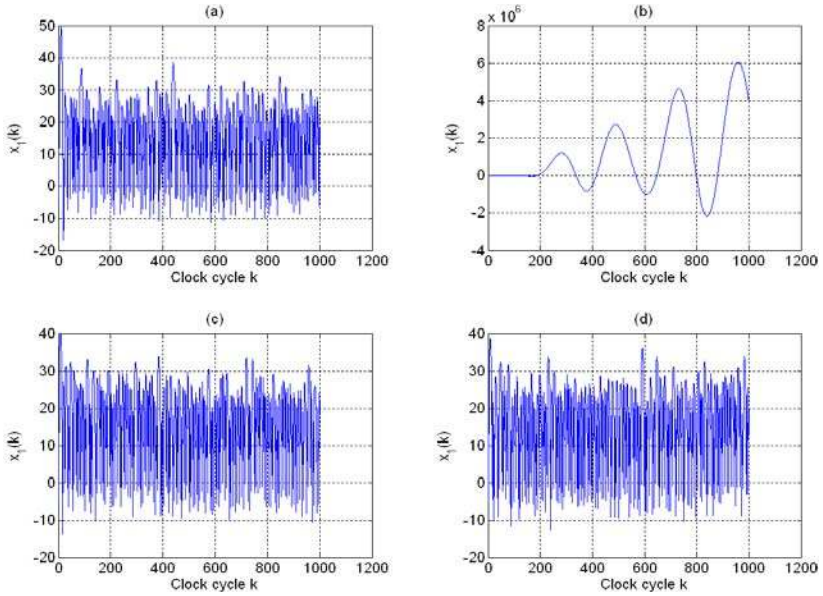

Fig. 9.4. The response of $x_1(k)$ when $\bar{u} = 0.75$ and (a) initial condition $\tilde{\mathbf{x}}(0) = [0,\ 0,\ 0,\ 0,\ 0]^T$ when no control strategy is applied. (b) initial condition $\tilde{\mathbf{x}}(0) = [0.001,\ 0,\ 0,\ 0,\ 0]^T$ when no control strategy is applied. (c) initial condition $\tilde{\mathbf{x}}(0) = [0,\ 0,\ 0,\ 0,\ 0]^T$ when the fuzzy impulsive control strategy with $V_{cc} = 40$ is applied. (d) initial condition $\tilde{\mathbf{x}}(0) = [0.001,\ 0,\ 0,\ 0,\ 0]^T$ when the fuzzy impulsive control strategy with $V_{cc} = 40$ is applied.

For comparison with other control strategies, consider the time delay feedback control strategy suggested in [6], in which the controller is in the form of $-K_c\left(1 - z^{-1}\right)$. Denote λ_i for $i = 1,2,\cdots,6$ be the poles of the effective loop filter. Since λ_i for $i = 1,2,\cdots,6$ depends on the value of K_c, it can be shown that $\max_{i=1,2,\cdots,6} |\lambda_i| > 1 \ \ \forall K_c \in \Re$ and the minimum value of $\max_{i=1,2,\cdots,6} |\lambda_i|$ occurs at $K_c = 0$. When $K_c = 0$, it reduces to the uncontrolled case. By selecting a value of K_c which is very closed to

zero, for example $K_c = 2\times10^{-5}$, and setting the initial condition and the input step size as the previous values, that is, $\mathbf{x}(0)=[0,\ -5,\ 28.5,\ 32.25,\ 35.9793,\ 39.5612]^T$ and $\bar{u}=0.75$ (the initial condition is determined based on zero initial condition of the Jordan form), it is found that the trajectory diverges as shown in Fig. 9.5. Hence, the time delay feedback control strategy fails to stabilize this SDM.

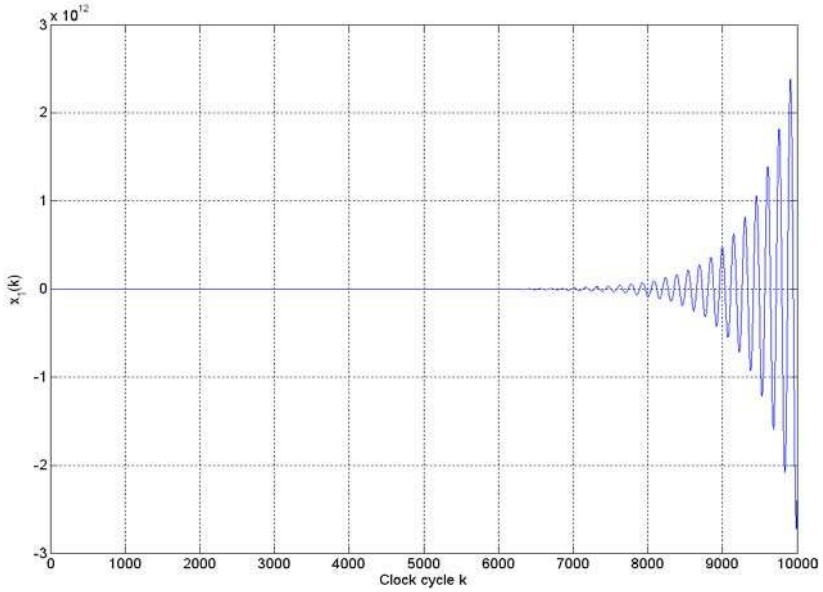

Fig. 9.5. The response of $x_1(k)$ with input step size $\bar{u}=0.75$ and initial condition $\mathbf{x}(0)=[0,\ -5,\ 28.5,\ 32.25,\ 35.9793,\ 39.5612]^T$ when the time delay feedback control strategy with $K_c = 2\times10^{-5}$ is applied.

To compare the fuzzy impulsive control strategy to the clipping control strategy, that is, set $x_i(k)=V_{cc}Q(x_i(k))$ if $|x_i(k)|\geq V_{cc}$ for $i=1,2,\cdots,N$, it is found that limit cycle behaviors may occur if the clipping control strategy is applied. Fig. 9.6 shows the magnitude response of $s(k)$ when $\bar{u}=0.75$, $\tilde{\mathbf{x}}(0)=[0,\ 0,\ 0,\ 0,\ 0]^T$ and the clipped level is set at 40. It can be seen from Fig. 9.6 that there is an impulse located at $\frac{\pi}{2}$ if the clipping control strategy is applied, which

demonstrates that the SDM exhibits a limit cycle with period 2. On the other hand, the spectrum is quite flat for the SDM when the fuzzy impulsive control strategy is applied with $V_{cc} = 40$, which demonstrates that the SDM exhibits acceptable behavior and the limit cycle behavior is avoided.

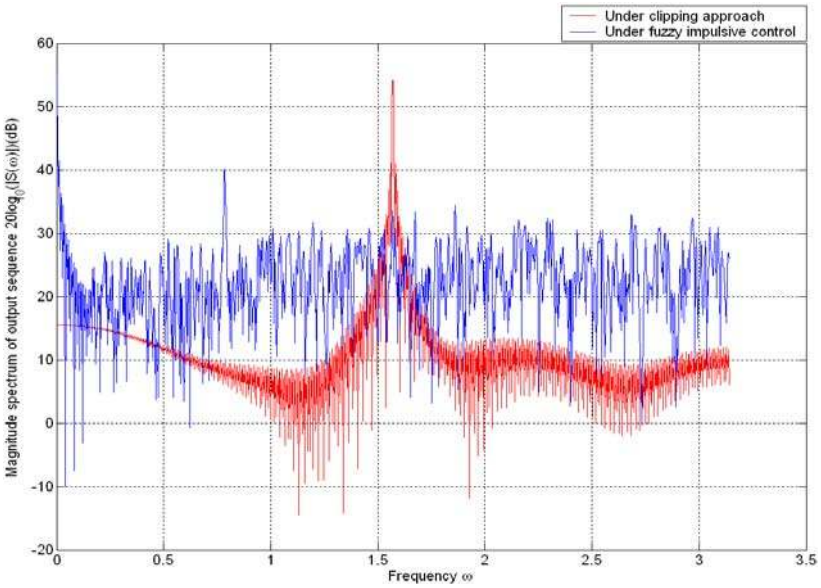

Fig. 9.6. Magnitude response of the output sequence when $\bar{u} = 0.75$ and initial condition $\tilde{\mathbf{x}}(0) = [0, \ 0, \ 0, \ 0, \ 0]^T$ for both the clipping and fuzzy impulsive control strategies are applied with the state variables bounded by 40.

Fig. 9.7 shows the SNR of SDMs under the clipping control strategy with the clipped level set at 28. SNR is calculated using [9], where the frequency of the input sinusoidal signals is $\frac{2}{3}$ of the passband bandwidth. The oversampling ratio is 64, and initial conditions are given by $\tilde{\mathbf{x}}(0) = [0, \ 0, \ 0, \ 0, \ 0]^T$. It can be seen from Fig. 9.7 that the SNR of both the clipping and fuzzy impulsive control strategies with the state variables bounded by 28 are the same when the input magnitude is less than 0.52. This is because both the maximum absolute value of the state variables (realized in the direct form) do not exceed 28 in this input magnitude range. However, if the input magnitude exceeds this range,

the SNR corresponding to the clipping control strategy may drop to less than 1.2562dB because of the occurrence of limit cycle behaviors. On the other hand, the SDM performs normally under the fuzzy impulsive control strategy. Hence, the SNR of the SDM under the fuzzy impulsive control strategy has an average of 41.8281dB improvement compared to the clipping control strategy for outside this input magnitude range.

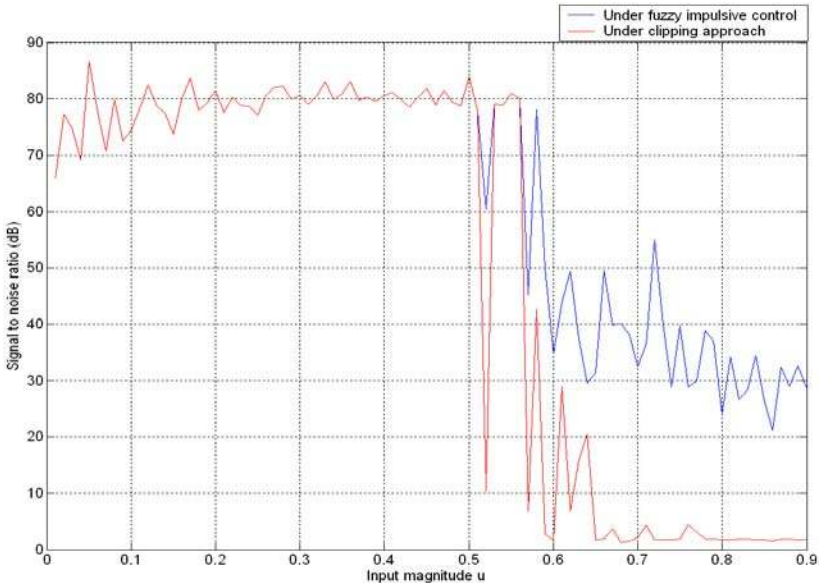

Fig. 9.7. SNR of SDMs when input sinusoidal frequency is $\frac{2}{3}$ of the passband bandwidth, initial condition $\tilde{\mathbf{x}}(0)=[0,\ 0,\ 0,\ 0,\ 0]^T$ and the state variables are bounded by 28.

It can be seen from Fig. 9.8 that the probability of the control force to be applied by the fuzzy impulsive control strategy is 0.0135 for the input magnitude range greater than or equal to 0.52, as opposed to a probability of 0.6926 for the clipping control strategy. Hence, the number of reset action on the state variables of the loop filter is much reduced when applying fuzzy impulsive control strategy. This is because the fuzzy impulsive control strategy tends to reset the state vectors inside the invariant set if it exists and the state vectors will tend to stay inside the invariant set without applying control force again soon afterwards. This demonstrates that the fuzzy impulsive control strategy is more efficient than the clipping control strategy.

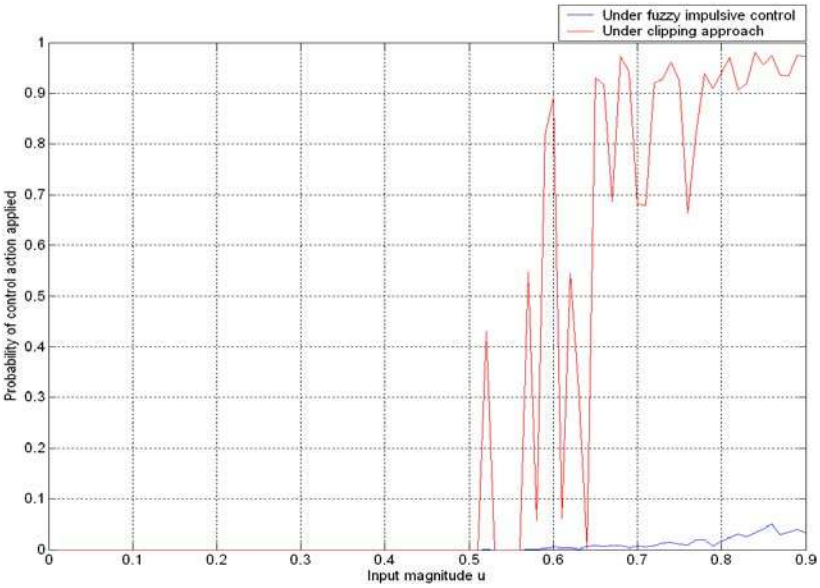

Fig. 9.8. Probability of control force applied to the SDM when the input sinusoidal frequency is $\frac{2}{3}$ of the passband bandwidth, initial condition $\tilde{\mathbf{x}}(0)=[0,\ 0,\ 0,\ 0,\ 0]^T$ and the state variables are bounded by 28.

To verify the independence of the filter parameters on the fuzzy impulsive control strategy, consider another fifth order SDM with the following transfer function [2]

$$\frac{0.7919z^{-1}-2.8630z^{-2}+3.9094z^{-3}-2.3873z^{-4}+0.5498z^{-5}}{1-5z^{-1}+10.0023z^{-2}-10.0069z^{-3}+5.0069z^{-4}-1.0023z^{-5}}. \quad (9.41)$$

This SDM is also widely used in the industry [2]. The trajectory of this SDM with $\bar{u}=0.59$ and $\tilde{\mathbf{x}}(0)=[0,\ 0,\ 0,\ 0,\ 0]^T$ is shown in Fig. 9.9a, and it can be seen from Fig. 9.9a that the trajectory diverges. On the other hand, when the fuzzy impulsive control strategy is applied with $V_{cc}=2$, according to Lemma 9.3, the maximum absolute value of the state variables (realized in the direct form) is always bounded by V_{cc} for $k>0$, $\forall a_i \in \Re$ for $i=0,1,\cdots,N$ and $\forall b_j \in \Re$ for $j=1,\cdots,N$, as shown in Fig. 9.9b.

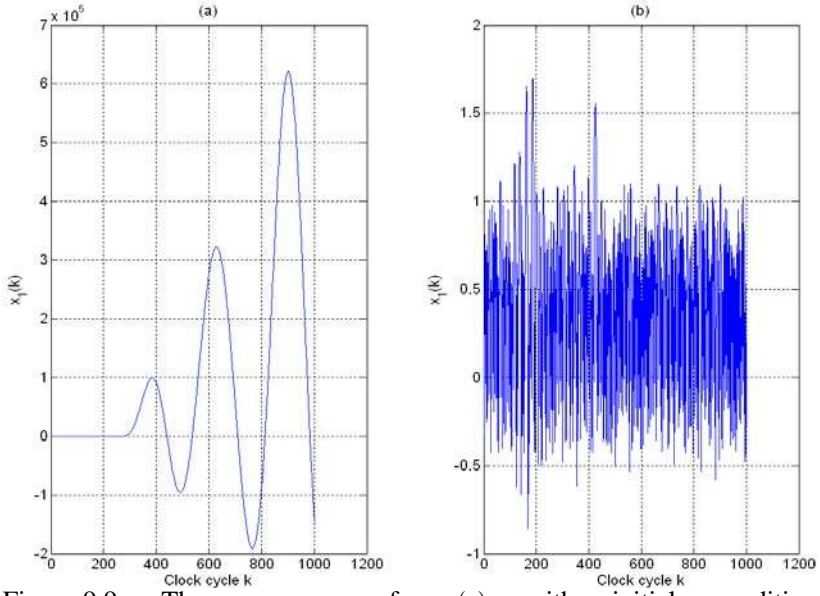

Fig. 9.9. The response of $x_1(k)$ with initial condition $\tilde{\mathbf{x}}(0) = [0,\ 0,\ 0,\ 0,\ 0]^T$ and input step size $\bar{u} = 0.59$ (a) when no control strategy is applied. (b) when the fuzzy impulsive control strategy with $V_{\infty} = 2$ is applied.

9.6. Conclusion

In this chapter, we have suggested the fuzzy impulsive control strategy for the stabilization of high order interpolative SDMs in which the occurrence of limit cycle behaviors and the effect of audio clicks are minimized. Since the effective poles of the loop filter are not affected by the control strategy, the SNR performance of the SDMs is maintained or improved after control. Moreover, the controlled trajectory is guaranteed to be bounded no matter what the input step size, the initial condition and the filter parameters are. Comparisons between the fuzzy impulsive control strategy and some existing control strategies show that the fuzzy impulsive control strategy is much effective in terms of producing much higher SNR and efficient in terms of requiring less control force applied to the system.

References

[1] J. C. Candy, A use of limit cycle oscillations to obtain robust analog-to-digital converters, *IEEE Transactions on Communications* **COM-22**, 298-305, (1974).

[2] D. Reefman and E. Janssen, Signal processing for direct stream digital: A tutorial for digital sigma delta modulation and 1-bit digital audio processing, *Philips Research*, *Eindhoven*, *White Paper* (2002).

[3] G. Ginis and J. M. Cioffi, Optimum bandwidth partitioning with analog-to-digital converter constraints, *IEEE Transactions on Communications* **52**, 1010-1018, (2004).

[4] S. Kawahito, A. Cerman, K. Aramaki and Y. Tadokoro, A weak magnetic field measurement system using micro-fluxgate sensors and delta-sigma interface, *IEEE Transactions on Instrumentation and Measurement* **52**, 103-110, (2003).

[5] T. Zourntos and D. A. Johns, Variable-structure compensation of delta-sigma modulators: stability and performance, *IEEE Transactions on Circuits and Systems—I: Fundamental Theory and Applications* **49**, 41-53, (2002).

[6] A. Uçar, Bounding integrator output of sigma-delta modulator by time delay feedback control, *IEE Proceedings—Circuits, Devices and Systems* **150**, 31-37, (2003).

[7] R, Schreier, M. V. Goodson and B. Zhang, An algorithm for computing convex positively invariant sets for delta-sigma modulators, *IEEE Transactions on Circuits and Systems—I: Fundamental Theory and Applications* **44**, 38-44, (1997).

[8] S. Chattopadhyay and V. Ramanarayaanan, A single-reset-integrator-based implementation of line-current-shaping controller for high-power-factor operation of flyback rectifier, *IEEE Transactions on Industrial Applications* **38**, 490-499, (2002).

[9] R. Schreier, *The delta-sigma modulators toolbox version 6.0* Analog Devices Inc., (2003).